Electromagnetic induction imaging through metallic shields

A thesis submitted to University College London
for the degree of Doctor of Philosophy
in the faculty of Mathematical and Physical Sciences

Brendan John Darrer

Department of Physics and Astronomy

January 2017

Declaration

I, Brendan John Darrer confirm that the work presented in this thesis is my own. Where information has been derived from other sources, I confirm that this has been indicated in the thesis.

Signed……………………………………………..……..Brendan Darrer

Date: 24th January 2016

Ph.D. thesis

Electromagnetic induction imaging through metallic shields

Brendan J. Darrer
January 2017

First Supervisor: Prof. Ferruccio Renzoni
Second Supervisor: Dr. Mark Ellerby

Abstract

Electromagnetic induction imaging has wide potential application in the disciplines of medicine, security, industry, geophysics and scientific research in general. The present study focuses on the applications in the security industry and in particular on providing a new tool for cargo screening in the context of the detection of illicit trafficking of special nuclear materials. The thesis reports a proof-of-concept study of electromagnetic imaging of metallic objects concealed inside electromagnetic enclosures. The sample object is imaged via phase variation measurements between the driver and sensor coils due to inductive coupling between the coils and the object, these images being proportional conductivity maps. For effective imaging through conductive barriers, subtraction of images at different frequencies was carried out in order to isolate the contribution of the concealed object. The present study validates electromagnetic induction imaging for nuclear security applications.

The resolution of the system was determined using an edge detection algorithm applied to the images and found to be ~30 mm. The instrumentation employs Helmholtz coils for the driving field and an array of 20 × 20 sensor coils mounted on a wooden apparatus, with fixtures being non-metallic to magnetically isolate the experiment. Further studies were made to determine the compatibility of the modality to image in 3D by imaging Copper and Aluminium disks raised above the sensor array. The experiment gave a positive result being able to detect up to 80 mm depth (lift-off height) for 150 mm diameter disks and up to 40 mm depth for the 20 mm diameter disks. A study was performed to determine the penetrating power of the system by imaging through

Aluminium enclosures of varying thickness. It was found that a Copper disk of 40 mm diameter by 2 mm thickness could be imaged through an Aluminium box even when the wall thickness was 20 mm, at 10 to 200 Hz driving frequency.

This work has been published by the author [1]–[4].

Acknowledgments

I wish to thank Prof. Ferruccio Renzoni (UCL) who directed this research, for his guidance, advice and patience. Similarly I am indebted to Dr. Paul Bartlett (UCL), Dr. Joseph Watson (AWE), Dr. Mark Ellerby (UCL), Dr. Neil Gaspar (AWE) and Dr. Caroline Shenton-Taylor (AWE) for their contributions.

This work was funded by AWE, the Home Office, the Ministry of Defence and UCL via the Impact Studentship scheme in the United Kingdom.

Contents

List of Figures

List of Tables

List of Symbols

B — Magnetic flux density (T or Wb·m^{-2})

D — Electric displacement field (C·m^{-2})

E — Electric field (V·m^{-1})

H — Magnetic field strength (A·m^{-1})

M — Magnetization (A·m^{-1})

J — Current density (A·m^{-2})

V — Electric potential / Voltage (V) / Potential difference (p.d.) in volts (V)

m — magnetic moment (A·m^{2})

$\phi_{B,S}$ — Magnetic flux through open surface area S (Wb)

δ — Skin depth (mm)

ε — Electrical permittivity (F·m^{-1})

μ — Magnetic permeability (H·m^{-1})

χ_v — Volumetric magnetic susceptibility (dimensionless)

σ — Electrical conductivity (S·m^{-1})

κ — Complex electrical conductivity (S·m^{-1})

ω — Angular frequency (rad/s)

ϕ or $\Delta\phi$ — Phase angle between the signal in the driver and a sensor coils (degrees / °)

ϕ or $\Delta\phi$ — Phase angle between primary magnetic field and total magnetic field detected by a sensor coil (degrees / °)

Nomenclature

MIT — Magnetic Induction Tomography

EII — Electromagnetic Induction Imaging

PEP — Passive Electromagnetic Properties

ECT — Electrical Capacitance Tomography

EIT — Electrical Impedance Tomography

ERT — Electrical resistance tomography

NDE — Non-Destructive Evaluation

MT — Magnetotellurics

OAM — Optical Atomic Magnetometer

1 Introduction

This study undertakes the development of a new Electromagnetic Induction Imaging (EII) system. The system images metallic specimens concealed inside metallic and ferromagnetic enclosures, developed from proof-of-principle to a practical technique. Work has been focused on penetration through metallic enclosures and the resolution of the system. This is to aid development of a device for security applications. The physics used in this study and most other MIT research is classical electromagnetism, i.e. Maxwell's equations.

Electromagnetic Induction Imaging also called Magnetic Induction Tomography (MIT) [5]–[14] is the youngest member of a family of non-invasive electrical imaging techniques that was first reported around 1992-3. Figure 1.1(a) shows a standard arrangement of eight coils for this type of tomography, where each coil acts as a transmitter and receiver of magnetic fields. Figure 1.1(b) shows a corresponding cross sectional image of two metallic screws placed upright in the upper right and lower left of the central part of the array, shown in aerial photograph of figure 1.1(a).

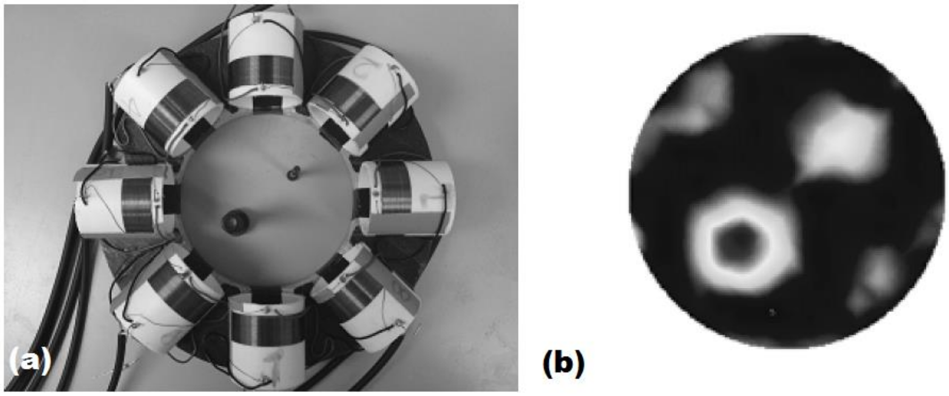

Figure 1.1. (a) Circular array of 8 coils of a standard MIT system. Each coil acts as a transmitter and receiver. (b) The Corresponding conductivity map shows a cross section of two metallic screws placed upright, in the upper right and lower left central region of the coil array as shown in (a) [13].

MIT is sensitive to a specimen’s passive electromagnetic properties (PEP) of conductivity, permeability and permittivity and is a non-contact electromagnetic imaging technique. It has been shown that MIT data can reconstruct images in the first two of these PEP parameters and possibly permittivity [11]. Images are normally reconstructed as conductivity maps as shown in the example image of figure 1.1(b).

MIT has been researched for medical imaging to produce cross sections of the human body and in industry for inspection of vessels, pipelines, materials and metal detection [9][14]. MIT has potential applications in security alongside the already established metal detecting devices at airports and other security locations.

In some studies MIT images are reconstructed via solution to an inverse problem. An ‘inverse problem’ is the calculation from a set of observations of the properties that caused these observations. In MIT this would be the calculation of the conductivity spatial distribution from a set of voltage measurements of coils arranged around the sample. This is shown in the block diagram of figure 1.2, where the solution to the inverse problem is represented by the reconstruction algorithm.

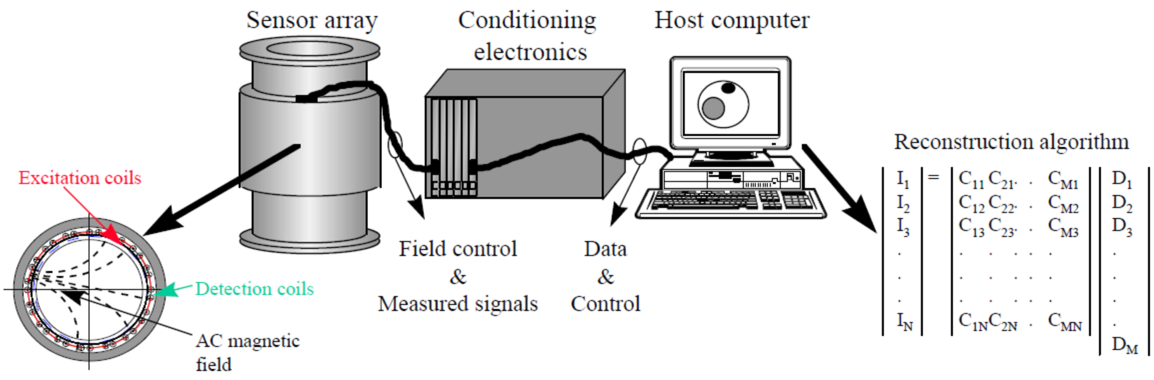

Figure 1.2. Block diagram of a standard MIT system [15].

Another example is calculating density regions of the earth from gravitational field measurements. Therefore the inverse problem calculates the cause from the results which is conceptually and technically challenging. It does this by first modelling the forward problem which are the results from the cause and determining the inverse of this. This is achieved by an iterative process starting from an initial first guess of, say, the conductivity of the sample. The forward problem is derived by applying Maxwell's equations to the set up [16][17].

For the work reported in this thesis the inverse problem has not been implemented and instead images are reconstructed by taking advantage of the planar geometry. The image is made up of the spatial distributions of phase difference measurements between the signal in the driver coil and the sensor coil (figure 1.3), representing the distributions of conductivity in the sample object.

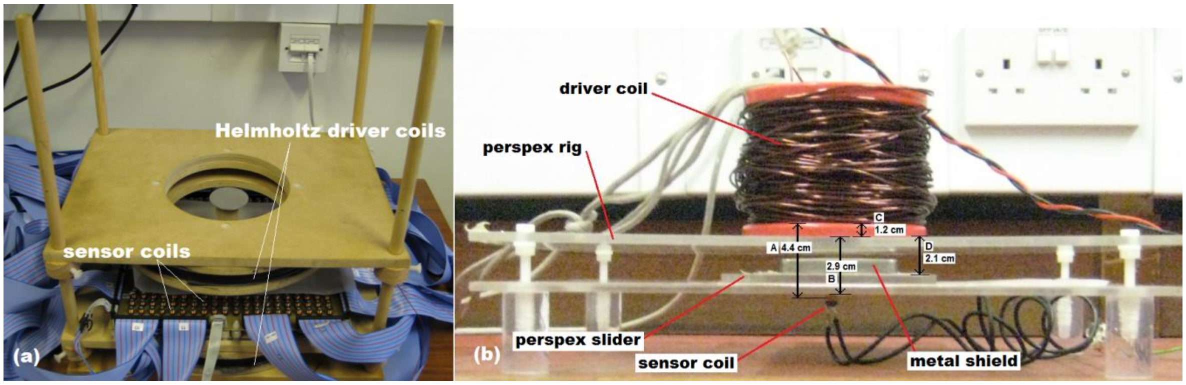

Figure 1.3. Imaging systems described in this work that take advantage of planar geometry. (a) Helmholtz coils and sensor coil array described in Section 2 and 4 onwards. (b) Single driver coil and ferrite cored inductor as the sensor coil, described in Section 3.

Electrical imaging techniques have been used in medicine, industry, environmental monitoring and archaeology [9]. Examples of such techniques are described as follows.

Electrical impedance tomography (EIT) is a technique used in medicine to estimate electrical properties inside the human body. Electrodes are attached to the surface of a human subject and small alternating currents applied. The resulting electrical potential measurements taken from other electrodes provide a data set from which conductivity or permittivity distributions can be inferred via ‘inverse problem’ methods [18]–[20]. Figure 1.4 shows an example of an EIT cross sectional image of human thigh and bone.

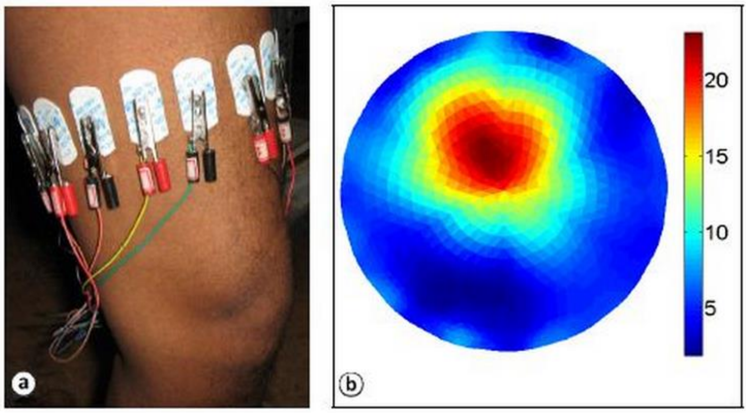

Figure 1.4. (a) EIT photo of electrodes attached around a human thigh. (b) Corresponding resistivity image of thigh with bone as a cross section [21].

Electrical resistance tomography (ERT) or electrical resistivity tomography is a geophysical imaging technique. It calculates the resistivity distribution of sub surface structures from a large number of resistance measurements. These are taken at the surface or by electrodes suspended in boreholes. It is similar to EIT but uses direct current, where the image reconstruction produces a conductivity or resistivity map of sub surface layers. An illustrative example is given in figure 1.5.

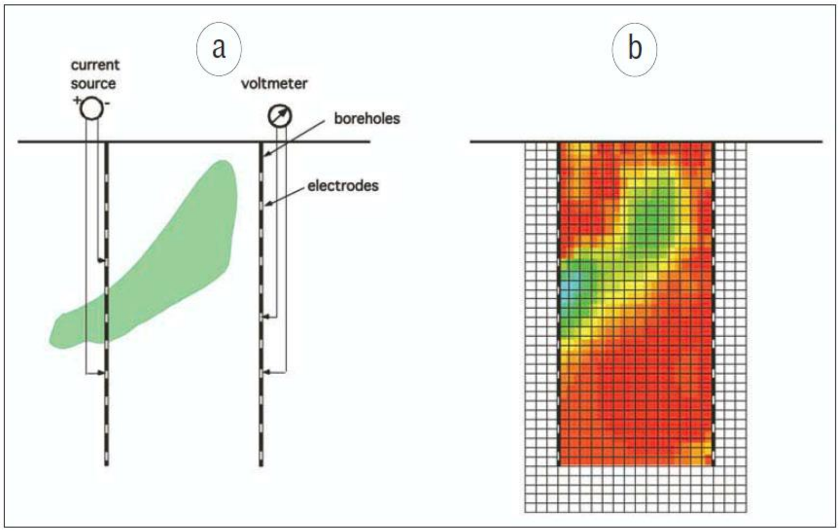

Figure 1.5. Schematic of ERT measurement and corresponding cross sectional image. (a) An electrode array is aligned down a borehole that provides a current source and a second borehole for measurement of voltage by other electrodes, using a cross borehole technique. Current is passed through two electrodes and the voltage is measured from two other electrodes, four measurements are required to scan the area or volume. (b) Illustrative reconstruction of the ERT cross sectional image [22].

ERT has applications in both geophysical prospecting and in imaging inside process vessels and pipelines [20] [22] [23].

Electrical capacitance tomography (ECT) involves calculation of the spatial distribution of dielectric permittivity inside an object from capacitive measurements taken on the outside. This calculation normally involves the solution to an inverse problem. The ECT electrodes need to be sufficiently large in order to detect significant changes in capacitance (figure 1.6).

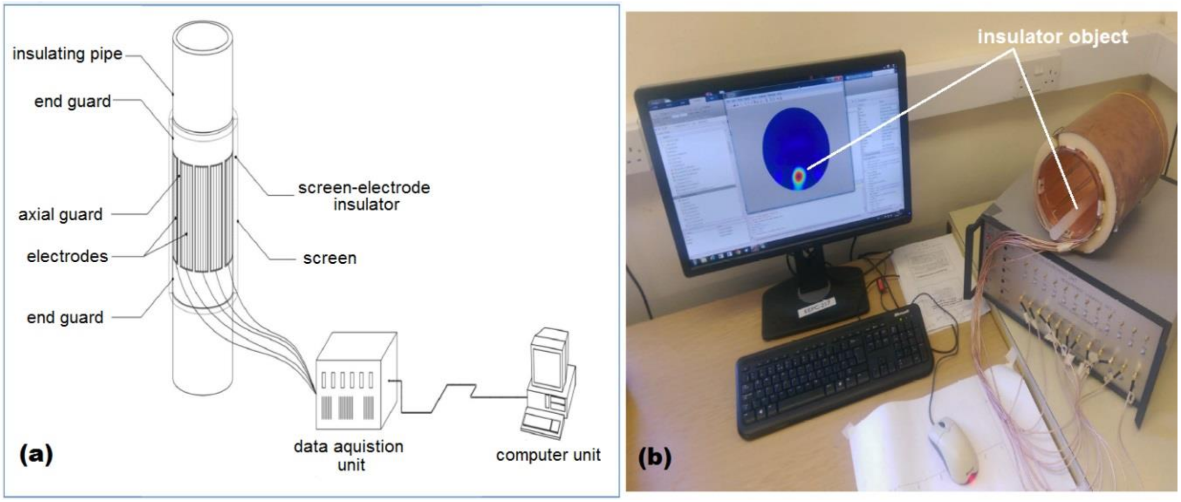

Figure 1.6. (a) Diagram of an ECT set up. (b) Photo of corresponding ECT system with an imaged insulator object on screen [24].

It has applications in the oil industry, distinguishing between oil and gas and between oil and water mixtures via image analysis. Although it is low resolution in comparison with other electrical imaging techniques, this has not been an impediment as only rough estimations of oil/water/gas mixtures are required. The speed of real time imaging in ECT makes up for the lack of resolution, where there are now imaging systems that can generate one image every 10 ms [20][25][26]. ECT imaging is fast due to the simplicity and speed of the linear back-projection algorithm implemented, but the low resolution is due to the limited number of capacitance measurements that can be made and the severely ill-posed ECT inverse problem [26].

Metal detection is related to MIT because it relies on the same principle of eddy current induction. It has a long history in both archaeological and forensic sciences [27] and is primarily used for the detection of foreign bodies in food, land mines and historical artefact hunting [20]. A typical metal detector is one based on the induction balance shown in figure 1.7.

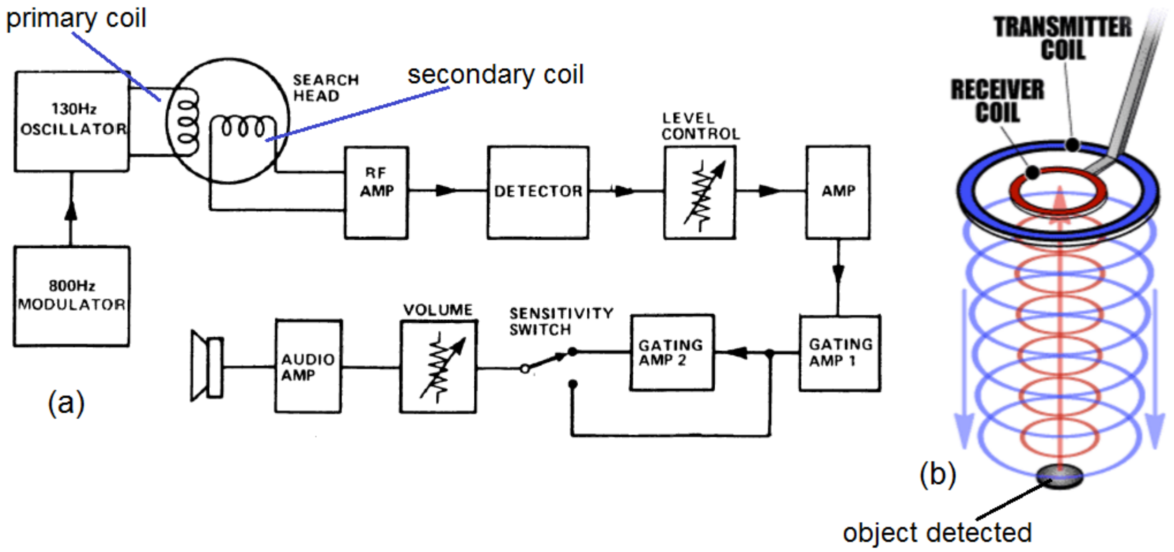

Figure 1.7. (a) Block diagram of an Induction Balance metal detector [28]. (b) Picture of transmitter (primary) and receiver (secondary) coils showing an object detected for the same type of metal detector [29].

A primary coil provides an AC magnetic field. The primary and secondary coils are arranged so as to have as low mutual inductance as possible between them. This is to minimize direct coupling between the transmitted and received fields so that virtually no signal is detected in the absence of a metal object. The gating module in figure 1.7(a) allows only the minutest signal when no object is present. When the metal object is brought into the vicinity of the coils, eddy currents are generated in it by the transmitted field and a secondary field is detected. This is due to a noticeable change in mutual inductance between the coils giving a higher contrast of signal compared to the absence of a metal object. As a result current increases in the secondary coil's circuit producing a louder volume through the speakers, indicating the object's presence. Voltage amplitude and phase responses in secondary coil signal contains information on the target's material properties [30][31].

Applications of eddy current imaging have been applied to geophysical surveys in the oil and gas industry. Schlumberger Ltd., a company supplying these surveys uses combined measurements of electrical and magnetic fields termed magnetotellurics (MT) to map out subsurface rock formations in search of oil fields as shown in figure 1.8.

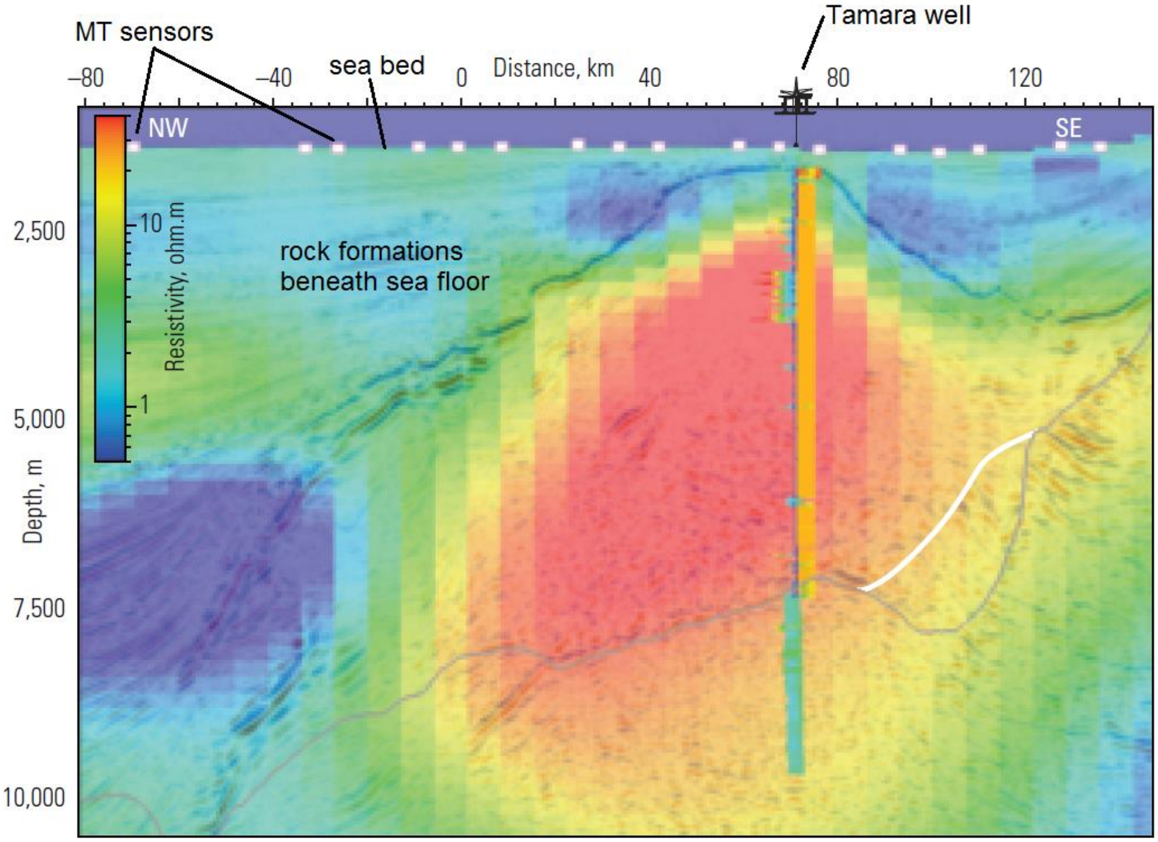

Figure 1.8. Example of resistivity map from MT measurements showing salt intrusion in pink. The data was confirmed by drilling at the Tarmara well [32].

MT makes use of naturally occurring ions emitted from the sun [32]. Some of these ions leak through the upper atmosphere ionizing particles and forming a plasma of charged particles, making the ionosphere a conducting layer. When this plasma combines with the earth’s magnetic field, electromagnetic (EM) pulses are generated, resonating in the ionosphere along the magnetic field lines. These planar EM fields propagate through the non-conducting lower atmosphere and through the sea to rocks below the sea bed, with a frequency range between 0.001 Hz and 10 kHz. A time varying EM signal induces eddy currents in the conductive rock layers depending on its resistivity. The eddy currents in turn induce a magnetic field that propagates back from the rock formation. Sensor coils on the sea bed can then detect this response. Being a poor conductor, oil shows up as low conductivity in the reconstructed image maps. The technique employs recent advances in 3D modelling and inversion technology. A similar technique using an artificial source field can penetrate up to 10 km beneath the sea floor, using a typical frequency range of 0.05 to 5 Hz [32].

More recently MIT methods have been developed using resonant LCR circuits to create Q-factor and resonant frequency images, providing a novel method of material characterisation [33]. The Q-factor of the circuit is $Q = R\sqrt{\frac{C}{L}}$ and resonant frequency, $f_{res} = \frac{1}{2\pi\sqrt{LC}}$, where R is resistance, C is capacitance and L is inductance. Example images are given in figure 1.9 of a 2 cm diameter Aluminium disk. A graph showing the relationship of Q-factor and resonant frequency with respect to conductivity, of 25 mm square by 1 mm thick metallic objects (metals with different conductivity), is shown in figure 1.10 [33].

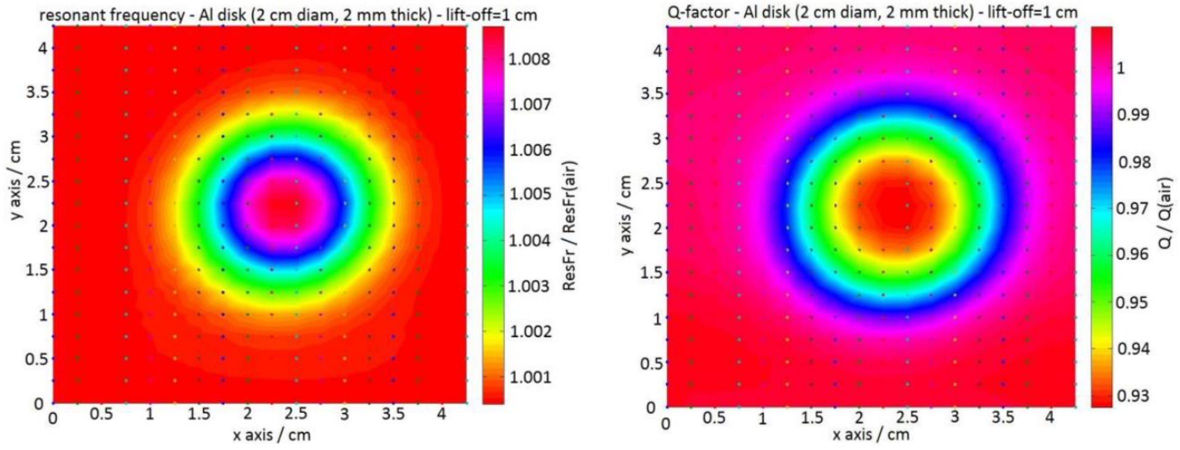

Figure 1.9. Aluminium disk of 20 mm diameter by 2 mm thick imaged by resonant frequency (left) and Q-factor (right) in 2 dimensional space [33].

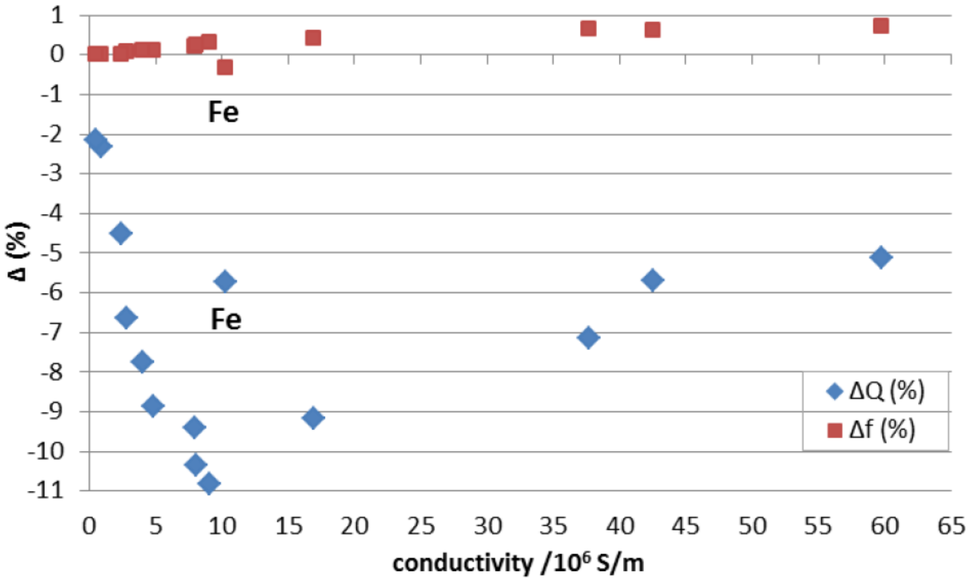

Figure 1.10. Percentage change in Q-factor (ΔQ) and resonant frequency (Δf), w.r.t. coils in air, versus conductivity of square metallic objects 25 x 25 x 1 mm. Q-factor was shown to vary more than resonant frequency [33].

Additionally a more major development in MIT has been its application in the quantum regime with laser-pumped optical atomic magnetometers (OAMs) [34], where these optical sensors have very high sensitivity compared with standard MIT coils, by a factor of 10^7. This is because the Rubidium (Rh) atoms, located in a vapour cell and used to measure the magnetic field via a laser, are much freer to respond to the magnetic field than a pick-up coil. In other words the Rubidium atoms do not have the constraints of a pick-up coil such as inducing electrons into motion and resistivity of coil wire [34][35]. This OAM technique may revolutionise the field and enable highly penetrating images of oil-gas-water inside metallic pipes.

In regards to understanding the principles of MIT as applied to imaging of metallic specimens, the literature of eddy current non-destructive evaluation (NDE) has proved beneficial, as it describes the principle of eddy currents and electromagnetic induction in more detail than standard physics textbooks. Eddy current NDE is a closely related field to metallic MIT, but uses a scanning probe over the sample object’s surface and has different image reconstruction algorithms than MIT. NDE textbooks [36] [37] [38] and [39] are useful resources. From P. B. Nagy [39], the cross over between these two disciplines (MIT and NDE) can be seen in terms of eddy current imaging of metallic specimens for examination of a range of its properties, such as conductivity images to show flaws and grain structure of Aluminium and Titanium alloy specimens [39] (see figure 1.11). Both MIT and NDE produce conductivity images, although they arrive at these by different methods.

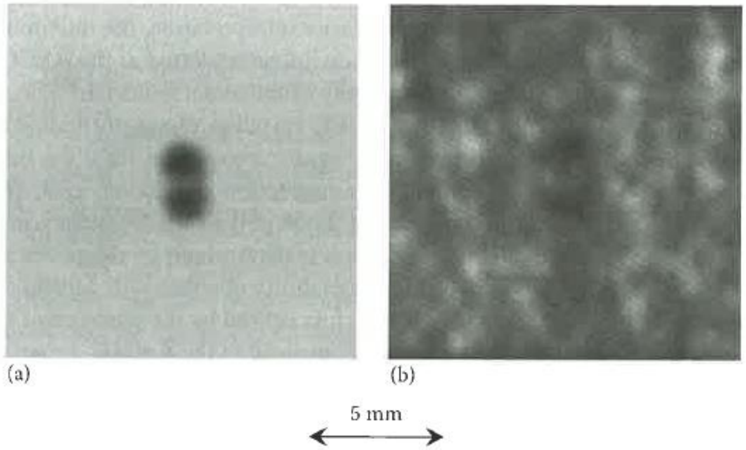

Figure 1.11. Eddy current conductivity images of 0.65 mm long cracks for: (a) Aluminium alloy (Al2024) and (b) Titanium alloy (Ti-6Al-4V). Aluminium alloy exhibits very uniform conductivity and the 8 shaped flaw is therefore easily seen. Titanium alloy by contrast exhibits highly non-uniform conductivity and therefore the 8 shaped flaw is barely separated from the background noise [39].

Eddy currents were first discovered by Foucault in 1830: in 1879 D. E. Hughes performed the first NDE experiments using eddy currents, being able to distinguish between some metal and alloy samples. This involved balancing coils by the use of sounds from a telephone receiver [31]. In place of an oscillator, Hughes employed ticks from a clock picked up by a microphone for the excitation signal. When a metallic sample was placed inside a pair of identical coils, a disturbance of the balance was registered due to induced eddy currents in the sample, changing the coils' inductance (figure 1.12).

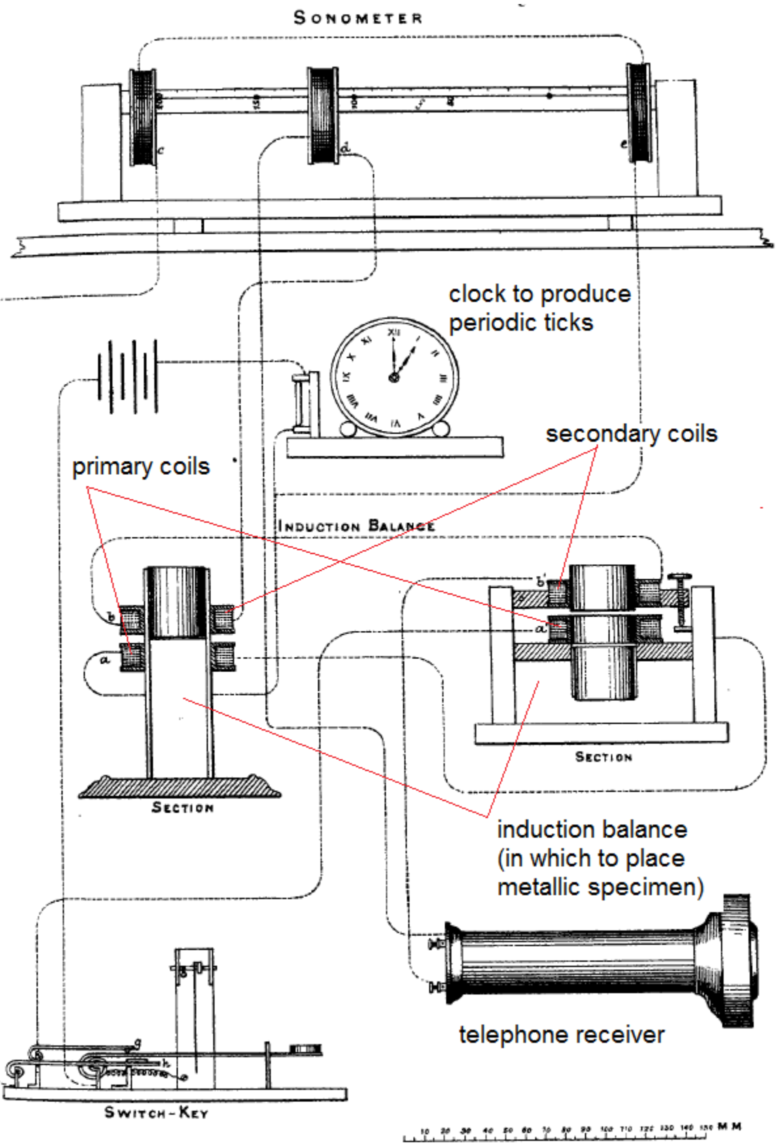

Figure 1.12. Original schematic of Induction Balance used by D.E. Hughes to measure conductivity of metal and alloy specimen [31].

By listening to ticks on the telephone receiver (invented by A. C. Bell two years earlier) connected to a sonometer (a sound measuring device), Hughes was able to adjust the coil's position on the sonometer until the sound was no longer heard. The distance in degrees of millimetres through which the sonometer's coil was moved determined the sample's material property [31][37]. Hughes determined the conductivity of different metals using Copper as a reference [31][37][40]. Little other progress was made until the 1920s when devices began to be used in the steel industry. In World War II instrumentation and theory improved and by the early 1950s began the modern era of this field [37].

A new MIT system was designed and built for this project (figure 1.13 (a & b)). It images the conductivity of a metallic specimen, represented as the voltage phase difference (phase) between the signals of the driver coil and pick-up-coil type sensors. A Helmholtz coil assembly establishes a sinusoidal near-to-uniform driving field (primary), pointing parallel to the vertical axis of the coils; and excites eddy currents in the specimen that generate a secondary field.

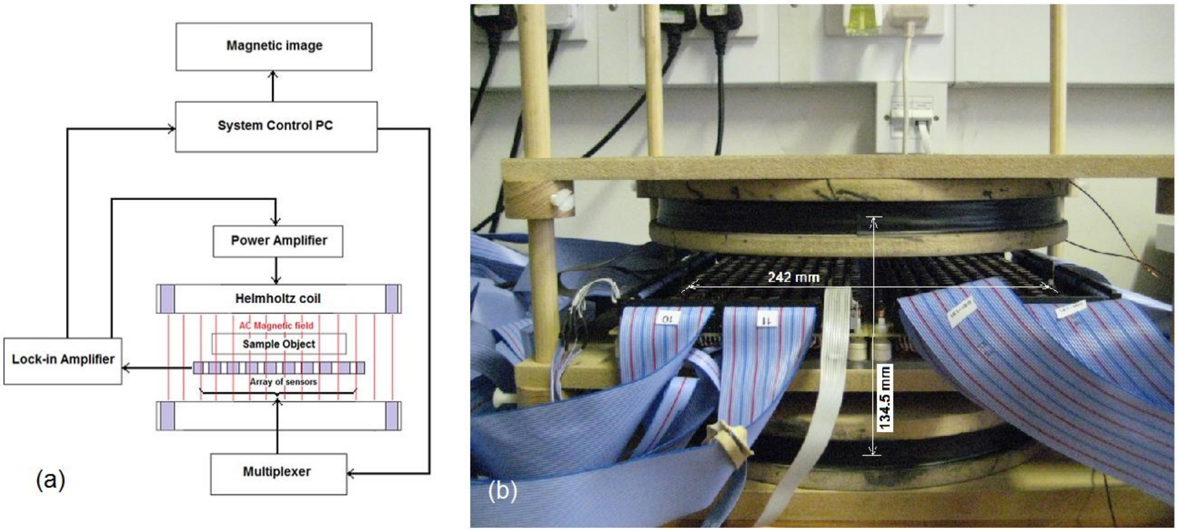

Figure 1.13. (a) Schematic of imaging set up. (b) Photo of side view of sensor coil array in between Helmholtz coils. See Section 4 for more details.

The resultant field is picked up by the sensor coils providing a set of spatially distributed phase measurements from the centre point of each coil. MATLAB code is used to interpolate the phase data (z axis) with respect to (x, y) position, enabling an image of the specimen to be created. The electromagnetic process to obtain the phase measurements is due to inductive coupling between the coils and the metallic specimen. In this set up the sensor array is placed inside the Helmholtz coil assembly, between the upper and lower coil, with the specimen placed on the array separated by a sheet of graph paper.

This thesis is organised as follows.

In Section 2 the theoretical principles underlying MIT are given as a qualitative description of the electromagnetic processes involved. This is given from the production of the primary field in the Helmholtz coils to the excitation of eddy currents in the metallic specimen and finally to detection of the resultant field across the sensor coils. Maxwell's Equations are used to describe the steps involved. Additionally a simple model of an MIT set up is derived adapting the work of Griffiths et al. [8] and Scharfetter et al. [41], to show the basic relationship of the phase difference measurements to the conductivity of the sample being imaged.

To start with a basic MIT system described in Section 3 was designed and constructed [1]. Images were created by taking measurements of the phase difference between the signals of a driver and a single sensor coil. This was achieved manually, moving the specimen into each *x*-*y* position on a perspex rig, performing a raster scan. The spatial resolution of the imaging modality was determined by its ability to differentiate two objects. Resolution of the system was determined at ~ 20 mm by estimating the smallest distance apart that two steel ball bearings, 6.34 mm in diameter, could be resolved as shown in Section 3.2. 2-D images were made of the 6.3 mm ball bearings in different arrangements of one, two and hexagon of six, that also gave indications of the resolution. To investigate penetration 1-D images were made of two 6.34 mm ball bearings covered over by an Aluminium foil shield at various separations apart. Additionally 1-D images were made of a mild steel bar through a plated mild-steel (ferromagnetic) shield. Changes in the shape of the images indicated detection through the shields, since they showed a metallic object was present underneath the shield, producing more eddy currents that increased the phase values in the image. Detection was only barely observed through the Aluminium shield, but the larger object a mild steel bar showed clear indication of detection when imaged through the ferromagnetic shield.

Combating illicit trafficking of Special Nuclear Materials may require the ability to image through electromagnetic shields. This is the case when the trafficking involves cargo containers. Thus suitable detection techniques are required to penetrate a ferromagnetic enclosure. This study considers techniques that employ an electromagnetic based principle of detection. It is generally assumed that a ferromagnetic metallic enclosure will effectively act as a Faraday cage to electromagnetic radiation and therefore screen any form of interrogating electromagnetic radiation from penetrating, thus denying the detection of any eventual hidden material. In contrast it was demonstrated that it is actually possible to capture magnetic images of a conductive object through a set of metallic ferromagnetic enclosures. This validates electromagnetic interrogation techniques as a potential detection tool for National Nuclear Security applications. The following introduces the set up and techniques involved.

Section 4 describes the design and construction of an MIT system to automatically generate magnetic images via a LabVIEW computer program. This was implemented with a sensor coil array for detecting signals and a Helmholtz coil assembly to provide the uniform-sinusoidal driving magnetic field. A planar sensor array was constructed of 20 × 20 sensor coils. The Helmholtz coils generated magnetic flux densities of 0.107 mT to 0.42 mT rms at 500 Hz to 200 Hz respectively, with the system being automated via a multiplexer that could generate 2-D images in 1 to 20 minutes.

In Section 5 a description is given of an algorithm by John Canny [42][17] originally used for edge detection in photographs, which was adapted to detect the edge of an MIT image. MATLAB code was written for this task.

Having set up the main experimental apparatus, Section 7 describes new techniques on penetration through metallic enclosures and how the resolution of the resultant images was determined. The Canny edge detection algorithm was applied to images of Copper and Aluminium disks of varying diameter and the edge detected diameter was compared to the actual diameter: the resolution was then determined by identifying the least diameter of disk that gave an edge detected diameter distinguishable from disks of smaller size. In order to image a specimen inside a metallic enclosure its phase data needs to be distinguished from that of the enclosure, which is originally obscured in the image, i.e. the specimen cannot be initially identified in the image. A proof-of-principle technique was invented that subtracted the phase data of the empty enclosure from that of the enclosure with the concealed specimen inside. The resultant images (figure 7.7) revealed a Copper disk extracted from the background of its enclosure [2][3].

Section 8 is introduced as follows. Firstly having access to an empty enclosure for imaging inside it is not always practical. This is because in a security setting – for example in airport baggage scanning – it is inefficient to open every bag: it is much more efficient to scan it with an imaging modality such as x-rays or MIT. Additionally there are cargo containers where it is near impossible to look through every container as it would take too long, nor even having access to an empty container. To improve upon the proof-of-principle method a technique was devised that could image the concealed specimen without removing it from the enclosure. This technique is called the dual frequency method [2]. It involves taking an image at high frequency (e.g. 2 kHz) to approximate the empty enclosure, where due to the skin effect more of its outer surface is picked up in the image. This is because magnetic field penetration of the enclosure is reduced, so the enclosure image appears to be partly empty (see Section 8.1). Another image is taken at low frequency (e.g. 200 Hz) to penetrate deeper into it. To make it the same scale as the high frequency image, the low frequency one was normalised at an arbitrary positional phase value, $f_{normalised}(x, y)$, away from the position of the concealed disk, but not at the edge of the enclosure. Due to the skin effect the low frequency image contains phase data that more clearly defines the disk. The skin effect of a conductor is when an alternating current becomes distributed in it so that its current density is greater near the surface and decreases with depth, due to eddy currents forming and producing secondary fields that oppose the primary field [37][43][44]. The skin depth, δ, gives the depth at which an electromagnetic or alternating magnetic field has been attenuated to 37 % of its surface value, due to propagating through the material [45][44]. With the normalised low-frequency image now containing phase values of similar scale to the high frequency one, subtraction of the two images enables the specimen disk to be distinguished from the background enclosure.

Section 9 describes an experiment to investigate penetration through different size enclosures and the skin effect property of the enclosure's material. Aluminium boxes of varying thickness were used: a Copper disk was then placed inside to be imaged. This test was performed with different driving frequencies. At higher frequencies (5 kHz) the primary field is weaker and additionally the skin depth is smaller, making it difficult to obtain images of the disk; the opposite is the case for lower frequencies (10 Hz to 2 kHz). The experiment demonstrated the capability of imaging through thick conductive barriers. The method used for penetration imaging, was the subtraction of phases of the full and empty enclosures, since this proof-of-principle method enabled penetration imaging for all enclosures tested, but the practical dual frequency method did not work for Aluminium enclosures greater than 1.6 mm thickness.

In Section 10 the ability of the system to image in 3D was tested and verified. This was done by conducting experiments to determine the edge detected diameter for varying heights of lift-off above the sensor array plane for Copper and Aluminium disks of varying sizes. This proved the system could be scaled up to 3D imaging by simply adding two more Helmholtz-coil pairs orthogonally to the existing one, with accompanying sensor arrays positioned at the three orthogonal faces of the Helmholtz coils. For this purpose a three-axis square Helmholtz coil assembly was designed and is described in more detail in Section 12.

Section 11 gives the summary and conclusions.

In Section 12 on future work, a three-axis Helmholtz coil assembly was designed and is in the process of construction to image in 3D. To test the system for imaging 2D slices (voltage images) through an Aluminium box, a filtered back-projection algorithm could be adapted using a Helmholtz coil pair on one of the axes and the object to be imaged, rotated on a turn table perpendicular to the source field. Referring to the work of Al-Zeibak and Saunders [5], it may be possible for the Helmholtz coils' source field to act like a hard field and therefore a technique similar to CAT scanning with x-rays could be implemented.

2 Theoretical principles of MIT

The approach to MIT taken here involves tomographic imaging of a metallic specimen, via phase variation measurements between excitation and sensor coils. A time varying near-to-uniform magnetic field (primary) is established by a Helmholtz coil assembly, as the excitation or driver coils and excites eddy currents in the sample object dependent on its conductivity. The eddy currents in turn generate a secondary magnetic field in opposition to the cause of their generation due to Lenz’s law. A diagram of the electromagnetic processes is shown in figure 2.1.

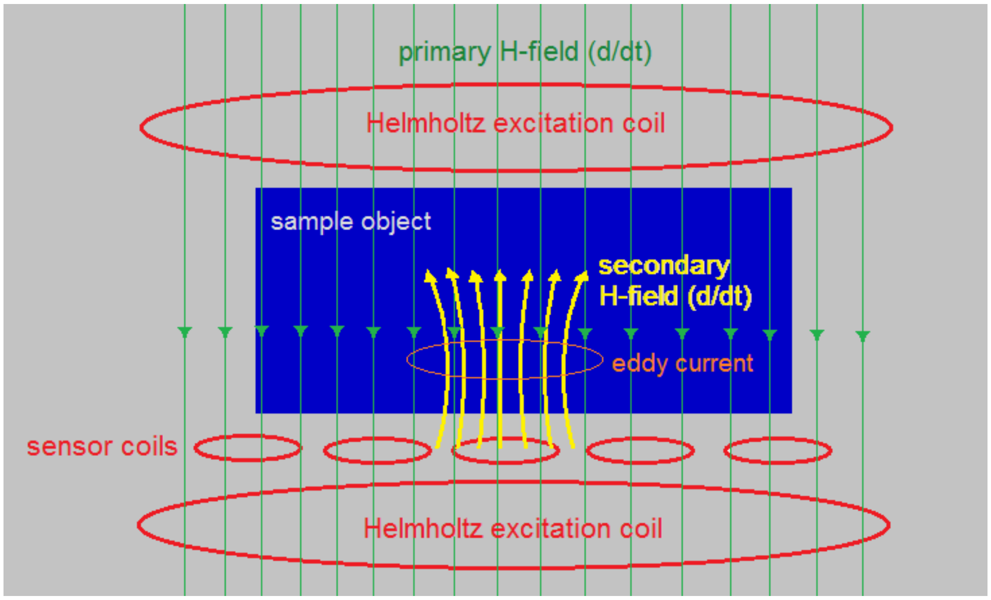

Figure 2.1. Illustration of the electromagnetic processes during measurement, showing an eddy current in a metallic sample after induction by the primary field. The combined primary and eddy current fields are detected by the sensor coils.

The resultant field induces an e.m.f. in a sensor coil that includes perturbations in the field due to the specimen (Faraday’s law). To generate magnetic images, the phase angle is measured between the primary (**B**) and the primary + secondary fields (**B** + Δ**B**) [9][10], as shown in figure 2.2. **B** is the magnetic flux density at the sensor coil due to the primary field and V is the e.m.f. induced across the sensor coil due to **B**. Figure 2.2 and Section 2.1 describes how the e.m.f. measured is directly proportional to the magnetic field detected.

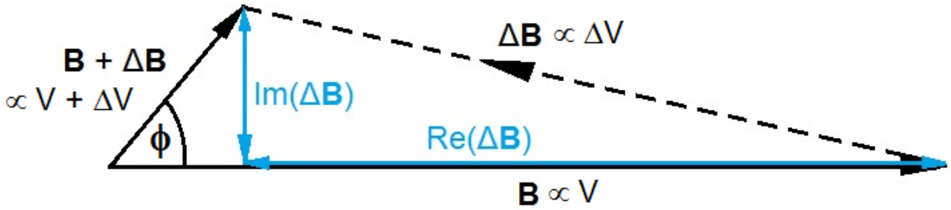

Figure 2.2. A phasor diagram of a highly conductive non-magnetic specimen, showing the B-fields detected by the sensor coil. In this case the specimen acts as a screen causing Re(Δ**B**) to become a large negative value and also affected by conductivity of the specimen [20]. The Im(Δ**B**) is positive due to the specimen being metallic and is dependent on its conductivity [9]. The phasor diagram represents the mid position of an Aluminium disk 150 mm diameter by 2 mm thickness, estimated from the voltage magnitude and phase measurements of figures 6.8a and 6.9a The B-fields are detected by the sensor in terms of the e.m.f. measured across it by a lock-in amplifier. The primary field (**B**) is due to the Helmholtz coils and the opposing secondary field (Δ**B**) is due to the sample. The total detected field (**B** +Δ**B**) leads the primary field by ϕ. Due to Faraday's law of induction [46], **B** and Δ**B** on this figure are directly proportional to amplitudes V and ΔV, respectively – that are e.m.f.'s induced in the sensor coil [5] [6].

ΔV is the e.m.f. induced across the sensor coil due to the secondary field, Δ**B**, generated by the eddy currents in the sample. The resultant field detected by the sensor is **B** + Δ**B**. For this set up the p.d. phase difference measured between driver and sensor coils accounts for the phase angle, ϕ, between **B** and **B** + Δ**B**. This is due to eddy currents induced in the specimen causing an opposing secondary field, so that the resultant field is generated in a time delay, shown as the angle, ϕ, between the primary and resultant fields. If there are no eddy currents then there is no secondary field and ϕ would be zero.

2.1 Non-magnetic conductive materials

For non-magnetic conductive specimens, i.e. diamagnetic Copper and paramagnetic Aluminium, the following is a qualitative analysis of electromagnetic processes involved. This is from the excitation of eddy currents in the specimen to measurement of p.d. phase difference (phase) between driver and sensor coils. From these electromagnetic processes the phase angle between primary and primary + secondary fields is related to the imaginary and real parts of the secondary field, Im (Δ**B**) and Re (Δ**B**). By measuring these two components it should be possible to determine the conductivity and permeability of the specimen, respectively [10] (figure 2.2), when the skin depth is much larger than its thickness. Sections 2.2.1 and 2.2.2 describe this aspect of the phasor diagram in more detail. When the metallic specimen's dimensions are comparable to its skin depth, it acts as a screen and Im (Δ**B**) and Re (Δ**B**) are both related to conductivity for non-magnetic specimens [20]. This is only partly dealt with in this study. Section 6.1 examines screening effects and images taken in Re (ΔV/V) and Im (ΔV/V) mediums for comparison.

It can be seen from figure 2.2 that ϕ changes with Im (Δ**B**) and Re (Δ**B**). The eddy current density, **J**, that generates Δ**B** is proportional to it. **J** is in turn proportional to the conductivity of the specimen, where **J** = σ**E** (see 2.10). There are three stages of physical process from the primary field, established by the Helmholtz coils, to the e.m.f. induced across a sensor coil [46].

1. Induction of eddy currents into the sample due to the primary field → Faraday's law.
2. Eddy currents in the sample generating a secondary field → Biot-Savart's law.
3. Induction of an e.m.f. across a sensor coil due to primary + secondary fields → Faraday's law.

Considering the specimen in (2.1), d**A** is the elemental area of an open surface, S, pointing normal to it. The flux of the primary field, $\phi_{B,S}$, passes through S, where S is also the area enclosed by the encircling eddy currents [46][44]. In (2.2) **E** is the electric field induced in the specimen and d**l** is an elemental length of the boundary ∂S of the eddy currents. An illustration of this is shown in figure 2.3.

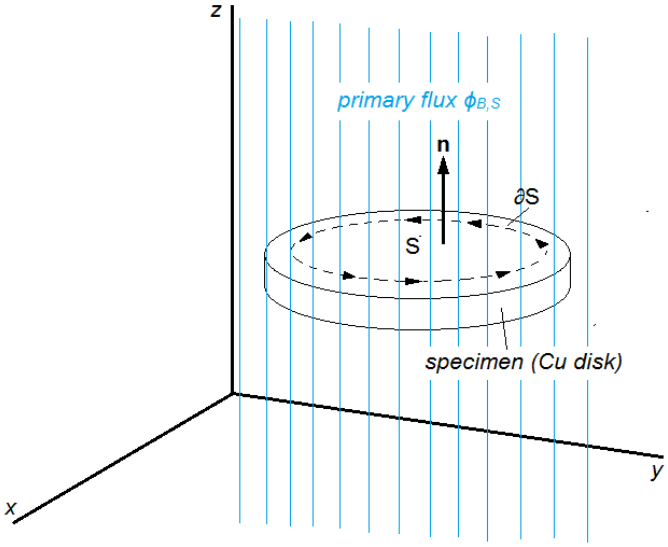

Figure 2.3. Diagram of surfaces and boundaries in the Maxwell-Faraday equation (2.2), with surface S of a Copper-disk specimen and the eddy current boundary ∂S. Elemental surface area points orthogonally to the disk as shown by **n** (right-hand rule).

$$\phi_{B,S} = \int_S \boldsymbol{B} \cdot d\boldsymbol{A} \quad , \qquad \boldsymbol{B} = \mu \mathbf{H} \tag{2.1}$$

$$\text{e.m.f.} = \oint_{\partial S} \boldsymbol{E} \cdot d\boldsymbol{l} = -\frac{d\phi_{B,S}}{dt} = -\frac{d}{dt}\int_S \boldsymbol{B} \cdot d\boldsymbol{A} \tag{2.2}$$

The integral in equation (2.2) shows Faraday's law for a time varying e.m.f. induced across the specimen due to the primary field [46]. In reference to the phasor diagram of figure 2.2, if the area of the specimen and rate of change of the field are both constant then the e.m.f. induced in it is directly proportional to the magnetic field **B**. The primary field **B** = μ**H** in the specimen is established by the Helmholtz coils and is derived from Biot-Savart's law shown in (2.5). **H** is the magnetic field strength and the permeability $\mu \approx \mu_0$ for a non-magnetic conductive specimen such as Copper or Aluminium.

The sinusoidally varying primary-field **B** is proportional to the current in the Helmholtz coils, where $I = I_0 e^{j\omega t}$, and can be written in complex wave notation shown in (2.3). ω is the angular frequency and *j* is $\sqrt{-1}$.

$$\boldsymbol{B} = \boldsymbol{B_0} e^{j\omega t} \qquad (2.3)$$

The time varying **B** field is simplified in complex notation:

$$\frac{\partial \boldsymbol{B}}{\partial t} = \frac{\partial (\boldsymbol{B_0} e^{j\omega t})}{\partial t} = j\omega \boldsymbol{B} \qquad (2.4)$$

The primary field **B** in (2.5) is established by the Helmholtz coils, representing the field at the centre of the coil system [47][48]. The two identical Helmholtz coils are separated along their co-linear axis by distance equal to the radius of the coils, in order optimize the uniformity of the field in its central region (Section 4.2.1). The field is near-to-uniform throughout, where *I* is a sinusoidal time varying current and $\mu = \mu_0\mu_r$ is the permeability of the medium through which the field travels ($\mu_r \approx 1$, for non-magnetic medium such as air). R is the radius of the Helmholtz coils and n is the number of turns per coil [47].

$$\boldsymbol{B} = \left(\frac{4}{5}\right)^{3/2} \frac{\mu_0 \mu_r n I}{R} \quad , \qquad I = I_0 e^{j\omega t} \qquad (2.5)$$

The time varying **E**-field induced in the specimen drives the eddy current density **J**. The primary field in the conductive sample is **B** = *μ***H** in (2.1) and (2.2), which is proportional to the eddy current density. In Ampere's circuital law (2.6) describing eddy currents generating an **H**-field and in the low-frequency limit with, $\omega\varepsilon \ll \sigma$, the displacement field can be neglected, $\frac{\partial \boldsymbol{D}}{\partial t}$ [16][31][37][49]. For metallic specimens, $\varepsilon = \varepsilon_0$. Therefore,

$$\nabla \times \boldsymbol{H} = \boldsymbol{J} + \frac{\partial \boldsymbol{D}}{\partial t} = \sigma \boldsymbol{E} + \varepsilon \frac{\partial \boldsymbol{E}}{\partial t} \; , \quad where \quad \boldsymbol{J} = \sigma \boldsymbol{E} \; , \quad \boldsymbol{D} = \varepsilon \boldsymbol{E} \qquad (2.6)$$

$$\varepsilon \frac{\partial \boldsymbol{E}}{\partial t} = \varepsilon \frac{\partial (\boldsymbol{E_0} e^{j\omega t})}{\partial t} = j\omega\varepsilon \boldsymbol{E} \tag{2.8}$$

$$but \;\; \omega\varepsilon \ll \sigma \;\; \therefore (2.6) \;\; becomes \quad \nabla \times \boldsymbol{H} = \sigma \boldsymbol{E} = \boldsymbol{J} \tag{2.9}$$

The eddy current density, **J**, is directly proportional to conductivity, *σ,* of the specimen and the electric field **E**, i.e. **J** = σ**E** (Ohm's law). For a metallic specimen of constant conductivity, **J** changes proportionally to **E**. Therefore if conductivity increases this will allow more eddy current to flow, due to Ohm's law and therefore a greater magnetic flux density is transmitted to the sensor coil. This is shown in (2.10). In this way the eddy current field detected by the sensor coils measures the conductivity of the specimen. An additional factor is that the skin depth of the metallic specimen may also contribute towards the ability to detect the eddy current field, as in the case of Copper and Aluminium, where Aluminium has larger skin depth but is less conductive. I.e. for Aluminium, although less eddy currents are generated the magnetic field can penetrate further through it, to be detected on the other side by the sensor coil.

In the second stage the magnetic flux density Δ**B** due to the eddy current field is transmitted to each point on the sensor coil. Δ**B** is directly proportional to the eddy current density, **J**, as shown in Biot-Savart's law (2.10) [46][19][37],

$$\Delta \boldsymbol{B} = \mu \int_V \frac{\boldsymbol{J} \times \boldsymbol{r} \, dV}{4\pi r^3} \quad , \qquad \boldsymbol{J} = \sigma \boldsymbol{E} \quad , \tag{2.10}$$

where *μ* is permeability of the specimen; d*V* is the volume element of the specimen, and **r** the distance from d*V* to a point in the sensor coil.

The time varying eddy current density induced in the specimen decays as it passes through the specimen. The current density is defined as [37]:

$$J = J_0 e^{-(x/\delta)} e^{-j(x/\delta)} e^{j\omega t} \quad . \qquad (2.11)$$

J_0 is the surface current density and δ the skin depth, where $\delta = \sqrt{2/\omega\mu\sigma}$ (see equation (3.1)). The first exponential term describes eddy current decay with depth, *x*, shown in figure 2.4. The eddy currents decay exponentially because they generate secondary magnetic fields that oppose the primary field, so that less and less of the primary penetrates as it moves deeper into the specimen, until at, 5δ, the primary field has almost decayed completely [50][37][43][44]. Note that the primary field is also generating the eddy currents, so that when primary has decayed the eddy currents decay as well.

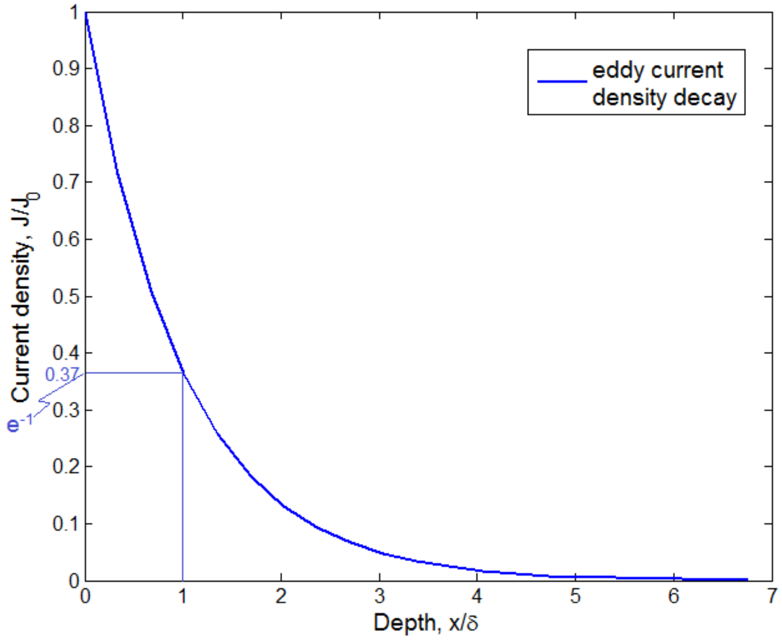

Figure 2.4. Eddy-current-density decay with depth, *x*, into a specimen material. J_0 is the surface current density and δ is the skin depth of the material at an arbitrary frequency. The current density and depth are normalised to, J/J_0 and *x*/δ respectively [37].

The second exponential term is a complex number denoting phase lag θ of the currents that increases linearly with depth, where $\theta = x/\delta$ (in radians) and referenced from phase at the surface of the material. The third exponential term is due to time dependence of the varying primary flux, indicating sinusoidal variation in complex notation [37]. Usually the first term is sufficient to express the concept of eddy current decay, which takes place due to the primary field being opposed by the eddy current field as it enters the conductive medium.

In the third and final stage of the electromagnetic process, the vector addition of primary and secondary fields, **B** + Δ**B,** induces an e.m.f. ($V + \Delta V$) across the sensor coil. From Faraday's law described earlier in (2.2):

$$\text{e.m.f.} = \oint_{\partial S} \boldsymbol{E} \cdot d\boldsymbol{l} = -\frac{d}{dt}\int_{S} \boldsymbol{B} \cdot d\boldsymbol{A}$$

and replacing the e.m.f. and **B** field with $V + \Delta V$ and $\boldsymbol{B} + \Delta\boldsymbol{B}$ respectively, then in complex notation using (2.2), (2.4) and (2.10):

$$V + \Delta V = -j\omega N \int_{P} (\boldsymbol{B} + \Delta\boldsymbol{B}) \cdot d\boldsymbol{A} \qquad (2.12)$$

V + ΔV is the vector sum of the time varying e.m.f.'s induced in the sensor coil. *N* is the number of turns of the coil; d**A** is the normal infinitesimal area to the open surface P, bounded by the sensor coil wire.

2.2 Relationship of phase angle to properties of specimen

In the following derivations it will be shown how conductivity can be inferred from the phase angle between the primary (**B**) and primary + secondary (**B** + Δ**B**) fields using voltage measurements. Firstly in Section 2.2.1 the general case will be derived, used by some MIT researchers, for two coils acting as a magnetic dipole. In Section 2.2.4 the specific case of interest for the present work will be derived for a Helmholtz coils (driver coil) and a single sensor coil. In these two cases a conductive specimen generates a phase difference between primary and primary + secondary fields, due to excitation of eddy currents which in turn is due to the specimen’s conductive property.

2.2.1 Eddy currents produce perturbation ΔB_e of primary field B_0

The following derivation has been adapted from the work of Griffiths et al. [8][10] and Scharfetter et al. [41]. Consider two small coaxially positioned coils, an excitation and a sensing coil, placed opposite each other as shown in figure 2.5. Due to their small radius compared to the displacement apart, the two coils can be considered magnetic dipoles.

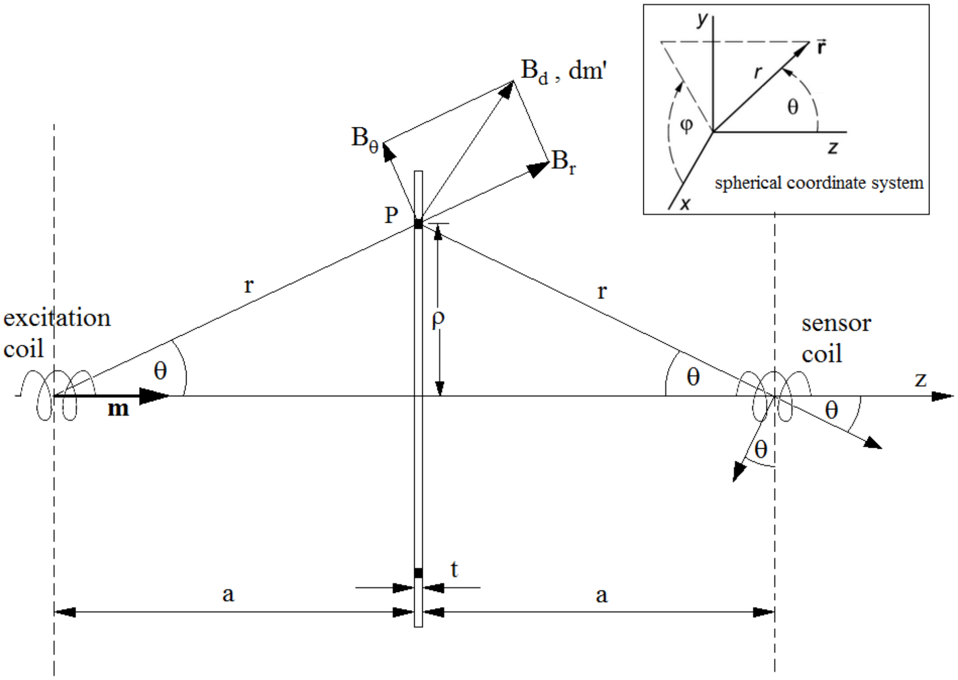

Figure 2.5. Diagram of inductive coupling between a thin disk (side view) and a magnetic dipole coil system [41].

A sinusoidal current of angular frequency, ω, in the excitation coil produces a magnetic field that is picked up by the sensing coil. A thin disk is positioned midway and the coils are a distance $2a$ apart. The radius of the disk is R and its thickness is t, where $t \ll 2a$. First consider the disk has conductivity σ and is non-magnetic with permeability μ_0. Later the magnetic case will be considered. It is assumed that the skin depth δ is much greater than t, so that only a small attenuation of the field takes place as it passes through the disk.

Far from the centre of a circular coil the magnetic field is well approximated in terms of a magnetic dipole, *AI*, where *A* is the area of the coil loop and *I* the current.

The magnetic field of a magnetic dipole can be resolved into radial and tangential components B_r and B_θ, as shown in figure 2.6 [44].

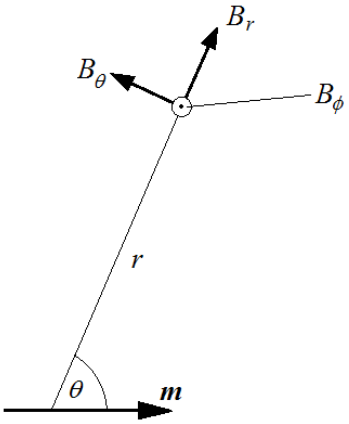

Figure 2.6. Radial and tangential components of the magnetic field, B, due to dipole moment of coil.

Using spherical coordinates (r, θ, ϕ), a point P on the disk has the following magnetic field components [44],

$$B_r = \frac{\mu_0}{4\pi}\frac{2m\cos\theta}{r^3}\ , \qquad B_\theta = \frac{\mu_0}{4\pi}\frac{m\sin\theta}{r^3}\ , \qquad B_\phi = 0 \quad , \qquad (2.13)$$

where m is the dipole moment of the excitation coil. The field along the z axis is obtained by subtracting the two horizontal components of B_r and B_θ in (2.13). Therefore,

$$B_z = \frac{\mu_0 m}{4\pi r^3}(2\,cos^2\theta - sin^2\theta) \ = \frac{\mu_0 m}{4\pi}\left[\frac{2a^2-\rho^2}{(a^2+\rho^2)^{5/2}}\right] \qquad (2.14)$$

where a and ρ are dimensions shown figure 2.5. The alternating magnetic flux in the disk, following a circular path of radius ρ and centred on the axis is as follows,

$$\Phi = \int B\, dA = \int_0^{\rho} B_z(\rho')2\pi\rho' d\rho' \qquad . \tag{2.15}$$

Therefore (2.14) into (2.15) gives,

$$\Phi = \frac{\mu_0 m}{2}\frac{\rho^2}{(a^2+\rho^2)^{3/2}} \tag{2.16}$$

The induced e.m.f. around the circular path of the disk is

$$e.m.f. = -\frac{d\Phi}{dt} = -j\omega\Phi \ , \tag{2.17}$$

which also equals the line integral, $2\pi\rho E_\phi$, where E_ϕ is the ϕ-component of the induced electric field.

$$\therefore \ e.m.f. = -j\omega\Phi \ = 2\pi\rho E_\phi \tag{2.18}$$

The current density in the disk is, $\boldsymbol{J} = \sigma\boldsymbol{E}$, so from (2.18) and (2.16),

$$\therefore \ J_\phi \ = \sigma E_\phi = \frac{\sigma(-j\omega\Phi)}{2\pi\rho} \ = \frac{\sigma\left[-j\omega\frac{\mu_0 m}{2}\frac{\rho^2}{(a^2+\rho^2)^{\frac{3}{2}}}\right]}{2\pi\rho}$$

$$= \frac{-j\omega\sigma\mu_0 m}{4\pi}\frac{\rho}{(a^2+\rho^2)^{3/2}} = \frac{-jm}{2\pi\delta^2}\frac{\rho}{(a^2+\rho^2)^{3/2}} \tag{2.19}$$

where the skin depth δ is given in (3.1). A small part of the disk between ρ and $\rho + d\rho$, carries a current d*I,* where,

$$dI = J_\phi t d\rho = \frac{-jmt}{2\pi\delta^2}\frac{\rho}{(a^2+\rho^2)^{3/2}}d\rho \tag{2.20}$$

To determine the B-field generated by the induced current in the disk at the sensing coil, first look at Biot-Savart's law in (2.21) and figure 2.7, for the magnetic field produced by a current carrying wire.

$$dB = \frac{\mu_0 I dl \sin\theta}{4\pi r^2} \tag{2.21}$$

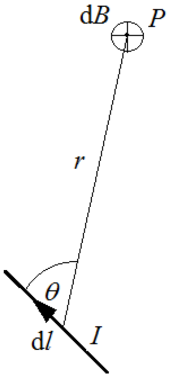

Figure 2.7 Biot-Savart's law.

From (2.21) the B-field can be determined on the axis of a single circular coil (figure 2.8),

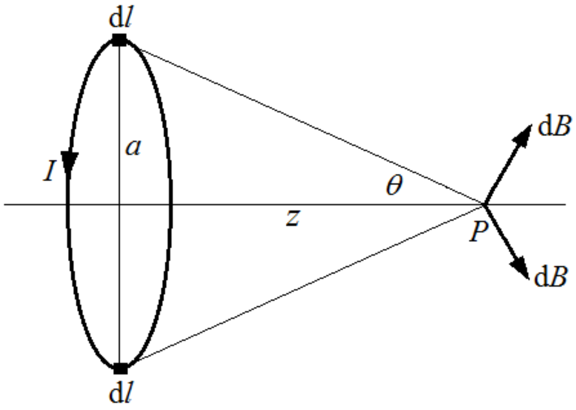

Figure 2.8. The B-field from a circular coil.

and noting that $B_x = 0$ and $B_y = 0$, (2.21) gives,

$$B_z = \frac{\mu_0 I a^2}{2(a^2 + z^2)^{3/2}} \quad . \tag{2.22}$$

Adjusting (2.22) to the model parameters in figure 2.5, where $z \rightarrow a$ and $a \rightarrow \boldsymbol{\rho}$ gives,

$$dB = dB_z = \frac{\mu_0 \rho^2 dI}{2(a^2 + \rho^2)^{3/2}} \tag{2.23}$$

Placing (2.20) into (2.23) gives the B-field generated by the induced current in the disk, between ρ and $\rho + d\rho$, where δ is the skin depth from (3.1),

$$dB = \frac{-j\mu_0 mt}{4\pi\delta^2}\frac{\rho^3\,d\rho}{(a^2+\rho^2)^3} \tag{2.24}$$

The B-field detected by the sensing coil due to the excitation coil only, is as follows, using (2.14),

$$B_0 = B_z = \frac{\mu_0 m}{4\pi}\left[\frac{2a^2-\rho^2}{(a^2+\rho^2)^{5/2}}\right], \qquad where\ \rho = 0\ \&\ a \rightarrow 2a,$$

$$\therefore\ B_0 = \frac{\mu_0 m}{4\pi}\left[\frac{2(2a)^2}{(2a)^5}\right] = \frac{\mu_0 m}{4\pi}\left[\frac{2}{(2a)^3}\right] = \frac{\mu_0 m}{16\pi a^3} \qquad . \tag{2.25}$$

Taking the ratio of d*B* w.r.t. B$_0$ gives,

$$\frac{dB}{B_0} = \frac{\dfrac{-j\mu_0 mt}{4\pi\delta^2}\dfrac{\rho^3\,d\rho}{(a^2+\rho^2)^3}}{\dfrac{\mu_0 m}{16\pi a^3}} = \frac{-j\mu_0 mt}{4\pi\delta^2}\frac{\rho^3\,d\rho}{(a^2+\rho^2)^3}\frac{16\pi a^3}{\mu_0 m} = \frac{-4jta^3}{\delta^2}\frac{\rho^3\,d\rho}{(a^2+\rho^2)^3} \tag{2.26}$$

To find the magnetic field, ΔB$_e$, due to the induced eddy currents in the whole disk requires integrating (2.26) using the radius of disk R.

$$\int\frac{dB}{B_0} = \int_0^R \frac{-4jta^3}{\delta^2}\frac{\rho^3\,d\rho}{(a^2+\rho^2)^3} \quad\rightarrow\quad \frac{\Delta B_e}{B_0} = \frac{-jta^3}{\delta^2}\left[\frac{1}{a^2} - \frac{a^2+2R^2}{(a^2+R^2)^2}\right] \tag{2.27}$$

If there is significant relative permittivity, ε$_r$, in the specimen disk, then complex conductivity, κ,

$$\kappa = \sigma + j\omega\varepsilon_0\varepsilon_r \tag{2.28}$$

is included in the skin depth, δ, of (3.1), where σ is the specimen's conductivity,

$$\delta = \sqrt{\frac{2}{\omega\mu_0(\sigma + j\omega\varepsilon_0\varepsilon_r)}} \quad . \tag{2.29}$$

Substituting the complex skin depth of (2.29) into (2.27),

$$\frac{\Delta B_e}{B_0} = \frac{-jta^3}{\left(\frac{2}{\omega\mu_0(\sigma + j\omega\varepsilon_0\varepsilon_r)}\right)}\left[\frac{1}{a^2} - \frac{a^2+2R^2}{(a^2+R^2)^2}\right]$$

$$\therefore \quad \frac{\Delta B_e}{B_0} = (\omega\varepsilon_0\varepsilon_r - j\sigma)\left(\frac{ta^3\omega\mu_0}{2}\right)\left[\frac{1}{a^2} - \frac{a^2+2R^2}{(a^2+R^2)^2}\right] \tag{2.30}$$

2.2.2 Additional perturbation ΔB_m due to magnetization of sample disk

In addition to the perturbation in the primary field from the eddy currents in the disk, ΔB_e, there is also a perturbation ΔB_m, due to magnetization of the disk. This will be partly derived as follows adapting the work by Scharfetter et al. [41].

The excitation field in the plane of the disk is B_d as shown in figure 2.5 and the excitation coil has a dipole moment, m. Therefore from (2.13),

$$B_d = \sqrt{B_r^2 + B_\theta^2} = \sqrt{\left(\frac{\mu_0}{4\pi}\frac{2m\cos\theta}{r^3}\right)^2 + \left(\frac{\mu_0}{4\pi}\frac{m\sin\theta}{r^3}\right)^2} = \sqrt{\left(\frac{\mu_0}{4\pi}\frac{2ma}{r^4}\right)^2 + \left(\frac{\mu_0}{4\pi}\frac{m\rho}{r^4}\right)^2}$$

$$\text{where} \qquad \cos\theta = \frac{a}{r} \;\; , \;\; \sin\theta = \frac{\rho}{r} \;\; \text{and} \;\; r^2 = a^2 + \rho^2$$

$$\therefore \; B_d = \frac{\mu_0 m(4a^2+\rho^2)^{1/2}}{4\pi(a^2+\rho^2)^2} \quad . \tag{2.31}$$

In a homogeneous medium the magnetization M is given as,

$$M = \chi_m H \tag{2.32}$$

Here, χ_m is the magnetic susceptibility and H is the magnetic field strength of the applied field. $\chi_m = \mu_r - 1$ and $H = B/(\mu_0\mu_r)$. Therefore,

$$M = (\mu_r - 1)H = \frac{(\mu_r - 1)B}{\mu_0 \mu_r} \tag{2.33}$$

The differential magnetic moment, dm, is of the form,

$$dm = MdV \tag{2.34}$$

with units $A \cdot m^2$, where dV is a volume element. The excitation field in the plane of the disk is B_d. Substituting B in (2.33) for B_d in (2.31) and multiplying it by the volume element of the disk (in cylindrical co-ordinates) as in (2.34) we obtain the differential magnetic moment,

$$\therefore \quad dm = MdV = \frac{(\mu_r - 1)B_d dV}{\mu_0 \mu_r} = \frac{(\mu_r - 1)}{\mu_0 \mu_r} \frac{\mu_0 m (4a^2 + \rho^2)^{\frac{1}{2}} t\rho d\rho d\phi}{4\pi (a^2 + \rho^2)^2}$$

$$= \frac{(\mu_r - 1)}{\mu_r} \frac{mt(4a^2 + \rho^2)^{\frac{1}{2}} \rho \, d\rho \, d\phi}{4\pi (a^2 + \rho^2)^2} \tag{2.35}$$

This can be written as two terms,

$$dm = \frac{B_d t\rho \, d\rho \, d\varphi}{\mu_0} - \frac{B_d t\rho \, d\rho \, d\varphi}{\mu_0 \mu_r} \tag{2.36}$$

representing the differential magnetic moment in a vacuum, as first term, minus the material contribution that is the second term; where the difference is a field induced by the dipoles [51]. As shown by Scharfetter et al. the ratio of $\Delta B_m / B_0$ can be obtained from the differential magnetic moment by integration over the disk volume,

$$\frac{\Delta B_m}{B_0} = \frac{[a^3 t R^2 (8a^2 - R^2)(\mu_r - 1)]}{[2\mu_r (a^2 + R^2)^4]} \; . \tag{2.37}$$

For low permeability materials that are paramagnetic or diamagnetic, $\mu_r \approx 1$. So the approximation $(\mu_r - 1)/\mu_r \approx (\mu_r - 1)$ can be used. Putting this together with the eddy current term, the complete equation using (2.30) and (2.37) is as follows.

$$\frac{\Delta V}{V_0} = \frac{\Delta B}{B_0} = \frac{\Delta B_e + \Delta B_m}{B_0}$$

$$\therefore \ \frac{\Delta V}{V_0} = (\omega\varepsilon_0\varepsilon_r - j\sigma)\left(\frac{ta^3\omega\mu_0}{2}\right)\left[\frac{1}{a^2} - \frac{a^2+2R^2}{(a^2+R^2)^2}\right] + \frac{[a^3tR^2(8a^2-R^2)(\mu_r-1)]}{[2\mu_r(a^2+R^2)^4]} \tag{2.38}$$

$$= \frac{a^3t}{2}\left\{ \chi_m \frac{R^2(8a^2-R^2)}{(a^2+R^2)^4} - j(\sigma + j\omega\varepsilon_0\varepsilon_r)\omega\mu_0\left[\frac{1}{a^2} - \frac{a^2+2R^2}{(a^2+R^2)^2}\right] \right\} \tag{2.39}$$

$$\chi_m = (\mu_r - 1)\ , \qquad \kappa = \sigma + j\omega\varepsilon_0\varepsilon_r$$

The following resultant equation (2.40) is valid only for a skin depth of the specimen that is much larger than its thickness. The thickness being the depth of material penetrated by the primary magnetic field [8].

$$\therefore \quad \frac{\Delta V}{V_0} = \frac{\Delta B}{B_0} = Q\omega\mu_0[\omega\varepsilon_0\varepsilon_r - j\sigma] + R_2(\mu_r - 1) \tag{2.40}$$

$$\therefore \quad \frac{\Delta V}{V_0} = Re\left(\frac{\Delta V}{V_0}\right) + jIm\left(\frac{\Delta V}{V_0}\right) = [Q\omega^2\mu_0\varepsilon_0\varepsilon_r + R_2(\mu_r - 1)] - jQ\omega\mu_0\sigma$$

where,

$$Q = \frac{a^3t}{2}\left[\frac{1}{a^2} - \frac{a^2+2R^2}{(a^2+R^2)^2}\right] \quad and \quad R_2 = \frac{a^3tR^2(8a^2-R^2)}{2(a^2+R^2)^4} \quad . \tag{2.41}$$

Griffiths et al. [10] [20] have shown that equation (2.40) is valid for the ratio of an induced voltage change, ΔV, over the primary voltage, V_0, detected by the sensor coil. Equation (2.40) is analysed in relation to phasor diagrams in Section 2.2.3, figure 2.12.

For small phase changes, $\phi \approx \frac{\Delta V}{V_0}$, i.e. the angle, ϕ, between the primary and primary plus secondary fields. $\phi = \tan^{-1}\left(\frac{\Delta V}{V_0}\right) \approx \frac{\Delta V}{V_0}$ is only valid for small angles, where the phasor diagram forms an approximate right angled triangle with, $V_0 + \Delta V \approx V_0$, as shown in figure 2.9.

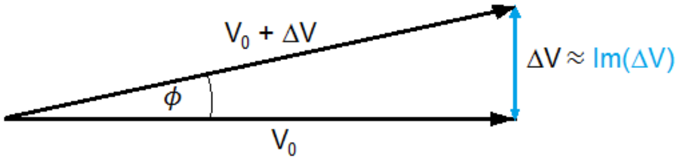

Figure 2.9. Phasor diagram for a metallic specimen with skin depth much larger than its dimensions. V_0 + ΔV is the resultant e.m.f. detected. V_0 is due to the primary field. ΔV is due to the secondary field.

This would be the case for a metallic specimen with skin depth that is large compared with its dimensions. Larger phase angles indicate a metallic specimen with skin depth comparable or smaller than its dimensions and the phasor triangle is no longer right angled, as shown in figure 2.10. In this case equation (2.40) breaks down and cannot be applied [20].

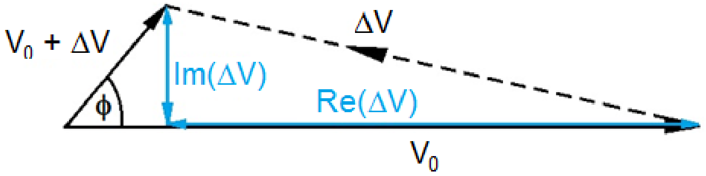

Figure 2.10. Phasor diagram for a metallic specimen with skin depth smaller or comparable to its dimensions. V_0 + ΔV is the resultant e.m.f. detected. V_0 is due to the primary field. ΔV is due to the secondary field.

Q and R_2 are constants of the coils' geometry in relation to the set-up, in terms of a, t and R as shown in figure 2.5. For low frequency imaging of high conductivity specimens, such as the ones studied here, $\omega\varepsilon \ll \sigma$, so the $\omega\varepsilon_0\varepsilon_r$ term is negligible. This term becomes important for a specimen with significant dielectric permittivity, such as biological tissue, where the real Re(ΔV) term in figure 2.11 can be used to image in the permittivity medium

[9][20]. Here higher interrogating frequencies are required, typically 10 MHz, in order to excite enough eddy currents in the specimen due to its low conductivity ($\sigma \approx 1$ Sm^{-1} for muscle tissue). As biological tissue has a very large skin depth higher interrogating frequencies can be applied (see skin depth equation (3.1)).

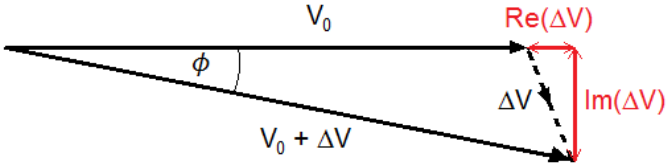

Figure 2.11. Phasor diagram for a biological tissue specimen of low conducitivty with skin depth much larger than its dimensions. V_0 + ΔV is the resultant e.m.f. detected. V_0 is due to the primary field. ΔV is due to the secondary field.

For the work presented in this thesis the specimens were metallic with relative permittivity $\varepsilon_r \approx 1$ and conductivities on the order of 10^7 Sm^{-1} [41][10].

Therefore for a metallic specimen that is non-magnetic ($\mu_r \approx 1$ and $\varepsilon_r \approx 1$), so that the real magnetic term, $(\mu_r - 1)$ in (2.40) can be dropped and with a skin depth that is large compared with its dimensions (2.40) becomes,

$$\phi \approx \frac{\Delta V}{V_0} = -jQ\omega\mu_0\sigma \qquad (2.42)$$

so at constant frequency the phase, ϕ , is directly proportional to conductivity σ,

$$\phi \approx \frac{\Delta V}{V_0} \propto \sigma \qquad . \qquad (2.43)$$

2.2.3 Phasor diagrams in broader MIT context

Figure 2.12 shows phasor diagrams for 3 different material specimens. Figure 2.12(a) and (b) shows the difference between two highly conductive non-magnetic specimens, with skin-depths comparable or smaller (a), or much larger (b) than the dimensions of the specimen. Figure 2.12(c) shows a ferromagnetic specimen and figure 2.12(d) shows one for biological tissue or saline solution. In both (c) and (d) the skin depths are again much larger than the specimen's dimensions.

(a) Highly conductive specimen with skin depth comparable or smaller than its dimensions

(b) Highly conductive specimen with skin depth much larger than its dimensions

(c) Ferromagnetic non-conductive objects with skin depth much larger than its dimensions

(d) Biological tissue specimen of low conductivity, with large skin depth in comparison with its dimensions.

Figure 2.12. Phasor diagrams, in terms of voltage detected by the sensor coil, for 3 material types [9]. This is in the context of the magnetic dipole coil-model, described in Section 2.2 and figure 2.5. V_0 is the voltage induced by the primary field, ΔV is due to the secondary field and $V_0 + \Delta V$ is the e.m.f. measured due to the resultant field. (a) A non-magnetic highly conductive specimen such as Copper or Aluminium with skin depth smaller or comparable with its dimensions. The specimen acts as a screen producing a large negative $\mathrm{Re}(\Delta V)$ component that is dependent on conductivity. The resultant voltage leads the primary voltage by angle ϕ. Equation (2.40) breaks down in this example [20]. (b) The same material as (a) but with skin depth of the specimen much larger than its dimensions. The phase angle is small due to a small perturbation in the magnetic field where $V_0 + \Delta V \approx V_0$. The resultant voltage leads the primary voltage by small angle ϕ. Equation (2.40) can be applied in this example. (c) A ferromagnetic non-conductive ceramic object. As no eddy currents are generated there is only a $\mathrm{Re}(\Delta V)$ component due to the permeability of the specimen. Equation (2.38) can be applied in this case. (d) A biological tissue of low conductivity, where the resultant voltage lags the primary voltage by small angle ϕ, due to small perturbation in the field. The $\mathrm{Re}(\Delta V)$ component is dependent on permittivity and the $\mathrm{Im}(\Delta V)$ component is dependent on conductivity. These two PEP mediums can be used in image reconstruction. Equation (2.40) can be applied in this case. [20][9].

In a more general context that includes biomedical and metallic MIT, the expression (2.40) can be analysed as follows. As can be seen in figure 2.12 a change in the e.m.f., ΔV, detected at a sensor coil due to the specimen's presence, produces both real and imaginary components. The total field detected leads the primary signal by an angle, ϕ, in metallic specimens (figure 2.12(a, b)), but lags it in low conductivity biological tissue specimens (figure 2.12(d)) [9]. In biological tissue conduction currents induced in the specimen, i.e. eddy currents, produce a component, ΔV, proportional to frequency and conductivity as shown in (2.44) [9],

$$\frac{\Delta V}{V} = \frac{\Delta B}{B} \propto \omega(\omega\varepsilon_0\varepsilon_r - j\sigma) \qquad (2.44)$$

that causes the conduction term to be imaginary and negative, lagging the primary field by 90°. In metallic specimens the imaginary conduction term leads the primary by 90° (figure 2.12(a-b)). In biological tissue (figure 2.12(d)) there are displacement currents due to the time varying electric field and polarization of the dielectric medium. A displacement current is defined as the rate of change of the electric displacement field, having units of electric current. It is not a current of moving charges, but of a time varying electric field [44], such as that experienced between the plates of a capacitor. Insulator materials placed in a time varying electric field experience displacement currents, that include a component due to the slight motions of charges bound in atoms, called dielectric polarization or polarization current [50]. For this reason a displacement current is experienced by the insulating biological tissue making up the Re(ΔV) term in figure 2.12(d) [9]. These give a real component in phase with the primary field and proportional to the square of the frequency and permittivity of the medium, shown in (2.44) and (2.40) [9][10]. This displacement current component does not apply to metallic specimens since polarization effects are overshadowed by conduction [46], where $\varepsilon_r \approx 1$. For biological tissue $\mu_r \approx 1$ in (2.40), so this term can be dropped for most situations and also for non-magnetic metallic specimens, unless the imaging system is designed to be sensitive to diamagnetic and paramagnetic properties. In figure 2.12(c) the ferromagnetic specimen according to Griffiths [9] has a ΔV component in phase with the primary, being both real and positive, which appears to indicate a ferrite object with low or no conductivity. It would therefore be made up of the last μ_r term in (2.38), as the (μ_r – 1) term in (2.40) only applies to diamagnetic and paramagnetic properties. Concerning ferromagnetic specimens one would normally expect them to have an imaginary conductive term as well and not just a real magnetization term, as ferromagnetic materials are usually highly conductive such as Iron. Therefore for conductive ferromagnetic specimen with skin depth much larger than its dimensions, a ΔV component may have a real positive and a positive imaginary term, as in figure 2.13.

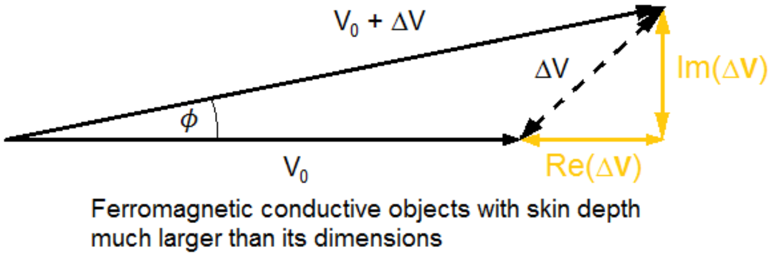

Figure 2.13. A possible phasor diagram, of voltage detected by a sensor coil, for a metallic-ferromagnetic specimen with a skin depth large in comparison with its dimensions. V_0 is the voltage induced by the primary field, ΔV is due to the secondary field and V_0 + ΔV is the e.m.f. measured due to the resultant field. This diagram is different from 2.12(c) because it is not a ceramic ferrite object with no conductivity, but a ferromagnetic object such as iron with high conductivity. The Im(ΔV) term indicates conductivity and the Re(ΔV) term indicates its permeability.

In principle the real and imaginary parts of (2.40) can be used for generating images of conductivity, permeability and possibly permittivity of the specimen [52] [10].

The images produced in this PhD work are of metallic specimens with skin depths comparable or smaller than the dimensions of the specimen. In this case the Re(ΔV/V) component will be influenced by the specimen's conductivity and equation (2.40) breaks down, failing to predict the correct Re(ΔV/V) values. The specimen in this case acts as a screen between the driver and sensor coils producing a negative Re(ΔV/V) [10][20], as shown in figures 2.12(a) and 4.31(a, c & e). However valid images can still be generated as well as imaging through metallic enclosures, although this cannot be modelled accurately by equation (2.40). The issue of images generated due to screening is dealt with in Section 6.1.

2.2.4 Deriving ΔB_e for a set up using Helmholtz coils

The set up used in the experiments of this thesis will now be considered.

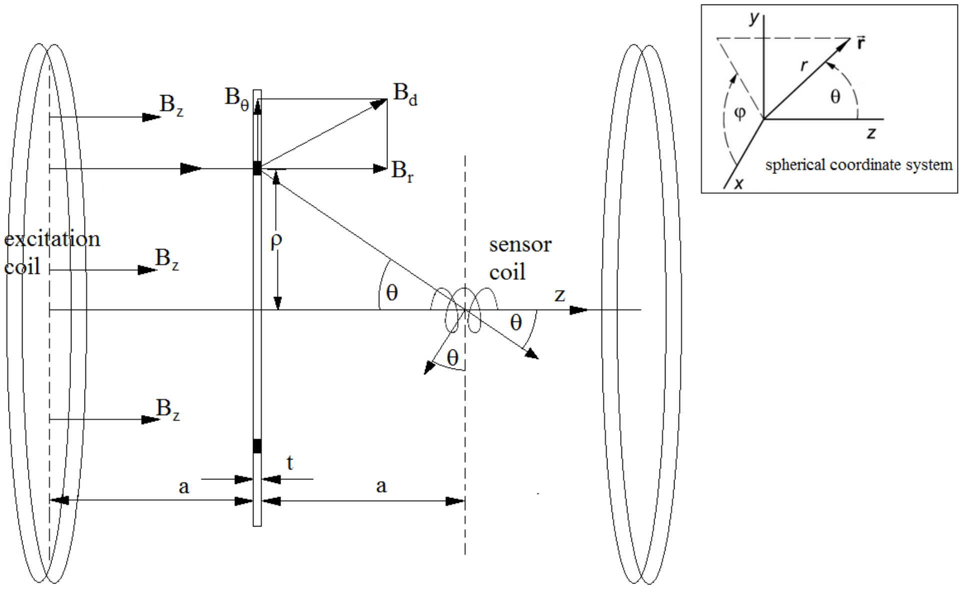

Figure 2.14. Diagram showing electromagnetic coupling between a thin cylindrical sample (disk), Helmholtz-excitation coils and a sensor coil.

In the following derivation of phase angle, ϕ, and secondary field, ΔB_e, follows a similar line of reasoning as shown in the magnetic dipole case of Section 2.2.1. The set up includes a Helmholtz coil assembly, generating a primary field passing through a thin metallic disk and detected by a sensor coil; with the skin depth of the disk being large in comparison with its dimensions. Firstly consider the primary magnetic flux density as being uniform throughout. For the Helmholtz coils,

$$B_z = \left(\frac{4}{5}\right)^{3/2} \frac{\mu_0 \mu_r n I}{R} \quad , \qquad I = I_0 e^{j\omega t} \qquad (2.45)$$

as described in Section 2.1 and equation (2.5), where R is the radius of the Helmholtz coils, n is the number of turns per coil and, *I*, is a time varying current.

Using figure 2.14 the time-varying magnetic flux through a circular surface of radius, ρ, centred on the axis of the disk is,

$$\Phi = \int B\, dA = \int_0^{\rho} B_z 2\pi\rho' d\rho' = B_z \pi\rho^2 = \left(\frac{4}{5}\right)^{\mathbf{3/2}} \frac{\mu_0\mu_r nI}{R}\pi\rho^2 \qquad (2.46)$$

The induced e.m.f. around the circular path of the disk bounding the surface is

$$e.m.f. = -\frac{d\Phi}{dt} = -j\omega\Phi\ , \qquad (2.47)$$

which also equals the line integral, $2\pi\rho E_\phi$, where E_ϕ is the induced electric field.

$$\therefore\ e.m.f. = -j\omega\Phi\ = 2\pi\rho E_\phi \qquad (2.48)$$

The current density in the disk is, $\boldsymbol{J} = \sigma\boldsymbol{E}$, so from (2.48) and (2.46),

$$\therefore\ J_\phi\ = \sigma E_\phi = \frac{\sigma(-j\omega\Phi)}{2\pi\rho} = \frac{\sigma\left[-j\omega\left(\frac{4}{5}\right)^{\mathbf{3/2}} \frac{\mu_0\mu_r nI}{R}\pi\rho^2\right]}{2\pi\rho}\ , \qquad where\quad \mu = \mu_0\mu_r$$

$$\therefore\quad J_\phi = \frac{-j\omega\sigma\mu}{2}\left(\frac{4}{5}\right)^{\mathbf{3/2}} \frac{nI\rho}{R} = \frac{-j}{\delta^2}\left(\frac{4}{5}\right)^{\mathbf{3/2}} \frac{nI\rho}{R} \qquad (2.49)$$

A small part of the disk between ρ and $\rho + d\rho$, carries a current dI_{disk}, where,

$$dI_{disk} = J_\phi t d\rho = \frac{-jt}{\delta^2}\left(\frac{4}{5}\right)^{\mathbf{\frac{3}{2}}} \frac{nI\rho}{R} d\rho \qquad (2.50)$$

From Biot-Savart's law for the B-field on the axis of a circular coil carrying a current, as shown in (2.21) to (2.22) of Section 2.2.1 is,

$$B_z = \frac{\mu_0 I a^2}{2(a^2 + z^2)^{3/2}} \qquad (2.51)$$

Adjusting (2.51) to the model parameters in figure 2.14, where *z* → *a*, *a* → $\boldsymbol{\rho}$:

$$dB = dB_z = \frac{\mu_0 \rho^2 dI_{disk}}{2(a^2 + \rho^2)^{3/2}} \tag{2.52}$$

Placing (2.50) into (2.52) gives the B-field generated by the induced current in the disk between ρ and $\rho + d\rho$,

$$dB = \frac{\mu_0 \rho^3}{2(a^2 + \rho^2)^{3/2}} \frac{-jt}{\delta^2} \left(\frac{4}{5}\right)^{\frac{3}{2}} \frac{nI}{R} d\rho \qquad . \tag{2.53}$$

The B-field detected by the sensor coil due to the excitation coil only, is the same as the Helmholtz coils' field in (2.45),

$$B_0 = B_z = \left(\frac{4}{5}\right)^{3/2} \frac{\mu_0 \mu_r n I}{R} \quad .$$

Taking the ratio of d*B* w.r.t. B_0 gives,

$$\frac{dB}{B_0} = \frac{\frac{\mu_0 \rho^3}{2(a^2 + \rho^2)^{3/2}} \frac{-jt}{\delta^2} \left(\frac{4}{5}\right)^{\frac{3}{2}} \frac{nI}{R} d\rho}{\left(\frac{4}{5}\right)^{3/2} \frac{\mu_0 n I}{R}} = \frac{-jt}{2\delta^2} \frac{\rho^3\, d\rho}{(a^2 + \rho^2)^{3/2}} \tag{2.54}$$

To find the magnetic field, ΔB_e , due to the eddy currents induced in the whole disk, requires integrating (2.54) using the radius of the disk R_d.

$$\int \frac{dB}{B_0} = \int_0^{R_d} \frac{-jt}{2\delta^2} \frac{\rho^3\, d\rho}{(a^2 + \rho^2)^{3/2}} \quad \rightarrow \quad \frac{\Delta B_e}{B_0} = \frac{-jt}{2\delta^2} \left[\frac{2a^2 + {R_d}^2}{\sqrt{a^2 + {R_d}^2}} - 2a \right] \tag{2.55}$$

If there is significant relative permittivity, ε_r , in the specimen disk then complex conductivity, κ, is included in the skin depth, δ, where,

$$\kappa = \sigma + j\omega\varepsilon_0\varepsilon_r \tag{2.56}$$

(2.56) into (3.1) gives,

$$\delta = \sqrt{\frac{2}{\omega\mu_0(\sigma + j\omega\varepsilon_0\varepsilon_r)}} \tag{2.57}$$

Substituting the complex skin depth of (2.57) into (2.55),

$$\frac{\Delta B_e}{B_0} = \frac{-jt}{2\left(\frac{2}{\omega\mu_0(\sigma + j\omega\varepsilon_0\varepsilon_r)}\right)}\left[\frac{2a^2 + {R_d}^2}{\sqrt{a^2 + {R_d}^2}} - 2a\right]$$

$$\therefore \quad \frac{\Delta V}{V_0} = \frac{\Delta B_e}{B_0} = (\omega\varepsilon_0\varepsilon_r \; - j\sigma)\left(\frac{t\omega\mu_0}{4}\right)\left[\frac{2a^2 + {R_d}^2}{\sqrt{a^2 + {R_d}^2}} - 2a\right] \;, \tag{2.58}$$

where $\frac{\Delta V}{V_0}$ is the voltage translation of $\frac{\Delta B}{B_0}$ due to Faraday's law. If the specimen is metallic and non-magnetic then relative permittivity and permeability can be approximated as unitary values. Therefore at constant frequency and for small phase angles, ϕ,

$$\phi \approx \frac{\Delta V}{V_0} = -jQ\omega\mu_0\sigma \qquad \therefore \qquad \phi \approx \frac{\Delta V}{V_0} \propto \sigma \tag{2.59}$$

where $Q = \frac{t}{4}\left(\frac{2a^2+{R_d}^2}{\sqrt{a^2+{R_d}^2}} - 2a\right)$ is a constant of coil geometry.

2.3 Magnetic conductive materials

Unlike non-magnetic conductive specimens ($\mu_r \approx 1$), ferromagnetic ones ($\mu_r \gg 1$) alter the primary field due to magnetization of the specimen, considerably more so than diamagnetic or paramagnetic materials, in addition to the field generated by eddy currents. This magnetization changes the inductance of the sensor coils. For a ferromagnetic specimen μ_r also changes during its hysteresis cycle in a time varying H-field [53].

When a ferromagnetic specimen such as iron is imaged by the MIT system the B-field in the specimen is increased in proportion to its permeability, $\boldsymbol{B} = \mu(T, f, p, MH, etc.)\boldsymbol{H}$; where T = temperature, f = frequency, p = pressure and MH = AC magnetic history of the specimen [53][54]. The statement that $\boldsymbol{B} = \mu\boldsymbol{H}$ for constant μ is meaningless for ferromagnets [50], as μ in this case is a complicated function of the above terms and more and can be visualized on a hysteresis B-H curve as the gradient of the curve (see figure 2.21). Inductance L of the sensor coil is also proportional to **B** [37]. There is a contribution to the resultant magnetic field at the sensor coils due to its ferrite cores, which would need to be taken into account if the system was to be modelled more accurately. However for the purposes of this work the phasor diagrams produced by ferrite cored inductors are proportional to air-cored coils, the only difference being the ferrite cored ones detect a proportionally larger magnetic field. This is because in relation to the phasor diagrams (figure 2.12), the same ferrite cores take part in measuring the primary and the secondary fields. The ferrite cores become magnetised in the presence of a magnetic field, increasing the field in the sensor coils and therefore exciting more eddy currents in them, generating a greater voltage across the coils. The ferrite cored inductor used in this work gives approximately constant inductance of 680 μH up to 0.2 A of current shown in figure 2.15 [55].

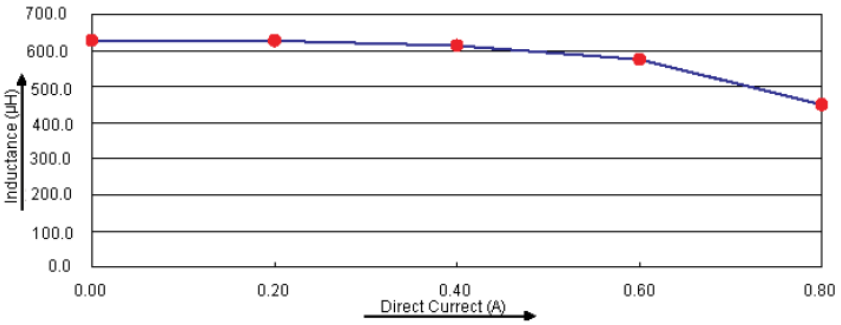

Figure 2.15. Inductance vs. direct current in ferrite cored inductor MCSCH895-681KU [55].

Magnetic flux $\Phi = LI \rightarrow L = \Phi / I$ [44], where L is inductance and I is the current in the coil and L is equal to the product of its permeability and a constant of its coil geometry [49]. Therefore from the figure 2.16(a), as inductance is approximately constant for an increase in current and therefore flux, its permeability is also constant because its geometry is constant.

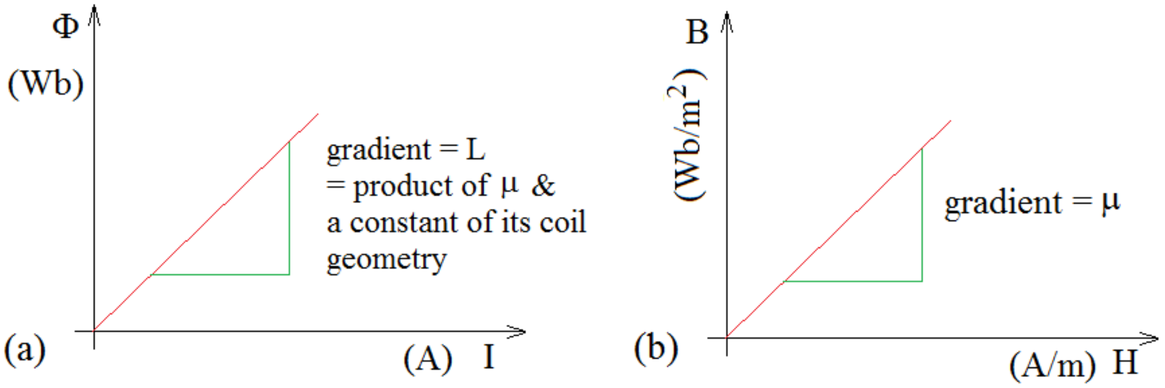

Figure 2.16. Sketched plots showing: (a) magnetic flux vs. current passing through a ferrite cored inductor with constant inductance and therefore constant permeability μ. (b) B-H curve for same ferrite inductor with constant permeability μ.

From the B-H curve in figure 2.16(b), for an increase in the H-field in the ferrite inductor the B-field increases proportionally, therefore the permeability is again constant with $H = \frac{NI}{l}\left[\frac{l}{\sqrt{l^2+d^2}}\right]$ and $B = \mu\frac{NI}{l}\left[\frac{l}{\sqrt{l^2+d^2}}\right]$, where N is the number of turns, I is the current, l is the length of the inductor and d is its diameter [56][44]. So the permeability of the core is approximately constant with currents experienced by the inductor of up to 34 mA in the experiments of this thesis [55]. The frequency dependence of these ferrite cores gives approximately constant permeability up to ~ 1 MHz [57]. With approximate constant permeability for the frequencies and currents experienced by the ferrite cores, the increase in voltage across the coils due to the ferrite is therefore proportionally larger than with air-cored coils. In other words the permeability μ is approximately constant in a small central region of the hysteresis loop of the ferrite (similar to figure 2.17 and 2.21), but is proportionally larger than μ_0 experienced by the air-cored coils.

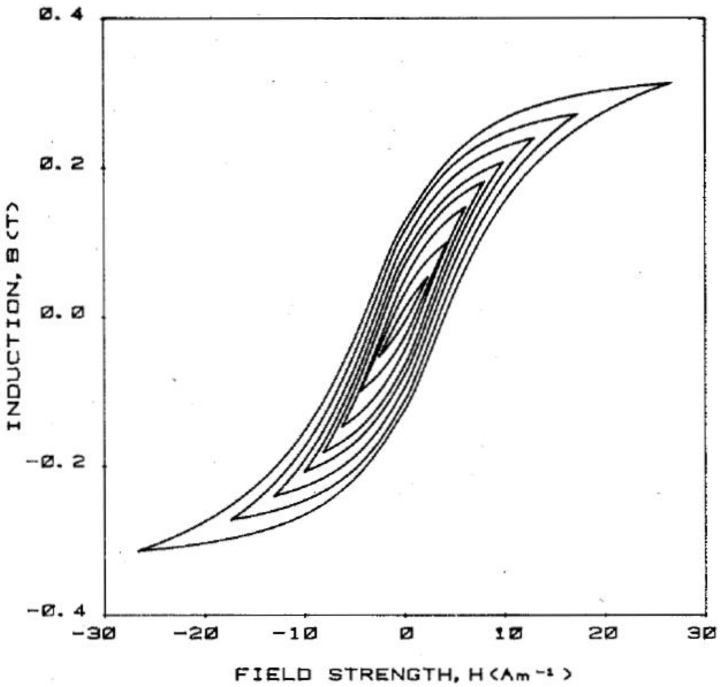

Figure 2.17. Example of B-H curve hysteresis loops of commercial ferroxcube [58]. The ferrite cores experience a hysteresis loop similar to the central loop above that is approximately linear in its gradient.

Ferrite cored inductors for operation below the megahertz range are made with Manganese-Zinc ferrite (Mn-Zn + Iron oxide). This soft ferrite is a ferrimagnetic material [56] with low coercivity, so that the ferrite's magnetization can be reversed easily with little energy loss due to hysteresis. Mn-Zn ferrites also have large permeability and their high resistivity prevent losses due to eddy currents [44][59][56].

From figure 2.18 the primary coil (coil 1) represents the Helmholtz coils with oscillating current $\frac{dI_1}{dt}$ flowing through them. The time varying flux $\frac{d\phi_{21}}{dt}$ generated by coil (1) is increased by the specimen's permeability and passes through the sensor coil

(coil 2). The rate of change of flux is proportional to the current in the Helmholtz coils and the mutual inductance M_{21}, between the Helmholtz coils and a sensor coil [44].

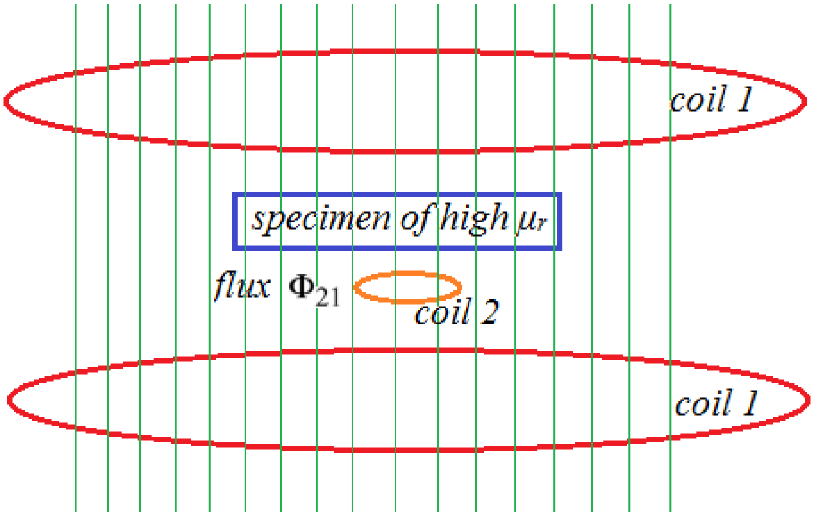

Figure 2.18. Schematic diagram of the primary field, increased by interaction with specimen of high μ_r.

The resultant e.m.f. from the primary field's interaction with the specimen, is induced across the sensor coil of N_2 turns, bounded by area A and expressed as,

$$V_{emf} = -\frac{N_2 d\phi_{21}}{dt} = -N_2 \frac{d}{dt} \iint_{coil\ 2} (\boldsymbol{B} + \Delta\boldsymbol{B}) \cdot d\boldsymbol{A} = -M_{21} \frac{dI_1}{dt} \qquad (3.61)$$

$$\text{where} \quad \Delta\boldsymbol{B} = \Delta\boldsymbol{B_e} + \Delta\boldsymbol{B_m}$$

where $\boldsymbol{B}$ is the primary field, $\Delta\boldsymbol{B_e}$ is the field due to eddy currents in the specimen and $\Delta\boldsymbol{B_m}$ is due to the specimen's magnetization.

The mutual inductance like the sensor coil's inductance increases with μ_r of the specimen, therefore increasing the voltage induced across the sensor coil.

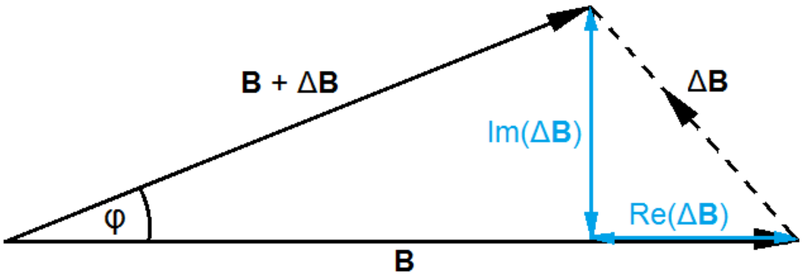

Figure 2.19. Phasor diagram for ferromagnetic specimen showing B fields detected by the sensor coil. The primary field (**B**) is due to the Helmholtz coil and the opposing secondary field (Δ**B**) is due to the specimen. The total detected field (**B** +Δ**B**) leads the primary field by φ. Due to Faraday's law of induction, **B** and Δ**B** on this figure are proportional to amplitudes V and ΔV respectively – e.m.f.'s induced in the sensor coil [9].

Recalling that **B** + Δ**B** ∝ V + ΔV in the phasor diagram of figure 2.19; the vector sum of e.m.f.'s for a ferromagnetic specimen (also see figure 6.10e) shows that,

$$\mathrm{V} + \Delta\mathrm{V} < V$$

across the sensor coil, compared to non-magnetic conductive specimens where $\mathrm{V} + \Delta\mathrm{V} \ll V$ (see comparison in figure 6.10). In figure 2.19 and 4.31(e) for the ferromagnetic specimen, the effect is shown as Re(Δ**B**) reducing in negativity with a positive Im(Δ**B**). This is different from the non-magnetic specimens in figure 6.10 (a, c), where Re(Δ**B**) has a larger negative component. The ferrite cores in the sensor coils have the same effect as the magnetic specimens, increasing sensor coil inductance and the B-field through them. This is because the B-field in the specimen and ferrite cores are in phase with the H-field of the Helmholtz coils, as μ_r becomes larger, neglecting hysteresis losses from the alternating field. The effect of eddy currents in the specimen is the opposite, reducing coil inductance and increasing coil resistance as its secondary field opposes the primary by 180° (ideally). Both the large μ_r effect and the eddy current effect change the impedance of the sensor coil [37]. The large μ_r effect may explain why the Iron disk has a smaller negative Re(Δ**B**) and a larger **B** + Δ**B** than the non-magnetic Aluminium and Copper disks [37].

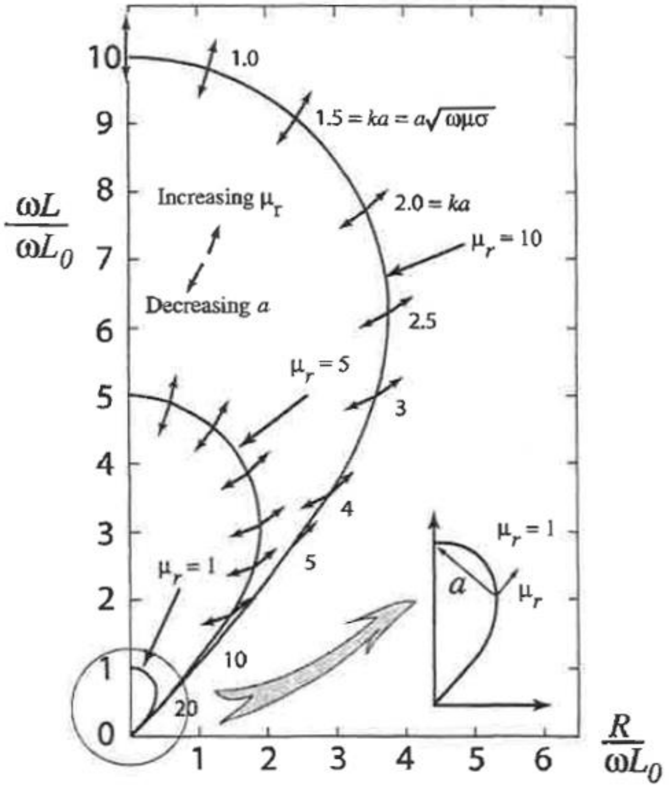

Figure 2.20. Impedance plane trajectories, as comma curves, for a specimen of relative permeability μ_r = 1, 5 and 10; for a probe coil encircling a ferromagnetic specimen. Displacement along the 'comma curve' for constant specimen permeability is determined by changes in angular frequency, ω, or conductivity, σ or 'a'. 'a' is the mean radius of a ferromagnetic specimen encircled by the sensor probe coil. ωL and R are the inductive reactance and reflected resistance respectively of the coil placed near the specimen. ωL_0 is the inductive reactance of the probe coil with no specimen present [37].

The following example shown in figure 2.20 explains the effect of a large μ_r specimen on the sensor coils, in this case on a probe coil (single coil as both exciter and receiver) encircling a ferromagnetic specimen with a time varying H-field applied by the probe. Using a normalised impedance plane diagram, where R = R' – R_0 is the reflected resistance due to the secondary field. R' is the total resistance of the coil, i.e. the coil's own resistance plus real resistive losses due to its interaction with the secondary field; and

R_0 is the resistance of the coil. L_0 is the inductance of the sensor in air or infinite lift-off and L is its inductance placed near the specimen [37]. Ideally the large μ_r effect would only increase the inductance of the probe. However in figure 2.20 both ωL and R increase with μ_r . The three 'comma curves' show $\mu_r = 1$, 5 and 10 for 100% coupling. The increase in reflected resistance R is due to hysteresis losses as the H-field varies sinusoidally, where energy is dissipated in aligning magnetic domains with the field. The heat loss due to hysteresis becomes part of the magnetic circuit connecting the probe coil and specimen, where both imaginary inductive and real resistive components are transmitted through the magnetic field. Hysteresis energy loss appears as increased resistance to the probe coil and is transmitted back to it in this way.

The small hysteresis loop about the origin in figure 2.21 relates to the above example. It shows how the H-field oscillates in the ferromagnetic specimen, where its permeability μ increases and decreases, represented as the changing slope of this B-H loop. This is indicated in figure 2.20 by arrows on the 'comma curve', as ωL and R increase and decrease with μ_r . In the example of figure 2.20, '*a'* is the mean radius of a specimen tube encircled by the sensor probe coil; ω is angular frequency of the applied field and σ is the conductivity of the specimen. A displacement along the comma curve for constant specimen permeability is determined by changes in angular frequency, ω, or conductivity, σ [37].

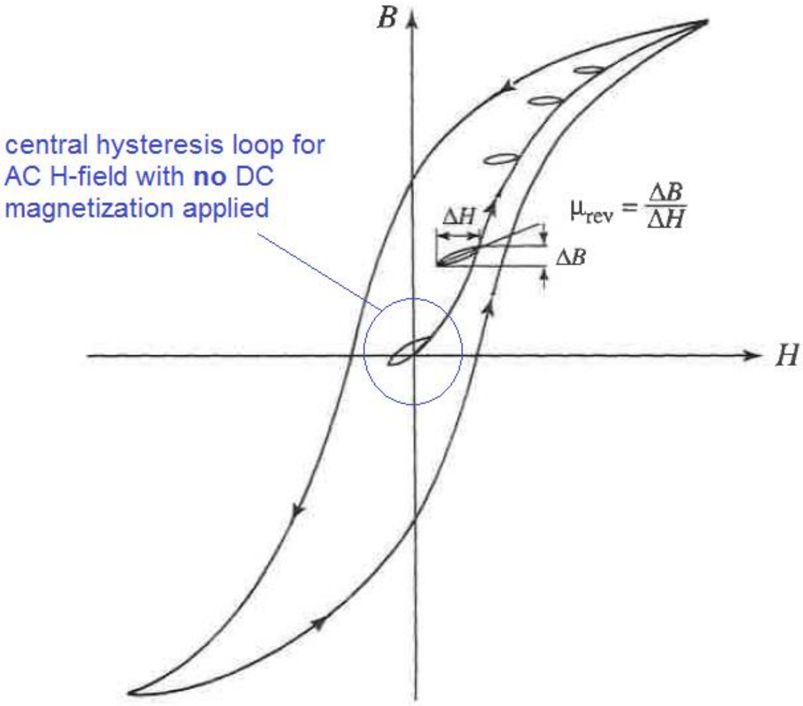

Figure 2.21. B-H curve showing small hysteresis loops in the ferromagnetic specimen, at varying levels of static DC magnetization [37].

Figure 2.21 shows a B-H curve of the magnetic history of a specimen. The small hysteresis loop at the centre represents the magnetic history of the specimen excited by the AC primary field, where no other fields are applied as is the case for ferromagnetic specimens investigated in this study.

Future work could involve application of a DC (static) magnetic field to ferromagnetic specimens such as Iron, where the hysteresis loop will be traced out at the upper right tip of B-H curve. The DC H-field will be applied for a value of H that gives magnetic saturation of the specimen, to in effect reduce the relative permeability of Iron to μ_r ~ 1, increasing its skin depth and therefore enabling greater penetrability of an Iron enclosure. The five small loops in figure 2.21 indicate AC magnetic history at various degrees of DC magnetization. The gradient μ_{rev} is the reversible permeability and is used instead of μ in these calculations [37].

3 Investigation of a basic MIT system

In the early stages of this study, a basic electromagnetic imaging system was designed and constructed [1] to understand the principles of MIT that would be the ground work for a more sophisticated set up later. At this stage a form of eddy current imaging was demonstrated by using the phase difference between the signals in the driver and sensor coils [7][9], via a lock-in amplifier.

The measurement of the phase difference between the two coils was used to image a sample object in two dimensions. This is performed by moving the sample, by hand, into each *x-y* position with respect to the common axis of the coils. The resolution of the MIT system was investigated by analysing images of different arrangements of steel ball bearings. The penetrating power of the system was investigated by imaging steel ball bearings and a mild steel bar through metallic shields.

For more details of MIT principles see Section 2.

3.1 System description

The set up for the basic system consisted of the instruments shown in figures 3.1 and 3.2. A driver coil supplies the primary AC magnetic field that impinges on a metallic sample. A single sensor coil measures the resultant field due to the addition of eddy currents excited in the sample. In order to image an object using eddy currents, an image medium had to be chosen. Seeing as the eddy currents in the sample produce a magnetic field opposing the primary one (Lenz's law), the resultant field is generated with a time delay [60]. This is represented as a phase shift between primary and resultant field and can be determined by comparing the background phase to the sample object's phase, from the potential difference (p.d.) induced across the sensor coil. As the driver coil's field is a constant amplitude and phase, the phase shift can be inferred by measuring the phase difference between the driver and sensor coils [61]. Therefore this was used as the medium of the image, which also happens to be representative of the conductivity of the sample [10][20] (see Section 2.2.1 and end of 2.2.2). The phase difference was measured by a lock-in amplifier to produce a 2D surface plot in *x-y* space via a MATLAB program. The operation of the imaging system will be described next.

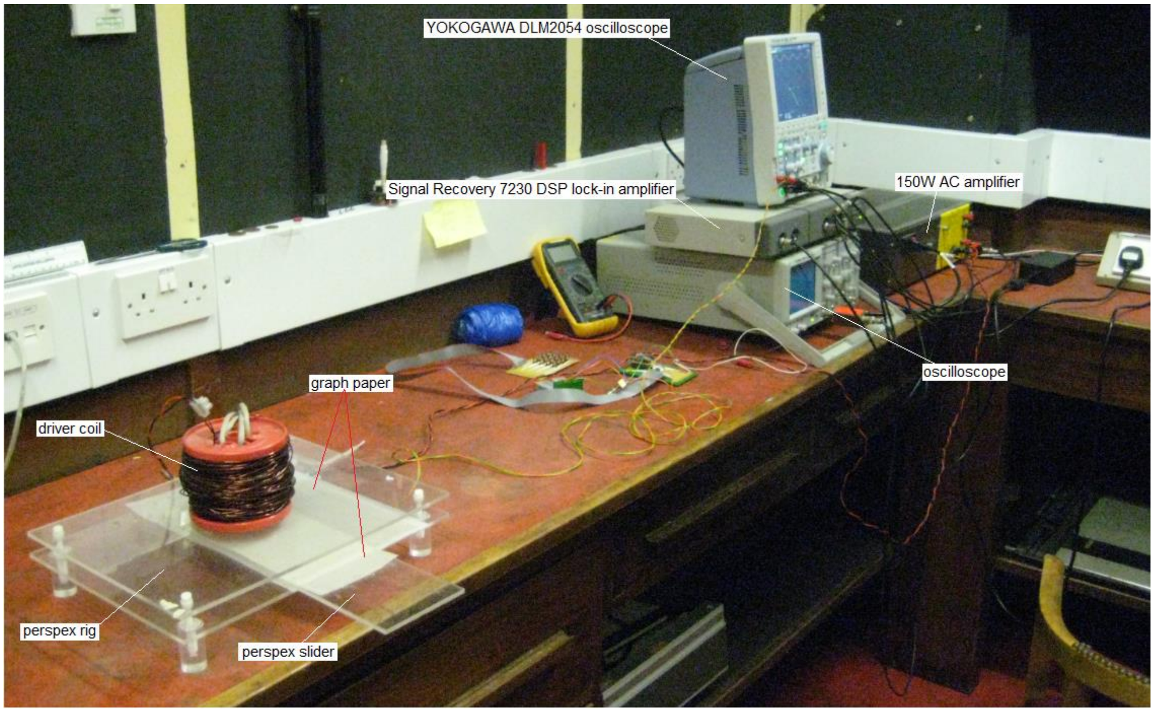

Figure 3.1. Photograph of experimental set up showing: Perspex rig, Perspex slider, graph paper on lower platform and slider of the Perspex rig, driver coil, YOKOGAWA DLM2054 oscilloscope, ISO-TECH ISR622 oscilloscope 20MHz (oscilloscope), Signal Recovery 7230 DSP lock-in amplifier (includes oscillator) and 150W AC amplifier.

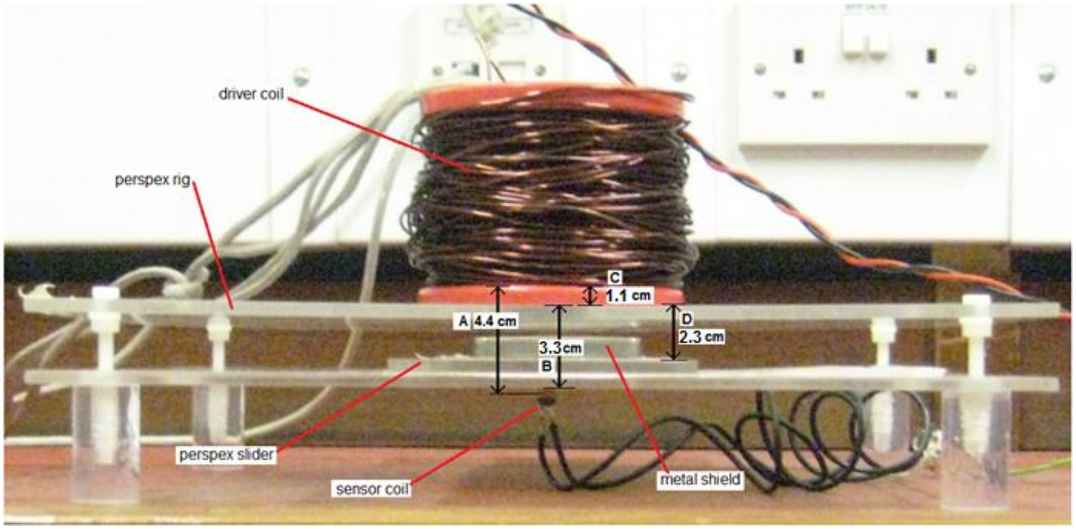

Figure 3.2. Photograph of Perspex rig, driver coil and sensor coil. Showing distances of key parts of the apparatus: A = 4.4 cm, B = 3.3 cm, C = 1.1 cm and D = 2.3 cm.

A Signal Recovery 7230 DSP dual-phase lock-in amplifier (see Section 4.3 and 4.3.1) measures the voltage phase difference between the signal in the sensor coil with respect to the signal in the driver coil (as reference). This measurement is the relative phase difference; it is not the absolute phase difference between the primary and primary + secondary voltages, which are proportional to primary and primary + secondary magnetic fields, induced in the sensor coil due to Faraday's law (see figure 2.2 and Section 2.1). The absolute phase difference can be determined from the difference between the specimen's phases (due to the primary + secondary voltage) and the background phases (due to the primary voltage) in the image (see figure 6.1 in Section 6). When the sample was placed between the coils the magnitude and phase of the sensor coil's p.d. change. This is due to the opposing magnetic field generated by the eddy currents, that are induced in the sample by the primary field [7][61] as illustrated in figure 3.3. This is described in more detail in Section 2, pages 39 to 40 and Section 2.1.

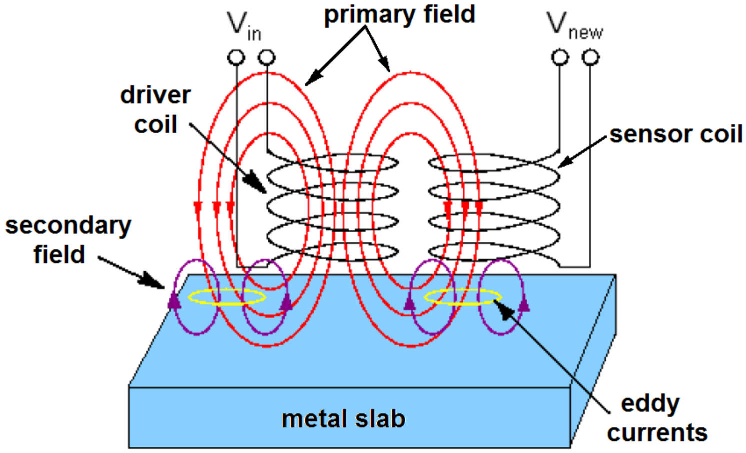

Figure 3.3. MIT principles can be explained by the induction of eddy currents in a metal slab. A driver coil provides the primary AC magnetic field, and a sensor coil detects the resultant field, that includes the opposing field due to the eddy currents [49].

The driver and sensor coil (figure 3.2), have external diameters (12.4 ± 0.1) cm and (6.90 ± 0.03) mm, respectively, and the sensor coil is a commercially available ferrite-cored inductor of (680 ± 10%) μH made by Multicomp, part number MCSCH895-681KU [55]. The driver coil (see table 3.1 for parameters) was chosen for the following reasons. Firstly a previous driver coil had been tested of 40 mm external diameter, with 1900 turns of 0.2 mm diameter Copper wire, giving a field of (0.30 ± 0.03) mT at the level of the sensor coil at 500 Hz. This previous driver coil gave satisfactory images when tested, but had been changed for the present driver coil because the present one gave a larger magnetic field for the same applied voltages, due to greater thickness of wire enabling a larger current, thus enabling greater penetration of the field. The present driver coil also gave a magnetic field at the level of the sensor coil of (0.76 ± 0.03) mT and (0.042 ± 0.003) mT RMS at 500 Hz and 5 kHz respectively. This was shown to produce images of a satisfactory quality for the purposes of this work. The sensor coil needed to be small so that changes in the secondary field coming from the specimen object could be resolved in different positions in 2D space. Having 146.5 turns of wire that was (0.241 ± 0.001) mm in diameter gave the sensor coil a large enough inductance to pick up the resultant field passing through the specimen that was shown to be satisfactory for imaging. Its inductance was also increased by having a ferrite core that gave it more sensitivity in detecting the resultant magnetic field. The frequency characteristics of the driver and sensor coils are shown in figure 3.4 (a & b) showing the measurement of parallel resonance of the coils. Parallel resonance gives the same resonant frequency of the coils as series resonance, the difference being that the parallel one shows a peak in impedance at resonance as opposed to a trough. The driver coil has a resonant frequency of 170.74 kHz and the sensor coil 689.26 kHz. Therefore the frequencies used in the experiments are much lower than the resonant frequency of either coil.

The sensor coil's axis is collinear with the driver coil's, and the coils are placed on a perspex rig to magnetically isolate the experiment (figure 3.1 and 3.2). The perspex is an insulator, so its conductivity is too small to disturb the magnetic fields, i.e. the eddy currents induced in it forming magnetic fields are negligible and undetectable by the imaging system. The sensor coil was attached to the underside of the lower platform of the perspex rig. The sample object (e.g. steel ball bearing) was fixed to a slider which could be moved in the *x-y* plane perpendicular to the coils' axis and whose position could be determined with an accuracy of 1 mm.

A 150 W AC amplifier (in-house made) supplies an AC signal at 27 V for most of the experiments and 31 V for imaging through ferromagnetic and Aluminium foil shields (see Section 3.3.2). AC frequencies applied across the driver coil in this study were 500 Hz, 5 kHz, 10 kHz and 20 kHz. The parameters of the experiment are given in table 3.1.

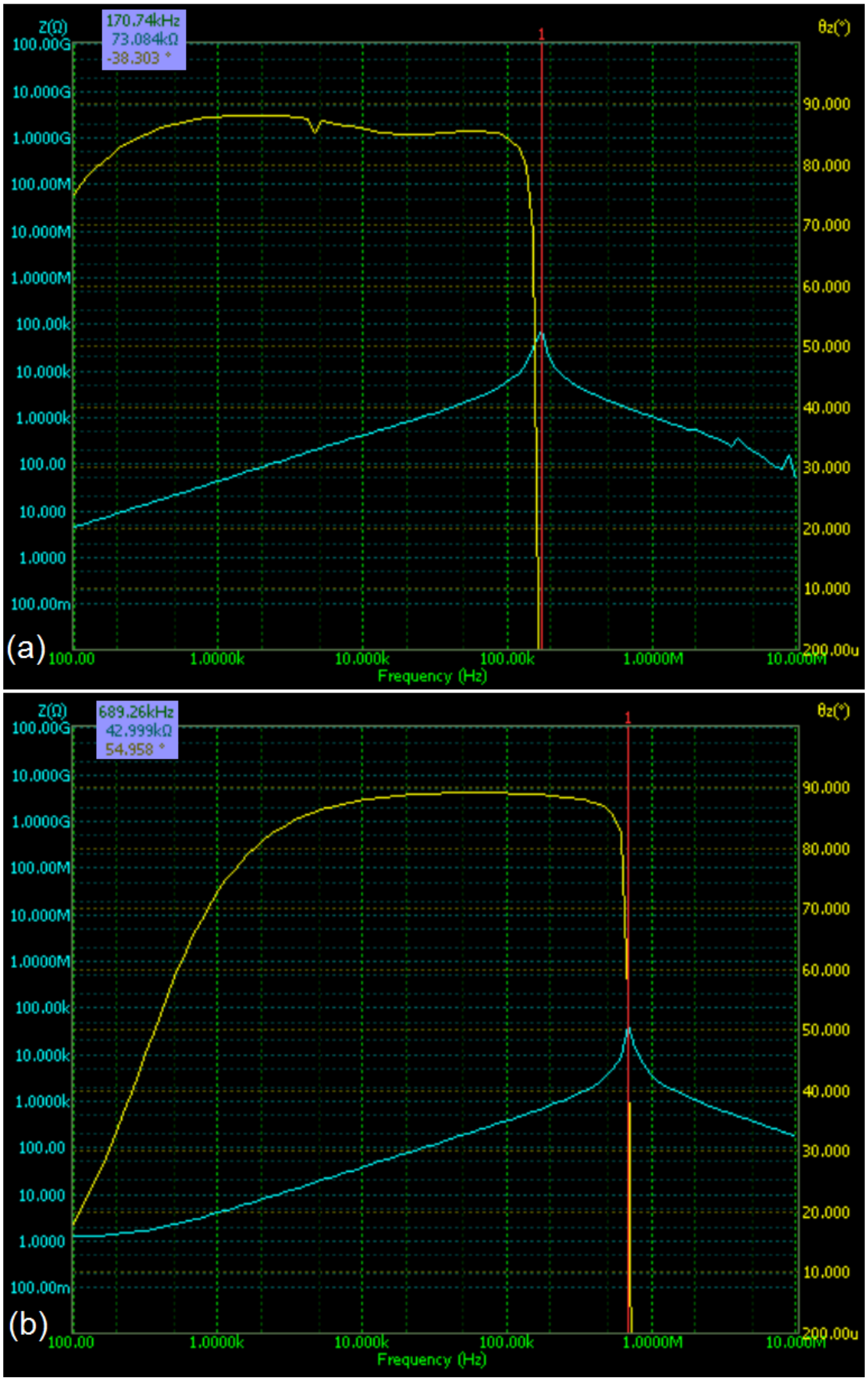

Figure 3.4. Plot showing frequency sweep of frequency vs. impedance (Z) for (a) driver coil and (b) sensor coil, indicating the resonant frequency of the driver coil at 170.74 kHz and the sensor coil at 689.26 kHz. Parallel resonance is measured in the plots that gives the same frequency as series resonance i.e. $\omega_0 = (1 / LC)^{½}$; where ω_0 is resonant angular frequency, L is inductance of the coil and C is capacitance of the coil.

Table 3.1: Measured parameters for basic MIT experiments (single driver and sensor coil)

Name of Parameter	**Measured Value**	**Measuring Instrument**
Electrical Properties of Driver and Sensor Coils		
RMS potential difference (p.d.) across driver coil at a) 500 Hz, b) 5 kHz (2 values)[1], c) 10 kHz	a) (27.2 ± 0.3) V b) (27 ± 2) V; (31 ± 2) V c) (27 ± 2) V	Black Star 3210M Digital Multimeter
RMS Current in driver coil at a) 500 Hz, b) 5 kHz (2 values) [1], c) 10 kHz	a) (1.24 ± 0.01) A b) (0.123 ± 0.009) A ; (0.142 ± 0.009) A c) (0.062 ± 0.005) A	Black Star 3210M Digital Multimeter and using **I** = V/Z $= \frac{V}{\sqrt{R^2 + (2\pi f\, L)^2}}$ and propagation of uncertainty
RMS p.d. induced across sensor coil with **no** sample present, at a) 500 Hz, b) 5 kHz (2 values) [1], c) 10 kHz, d) 20 kHz	a) (73.69 ± 0.02) mV b) (70.98 ± 0.02) mV ; (81.71 ± 0.03) mV c) (71.99 ± 0.02) mV d) (74.55 ± 0.03) mV	YOKOGAWA DLM2054 Oscilloscope
RMS p.d. induced across sensor coil – at a) 500 Hz, b) 5 kHz (2 values) [1], c) 10 kHz, d) 20 kHz (all with 6.34 mm diameter steel ball bearing directly between driver & sensor coil)	a) (74.96 ± 0.03) mV b) (72.04 ± 0.02) mV ; (82.97 ± 0.03) mV c) (72.99 ± 0.02) mV d) (75.41 ± 0.03) mV	YOKOGAWA DLM2054 Oscilloscope
RMS Current induced in sensor coil at a) 500 Hz, b) 5 kHz (2 values) [1], c) 10 kHz, d) 20 kHz (no sample present)	a) (33.9 ± 0.8) mA b) (3.58 ± 0.06) mA ; (4.12 ± 0.10) mA c) (1.82 ± 0.03) mA d) (0.94 ± 0.01) mA	Black Star 3210M Digital Multimeter and using **I** = V/Z $= \frac{V}{\sqrt{R^2 + (2\pi f\, L)^2}}$ and propagation of uncertainty
AC frequencies applied across driver coil	500 Hz, 5 kHz, 10 kHz, 20 kHz	YOKOGAWA DLM2054 Oscilloscope
AC frequencies induced across sensor coil	500 Hz, 5 kHz, 10 kHz, 20 kHz	YOKOGAWA DLM2054 Oscilloscope
Resistance of driver coil	(1.4 ± 0.2) Ω	Radio Shack 22-7225 Digital Multimeter
Resistance of sensor coil	(0.9 ± 0.1) Ω	Radio Shack 22-7225 Digital Multimeter
Magnetic Properties of Driver Coil		
RMS AC magnetic flux density - level with the bottom of the driver coil and at its centre, for: a) 500 Hz - 27.2 V across driver coil b) 5 kHz - 27 V across driver coil c) 5 kHz - 31 V across driver coil	a) (2.51 ± 0.01) mT b) (0.170 ± 0.003) mT c) (0.197 ± 0.002) mT	Hand-held Gauss/Tesla Meter Model 4048 - F. W. Bell

[1] The 2 values, are for RMS p.d. across driver coil = (27 ± 2) V and (31 ± 2) V both at 5 kHz.

Magnetic Properties of Driver Coil - Continued…		
RMS AC magnetic flux density - at the level of the sensor coil, for: a) 500 Hz - 27.2 V across driver coil b) 5 kHz - 27 V across driver coil c) 5 kHz - 31 V across driver coil	a) (0.76 ± 0.03) mT b) (0.042 ± 0.003) mT c) (0.060 ± 0.005) mT	Hand-held Gauss/Tesla Meter Model 4048 - F. W. Bell

Name of Parameter	**Measured Value**	**Measuring Instrument**
Inductance of Driver and Sensor Coils		
Inductance of the driver coil	(6.97 ± 0.01) mH	WAVETEK LM22A Digital LCR Meter
Inductance of sensor coil	(0.63 ± 0.01) mH	WAVETEK LM22A Digital LCR Meter
Dimensions of Driver and Sensor Coils		
Sensor coil external diameter	(6.9 ± 0.1) mm	Standard Ruler
Number of turns of copper wire in sensor coil	146.5	
Diameter of lacquered copper wire in sensor coil	(0.241 ± 0.001) mm	Micrometer – Moore and Wright N^{0}961M
Driver coil external diameter	(12.4 ± 0.1) cm	Standard Ruler
Number of turns of copper wire in driver coil	unknown	
Diameter of lacquered copper wire in driver coil	(1.78 ± 0.02) mm	Micrometer – Moore and Wright N^{0}961M
Mild Steel bar, Shields and Perspex Rig		
Thickness of mild steel bar	(2.29 ± 0.02) mm	Micrometer – Moore and Wright N^{0}961M
Dimensions of mild steel bar	2.6 cm (width), 7 cm (length)	Standard Ruler
Thickness of ferromagnetic shield	(0.200 ± 0.002) mm	Micrometer – Moore and Wright N^{0}961M
Dimensions of ferromagnetic shield – as lid placed over sample	7.45 cm (length), 7.2 cm (width), 1.5 cm (height)	Standard Ruler
Thickness of Aluminium foil	(0.0130 ± 0.0003) mm	Micrometer – Moore and Wright N^{0}961M
Dimensions of Aluminium foil shield – as lid placed over sample	14.15 cm (length), 9.6 cm (width), 1.6 cm (height)	Standard Ruler
For dimensions and photos of mild steel bar, shields and Perspex rig, see figure 3.2 and 3.8.		

3.2 Determining resolution by imaging steel ball bearings

An imaging system is a modality that produces a visual representation of an object for diagnosis or data collection, using a variety of techniques e.g. ultra sound, x-rays etc. In the case of this study it is via eddy current induction using magnetic fields for the detection of concealed metallic objects.

In order to estimate the resolving power of the imaging system steel ball bearings of were imaged, either individually or arranged as different 1D and 2D planar structures. Spatial resolution is determined by the ability of an imaging modality to differentiate two objects. In the following steel ball bearings of 6.34 mm diameter were imaged at different separations apart to determine the resolution. The size and dimension of the ball bearings was chosen because it was large enough to be detectable and small enough to be imaged by the imaging system. They could also be placed 1 cm apart and still have a gap between them, where 1 cm apart is a distance that cannot be resolved (see end of this sub section). The steel ball bearing also has high conductivity allowing eddy currents to form and therefore phase measurements can be obtained.

Two dimensional images were produced by moving the metallic object by hand, in steps in the *x* and *y* directions and by taking one phase measurement for each position. The step size is 2 mm in *x* and *y* for the part of the image containing the ball bearing and 5 mm for the remaining parts of the image. Figures 3.5, 3.6 and 3.7 show the 2D surface plots of 6.34 mm diameter steel ball bearings in various arrangements, imaged with 500 Hz driving field. Figure 3.5 shows the image of a single ball bearing.

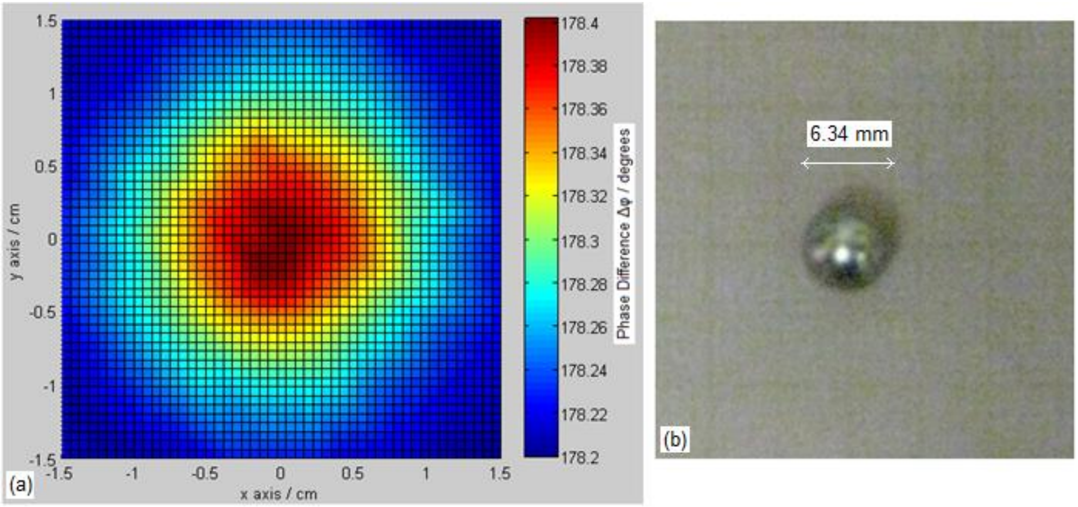

Figure 3.5. (a) 2D MIT surface plot of a 6.34 mm diameter steel ball-bearing imaged at 500 Hz. The plot was created from 121 (*x*, *y*, phase) measurements. (b) Photograph of the ball bearing is to approximate scale with the plot. The ball-bearing were fixed to graph paper using Blu-Tack and the graph paper was attached to the perspex slider using Blu-Tack.

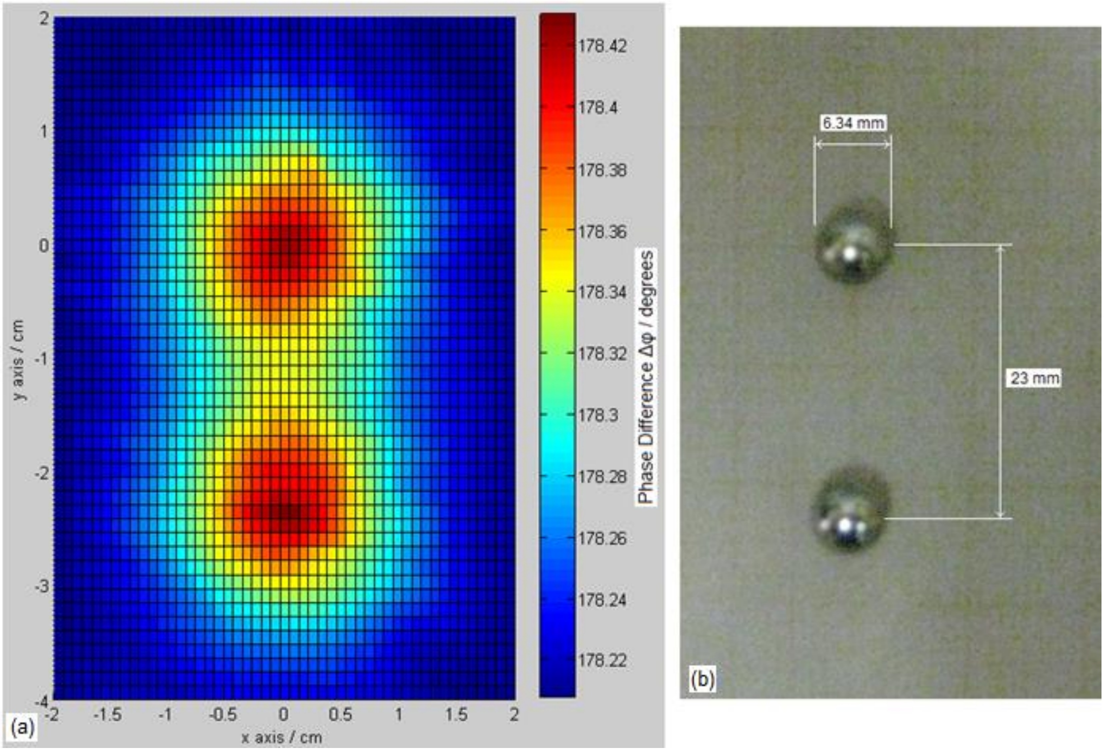

Figure 3.6. (a) 2D MIT surface plot of a 2 × 6.34 mm diameter steel ball-bearings separated by 2.3 cm and imaged at 500 Hz. The plot was created from 261 (*x*, *y*, phase) measurements. (b) Photograph of ball bearings is to approximate scale with the plot. The ball-bearings were fixed to graph paper using Blu-Tack and the graph paper was attached to the perspex slider using Blu-Tack.

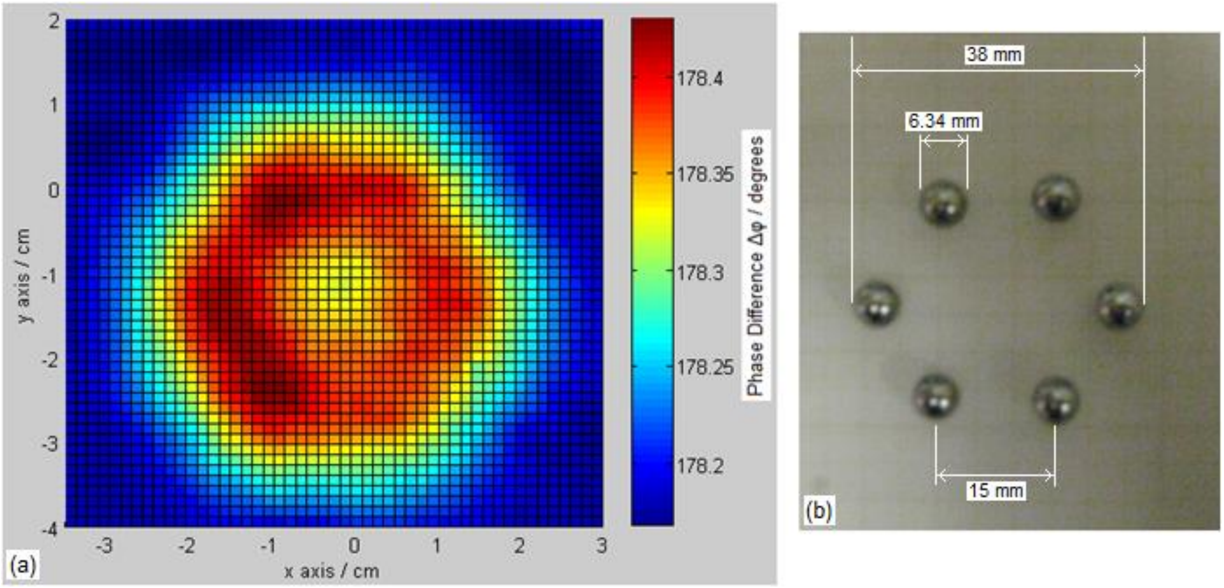

Figure 3.7. (a) 2D MIT surface plot of 6 × 6.34 mm diameter steel ball-bearings arranged as a hexagon and imaged at 500 Hz. The plot was created from 455 (*x*, *y*, phase) measurements. (b) Photograph of the hexagon is to approximate scale with the plot. The ball-bearings were fixed to graph paper using Blu-Tack and the graph paper was attached to the perspex slider using Blu-Tack.

The arrangement of two ball bearings separated by a distance of 2.3 cm is used for the measurements shown in figure 3.6. Those measurements demonstrated that the two ball bearings can be resolved, thus providing an indication that the resolving power of the MIT system is at least 23 mm. Additional measurements were performed for six ball bearings arranged as a hexagon of side 15 mm. Figure 3.7 shows that while the hexagon shape can be clearly identified the individual ball bearings cannot be resolved. Thus the combination of the results of figures 3.6 and 3.7, gave a resolving power of the system between 15 and 23 mm, for these steel test objects. In the blue plots of figures 3.9 and 3.10 showing separations of these ball-bearings as 1D plots it can be seen that at 2 cm apart they are still resolved but at 1 cm they are not. Therefore there is an indication that the resolving limit for this system is about 20 mm, in agreement with the conclusions based on the images of different arrangements of two and six ball-bearings. This estimate of the resolution was based on steel ball bearings, a further study would require different metals and shapes of object to determine if the resolution remains similar or how much does it vary for different objects?

3.3 Penetrating power through metal shields

Photographs of the following set ups for investigating penetration through metal shields, are shown in figure 3.8. The shields shown in this figure do not completely enclose the ball bearings but act as shields separating them from the driver coil directly above as shown in figure 3.1 and 3.2. The purpose of these experiments was to demonstrate the ability to image through one shield separating the sample from the driver coil, imaging through enclosures has been undertaken in Sections 6 to 9.

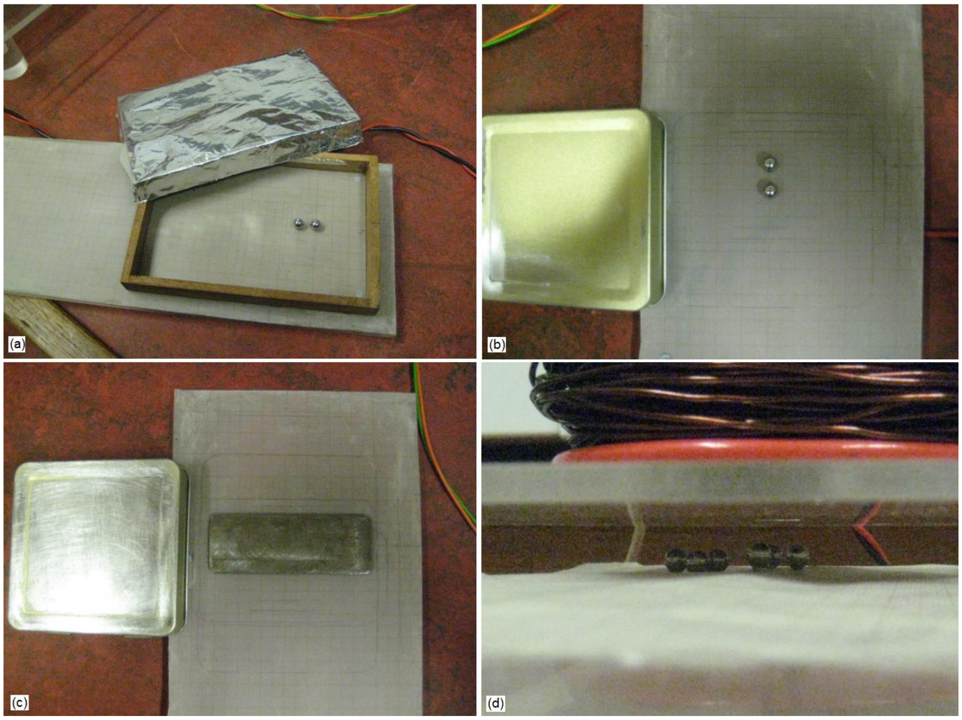

Figure 3.8. Photographs of (a) Aluminium foil shield: thickness = 0.013 mm, length = 14.15 cm, width = 9.6 cm, height = 1.6 cm. (b) Ferromagnetic shield: thickness = 0.2 mm, length = 7.45 cm, width = 7.2 cm, height = 1.5 cm (c) Ferromagnetic shield (see (b) for dimensions) with mild steel bar of thickness = 2.29 mm, width = 2.6 cm, length = 7 cm. See table 3.1 for more details. (d) Hexagon arrangement of 6 steel ball bearings of diameters 6.34 mm showing slight bumps in the graph paper where the left hand ball bearings are lower than the right hand ones. The ball bearings were fixed to graph paper using Blu-Tack and the graph paper was attached to the perspex slider using Blu-Tack.

3.3.1 Imaging two ball bearings through a ferromagnetic shield

An interesting issue is whether electromagnetic techniques can be used to image metallic objects through a metal screen. Clearly such a possibility depends on many parameters; the size and material of the object in the enclosure; the thickness and material of the enclosure; and the frequency of the driving field.

Presented here are the early results for a small sample of different configurations. Firstly a configuration of two 6.34 mm diameter ball bearings with centres separated by 3 cm (figure 3.9a), 2 cm (figure 3.9b) and 1 cm (figure 3.9c).

The 1D plots of figure 3.9 show the ball bearings imaged through a ferromagnetic shield of thickness 0.2 mm and height 1.5 cm (figure 3.8b), in the red plots and unshielded in the blue plots. The shielded (red plots) have 31 V (RMS) at 5 kHz applied across the driver coil. This is because at lower frequency and higher AC p.d. there is more penetration through the metallic shield. This is due to the skin depth [45][62]

$$\delta = \sqrt{\frac{2}{\omega\mu\sigma}} \quad . \qquad (3.1)$$

The skin depth, δ, gives the depth at which the alternating magnetic field has been attenuated to 37 % of its surface value, due to propagating through the material. Here $\omega = 2\pi f$ is the angular frequency; μ is the permeability of the metal shield and σ its conductivity. However the frequency has to be large enough to produce a noticeable phase difference in the ball bearings. Therefore 5 kHz was chosen as 2 kHz gave a poorer image. In the unshielded (blue) plots the ball bearings were imaged in exactly the same positions but at 10 kHz and a current of 62 mA (RMS) through the driver coil.

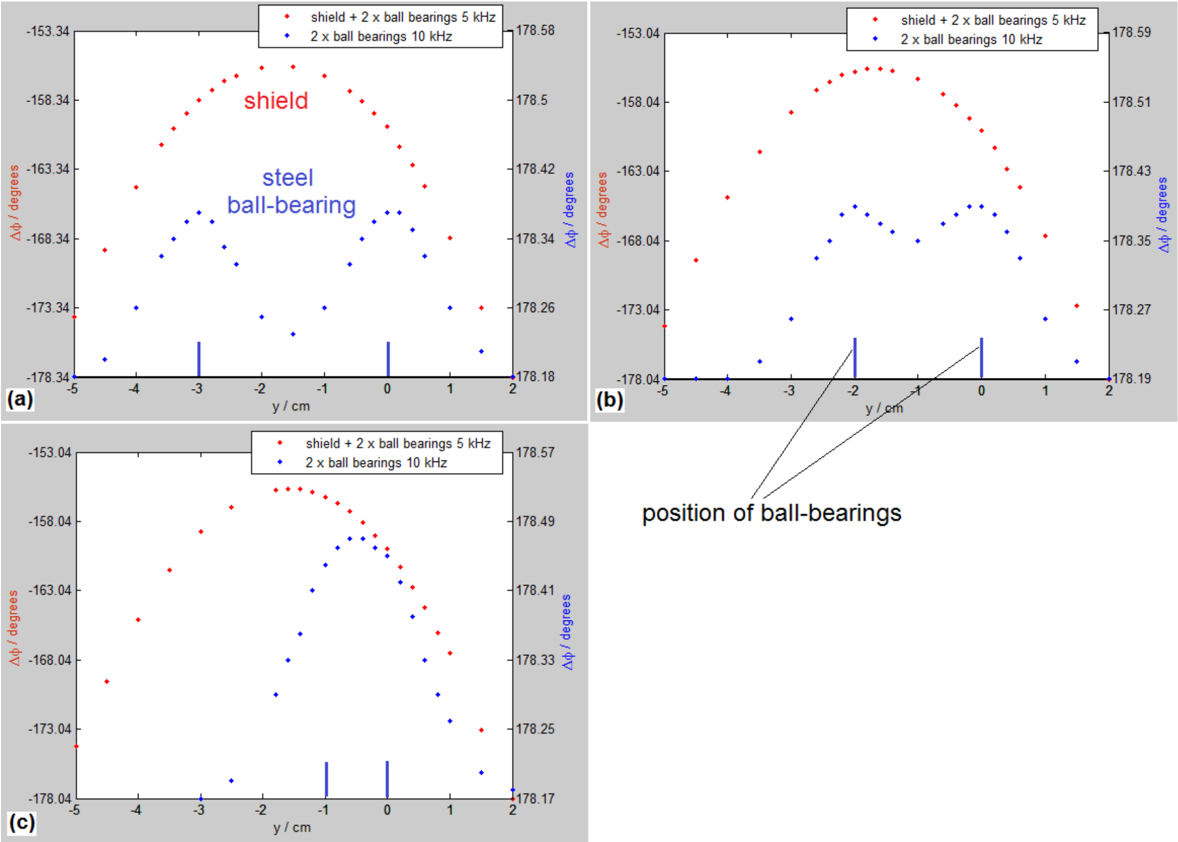

Figure 3.9. For the red plots (with caption on the left): 1D plots of p.d. phase-difference, Δφ, along the *y* axis of 2 × 6.34 mm diameter ball bearings shielded by a ferromagnetic lid of thickness 0.2 mm and height 1.5 cm. Imaging took place along the centre of the shield and ball bearings. An AC p.d. = 31 V (RMS) at 5 kHz was applied across the driver coil. The centres of the two ball bearings are separated by (a) 3 cm, (b) 2 cm and (c) 1 cm. The position of the ferromagnetic shield with respect to the plot is -5.5 cm to +2 cm on the horizontal axis. The blue plots (with caption on the right) show the ball bearings in the same positions but unshielded and AC p.d. = 27.0 V (RMS) at 10 kHz across the driver coil. Uncertainty in Δϕ measurement is ± 0.01°.

Above 31 V (RMS) across the driver coil the sinusoidal AC signal in it becomes distorted when imaging through the ferromagnetic shield. It was also found that the ball bearings gave largest phase differences at ~27 V (RMS) across the driver coil, when the frequency was set to 10 kHz and so this was used in most of the experiments.

It can be seen from these three figures (3.8a, 3.8b and 3.8c) that no distortion in the curve of the red plots were observed to indicate the presence of the ball bearings, when attempting to image them through a ferromagnetic shield. It can be seen from the red plots that the p.d. phase differences due to the presence of the shield was much larger than for the ball bearings, whose effect is dwarfed in comparison. The bearings giving a maximum phase of 0.18° to 0.3° compared with 18° for the shield. As a result there is negligible detection of the ball bearings in these images. The phase here is the medium of the 1D image. As can be seen from the plots the ball bearings have been magnified to show them clearly on the plot.

In figures 3.9 and 3.10, the shielded phase-difference data is at 5 kHz and the ball bearings on their own are at 10 kHz. This was due to a small error in conducting the experiments. Although this is not the most ideal comparison they are not too dissimilar, as the maximum phase difference (above the background phase) for a single 6.34 mm diameter ball bearing at 5 kHz is 0.18° and at 10 kHz it is 0.2°, with 27 V applied across the driver coil in both cases.

3.3.2 Imaging two ball bearings through an Aluminium foil shield

As a next step an attempt was made to image the ball-bearings through a thinner shield of Aluminium foil. Figure 3.10 (a, b, c) show 1D images of two ball bearings with 3 cm, 2 cm and 1 cm separations between their centres, with the images being taken through Aluminium foil of thickness 0.013 mm and height 1.6 cm (figure 3.8a), held in place by a wooden frame. The shield was constructed in these dimensions so that it could fit inside the perspex rig (see figure 3.1) and be in close proximity to the magnetic field of the driver coil, as well as a close distance from the sensor coil directly underneath it that would enable detection and imaging. The blue plots show the 6.34 mm diameter ball bearings, imaged without the shield at 10 kHz with 27 V (RMS) applied across the driver coil. In the red plots the ball bearings are imaged through the Aluminium shield at 5 kHz with 31 V (RMS) applied across the driver coil. 31 V (RMS) is the maximum voltage that the AC amplifier can deliver to the driver coil before the signal becomes distorted. It therefore delivers the largest magnetic field to penetrate the shield. At 27 V (RMS) applied across the driver coil, it gives the largest phase reading of the ball bearings in the 1D images compared with higher or lower voltages, so this was considered an optimum value of voltage.

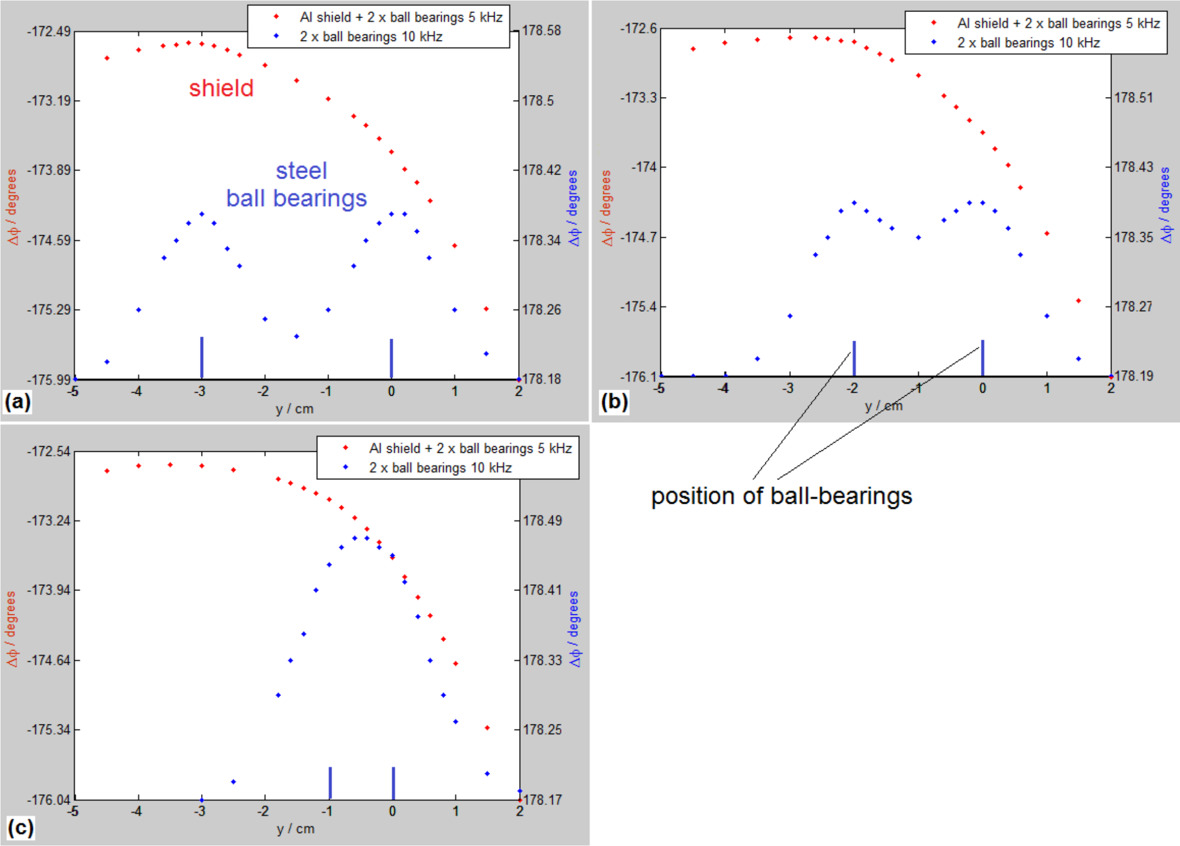

Figure 3.10. 1D plots of p.d. phase-difference, Δφ, for 2 × 6.34 mm diameter ball bearings positioned along the *y* axis and imaged through an Aluminium (Al) foil shield of thickness 0.013 mm and height 1.6 cm. Imaging took place along the centre of the shield and ball bearings. The ball bearings have their centres separated by: (a) 3 cm (b) 2 cm and (c) 1 cm. The plots show both shielded (red plots with caption on the left) and unshielded (blue plots with caption on the right). For shielded (red plots): AC p.d. across driver coil = 31 V (RMS) at 5 kHz. For unshielded (blue plots): AC p.d. across driver coil = 27 V (RMS) at 10 kHz. The position of the shield with respect to the above plots is -10.6 cm to +3.45 cm on the horizontal axis. Uncertainty in Δϕ measurement is ± 0.01°.

In comparing the three figures 3.10 (a, b, c) it can be seen that the shielded images (red) change shape slightly between each plot, in relation to the position of the ball bearings, shown as slight rises in the curve. In figure 3.10a this is at *y* = -3 cm and *y* = 0 cm, in figure 3.10b at *y* = -2 cm and *y* = 0 cm and in figure 3.10c at *y* = -0.5 cm. This result shows that steel ball bearings appear to be imaged through an Aluminium shield. Although it is not a decisive result as the changes in the shielded images could be due to the delicate Aluminium foil changing shape slightly as it was removed and placed back again in between experiments. Figure 3.11 shows comparisons between 1D images of the Aluminium foil for ball bearing separations of 3 cm compared with 1 cm apart in figure 3.11a and 3 cm compared with 2 cm apart in figure 3.11b. The comparison of the plots shows small changes corresponding to the position of the different ball bearings. This result is not decisive because the ball bearing is a relatively small object to detect through a shield for this imaging system.

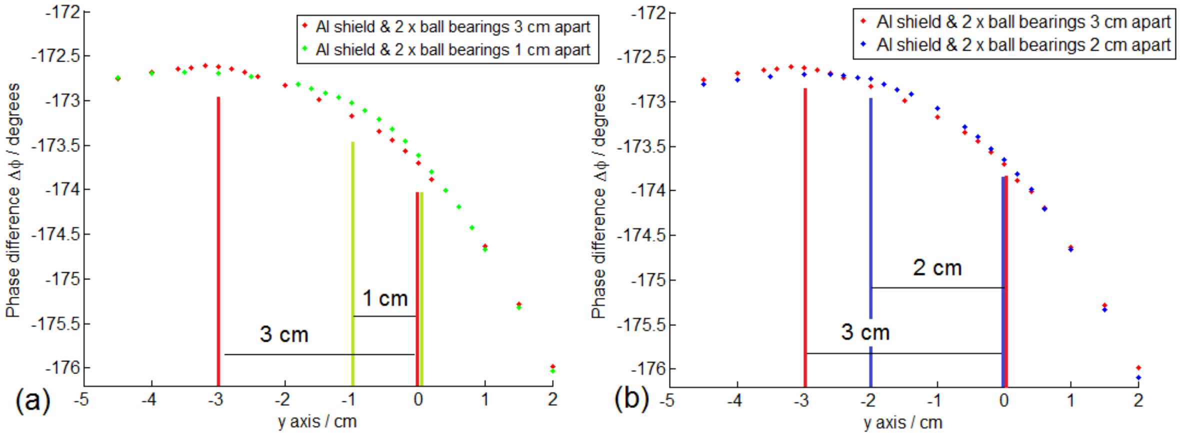

Figure 3.11. (a) 1D phase plot of the Aluminium shield comparing its image whilst shielding 2 ball bearings 3 cm (red) apart and 1 cm apart (green). The ball bearing at -3cm on the horizontal axis shows a rise in phase indicating its position. At -0.5 cm on the horizontal axis the combined effect of 2 ball bearings 1 cm apart shows a rise in phase again indicating its position. (b) Similar to (a) but comparing 2 ball bearings 3 cm apart (red) and 2 cm apart (blue). The ball bearing at -2 cm (blue) shows a rise in phase indicating its position compared with the red plot. Uncertainty in Δϕ measurement is ± 0.01°.

3.3.3 Imaging a mild steel bar through a ferromagnetic shield

Detecting smaller than 6.34 mm diameter steel ball bearings through a metallic shield involves testing this MIT system to its limits, as these objects are on the smallest end of the scale that can be imaged. The 6.34 mm ball bearing requires high frequencies to obtain a satisfactory image, i.e. 5 kHz and above. This is because being a small metallic object it requires a high frequency in order to excite enough eddy currents in it to be detectable. From Faraday's law (Section 2, Equation (2.2)) a small surface area requires a faster rate of change of magnetic field in order to produce a large enough detectable voltage.

A more decisive result would be to image a larger metallic object through a metal shield. This is described next and shown in the results of figure 3.12, imaging a mild steel bar through the same ferromagnetic shield.

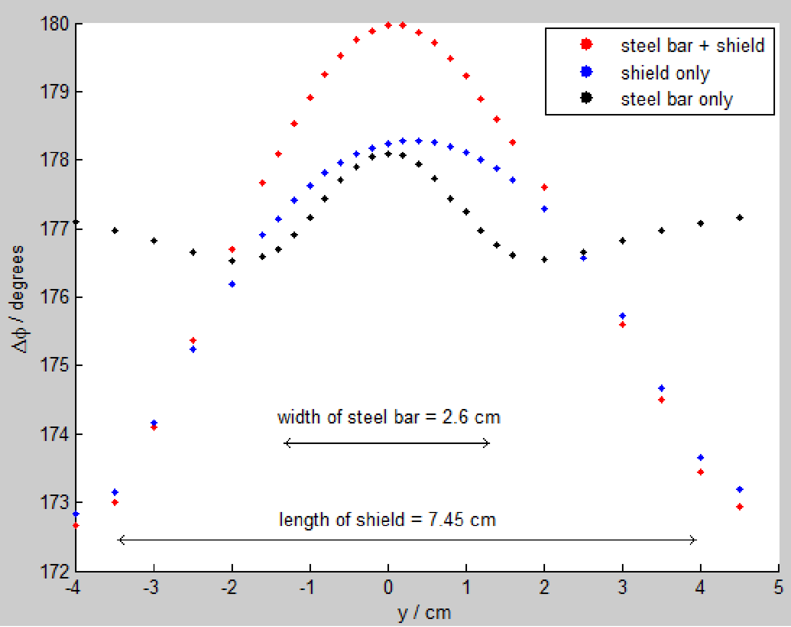

Figure 3.12. 1D image plot of p.d. phase-difference, Δφ, along the *y* axis for a mild-steel bar imaged through a ferromagnetic shield (red plot); the ferromagnetic shield imaged on its own (blue plot); and steel bar imaged on its own (black plot). For this experiment the AC p.d. across the driver coil was 27.2 V (RMS) at 500 Hz. Imaging took place along the centre of the shield and mild steel bar.

In figure 3.12 the red plot shows the 1D image of a mild-steel bar of width 2.6 cm, and thickness 2.29 mm, imaged through the ferromagnetic shield of length 7.45 cm and thickness 0.2 mm (figure 3.8c). The black plot shows the mild steel bar on its own and the blue plot is the ferromagnetic shield on its own. In comparison, the red plot (steel bar + shield) shows higher phase difference than the blue plot (shield only). This is a clear result of the steel bar in a static position being successfully imaged through a ferromagnetic shield.

In figure 3.12, the bar on its own (black plot), peaks in phase in the central region where the effect of the most eddy currents is experienced. The plot dips in phase at the edges of steel bar where edge effects take place. Edge effects are due to the eddy currents condensing as they meet non-conducting air boundary (see Section 6.2). After a dip in phases due to edge effects they then rise to constant background values as it moves away from the sample. This description also applies to the bar and shield (red plot) and the shield on its own (blue plot). Although this cannot be seen on the plot of figure 3.12 for these two objects, only the beginnings of curvature can be seen. If the plot was extended there would be dips in the plot at the edges of the shield and rises again moving further away from the edge. This can be in figure 7.6 (ai) from 2D imaging of an enclosure.

3.4 Conclusion

In this study, a set of metallic objects (ball bearings and coins), have been used to explore the imaging capabilities of a simple MIT system, based on a commercially available inductor as the sensor-coil. The resolving power of the MIT system was estimated by determining the minimum distance apart that two ball bearings could be resolved by the MIT measurements and found to be at about 20 mm.

The possibility of imaging metallic objects through ferromagnetic shields was also explored. Initial experiments with two ball-bearings imaged through ferromagnetic shields of thickness 0.2 mm gave negative results, with the signal due to the ball bearings being dwarfed in comparison with that of the shield, so that any effect was negligible and could not be determined from visual examination of the images. The same experiment repeated with an Aluminium-foil shield showed slight rises in the curve where the ball bearings were placed. It was unclear whether the slight rises in the curve were due to the ball bearings themselves or a disturbance in the shape of the Aluminium foil, when it was removed in-between experiments. This would need further investigation to determine any real effect. Finally a mild-steel bar was successfully imaged through a ferromagnetic shield using a low frequency driving field of 500 Hz. This seems to validate the possibility to image larger metallic samples through a ferromagnetic shield, provided they are not so large that they block the magnetic fields from reaching the sensor coil due to the skin effect.

4 Automated MIT system

4.1 Introduction

As anticipated in Section 1, the MIT set up was developed into an automated system to create magnetic images quickly and efficiently. A sketch of the apparatus is shown in figure 4.1. The instrumentation consists of a Helmholtz coil assembly for the driving field and an array of 400 sensor coils mounted on a non-magnetic support structure. This array size was suitable for imaging metallic enclosures on the order of 10 cm by 10 cm base area used in the experiments. The sample object was imaged via phase variation measurements between the signals of the driver and sensor coils, with the imaging process being automated via LabVIEW.

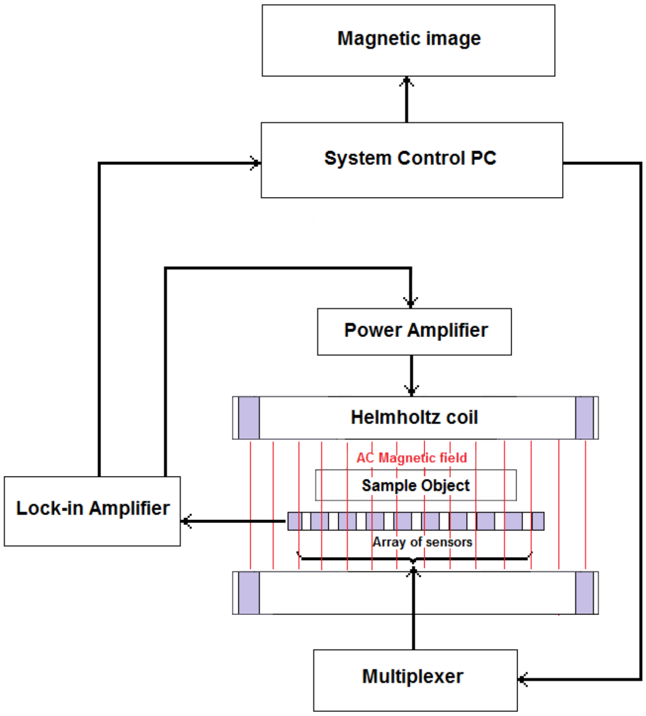

Figure 4.1. Schematic of experimental set up to create a magnetic image.

A multiplexer of 400 channels was used to sequentially connect each sensor coil to a dual-phase lock-in amplifier (see Section 4.3.1), so that measurements of voltage phase difference between the two coils could be taken. From these phase measurements a magnetic image was generated in 2D positional space. The acquisition time of this whole process takes 1.0 to 3.3 minutes. The quality of the image depends on the acquisition time. For example with 1.0 minute acquisition time then 150 ms (coil time) is given for each sensor coil to take a phase reading. This is too short a time for the lock-in amplifier to settle, so the resultant image will be of poor quality. The word ‘settling’ here means that the lock-in amplifier phase reading oscillates until it settles to a fixed value. For a coil time of 500 ms the lock-in amplifier settles nearly completely producing a better quality image, hence the acquisition time will be 3.3 minutes.

The following sub sections describe in detail the automated system. Photographs of the set up are shown in figures 4.2 and 4.3.

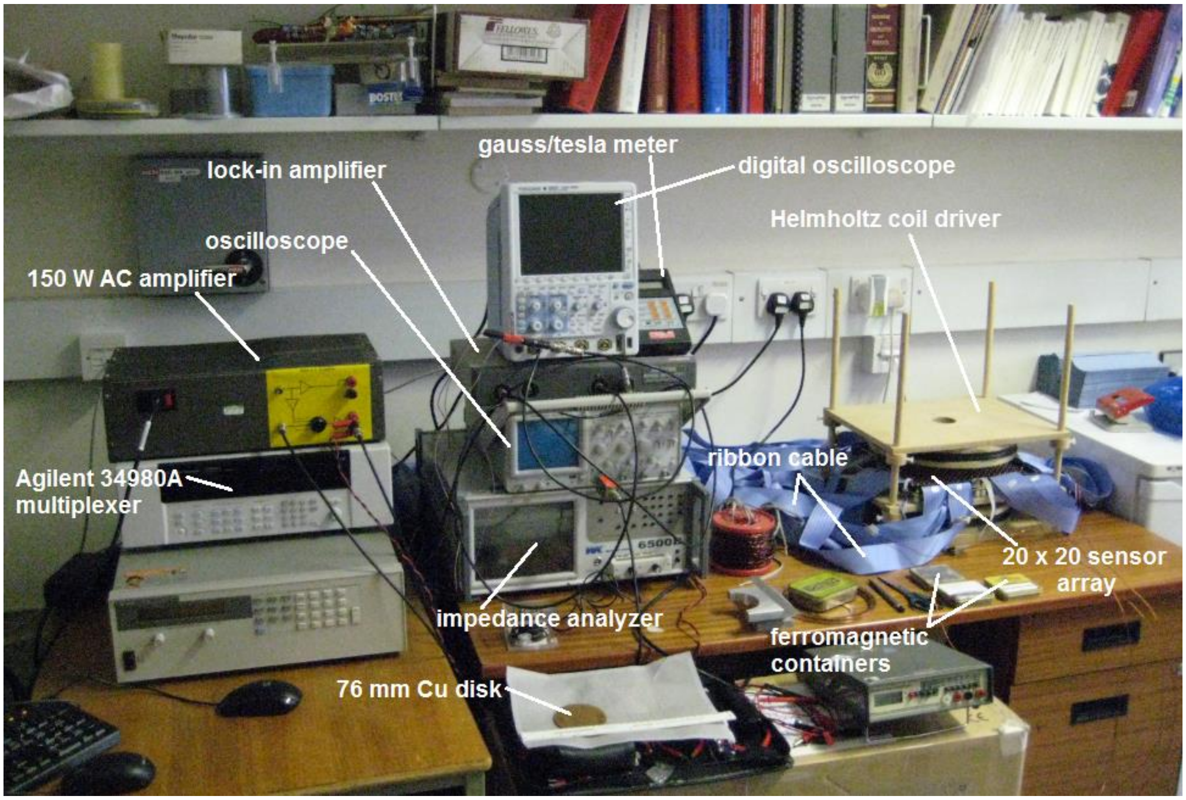

Figure 4.2. Photograph of the MIT experimental set up.

This is followed by the characterisation of the MIT system and a description of the technique used, to extract an image of a Copper disk from inside a single and double ferromagnetic enclosure.

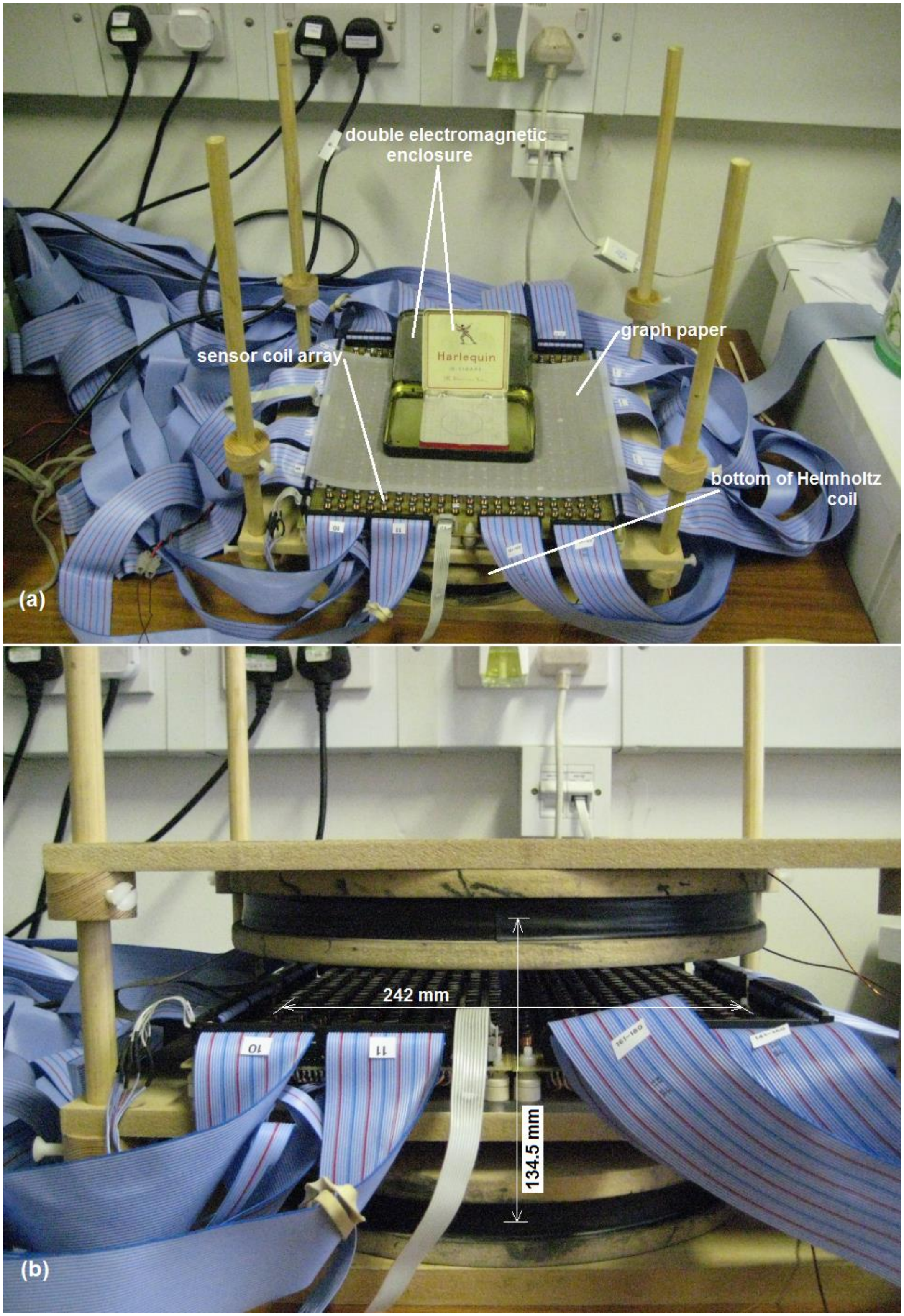

Figure 4.3. Photographs of the Helmholtz coil driver and 20 × 20 sensor array. (a) The set up with top Helmholtz coil removed and (b) shows a side view.

4.2 Driving and sensing coils

4.2.1 Helmholtz driver coils

The Helmholtz coil system (figure 4.4) is constructed from wooden formers, a wooden support structure and non-metallic fixtures.

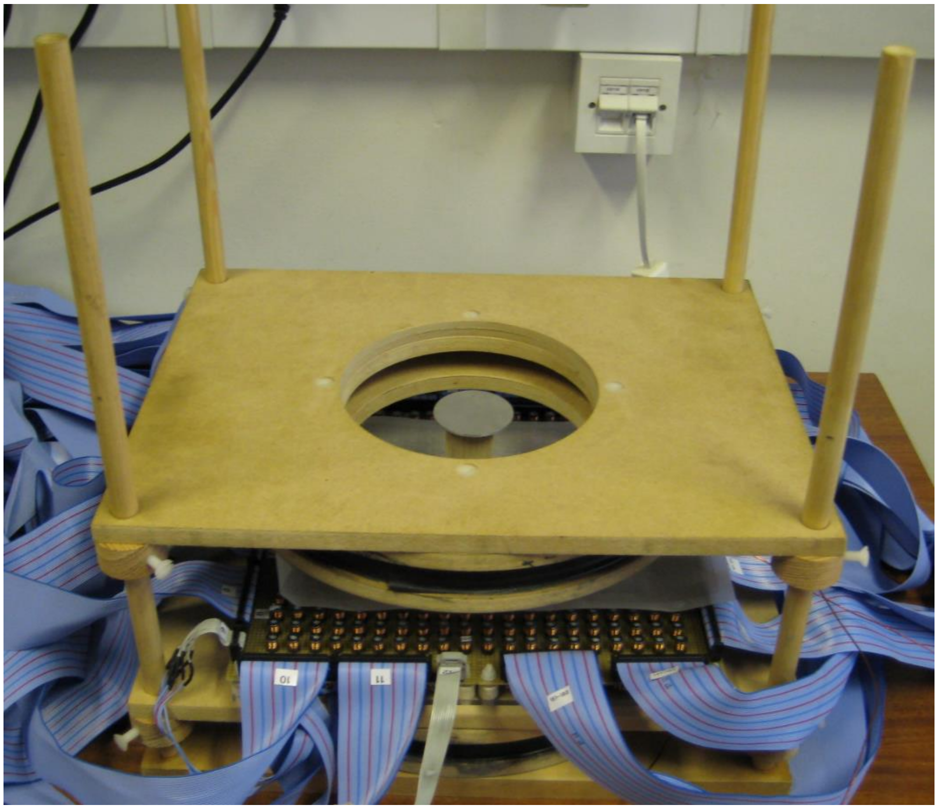

Figure 4.4. Photograph of Helmholtz coils and sensor coil array.

This is to magnetically isolate it from the experimental instruments and any other metallic objects in the vicinity. It consists of two identical coils having the same radius and identical currents and being arranged coaxially so that their fields add along the axis. The separation of the coils being equal to the radius, allows a highly uniform field to be generated midway at the axial point of the coil system [44][48][63]. Each of the two coils comprising the Helmholtz coil assembly was wound with 1 mm diameter enamelled

Copper wire; 300 turns in each coil, with external diameter 28.8 cm, inner diameter 25 cm and radius 13.5 cm and to within ~1 mm precision. The vertical thickness of each coil is 1.8 cm. This choice of coil parameters was chosen so that the sensor array would fit inside the Helmholtz coils, giving a magnetic flux density at the level of the sensor coils of 2.9 mT to 0.03 mT at 10 Hz to 5 kHz respectively [4]. These were adequate values for the experiments to be conducted.

The Helmholtz coil driver has the following electrical and magnetic properties. Firstly it has resistance (11.5 ± 0.1) Ω. For calibrating the resolution of the MIT system, Copper disks of varying diameter were used with the frequency of driving field set to 500 Hz. At 500 Hz the inductance and impedance of the Helmholtz coils were measured as (100.17 ± 0.02) mH and (314.9 ± 0.1) Ω, respectively. The inductance of the Helmholtz coils varies a small amount between 10 Hz and 5 kHz driving frequency used in the experiments, giving between (101.1 ± 0.3) mH to (101.921 ± 0.002) mH, respectively.

For the imaging of Copper disks concealed in ferromagnetic enclosures the frequency was set to 200 Hz for greater penetration, where inductance and impedance were measured as (100.18 ± 0.01) mH and (126.40 ± 0.01) Ω, respectively. The magnetic flux density generated by the Helmholtz coils, at its centre and level with sensor array, was (0.107 ± 0.004) mT rms at 500 Hz and (0.42 ± 0.02) mT rms at 200 Hz. These measurements were made with a Hand-held Gauss/Tesla Meter (Model 4048 - F. W. Bell) with (27 ± 1) V rms applied across the Helmholtz coils. The current through these coils was (86 ± 3) mA rms at 500 Hz and (215 ± 2) mA rms at 200 Hz.

4.2.2 Sensor coil array

The automated system uses an array of 20 × 20 coils. The array shown in figure 4.5 is connected up to an Agilent 34980A multiplexer (Section 4.3) that switches between each of the four hundred sensor coils, via LabVIEW computer automation, retrieving the phase measurements from each sensor in 500 millisecond to 3 second intervals.

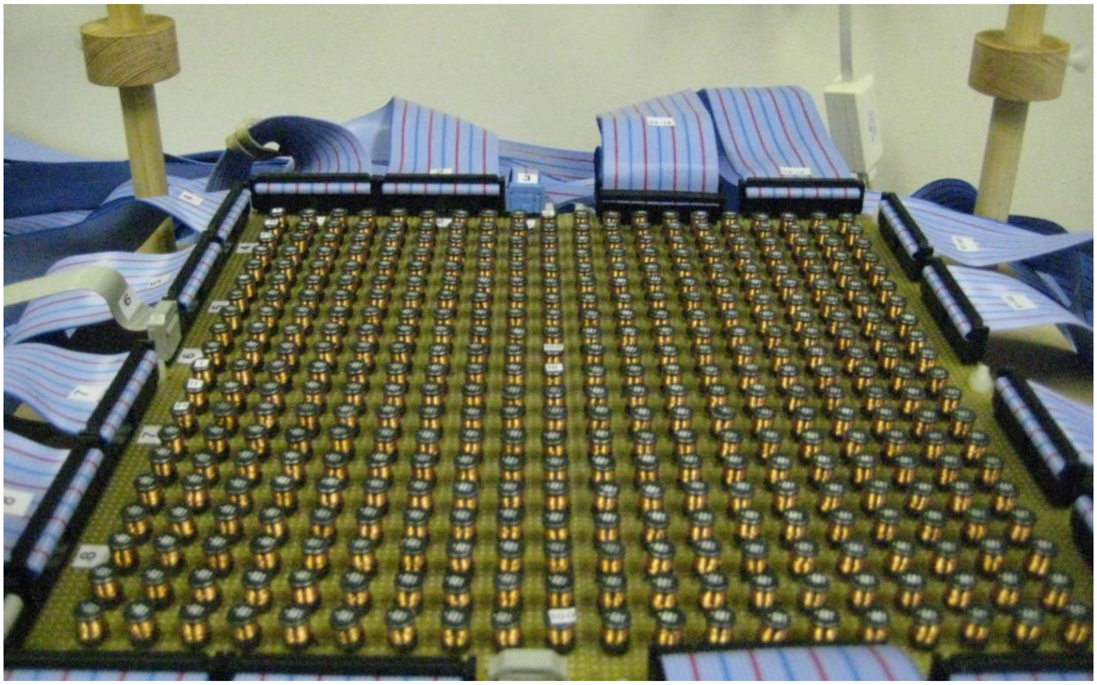

Figure 4.5. Photograph of 20 × 20 sensor-coil array.

The four hundred sensor coils are commercially available inductors of (680 ± 10%) μH, with ferrite cores, manufactured by Multicomp [55]. The inductance of the sensor coils varies between (0.60 ± 0.04) mH and (0.635 ± 0.002) mH for 10 Hz to 5 kHz driving frequencies respectively. These values include 3 m of ribbon cable connected to the sensor coils. This inductor was chosen as the sensor coil because of its narrow shape and small size, with a ferrite core that increased the sensitivity of the coils to detecting a magnetic field. Therefore soldering 400 coils onto a veroboard with a spacing of (13 ± 2) mm between their centre points allowed sufficiently well resolved images to be created for the experiments conducted, after testing the imaging system out.

The sensor coils were soldered onto two veroboards connected together, covering an area of (242 × 242) mm. Ribbon cable (multi-wire planar cable) connects the sensor coils via terminal blocks to the multiplexer, so that each sensor coil can be selected in sequence via the multiplexer switching mechanism. The sensors are electrically isolated on the veroboard with separate input and output terminals. The output signal of the sensor coils passes to the lock-in amplifier through the multiplexer, where the sensor coil's potential difference (p.d.) is referenced with the driver coil's one, for p.d. phase difference measurements used to create the magnetic image.

The sensor coils have resistance (0.9 ± 0.1) Ω and external diameter (6.90 ± 0.03) mm. The average current through ten arbitrary sensor coils was measured, but does not include sensors at the edges - outside of the uniform driving field, nor does it include five sensors giving anomalous peaked phase readings (see Section 7.3). This was because all sensor coils in the imaging region were receiving approximately the same magnetic field; therefore taking the average of 10 sensor coils was enough to obtain a satisfactory sample. The coils at the edges are outside the imaging region and are not included in an image, their values were taken from the average of nearby sensors and therefore suppressed (see Section 7.3), otherwise, they would dwarf the specimens being imaged. Without suppression the coils at the edges of the array give very high phases due to being outside the Helmholtz coils' uniform field (see figure 4.4).

The current through 10 sensor coils was calculated from the voltage across the sensor coils and their impedance. These were measured from the output terminals, with no sample present and (27 ± 1) V rms applied across the Helmholtz coils. At 200 Hz the average current through ten sensor coils was (0.044 ± 0.009) mA with average impedance of (205 ± 1) Ω and average p.d. across the sensors of (9 ± 2) mV. The large impedance is due to 3 meters of ribbon cable and the multiplexer that the current passes through before being measured. At 500 Hz the average current was (0.043 ± 0.009) mA with average impedance (205 ± 1) Ω and average p.d. across the sensors of (9 ± 2) mV. These measurements were taken with a Wayne Kerr precision impedance analyser model 6500B.

4.3 Instrumentation

A 150 W AC amplifier assembled in house by UCL, increases the voltage from an oscillator located in the Signal Recovery 7230 DSP dual-phase lock-in amplifier, to 27 V rms for most purposes. This amplified signal is applied across the Helmholtz coils to provide a uniform driving magnetic field. The current through it and therefore the field is dependent on the impedance for a given frequency. The AC amplifier has a frequency range of ~10 Hz to 20 kHz.

Two oscilloscopes monitor the signals across driver and sensor coils. A digital oscilloscope monitors both signals and also provides a Lissajous figure as a visual display of the dynamic p.d. phase difference, as each sensor measures the secondary field in a different part of the sample object and the array. The second oscilloscope monitors the signal across the driver coil directly, as the digital oscilloscope only monitors this signal before amplification, to protect it from damage due to the high voltages applied of 27 V rms.

The dual-phase lock-in amplifier [64] measures the p.d. phase difference between driver and sensor coils (see Section 4.3.1 for more detailed description). It does this by measuring the p.d. induced across the sensor coil with respect to the reference p.d. applied across the driver coil. For most measurements in this study a 2.6 V rms oscillator signal was amplified to 27 V rms across the driver coil, with the following lock-in amplifier parameters: time constant = 500 ms or 50 ms, and sensitivity = 50 mV. The sensitivity setting is adjusted manually for the DSP lock-in amplifier to give a gain of ‘2’, so that the DC output signal is equal to the input signal amplitude. When the input signal suddenly changes the time constant represents how long it takes before 63% of the output can adjust to it. The lock-in amplifier was also set to filter out mains frequency of 50 Hz.

The Agilent 34980A multifunction switch/measure unit has six low frequency multiplexer modules inserted (6 × Agilent 34924A), that make up the multiplexer described in this thesis. This multiplexer was chosen because it could accommodate 400 switches for the 400 sensor coils, as well as having a LabVIEW capability so that it could be automated with the other instruments in the set up. Each module is a 70 channel reed switch multiplexer. The sensor array, operated by the Agilent multiplexer via LabVIEW automation, is separated in four sections making input-output connections to 400 coils (figure 4.6).

Figure 4.6. (Left) Photograph of 20 x 20 Sensor coil array with ribbon-cable connector blocks around the perimeter. (Right) Rear photograph of the Agilent multiplexer showing cable connections from the sensor array. It is made up of 6 modules with 2 banks per module. Each bank has 35 input-output connections to the sensor coils.

Therefore each section has 100 coils. In the first module of 2 banks all 70 channels are used and then 30 channels in the first bank of the 2nd module, to make the first 100 coil connections. The 2nd 35 channels in module 2 and 65 channels in module 3 make up the 2nd 100 coils, etc. up to 400 coils.

4.3.1 Principle of the Lock-in Amplifier

The lock-in amplifier measures the amplitude and phase of a signal. In most cases this is to extract a signal of a known frequency from a potentially noisy background or interference [65]. For this study it is used as a phase sensitive detector to determine the voltage phase difference between driver and sensor coils after inductive coupling between the coils and the metallic specimen.

The lock-in amplifier is basically a homodyne detector preceding a low-pass filter. A homodyne detector [66] is used in optical interferometry to provide a reference from the oscillator which is the same source as the signal, before modulation of the two. The lock-in amplifier is similar because the reference is the same frequency as the signal and often derived from the same source. In the current set up it is from the same source, i.e. a driver coil's field (reference to its voltage) inducing an e.m.f. across the sensor coil (signal). The low-pass filter allows signals to pass through that have frequencies lower than the cut-off frequency and blocks frequencies that are higher [65][67]. In the lock-in amplifier this serves to attenuate the AC frequency component and allow the DC part to pass through. A simple low-pass filter consists of resistor and capacitor arranged as in figure 4.7 below. The resistor is in series with the output load and the capacitor is in parallel with it. The capacitor blocks low frequencies, in our case the DC signal, due to the capacitor's high reactance, so that the DC signal passes to the load. Higher frequencies give lower reactance in the capacitor so it essentially acts as a short circuit to earth for these frequencies. In the lock-in amplifier this process filters out the double frequency component described below.

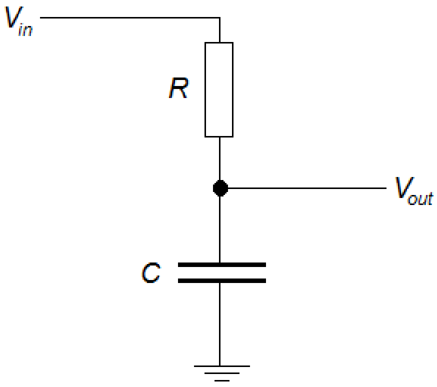

Figure 4.7. Simple low-pass filter.

The resistance and capacitance in this set up give the time constant of the filter, $\tau = RC$. The cut-off frequency, f_c, is determined by the time constant.

$$f_c = \frac{1}{2\pi\tau}$$

The time constant of the lock-in amplifier is a parameter that can be changed by the user. When the input signal suddenly changes, the time constant represents how long it takes before 63% of the output can adjust to it (figure 4.8).

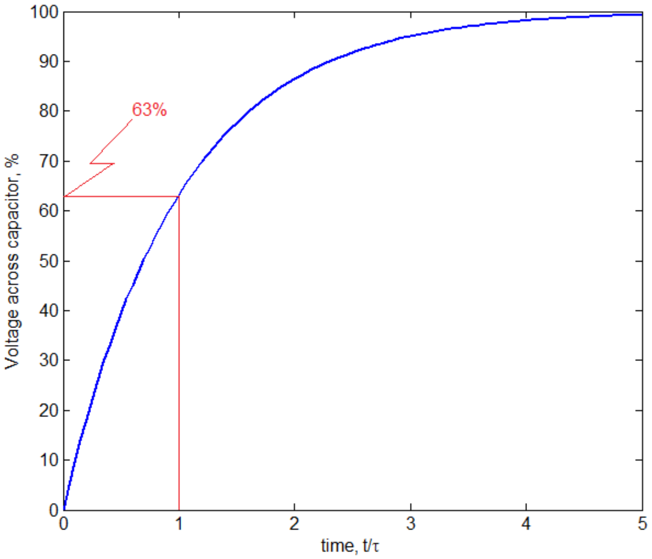

Figure 4.8. Percentage charging of capacitor in RC circuit, with time in units of τ = RC.

This describes the principle of filtering and frequency mixing of traditional analogue lock-in amplifiers. The one used in this work is a Signal Recovery 7230 DSP and it implements both steps by Digital Signal Processing. The operation of this dual-phase lock-in amplifier makes use of orthogonality of sinusoidal signals, described as follows.

Traditional Lock-in Amplifier

Firstly a description of a traditional lock-in amplifier will be given to explain the underlying principle [68][65]. In this instrument the input signal is amplified, where the amplifier's gain, g, is adjustable representing the sensitivity of the instrument [69]. The reference signal is passed to a sine-former to make it into a sinusoid with specific amplitude. A diagram is shown in figure 4.9; and is a simplification of part of the schematic for the Signal Recovery 7230 DSP [64][65].

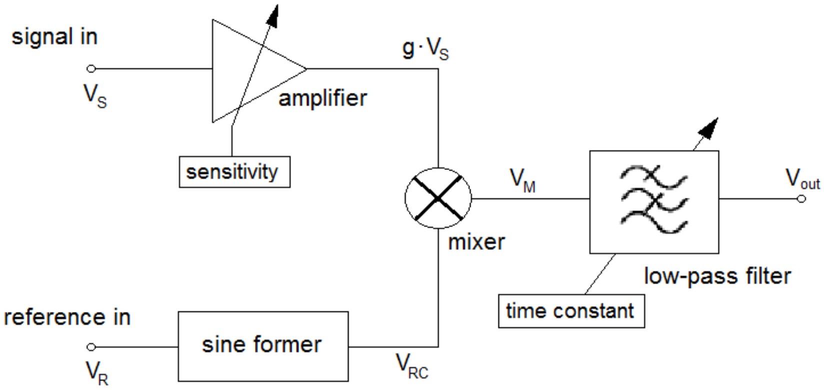

Figure 4.9. Simple Lock-in amplifier.

The input signal, V_S, has amplitude *K* and frequency *f*.

$$V_S = Kcos(2\pi ft + \phi_S) \qquad (4.1)$$

The reference signal,

$$V_{RC} = cos(2\pi ft + \phi_R) \, , \qquad (4.2)$$

has the same frequency. The mixer multiples the signals of (4.1) and (4.2) as follows, to give V_M.

$$V_M = Kgcos(2\pi ft + \phi_S) \cdot cos(2\pi ft + \phi_R)$$

$$= \frac{Kg}{2} [\, cos(\phi_S - \phi_R) + cos(2\pi 2ft + \phi_S + \phi_R) \,] \qquad (4.3)$$

Equation (4.3) results in a double frequency component, *2f*, and a zero frequency one as the DC signal. The low-pass filter should be set to remove the double frequency as described above with the RC circuit. The output signal is therefore,

$$V_{out} = \frac{Kg}{2} cos(\phi_S - \phi_R) \qquad (4.4)$$

The output is a DC signal proportional to K, which is the amplitude of the input signal we are measuring. The amplifier gain is *g* and if we make the assumption that $\phi_S = \phi_R$, then the output is 10 V if the RMS value of the input signal is the same as the sensitivity. Therefore,

$$g = \frac{10V\sqrt{2}}{sensitivity} = 2 \, , \qquad sensitivity = \frac{10V}{\sqrt{2}} \qquad (4.5)$$

The value of g = 2, cancels the ‘2’ in equation (4.4), to give the DC output signal. This is equal to the amplitude of the input signal. The sensitivity setting can be controlled on the lock-in amplifier panel.

Dual-phase lock-in amplifier

It may be difficult to measure K from V_{out} if $\phi_S \neq \phi_R$, although some lock-in amplifiers provide the ability to change ϕ_R until they are the same. A dual-phase lock-in amplifier solves this problem by implementing two mixers with corresponding low pass filters [65]. The first mixer multiplies the reference and signal as previously described and the second mixer multiplies them but with the reference shifted by 90°. This is shown in figure 4.10, which is a simplification of the schematic in the Signal Recovery Model 7230 DSP Lock-in Amplifier Instruction Manual [64].

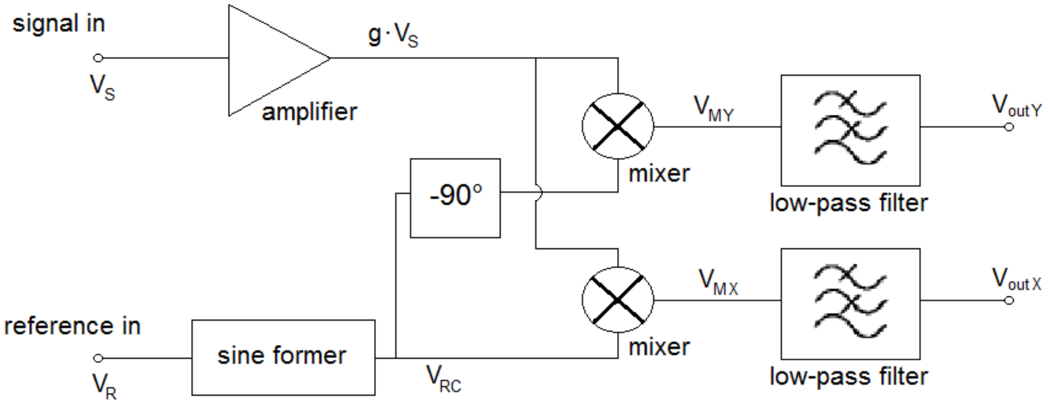

Figure 4.10. Dual-phase Lock-in amplifier.

The resulting outputs are the in-phase X component and the quadrature Y component as follows,

$$V_{outX} = \frac{1}{2} Kg \cos(\phi_S - \phi_R)$$

$$V_{outY} = \frac{1}{2} Kg \sin(\phi_S - \phi_R) \qquad (4.6)$$

This is usually expressed as a complex notation in (4.7). The amplitude K of the input signal can be found from, $\frac{1}{2}Kg$, shown in (4.8), no matter what the value of $\phi_S - \phi_R$. This is described above in the case for the traditional instrument. The phase angle between the reference and input signal ($\Delta\phi = \phi_S - \phi_R$) is obtained from the inverse tangent as in (4.9).

$$V_{outC} = V_{outX} + iV_{outY} \tag{4.7}$$

$$\frac{1}{2}Kg = |V_{outC}| = \sqrt{{V_{outX}}^2 + {V_{outY}}^2} \tag{4.8}$$

$$\Delta\phi = \phi_S - \phi_R = \tan^{-1}\left(\frac{V_{outY}}{V_{outX}}\right) \tag{4.9}$$

4.4 Automation via LabVIEW

The generation of magnetic (MIT) images as 2-D surface plots was automated using LabVIEW 2012, via Ethernet connections between a PC, an Agilent 34980A multiplexer and a Signal Recovery 7230 DSP dual-phase lock-in amplifier. In LabVIEW a timed sequence structure is set up. Firstly the multiplexer is initiated and the first switch is closed from in an array of 20 × 20 switches that connects input and output of 20 × 20 sensor coils. The four hundred switches are made up from six multiplexer modules within the Agilent 34980A unit. Two ‘for loops’ in LabVIEW enclose the time sequence structure and automatically select each sensor in the array by columns – inner ‘for loop’, and rows – outer ‘for loop’. When a sensor coil is selected and its circuit closed the timed sequence structure waits between 500 ms and 3 s for the lock-in amplifier to settle (the amplifier oscillates until it settles at a fixed value of phase), then a LabVIEW module of the lock-in amplifier specific to phase readings and located in the second part of the structure, sends the phase difference measurement to an array of output phase values. The third part of the structure then opens the sensor coil switch in the multiplexer to disconnect its circuit; the nested ‘for loops’ then select the next sensor in the array. This whole process is repeated four hundred times, once for each sensor coil. An output array of phase values is then stored by LabVIEW in a directory of choice. The procedure just described is contained within another non-timed sequence structure. When the first part of this structure is complete the second part executes a MATLAB script within LabVIEW, which calls the output file containing the phase data array. The MATLAB script also contains an array on the 2-D positional data of the sensor coils. The phase data and positional data arrays are concatenated to produce a single array of (*x, y, phase*) – three columns by four hundred rows. Lastly the MATLAB script generates a 2-D surface plot as the 'magnetic image' of the sample object, by interpolation of the data with respect to position using a cubic piecewise fit [70].

5 Canny edge detection algorithm in MIT

5.1 Canny edge detection

In order to progress with magnetic (MIT) images it is useful to detect the edge of the sample object by computer, to determine its dimensions directly from the magnetic image. To achieve this one of the most widely used edge detecting algorithms was implemented, developed by J. F. Canny in 1986 [42]. The Canny edge detection algorithm was applied to the magnetic images using a MATLAB program described below in Section 5.2. The ‘Canny’ function is also built into the MATLAB package as one of its edge detectors. The Canny method works in a multi-stage process. A description of this process is as follows.

Canny aimed to develop an edge detector that addressed the following criteria [71][42].

1. **Detection**: Finding real edges should be maximised and falsely detecting an edge should be minimized. In mathematical terms the signal-to-noise ratio (SNR) should be maximised.
2. **Localization**: The distance between the detected edge and the real edge should be as small as possible.
3. **Number of responses:** One real edge should not give more than one detected edge.

The Canny method assumes that the image comprises of ‘step edges’ corrupted by white Gaussian noise [42]. The edge detector is taken to be a convolution filter *f* that smooths the noise in the image and finds the edges. The problem is to find a function, *f*, that meets the three criteria.

In 1D the response of the filter to an edge, G, is given by the convolution integral, H, within a region $\pm W$ [42],

$$H = \int_{-W}^{W} G(-x) f(x) dx \qquad where \;\; f(\pm W) \approx 0 \tag{4.10}$$

The quantities relevant for the three criteria above are,

$$SNR = \frac{\int_{-W}^{W} G(-x) f(x) dx}{n_0 \sqrt{\int_{-W}^{W} f^2(x) dx}} \tag{4.11}$$

$$Localization = \frac{\left| \int_{-W}^{W} G'(-x) f'(x) dx \right|}{n_0 \sqrt{\int_{-W}^{W} {f'}^2(x) dx}} = \frac{1}{\delta x_0} \qquad , \tag{4.12}$$

n_0 is the mean-noise amplitude per unit length and δx_0 approximates the standard deviation of x_0, where x_0 is the position of the local maximum. The local maximum is due to the response of the filter, *f*, to a noisy step edge [42]. The distance,

$$x_{zc} = \pi \left(\frac{\int_{-\infty}^{\infty} {f'}^2(x) dx}{\int_{-\infty}^{\infty} {f''}^2(x) dx} \right)^{1/2} \tag{4.13}$$

is the average distance between the zero-crossings of, *f* ’(*x*). The signal-to-noise ratio or error rate needs to be large so that there is a lot of signal and as little noise as possible. The localization is the reciprocal of the distance of the detected edge to the ‘true’ edge, and therefore needs to be as large as possible. The constraint on x_{zc} constrains the edge detector *f* (*x*) from having too many responses to the same edge in a small region [42][71]. Finding a filter, *f*, that maximizes the product, SNR × localization, whilst implementing the multiple response constraint on, x_{zc} , is too complex to be solved analytically. However an efficient approximation to this filter happens to be the first derivative,

$$G'(x) = \left(-\frac{x^2}{\sigma^2} \right) e^{-\frac{x^2}{2\sigma^2}} \tag{4.14}$$

of a Gaussian function [42],

$$G(x) = e^{-\frac{x^2}{2\sigma^2}} \quad . \tag{4.15}$$

<u>*Noise Reduction*</u>

The Canny edge detector is susceptible to noise in the raw image data. The raw image data is therefore filtered or smoothed by convolving it with a 2-D circularly symmetric Gaussian, distributed as a ‘point-spread’ function, meaning its response to a point source [42]. The result is a blurring of the raw image, so that it is not significantly affected by any noisy pixels and therefore it prevents noise from being mistaken for edges. The amount of smoothing is controlled by the standard deviation (σ) of the Gaussian. Let $f_i(x, y)$ be the input image and $G(x, y)$ the Gaussian function in 2D, so,

$$G(x,y) = e^{-\frac{x^2+y^2}{2\sigma^2}} \tag{4.16}$$

The smoothed image, $f_s(x, y)$, is formed from the convolution [72],

$$f_s(x,y) = G(x,y) * f_i(x,y) \tag{4.17}$$

$$G = \frac{1}{273} \cdot \begin{bmatrix} 1 & 4 & 7 & 4 & 1 \\ 4 & 16 & 26 & 16 & 4 \\ 7 & 26 & 41 & 26 & 7 \\ 4 & 16 & 26 & 16 & 4 \\ 1 & 4 & 7 & 4 & 1 \end{bmatrix} \quad , \tag{4.18}$$

where the Gaussian operator is applied to each pixel, i.e. G is applied to 1st pixel, then it is applied to the 2nd pixel, 3rd etc. until it is applied all of the pixels in the image. $f_s(x, y)$ can be obtained using for example the kernel G of a Gaussian filter with σ = 1.0 as in (4.18), applied to $f_i(x, y)$ in (4.17), in a matrix convolution. Convolution in image processing is a way of multiplying two matrices together of different sizes but of the same dimensionality, to produce a third resultant matrix. A kernel is a matrix used as part of image convolution and is usually smaller than the image. Convolution involves applying the kernel to one of the (x, y) pixels of the image and multiplying each corresponding pixel-number of the kernel and image, then summing the multiplications. This is repeated for each pixel in the image to give a new matrix of numbers.

If a large σ is chosen the kernel of the Gaussian filter also needs to be made large by the computer program, in order to accurately represent it. This is the case for the work presented in this PhD study, where $\sigma = \sqrt{1000}$. Figure 5.1 shows a diagram of an image with *x* and *y* axes and a 3 × 3 kernel being applied to each pixel of the image, representing a convolution of the kernel with the image.

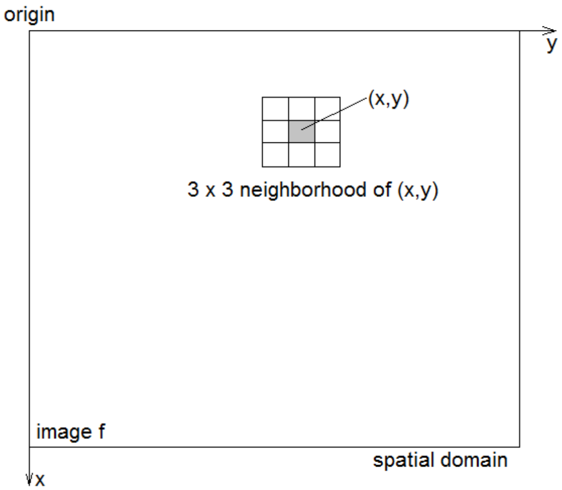

Figure 5.1. Diagram representing a 3 x 3 kernel being convoluted with an image f_i (x, y) [72].

Locating the intensity gradients of the image

Canny shows that the first derivative of the Gaussian is a close approximation to the optimized product of signal-to-noise ratio and localization [42]. A 2-D first derivative operator detects regions of the smoothed image with high first derivatives. An edge may point in a number of directions. The direction of the slope's surface can then be found from differentiating in just two directions of *x* and *y* [42].

Therefore following on from (4.17) the first derivative of the Gaussian in *x* and *y* is $g_x = \partial f_s/\partial x$ and $g_y = \partial f_s/\partial y$. Where, g_x and g_y can be obtained applying the Sobel operator [72] in (4.19) to the smoothed image, f_s,

$$K_{GX} = \begin{bmatrix} -1 & 0 & 1 \\ -2 & 0 & 2 \\ -1 & 0 & 1 \end{bmatrix}, \qquad K_{GY} = \begin{bmatrix} -1 & -2 & -1 \\ 0 & 0 & 0 \\ 1 & 2 & 1 \end{bmatrix} \tag{4.19}$$

The gradient magnitude and direction are (4.20) and (4.21), respectively,

$$M(x,y) = \sqrt{g_x^2 + g_y^2} \tag{4.20}$$

$$\alpha(x,y) = \tan^{-1}\left[\frac{g_y}{g_x}\right] \tag{4.21}$$

M(*x, y*) and α(*x, y*) are always the same size as the image.

Non-maximum suppression

The edges form ridges from the gradient magnitude in the new image. The ‘Canny’ operator follows the peaks of the ridges and sets all pixels that are not peaks to zero. The result is a line of the ridge peaks [73] [74], an example is shown in Figure 5.2.

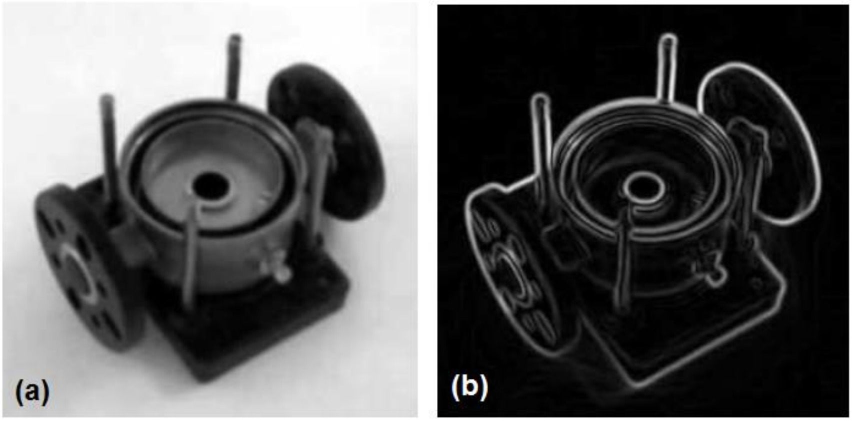

Figure 5.2. Example of: (a) Smoothed image. (b) Gradient magnitudes in smoothed image that includes directions after applying Sobel operator [75].

As M(*x, y*) is calculated using the gradient, it usually produces wide ridges about local maxima, because it includes edge directions that have not been quantised yet as the edge is still blurred. The following process aims to sharpen the edges [75]. Non-maximal suppression aims to thin these wide ridges. This is performed by determining the orientations of the edge normal. The edge direction is quantised into four possible directions that are, horizontal, vertical, +45° and -45°. The gradient M(*x*, *y*) is rounded to the nearest 45°, as shown in figure 5.3.

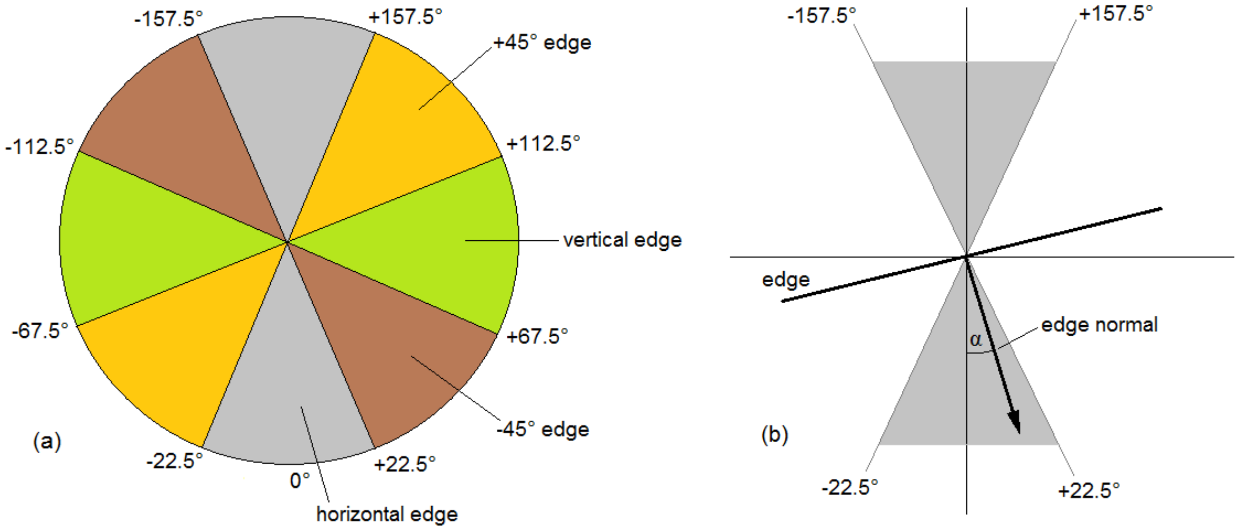

Figure 5.3. (a) Quantising edge-directions in four directions, showing angle ranges of the edge normal. For example α is horizontal if it is between -22.5° and 22.5° as well as -157.5° and 157.5°, as shown in (b) [72].

The edge strength of a pixel (*x*, *y*) is compared to its neighbour in the positive and negative direction, for example if the gradient is pointing north, the pixel is compared with those in the north and south directions. If the edge strength of the subject (*x*, *y*)-pixel is greater than those of its neighbours it is preserved, i.e. $g_N(x, y) = M(x, y)$, otherwise it is suppressed so $g_N(x, y) = 0$. An example in figure 5.4 shows the preserved pixels in white, after comparison.

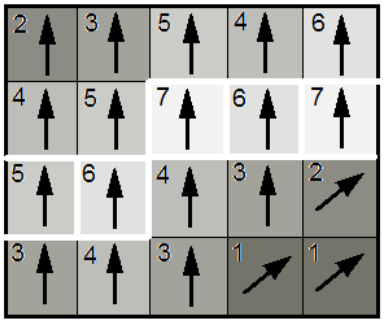

2 ↑	3 ↑	5 ↑	4 ↑	6 ↑
4 ↑	5 ↑	7 ↑	6 ↑	7 ↑
5 ↑	6 ↑	4 ↑	3 ↑	2 ↗
3 ↑	4 ↑	3 ↑	1 ↗	1 ↗

Figure 5.4. Non-maximal suppression example.

Edge strengths are shown as grey tones and numbers, with gradients as arrows. The selected edge is given as a white outline.

The array $g_N(x, y)$ is the image after non-maximum suppression containing the thinned edges [72]. Figure 5.5 shows an example of an image before and after non-maximal suppression.

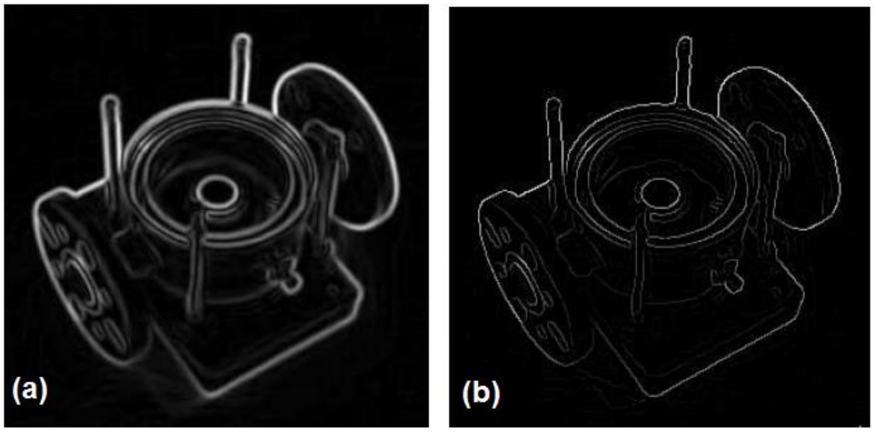

Figure 5.5. Example image showing: (a) Gradient edge outline. (b) Non-maximum suppression, where edge pixels are only at local maxima [75].

Double thresholding

The edge pixels remaining after the last step will contain true edges, but some may be due to noise or rough surfaces. So to reduce the false edges thresholding is implemented, where all values below the threshold are set to zero. If it is set too low some false edges will be kept, if it is too high then valid edges will be missed. Therefore Canny edge detection uses double thresholding with a high (T_H) and low (T_L) threshold, where the suggested ratio of these is two or three to one in magnitude, i.e. $T_H = 3T_L$. Therefore two additional images are produced in the algorithm,

$$g_{NH}(x,y) = g_N(x,y) \geq T_H \qquad (4.22)$$

$$g_{NL}(x,y) = g_N(x,y) \geq T_L \qquad (4.23)$$

Initially, $g_{NH}(x,y)$ and $g_{NL}(x,y)$ are set to zero. After thresholding, $g_{NH}(x,y)$ will have fewer values than $g_{NL}(x,y)$, but all of $g_{NH}(x,y)$ is contained in $g_{NL}(x,y)$. The next step involves all of the high threshold pixels in $g_{NH}(x,y)$ being removed from $g_{NL}(x,y)$ so that,

$$g_{NL}(x,y) = g_{NL}(x,y) - g_{NH}(x,y) \qquad (4.24)$$

Edge tracking with hysteresis

There are now two arrays and the pixels in $g_{NH}(x,y)$ are now marked as ‘strong’ and those in $g_{NL}(x,y)$ as ‘weak’. All strong pixels are assumed to be edges if the value of the threshold, T_H , is selected correctly and will most likely have gaps. Weak edges are selected if they are connected to the strong ones using the 8-connectivity. That is pixels are identified as connected to edge if they are neighbours, horizontally, vertically, and diagonally. Noise and rough surfaces are probably not connected to a ‘true’ edge, being distributed independently of an edge and only a small number adjacent to an edge. The final edge detected image is an array $g_{NH}(x,y)$ that includes all relevant pixels from $g_{NL}(x,y)$ [72]. A resultant binary image gives each pixel as either an edge or not an edge.

In the implementing of Canny edge detection applied to the 2-dimensional magnetic images it was found that a value of the standard deviation, σ equal to $\sqrt{1000}$, was a suitable arbitrary choice for the Gaussian smoothing operator; for detecting and tracing the edge of a sample object. MATLAB gives a default value of σ equal to $\sqrt{2}$. As regards the threshold, an arbitrary threshold = 0.61 was chosen, where MATLAB assigns this to the higher value and 0.4 × threshold to the lower value. It was noted that for magnetic images the 'detected edge' was much less sensitive to the threshold value than it was to the sigma value of the Gaussian smoothing operator. Figure 5.6 shows images of a mild steel box enclosure (75 mm × 77 mm × 15 mm) with Canny edge applied for different values of σ, where σ = $\sqrt{1000}$ gave the most accurate edge detection.

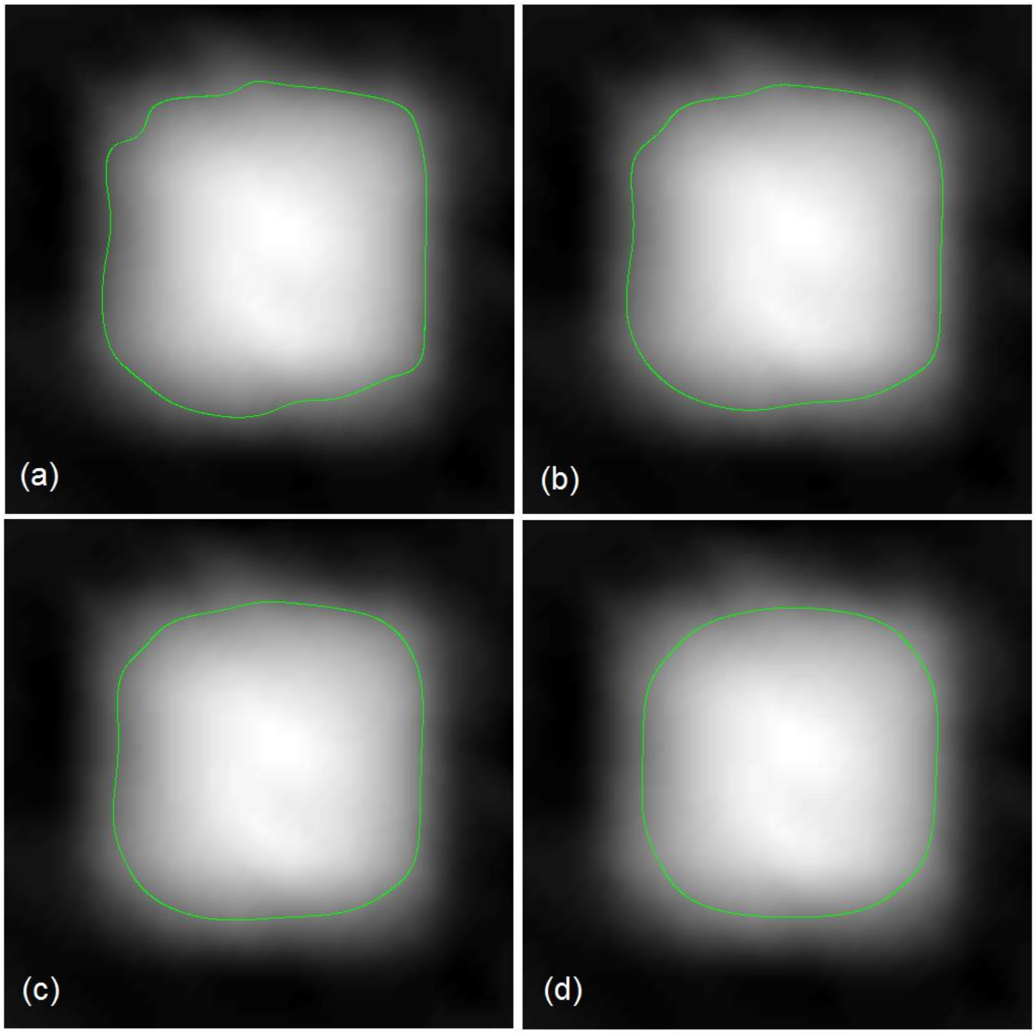

Figure 5.6. Images of a mild steel box enclosure (75 mm × 77 mm × 15 mm), with Canny edge applied for difference values of Gaussian smoothing and detection operator σ. (a) σ = √400 (b) σ = √700 (c) σ = √1000 (d) σ = √2000 . In each case high threshold = 0.61 and low threshold value = 0.4 × 0.61.

5.2 Description of program to create image and detect edge

The MATLAB routine was written to create an image of the specimen, as a 2-D surface plot in 3 dimensions of (*x, y, phase*) and also detect its edge. This is described as follows and the code is displayed in Appendix 14.1.1. After magnetic images have been created of a Copper disk, as well as a background image with no disk present; the LabVIEW control program stores these images as two arrays of phase data for each positional point. The positional points are the centre points of the coils in the 20 × 20 sensor coil array. Positional data is prepared separately and is loaded into the MATLAB program as a 2 × 400 array of sensor positions in *x* and *y*. The background and disk image, as two arrays of phase values, are also loaded into MATLAB. The program also corrects the five ‘peaked anomalous’ sensor coil readings and the four corners of the image that are outside the Helmholtz coils’ uniform field, as described in more detail in Section 7.3. The background and disk phase data as 20 × 20 arrays are processed as 10 × 40 arrays, due to the format with which the Agilent 34980A multiplexer scans the sensor array. Background and disk images are then transposed twice in MATLAB to form an array, one row and four hundred columns long in both cases. The background phases are subtracted from the disk image phases in a ‘for loop’. The minimum value of the resultant phase array is obtained and then subtracted from the phases in the array, so that the minimum phase value in the array starts at zero. This resultant array as a single row is then transposed again to make it into a single column (1 × 400), and concatenated with the positional data array (2 × 400) to make an array of (*x, y, phase*) becoming a 3 × 400 array. The MATLAB program assigns (*x, y, phase*) to the three columns of this array to be ready for interpolation by a cubic-piecewise fit, to produce a 2D surface plot – the MIT/magnetic image.

Firstly an image using the cubic-piecewise interpolation function is fitted that cannot be viewed in 3D, but shows contours in the image in 2D (figure 5.7); this fit produces a function $f_{contour}$ (x, y) of the image that will be needed later on.

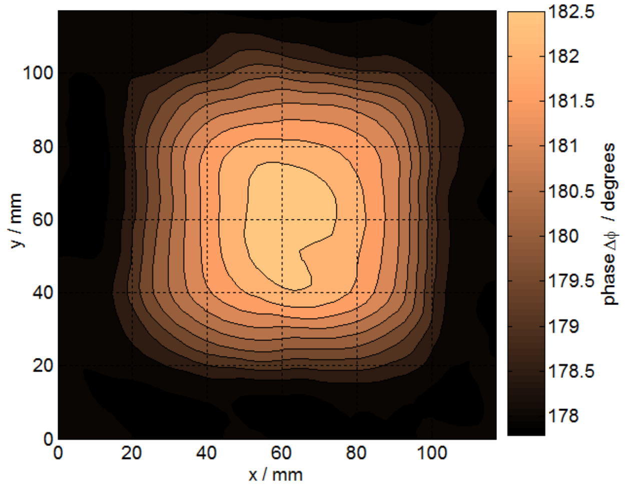

Figure 5.7. 2D cubic-piecewise contour plot of a cigar tin to obtain $f_{contour}$ (x, y) function of image.

This function is accessed later to map the edge detected boundary of the image onto a 3D plot. The main interpolation using again the cubic-piecewise fit is then performed that is viewable in 3D, although the f_{3D} (x, y) function of this fit was not accessible. The image was oriented into an aerial view and made to fill the whole window of the figure, as a greyscale image so that a Canny edge detection algorithm could be applied, without axes labels affecting the result (figure 5.8). This figure was saved as a jpeg image file, and then opened within MATLAB.

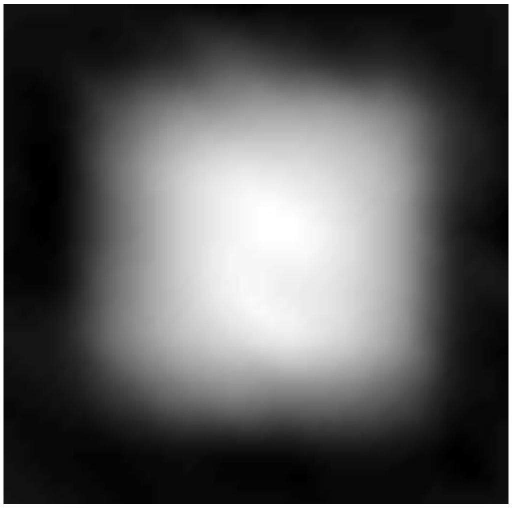

Figure 5.8. Greyscale image of example cigar tin filling whole screen with no axes. This image is saved as a jpeg file and reopened in MATLAB for applying Canny edge detection.

The jpeg image is now resized to a 1000 × 1000 pixel image to give it square dimensions of the 20 × 20 array of sensor coils. Canny edge detection was applied to the jpeg image, with arbitrary high threshold = 0.61 and lower threshold = 0.4 × 0.61. The standard deviation of the Gaussian smoothing operator is set to $\sqrt{1000}$, as the magnetic image required a large amount of smoothing in order to generate a suitable edge. This is because the edge of the magnetic images slope gently and are not sharp. A MATLAB procedure called ‘imoverlay.m’ was used to overlay the detected edge in green onto the jpeg magnetic image, as shown in figure 5.9.

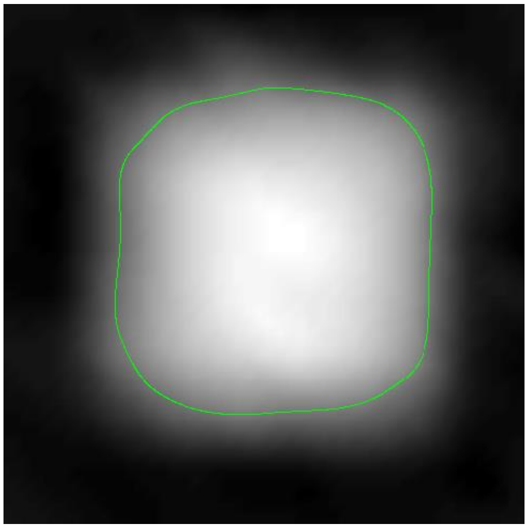

Figure 5.9. Canny edge applied to the greyscale image as a green boundary line.

Overlaying the detected edge onto the 3D magnetic image is now described. By using a nested 'for loop' on the overlaid image, each pixel in the 1000 × 1000 image was checked to determine the green boundary line of the edge of the magnetic image.

Within the nested 'for loop' an array was created, three columns wide, for each column representing (*x, y, phase*) co-ordinates. Each green pixel representing the edge was scaled to the *x-y* coordinates of the 2D surface plot of the magnetic image and assigned to the first two columns, the *x* and *y* axes of the new array. In other words, the green pixel location of the boundary is converted to the *x-y* coordinates of the image. The cubic-piecewise function ($phase = f_{contour}(x, y)$) from the contour image mentioned above, was then used to find the phase values of the detected edge and assigned these to the third column in the new array. This new array, the 'Canny-edge array', now has (*x, y, phase*) values for the three columns. The original (*x, y, phase*) array of the magnetic image is interpolated again with the cubic-piecewise fit and plotted with visible axes and labels present. Lastly the Canny edge array was added to the 2D surface plot, as marker points that trace the edge boundary onto the magnetic image in yellow. The end result is shown in figure 5.10.

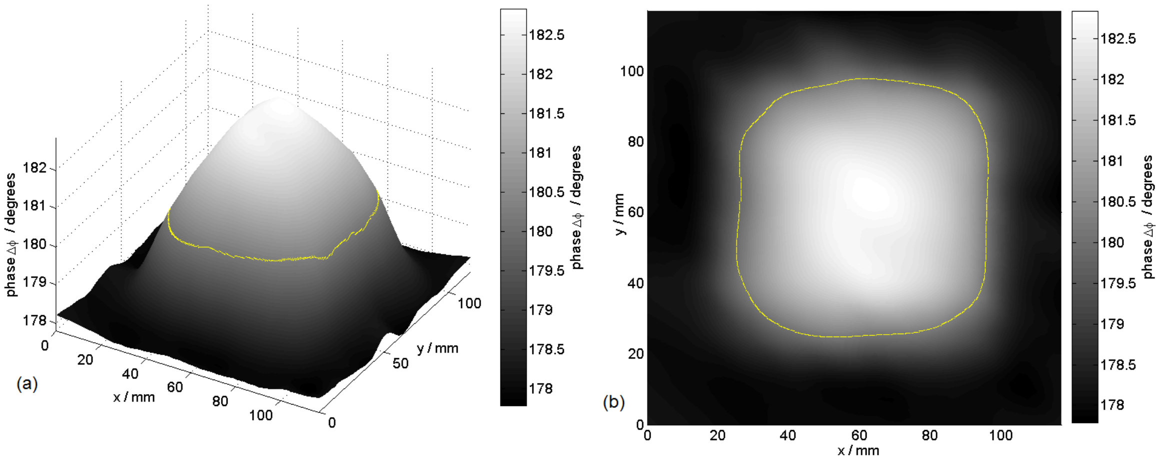

Figure 5.10. (a) Edge boundary translated onto a 3D magnetic image in the form of yellow marker points. In (b) is shown the aerial view.

6 Exploring screening, edge effects and B + ΔB

In this section some experiments were undertaken to explore effects of screening when the thickness of the enclosure is comparable to or smaller than the skin depth. Edge effects were observed when imaging takes place at the edge of the sample, as it meets the air boundary. Additionally the behaviour of **B** + Δ**B** was inspected in various parts of three identically shaped Aluminium, Copper and Iron disks, including its edges.

In the case of the Helmholtz coils and sensor coil array, the phase angle between the primary and the primary + secondary fields, illustrated in figure 6.1, is also the phase difference between the background of the image and the part of it containing the specimen.

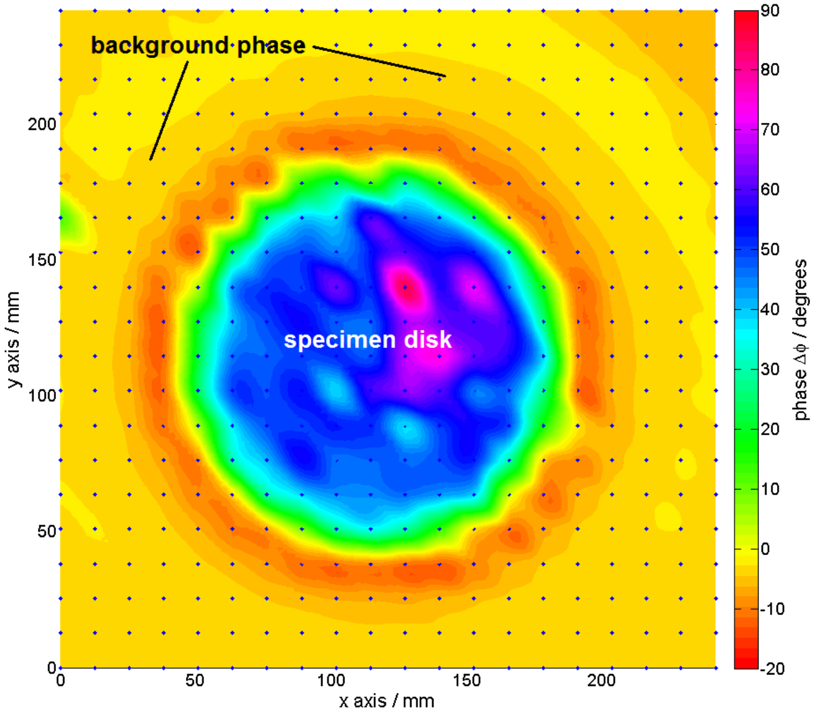

Figure 6.1. Image of 150 mm diameter Copper disk, showing background phase at ~ 0° due to primary field **B** and phase due to specimen disk between -20° and 90° due to **B** + Δ**B**.

6.1 Images generated due to sample acting as a screen

In order to understand what is happening in most of the images generated for this study, images were made in both mediums of Re (ΔV/V) and Im (ΔV/V). When the metallic sample acts as a screen it causes Re (ΔV/V) to become large and negative as shown in figure 2.12a. The derivation of the algorithm to be implemented in reconstructing these images is given in equation (6.1).

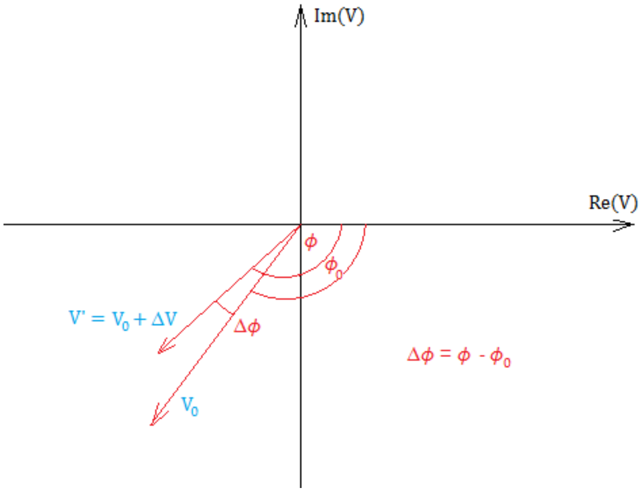

Figure 6.2. Phasor diagram in the complex plane, of voltages measured by a sensor coil, due to the primary field (V_0) and primary + secondary fields (V' = V_0 + ΔV). Phase angle between V_0 and V_0 + ΔV is $\Delta\phi$.

From figure 6.2, let $V = V_0$, $V' = V_0 + \Delta V$. $V'e^{i\phi}$ is due to the primary + secondary fields (specimen) and $V_0 e^{i\phi_0}$ is due to the primary field only (background). The sinusoidal current in the Helmholtz coils is detected at the sensor coils as time varying magnetic field that induces a p.d. across the sensors, which is also a sinusoid. Therefore let $i = \sqrt{-1}$ and ϕ_0 be the phase reading on the lock-in amplifier in figure 6.2, due to the primary field. Then $V_0 e^{i\phi_0}$ is detected at the sensor is due to the primary field only, and $V'e^{i\phi}$ is due to the resultant field, after it has passed through the specimen (primary + secondary fields). Using voltage vector subtraction: $\Delta V = V' - V_0$ (figure 6.2). The form of $\frac{\Delta V}{V}$ is required because it represents equation (2.40) from where conductivity, permeability and permittivity images of an object can be obtained providing the specimen does not act as a screen. Therefore,

$$\frac{\Delta V}{V} = \frac{V' - V_0}{V_0}$$

$$\therefore \; \frac{\Delta V}{V} = \frac{V' e^{i\phi} - V_0 e^{i\phi_0}}{V_0 e^{i\phi_0}} = \frac{V' e^{i(\phi-\phi_0)} - V_0 e^{i(\phi_0-\phi_0)}}{V_0} = \frac{V' e^{i(\phi-\phi_0)} - V_0 e^{0}}{V_0}$$

$$e^{i\phi} = \cos\phi + i\, sin\phi$$

$$\therefore \; \frac{\Delta V}{V} = \frac{V' e^{i(\phi-\phi_0)}}{V_0} - 1 = \frac{V'[\cos(\phi-\phi_0) + i\, sin(\phi-\phi_0)]}{V_0} - 1$$

$$\therefore \; \frac{\Delta V}{V} = Re\left(\frac{\Delta V}{V}\right) + i\, Im\left(\frac{\Delta V}{V}\right) = \left(\frac{V'}{V_0}\cos(\Delta\phi) - 1\right) + i\left(\frac{V'}{V_0}\sin(\Delta\phi)\right) \quad . \qquad (6.1)$$

Images in $Re\left(\frac{\Delta V}{V}\right)$ and $Im\left(\frac{\Delta V}{V}\right)$ are created from equation (6.1) utilising a voltage magnitude image of the background voltage (amplitude V_0 with no specimen present) and the resultant voltage image (amplitude V' with specimen present). Similarly the value $\Delta\phi$ is taken from the difference in the background and resultant phase images.

Images in $Re\left(\frac{\Delta V}{V}\right)$ and $Im\left(\frac{\Delta V}{V}\right)$ are shown in figures 6.3 to 6.5. Figure 6.3 shows images for a plated mild-steel enclosure with dimensions 145 mm × 113 mm × 17 mm and thickness 0.3 mm, at 200 Hz driving frequency and with a Copper disk 30 mm diameter by 0.71 mm thickness, positioned at the centre. In figure 6.4 an Aluminium enclosure of 142 mm × 86 mm × 17 mm by 1.6 mm thickness, has a Copper disk 30 mm diameter by 2 mm thickness slightly to the left, with a driving frequency of 100 Hz. In figure 6.5 an

Aluminium foil shield is imaged of thickness 0.013 mm and dimensions 141.5 mm × 96 mm × 16 mm, but with no disk present and a driving frequency of 200 Hz.

What is important about the images in figures 6.3 to 6.5 is that the imaginary component of $\frac{\Delta V}{V}$ proportional to conductivity, starts to break down when the thickness of the enclosure becomes comparable to the its skin depth, as seen in figures 6.3b and 6.4b. Here the skin depth of mild steel in figure 6.3 is ~1.3 mm at 200 Hz, with the enclosure having thickness of 0.3 mm. For the Aluminium enclosure in figure 6.4, the skin depth is ~8.5 mm at 100 Hz, with enclosure thickness of 1.6 mm. Compared with figure 6.5b for an Aluminium foil shield, the image of Im(ΔV/V) is almost identical to the phase image (figure 6.5c) of the same situation, where the foil thickness is 0.013 mm, with a skin depth of ~6 mm at 200 Hz. Therefore the expression (2.40) and (2.43) has been validated, in the fact that figure 6.5b and 6.5c are so closely identical.

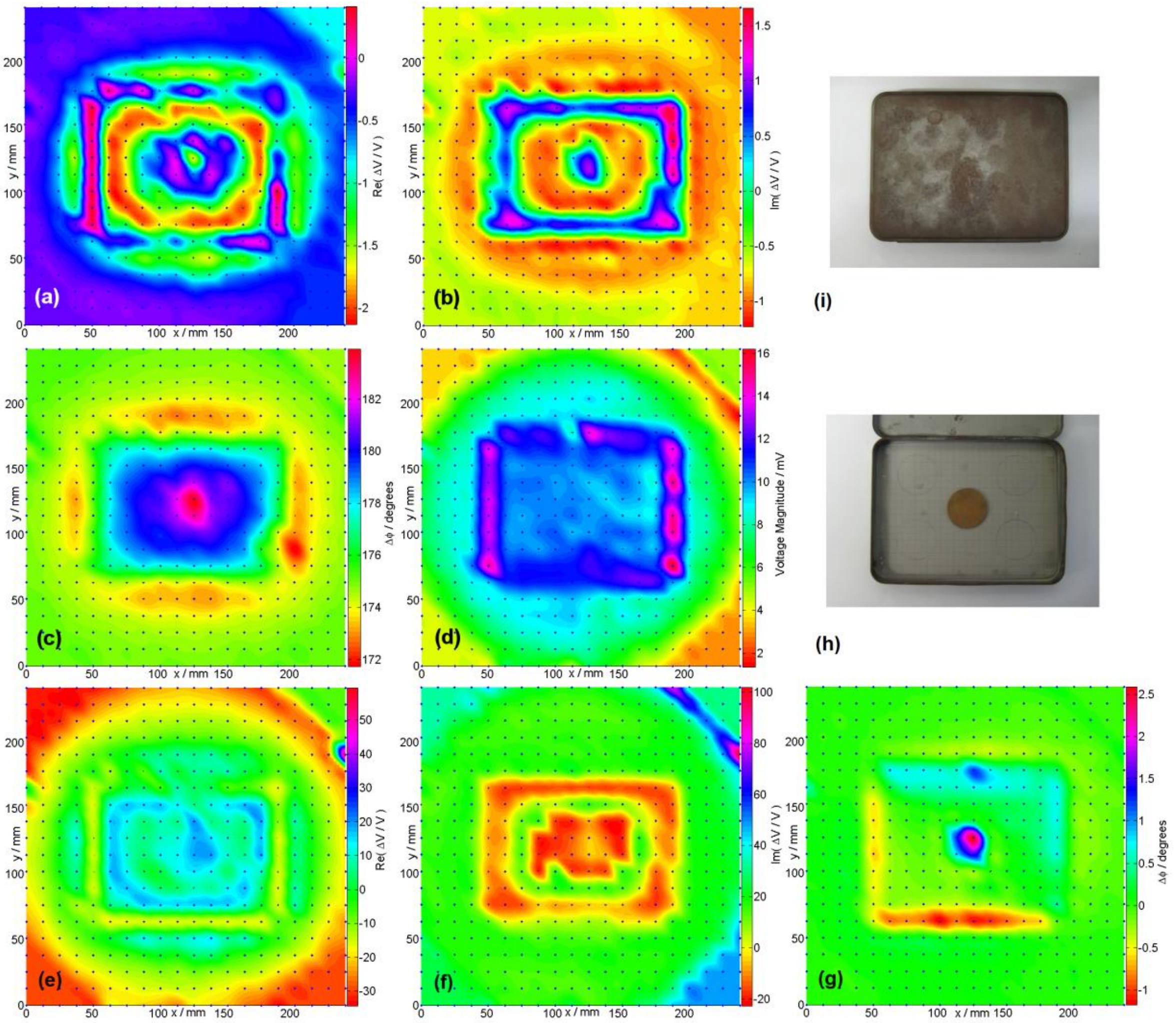

Figure 6.3. Images of a ferromagnetic plated mild-steel enclosure of 0.3 mm thickness, with Copper disk concealed in the central position. (a) Raw image taken in the Re (ΔV/V) medium. (b) Raw image taken in the Im (ΔV/V) medium. (c) Phase difference ($\Delta\phi$) image; that is phase between driver and sensor coil signals. (d) Voltage image, where voltage is measured by the sensor coils, via a lock-in amplifier; this is used calculate the images in (a) and (b), with the aid of the background voltage image and phase image (c). (e) to (g) are resultant images of the subtraction-of-the-empty-enclosure method, to penetrate through the enclosure in mediums of Re (ΔV/V), Im (ΔV/V) and phase ($\Delta\phi$), respectively. (h) and (i) are photographs of the enclosure with lid open in (h) and closed in (i). All images were taken with enclosure lids closed.

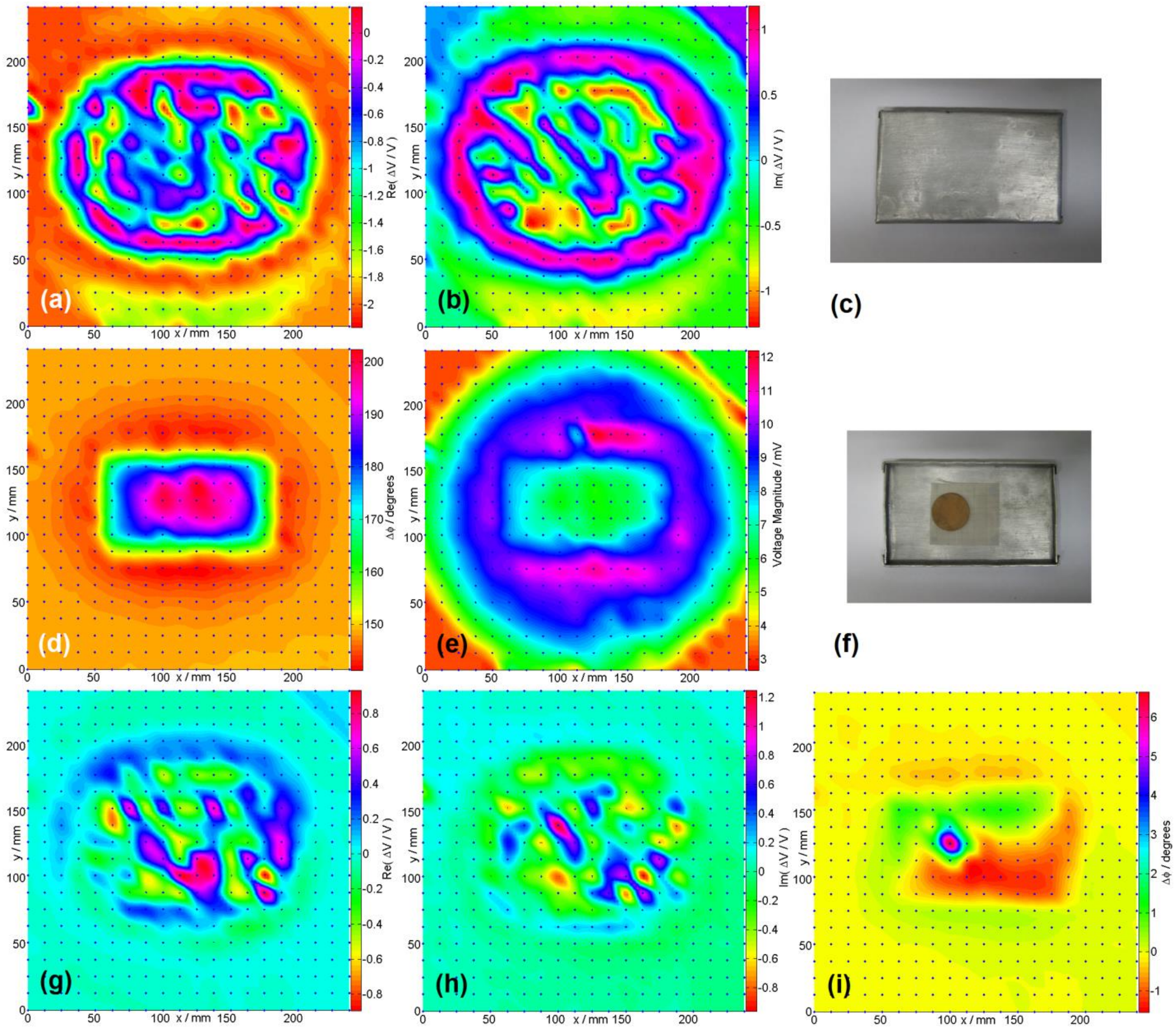

Figure 6.4. Images of an Aluminium enclosure of 1.6 mm thickness, with Copper disk concealed in the left-of-centre position. (a) Raw image taken in the Re (ΔV/V) medium. (b) Raw image taken in the Im (ΔV/V) medium. (d) Phase difference ($\Delta\phi$) image; that is phase between driver and sensor coil signals. (e) Voltage image, where voltage is measured by the sensor coils, via a lock-in amplifier; this is used to calculate the images in (a) and (b), with the aid of the background voltage image and phase image (d). (g) to (i) are resultant images of the subtraction-of-the-empty-enclosure method, to penetrate through the enclosure in mediums of Re (ΔV/V), Im (ΔV/V) and phase ($\Delta\phi$), respectively. Phase images are the phase angles between driver and sensor coils from which phase between primary and resultant magnetic fields can be inferred. (c) and (f) are photographs of the enclosure with lid open in (f) and closed in (c). All images were taken with enclosure lids closed.

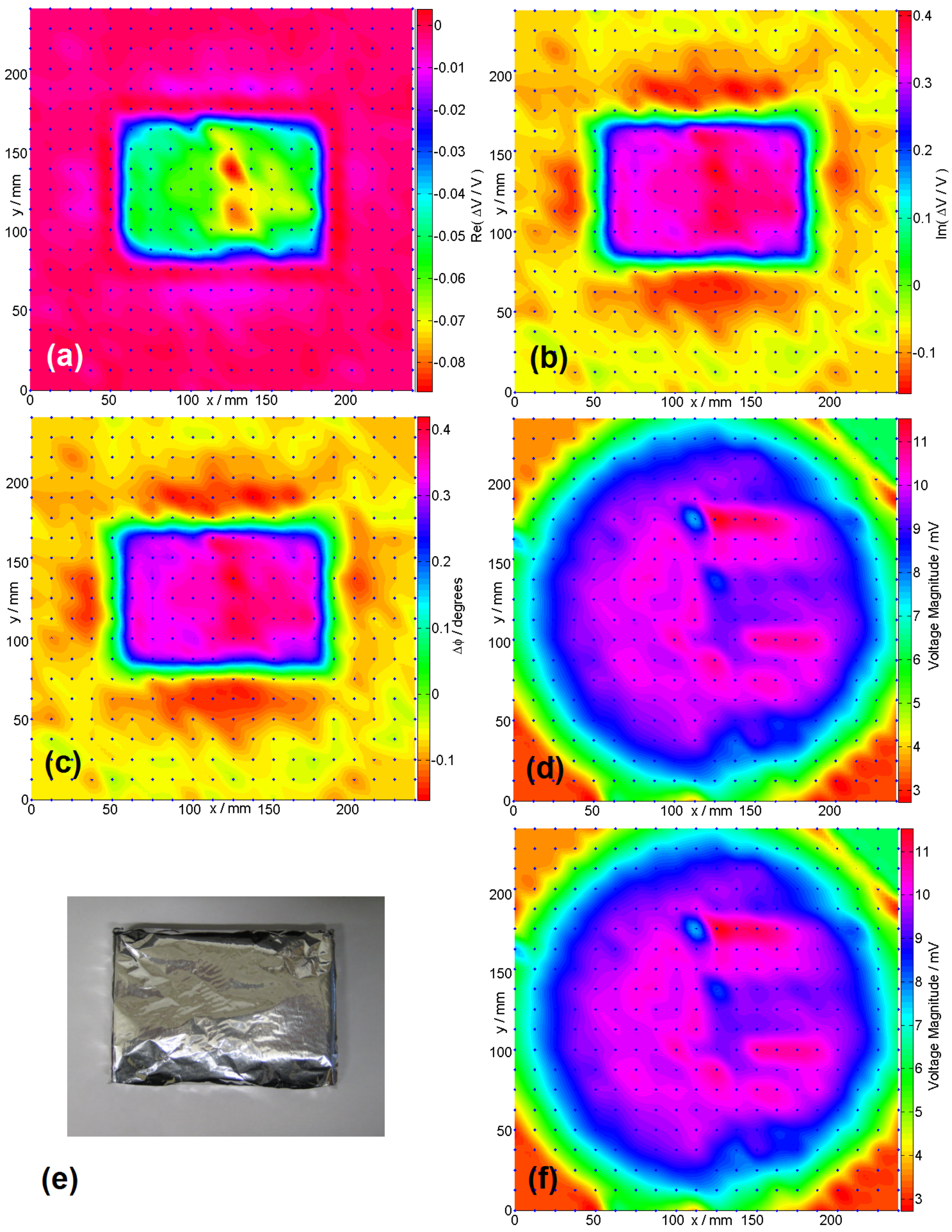

Figure 6.5. Images of an Aluminium foil shield only, of 0.013 mm thickness. (a) Raw image taken in the Re (ΔV/V) medium. (b) Raw image taken in the Im (ΔV/V) medium. (c) Phase difference ($\Delta\phi$) image; that is phase between driver and sensor coil signals. (d) Voltage image of enclosure, where voltage is measured by the sensor coils via a lock-in amplifier; this is used calculate the images in (a) and (b), with the aid of the background voltage image (f) (that has no sample present) and phase image (c). (e) is a photograph of the Aluminium foil shield. The difference between (d) and (f): (d) is the resultant voltage image including the enclosure specimen, (f) is the background voltage with no specimen present. They closely identical here because at small phase angles V + ΔV (voltage vector addition) in (f) is approximately equal to V in (d), see figure 2.12(b).

This shows that the dimensions of the specimen need to be smaller than the skin depth by at least a factor of 462, in order to apply expression (2.40). The value 462 is obtained from dividing the skin depth by the thickness of the specimen, in this case the factor $462 = \frac{6\,mm}{0.013\,mm}$. The images of figures 6.3(c) and 6.4(d) show that the phase images still give valid information on the specimen's electromagnetic properties and position, up to thicknesses comparable to 0.188 and 0.231 skin depths (and even up to 7 skin depths shown in Section 9.4). This is well after real and imaginary images of $\frac{\Delta V}{V}$ have broken down, giving very fragmented images as seen in figures 6.4 (a, b), compared with the phase image in figure 6.4d. Figures 6.3 (a, b) are less fragmented, but the Im(ΔV/V) image does not closely resemble the phase image in 6.3c.

The real component image of Re (ΔV/V) in figure 6.5a would appear to indicate permeability of the Aluminium foil, in reference to equation (2.40). In this case giving small negative Re (ΔV) values; therefore the phasor diagram of figure 2.12b may now be similar to figure 6.6 below. This diagram was drawn by making use of the voltage magnitudes of Aluminium foil (V_0 + ΔV) and the background (V_0) in figures 6.5 (d, f); where we notice they are both very similar due to the small angle in phase ϕ.

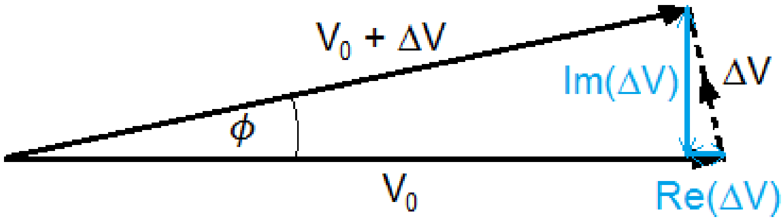

Figure 6.6. Phasor diagram of voltages detected at the sensor coils, for a highly conductive specimen with skin depth much larger than its dimensions (by a factor of at least 462).

In Section 7 more will be described about imaging through enclosures. As an introduction to penetration imaging some images are given here in figures 6.3 (e, f, g) and figures 6.4 (g, h, i). It can be seen from figure 6.3 (e and f) that subtraction of the empty enclosure from the full one (see Section 7.2 for more detailed description), in order to reveal the concealed disk, does not quite work for Im (ΔV/V) and Re (ΔV/V) images, although they give the outline of the enclosure and the Im (ΔV/V) image gives some hint of the disk's presence. The Re (ΔV/V) image detects a vague and general area of it. However the phase subtraction process clearly detects the disk in figure 6.3g, validating that phase images are the most appropriate for penetration imaging. In figures 6.4 (g, h) the subtraction-of-images in Im (ΔV/V) and Re (ΔV/V) mediums of the full and empty enclosure, do not clarify anything more about the ΔV/V medium, where the result is fragmented with no indication of the disk's position. This is of course being due to the skin depth limitation of equation (2.40). The phase image of figure 6.4i again gives a clear detection of the disk, extracted from the background of the enclosure.

6.2 Edge Effects and B and ΔB

In all images made by the MIT system edge effects take place, due to the edge of a specimen object as indicated in the images, e.g. figures 6.8a and 6.9a. These distort phase and voltage measurements at the edge of the specimen image. The eddy currents induced in the specimen compress and become larger at the edges as they meet the non-conducting air boundary [38]. This is due to the E-field compressing at the boundaries as shown in figure 6.7.

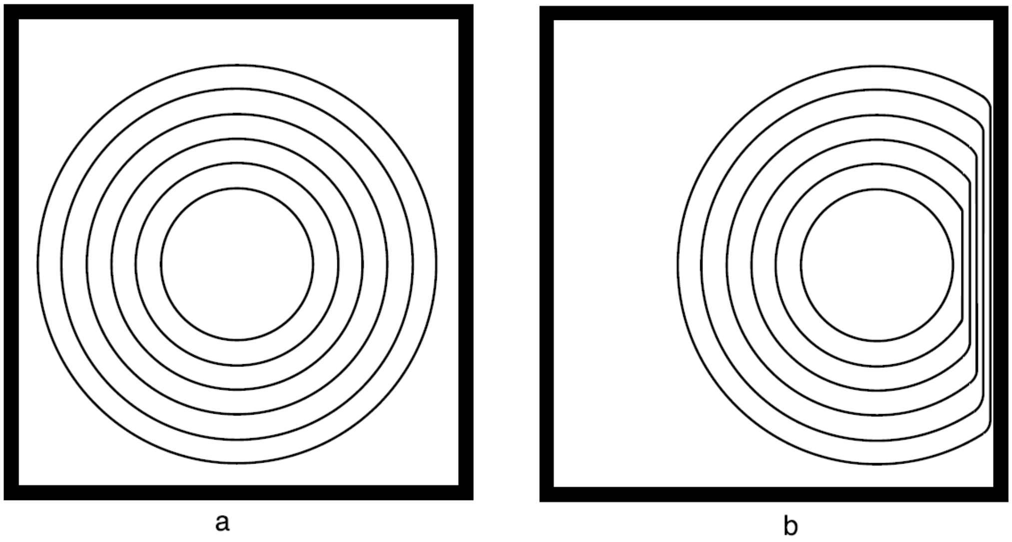

Figure 6.7. (a) Eddy currents unaffected by the specimen boundary. (b) Eddy currents compressed by a specimen boundary [38].

In the following, three disks were imaged that show edge effect behaviour. Identical Aluminium (Al) and Copper (Cu) disks, 150 mm diameter by 2 mm thickness, were imaged in terms of phase in figures 6.8 (a, b) and voltage magnitude in figures 6.9 (a, b). This was at 500 Hz with a primary field of 0.107 mT rms at the level of the sensors, measured with an “F. W. Bell, Hand-held Gauss/Tesla Meter, Model 4048”. An Iron (Fe – 99.5% purity) disk was also imaged (figures 6.8 (c, e) and figures 6.9 (c, e)) under the same conditions with identical dimensions except for thickness 1 mm.

In the Aluminium disk the phase values peaked above the background in the central region and main body of the disk image (average ~50°, max. ~80°) reducing in value as the edge was approached (figure 6.8a), but with varying phase peaks in this region, most likely due to resolution of the sensor coils. The phase dips lower than the background (~ -15°) at the edge of the Al disk and rises again to the background value (~0°) as the region of the disk is left behind. A similar phase profile can be seen with an identical Copper disk (figure 6.8b), however it gives lower phase values with an average of ~40°, a maximum of ~70° in the main body and ~ -12° at the edge.

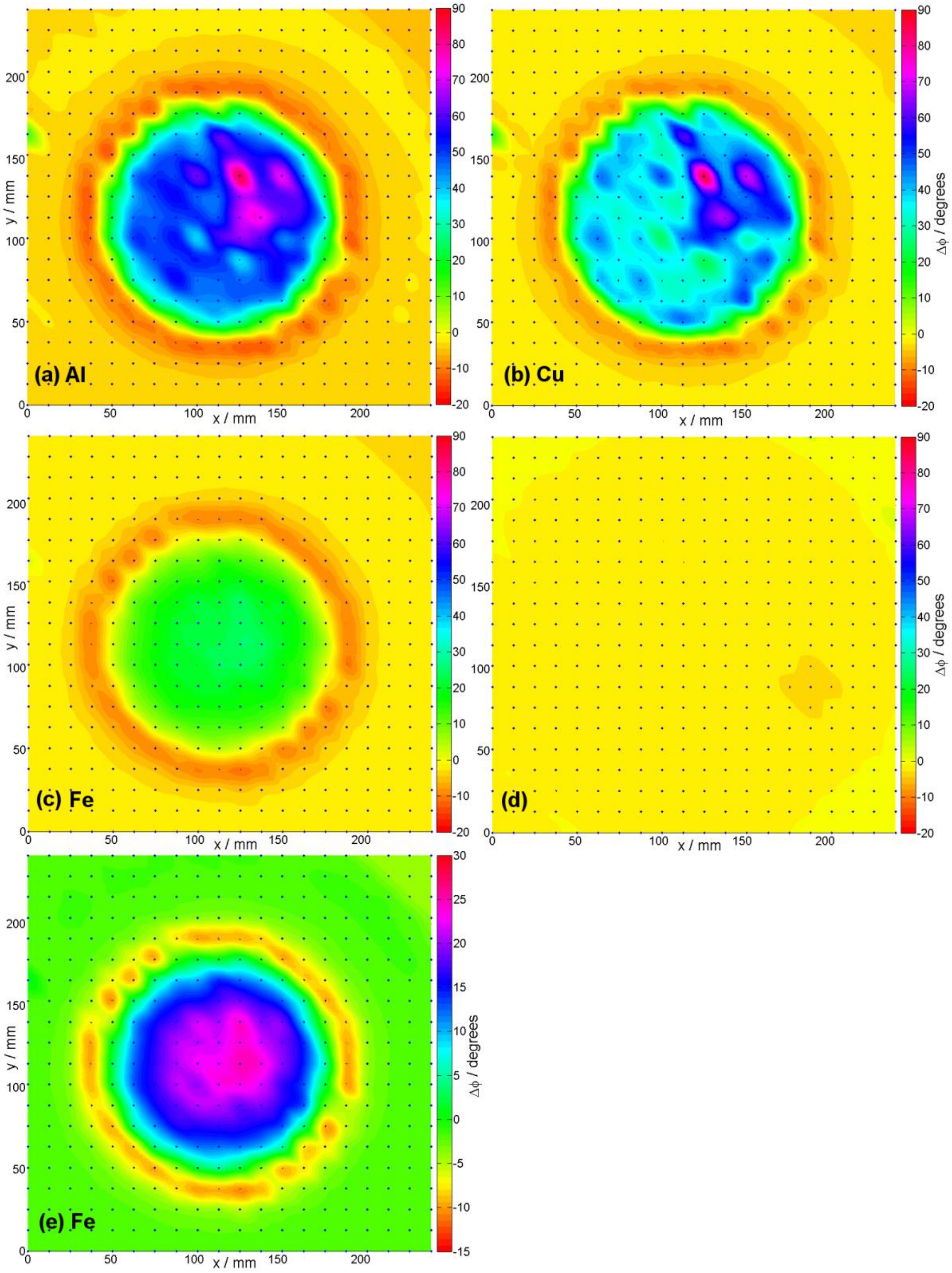

Figure 6.8. Phase-images of (a) Aluminium (Al) disk, (b) Copper (Cu) disk, (c) & (e) Iron (Fe) disk and (d) background with no specimens present. The disks are 150 mm diameter by 2 mm thick for Al & Cu; and 150 mm diameter by 1 mm thick for Fe. Figure (e) is the same as (c), but with phase scale: -15° to 30°.

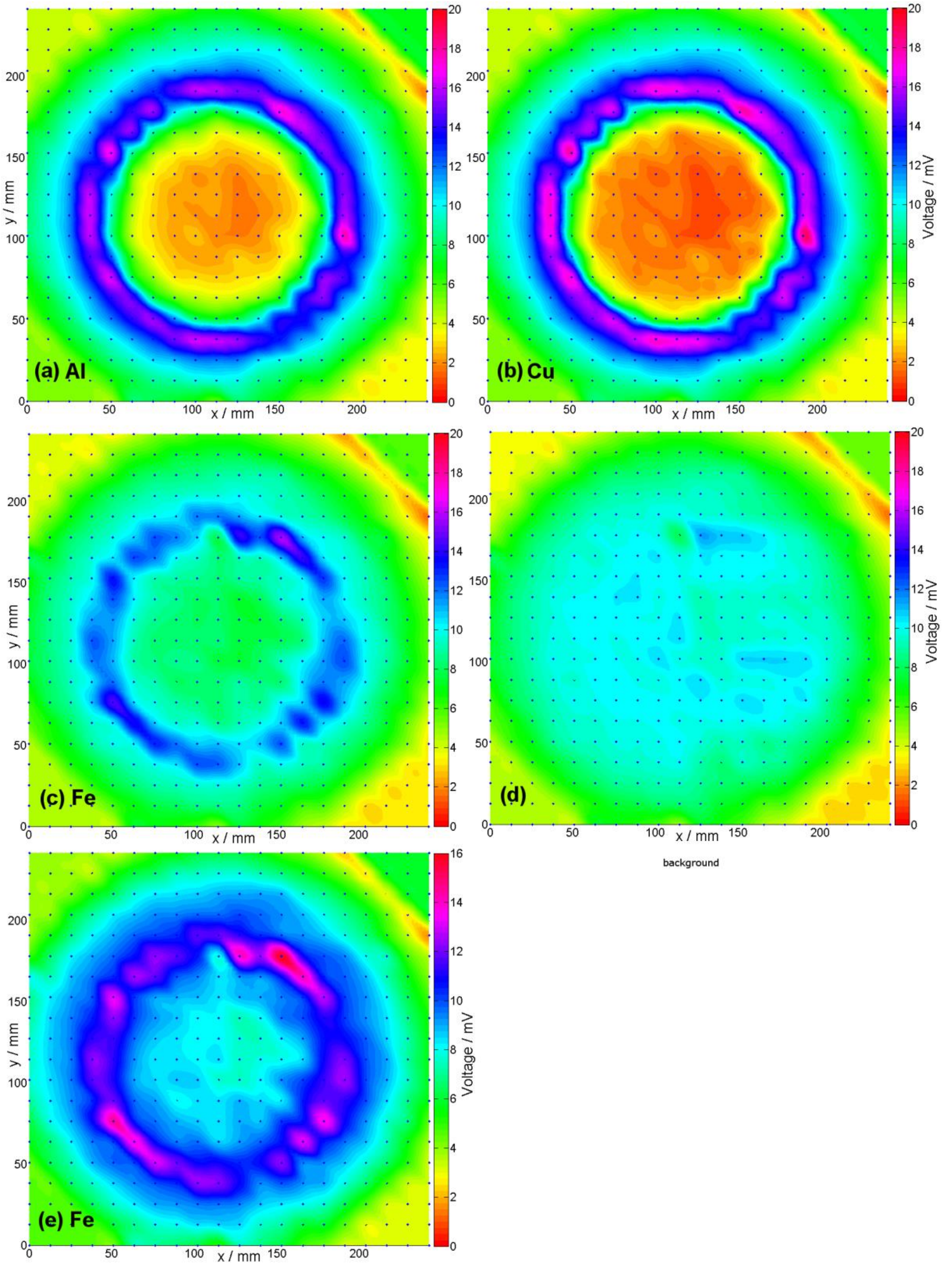

Figure 6.9. Voltage amplitude-images of (a) Aluminium (Al) disk, (b) Copper (Cu) disk, (c) & (e) Iron (Fe) disk and (d) background with no specimens present. The disks are 150 mm diameter by 2 mm thick for Al & Cu; and 150 mm diameter by 1 mm thick for Fe. Figure (e) is the same as (c), but with voltage scale 0-16 mV.

Voltage magnitude images showing e.m.f.'s induced in sensor coils were made for the same disks. Voltage was minimum and less than the background in the central body by a factor of ~0.25 for Al and ~0.18 for Cu. It gradually increased towards the edge and peaked to a high value at the edge by a factor ~1.68 higher than the background for Al and ~1.74 for Cu. The Iron (Fe) disk in figure 6.8e, gives lower phase values than both Al and Cu, with an average ~20° in the main central body, and maximum ~25°. The Fe edge values were ~ -11°. For voltage magnitude, the Fe disk in the main body gave a small amount less than the background by 2 mV, a factor of 0.79 that was significantly higher than Al and Cu. This as can be seen in figure 6.9c compared with 6.9 (a, b and d). What was noticeable with Iron is that its edges are more distorted than Al and Cu, showing a wave like pattern as seen in figure 6.9 (c and e). The Fe disk edge gave voltage magnitude of factor ~1.26 higher than the background. A summary of these findings is given in table 6.1.

Table 6.1: Approximate phase[1] and voltage-magnitude[2] measurements in different parts of the disk, for an Aluminium and Copper disk, 150 mm diameter by 2 mm thickness and an Iron disk 150 mm diameter by 1 mm thickness.

Disk - type of metal	Aluminium	Copper	Iron
Phase[1] (approx. in central body)	50°	40°	20°
Phase (approx. max.)	80°	70°	25°
Phase (approx. edge effect)	-15°	-12°	-11°
Voltage[2] - central body (ratio of backgrd. ~ 10 mV)	0.25	0.18	0.79
Voltage - edge effect (ratio of backgrd. ~ 10 mV)	1.68	1.74	1.26

[1] Phase is phase-difference between driver and sensor coils.
[2] Voltage is e.m.f. induced across the sensor coils.

In the phase images rounded peaks are seen due to the sensor coils' interaction with the disk, indicating how resolution affects these images. These rounded peaks are the rises in phase above the troughs in phase in the disk image, that appear to be more due to the sensor coils themselves rather than the metallic disk. Section 7.3 and figure 7.11 show the peaks remaining in the same place even when the disk is rotated 90°.

Due to Faraday's law Δ**B** ∝ ΔV; Δ**B** is the magnetic field at the sensor coil due to eddy currents and magnetization in the specimen. ΔV is the e.m.f. induced in the sensor due to Δ**B.** Griffiths [9] states that Δ**B,** in highly conductive non-magnetic specimens, has a negative real and positive imaginary component (figure 6.10 (a, c)). This agrees with these results, where the phasor diagrams of figure 6.10 (a, c) represents the experimental data shown in figures 6.8 (a, b) and 6.9 (a, b), of phase and voltage magnitude images of the Al and Cu disks. However Griffith's [9] statement that ferromagnetic specimens gives Δ**B** as real and positive and in phase with the primary signal, does not agree with the images obtained here that show Δ**B** with a negative real and positive imaginary components (figure 6.10e).

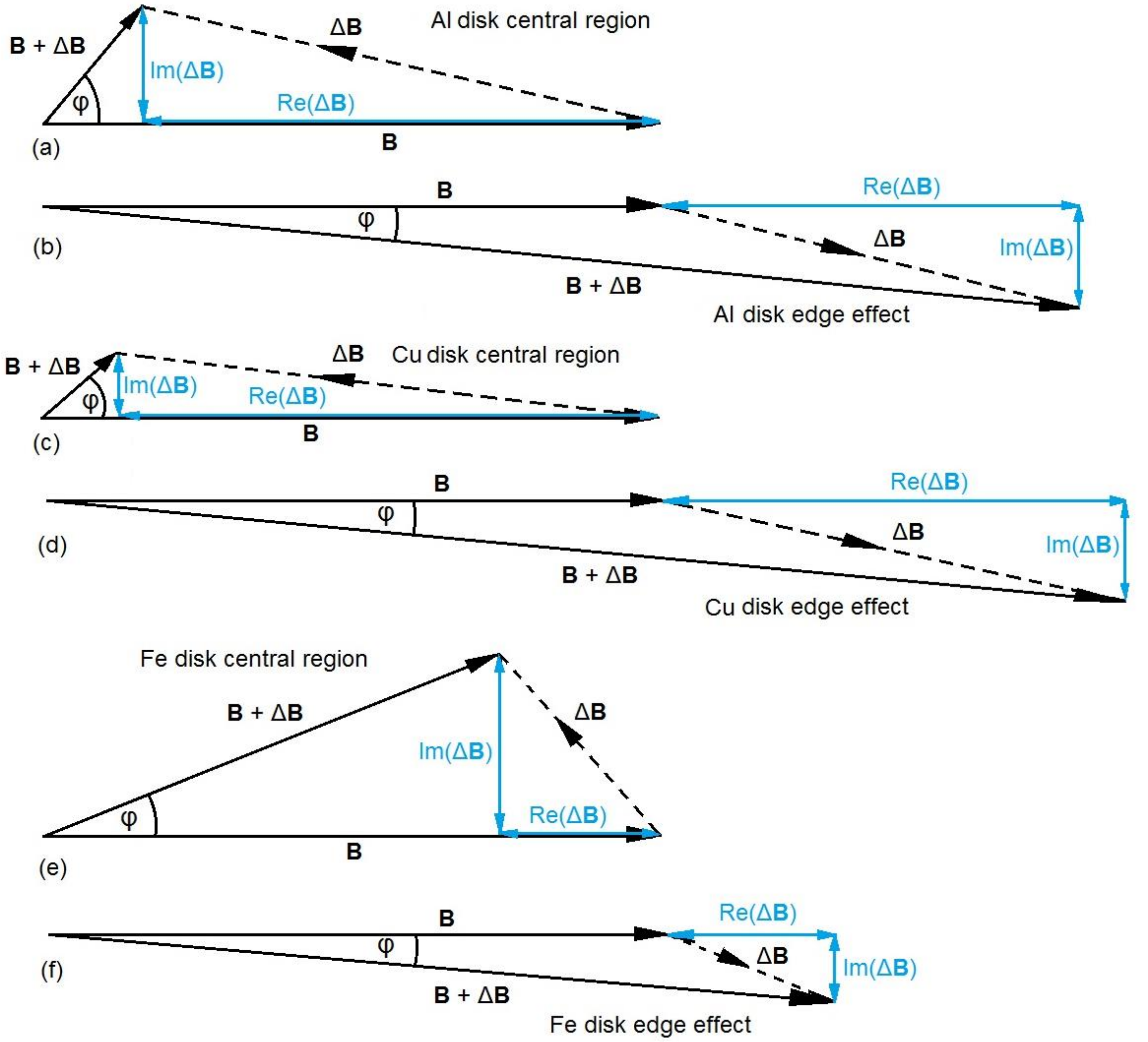

Figure 6.10. Phasor diagrams of Copper, Aluminium and Iron disks showing resultant field (**B** +Δ**B**) detected in sensor coils. The primary field (**B**) is due to the Helmholtz coils and the opposing secondary field (Δ**B**) is due to the eddy currents and magnetization in the specimen. These diagrams were estimated using voltage magnitude and phase images of figures 6.8 to 6.9. They show the phasor diagrams in central region of the disks and at their edges. Specimen disks 150 mm diameter by 2 mm thick in (a-d) are for non-magnetic conductive Aluminium and Copper respectively. (e-f) shows 150 mm diameter by 1 mm thick ferromagnetic Iron disk.

As described in Section 2.2.3, this is most likely due to the ferromagnetic objects being non-conductive in [9]. Additionally the disks imaged above in figures 6.8 to 6.9 act as screens causing Δ**B** to have a large negative real term [10][20]. The real component is significantly less in the Iron disk than it is in the non-magnetic Aluminium and Copper disks. Both the **B** and Δ**B** are detected by the sensor coils [9], and apart from penetrating the specimen, the total **B**-field also flows around it forming a magnetic circuit to the sensor coils on the other side. If the phase images represent conductivity, one may expect Copper to give higher phase values than Aluminium, as Aluminium is slightly less conductive. This does not appear to be the case with Copper and Aluminium disks shown here in figures 6.8 (a, b). However this may be due to the skin effect in both metals, where Aluminium has a slightly larger skin depth than Copper and therefore allows more penetration of the magnetic field.

6.3 Summary

From the above findings Aluminium gives higher phase values than Copper in the main body of the disk. The opposing secondary field of Copper is larger than Aluminium, giving Copper a smaller resultant field detected. The edge effect voltage of the Copper was also larger than Aluminium, with Iron giving the smallest edge effect voltage. Iron shows a smaller secondary field and smaller phase in the main body of the disk than in the other two disks. This is probably due to the magnetization of the Fe disk, producing a positive real component of Δ**B** in opposition to the eddy current field, as described in Section 2.3.

7 Resolution and penetration imaging

7.1 Determining resolution of MIT system using Canny method

The method of generating a magnetic image of the metallic specimen is described in Section 4.1, with more details in Section 4.2 and 4.4.

In order to calibrate the MIT system and determine its resolution a technique was implemented to measure the diameters of eleven Copper and eleven Aluminium disks of varying sizes, directly from the magnetic images using an edge detection algorithm described above in Sections 5.1 and 5.2. The disks are all 2 mm thickness and have diameters: 15 mm, 17.5 mm, 20 mm, 30 mm, 40 mm, 50 mm, 60 mm, 76 mm, 90 mm, 100 mm, 150 mm. The edge detected diameter determined from the image was compared with the 'true' diameter measured with a ruler. The resolution of the system was determined by the Copper and Aluminium disks, to be the least diameter of the disks that gave an edge detected diameter distinguishable from disks of smaller size. The frequency of the driving field for these measurements was 500 Hz. Two sets of magnetic images were created for each of the eleven Copper and eleven Aluminium disks. In the first set the disks were centred on a single sensor, in the second set they were centred between four sensors. This was to show differences in the size of the resultant image, depending on the position of the disk relative to the sensors. Figures 7.2 to 7.5 show the images for the Copper disks 15 to 150 mm diameter.

Figure 7.1 shows the comparison of edge detected diameter to the 'true' diameter measured with a ruler. A linear fit was made to the disks with diameter ≥ 50 mm, that includes both sets of data and indicated a relationship close to unity for disks of this size. Therefore from the linear fit of,

$$y = 0.9988x - 17.89 \quad \rightarrow \quad x = \frac{y + 17.89}{0.9988} \qquad (4.25)$$

the ‘true’ diameter for disks ≥ 50 mm can be estimated from the edge detected diameter, where edge-detected one is less by about 17.9 mm.

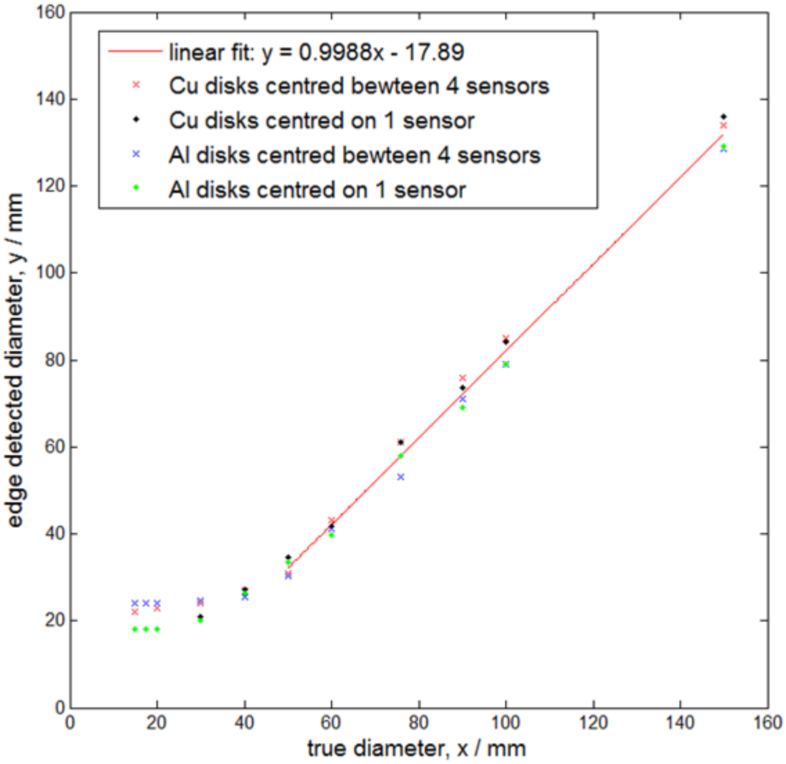

Figure 7.1. Canny edge detected diameter versus ‘true’ diameter as measured for Copper (Cu) and Aluminium (Al) disks of 2 mm thickness. Red and blue data sets denote Copper and Aluminium disks, respectively, centred between four sensors; the black and green data sets denote Copper and Aluminium disks, respectively, centred on one sensor. The solid line represents the linear fit to all the data with values of diameter greater than 50 mm.

As shown in figures 7.2 to 7.5, the disks centred on one sensor coil gave much larger phase values than those centred between four coils for disk diameter ≤ 30 mm. However they gave smaller edge detected diameters. For example for the 17.5 mm diameter Copper disk in figure 7.2b, the edge detected diameter is 18 mm, compared with figure 7.4b that gives 24 mm.

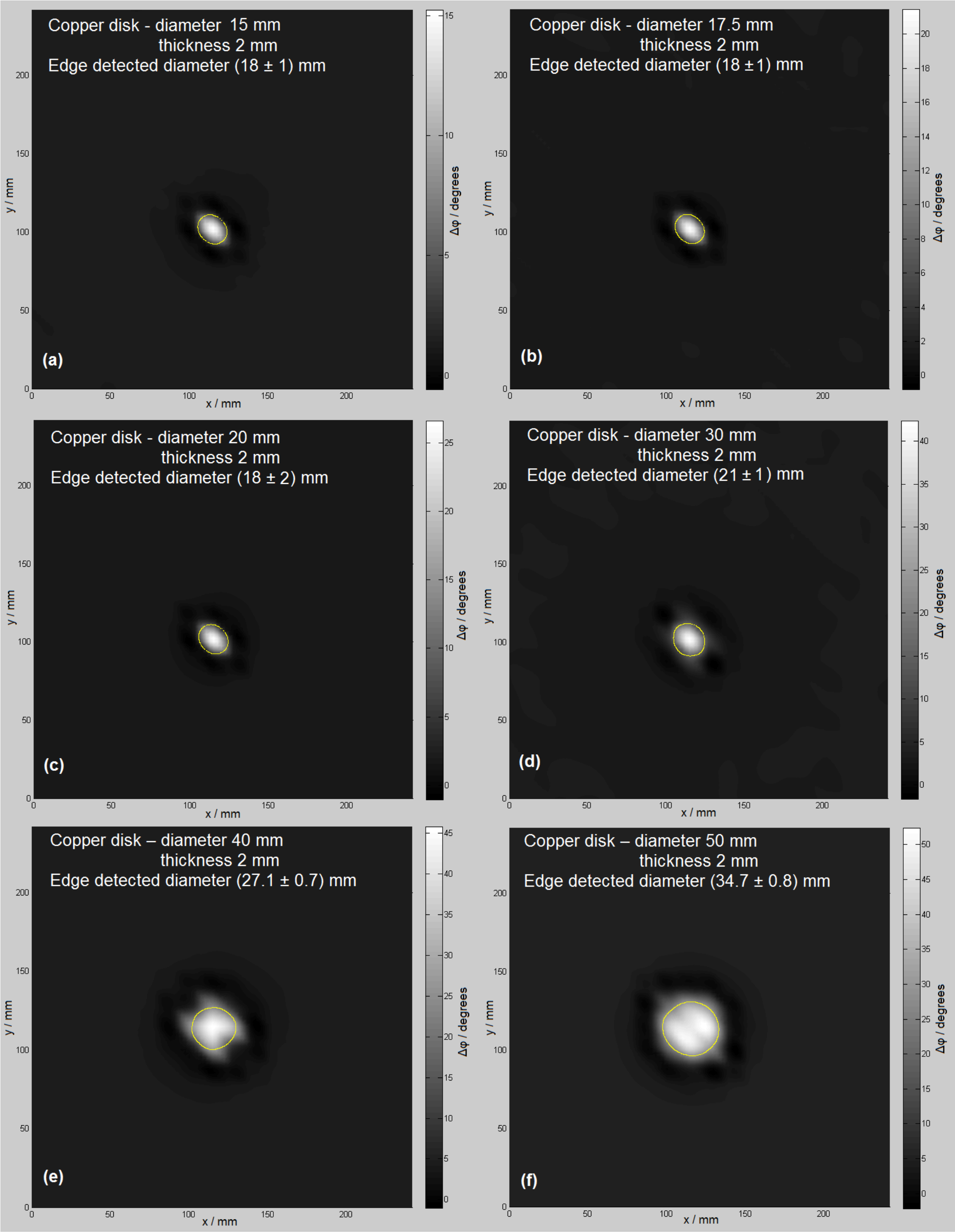

Figure 7.2. Images (a) to (f) of six Copper disks, 15 to 50 mm diameter, showing edge detection, with the disks centred on one sensor coil.

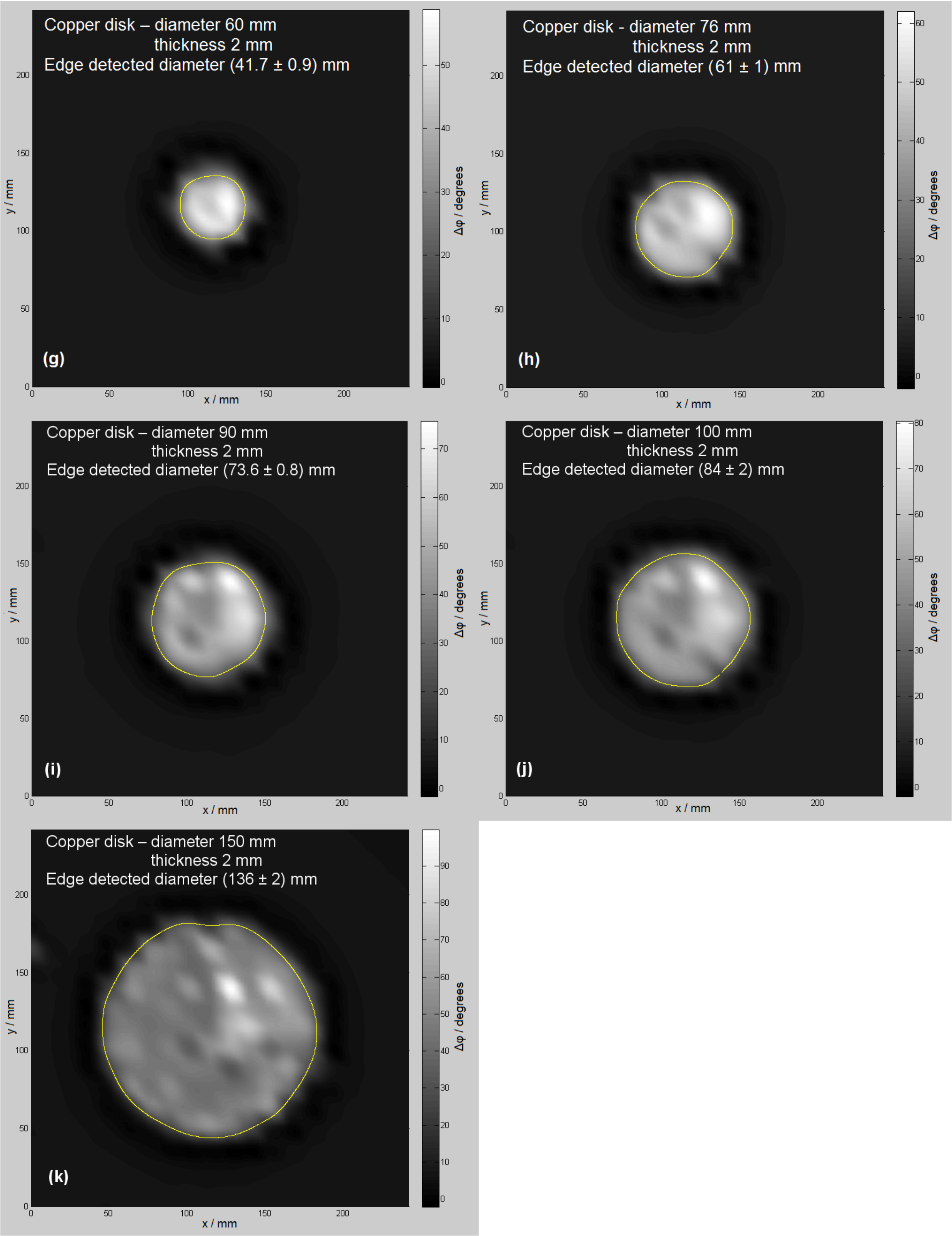

Figure 7.3. Images (g) to (k) of five Copper disks, 60 to 150 mm diameter, showing edge detection, with the disks centred on one sensor coil.

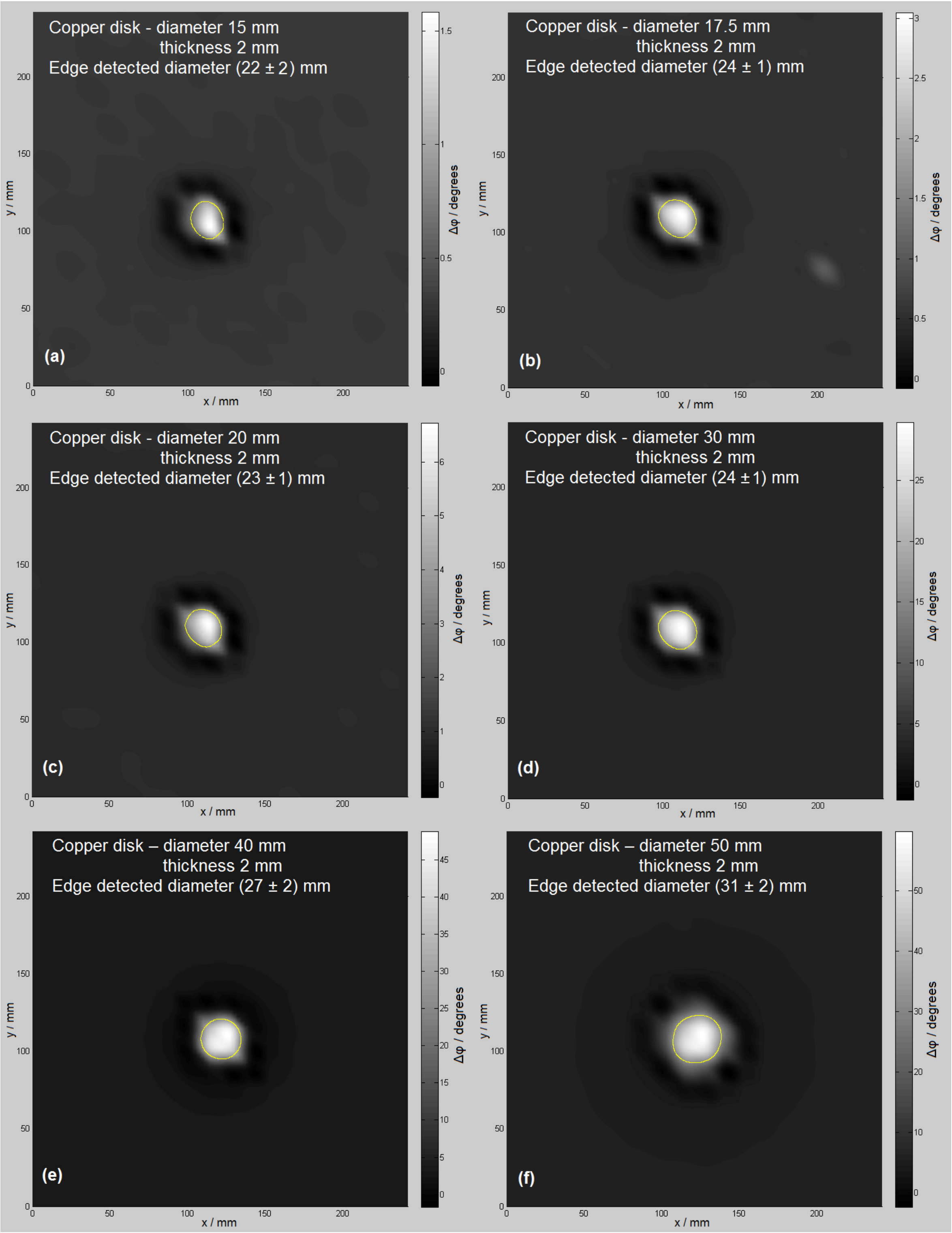

Figure 7.4. Images (a) to (f) of six Copper disks, 15 to 50 mm diameter, showing edge detection, with the disks centred between four sensor coils.

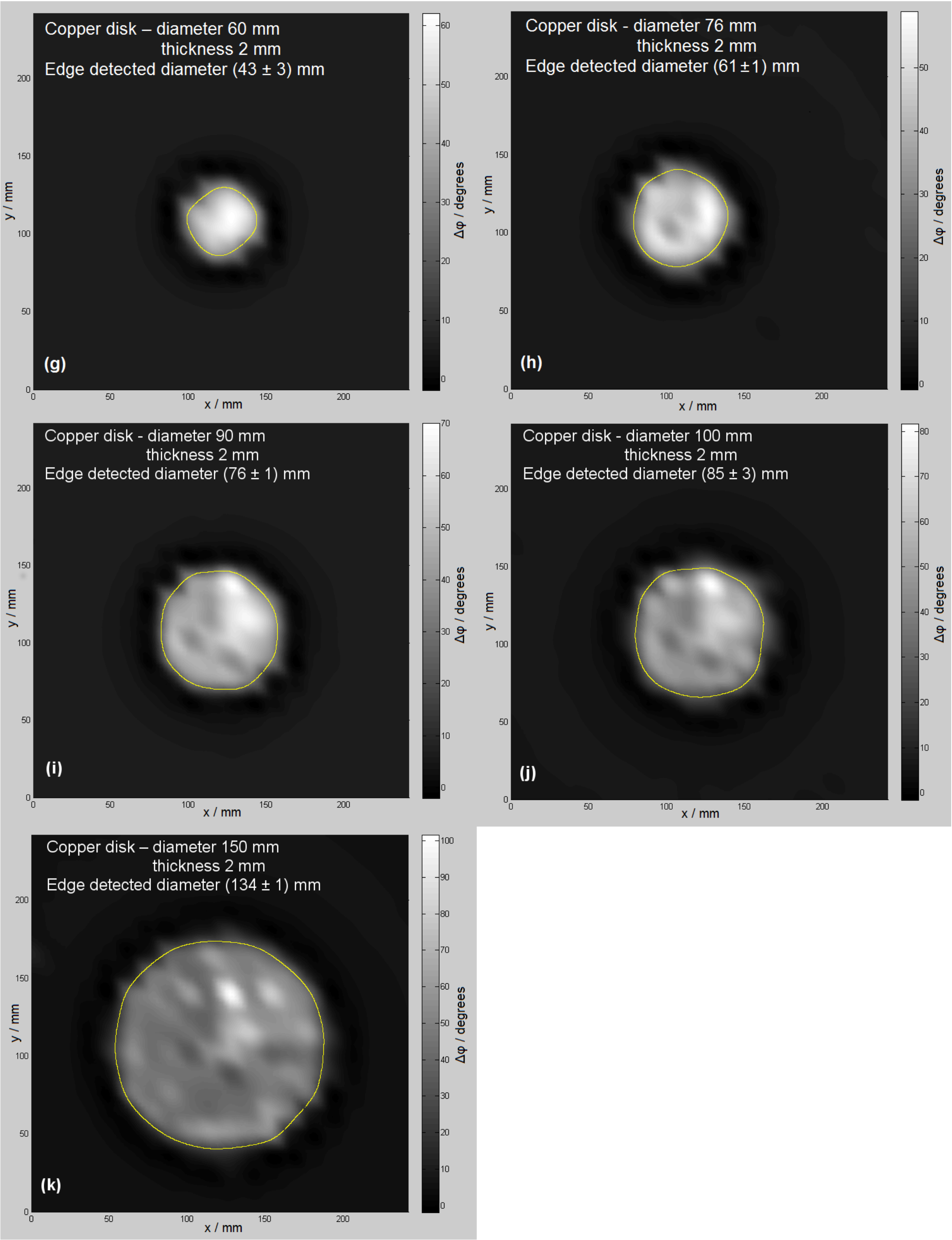

Figure 7.5. Images (g) to (k) of five Copper disks, 60 to 150 mm diameter, showing edge detection, with the disks centred between four sensor coils.

This is because the disk centred on one sensor is nearer to one whole sensor and therefore giving it higher phase as it receives more secondary field from the disk at that point. However it is further away from the surrounding sensors than the disks centred between four sensors. Therefore the disks centred between four sensors, enables these sensors to receive more secondary field and therefore a broader image of the disk is generated. The resolution limit for this MIT system, utilising figure 7.1 was estimated at ~30 mm, as it was the first size that could be distinguished from smaller disks. So that at ≥ 30 mm diameter the disks could be distinguished from smaller ones, but at < 30 mm the edge detected diameter was about the same for disks 15 mm to 20 mm. I.e. the imaging system cannot adequately resolve disks less than 30 mm diameter.

The MATLAB routine in Appendix 14.1.1 was implemented, which plots a magnetic image of the disks and then applies edge detection in an attempt to determine the diameter from the image.

The uncertainty in the edge detected diameter of the magnetic images (shown in figures 7.2 to 7.5) was based on four measurements of this value from the plot. These were taken directly from the MATLAB generated plot, by attaching the cursor onto the edge which is accompanied by the (*x, y, phase*) data at each point along it. The mean value of the edge diameter was taken from vertical and horizontal measurements in the shape of a ‘+’ and two diagonal measurements in the shape of an ‘×’. All these measurements were made from visual estimation of the edge detected diameter on an enlarged plot and the uncertainty in the mean value was determined from the unbiased estimate of the standard deviation [76].

7.2 Imaging through single and double ferromagnetic enclosures

Security applications may require the ability to image through electromagnetic shields. This is for example the case when trafficking of illicit material involves cargo containers on the scale of 10 cm × 10 cm × 5 cm. Thus suitable detection techniques are required to penetrate a ferromagnetic enclosure. In the following a demonstration is given of the ability of the imaging system to create magnetic images of metallic objects concealed within such enclosures. The penetrating power through single and double ferromagnetic enclosures was investigated.

A ferromagnetic enclosure acts as a Faraday cage [77][78] screening electromagnetic waves and therefore not allowing them to penetrate. However it will allow slowly varying or static magnetic fields to penetrate, thus enabling detection of hidden metallic objects using the following technique.

Imaging through metallic enclosures has been demonstrated for the specific case of 50 μm thickness of Copper pipe [79]. Recent work by Lu Ma [80] has imaged external damage to magnetic steel pipes of 5 mm thickness, although in that study objects were not imaged inside the pipe, where the primary field could not penetrate the steel pipes at the frequencies used. In the current study imaging was undertaken through a double enclosure of plated mild steel of 0.24 mm and 0.33 mm thickness, with resultant images shown in figure 7.8. This demonstrates that it is possible to penetrate through such a thick enclosure assembly to image a concealed conductive object. These experiments therefore validate electromagnetic detection as a potential imaging technique for the security industry [2].

The material of the enclosures is tinplate (mild steel thinly coated with tin), often used in products such as tin cans and similar types of containers.

Imaging a Copper disk, 30 mm diameter by 2 mm thickness, concealed inside a single enclosure and a Copper disk 40 mm diameter by 3 mm thickness inside a double enclosure is described as follows.

Single Enclosure

Firstly the disk was imaged inside a single enclosure. This involves a procedure of taking phase readings from a background image, in this case the empty container and subtracting it from phase readings of the container with the concealed Copper disk inside (i.e. the full enclosure). The resultant image reveals the disk with surrounding container removed or only vaguely present. In the single and double enclosure experiments a uniform driving field of (0.42 ± 0.02) mT at 200 Hz was generated by the Helmholtz coils at the level of the sensor coils, with (215 ± 2) mA passing through Helmholtz coil system. An average of (44 ± 9) μA was measured in the sensor coils. The single enclosure is a ferromagnetic container with dimensions 75 mm × 77 mm × 15 mm and material thickness 0.2 mm. Five images were made of the Copper disks in different positions to identify that the disk was actually being detected. The background image of the empty container was imaged once then carefully opening the lid, the Copper disk was placed inside, the lid closed and an image taken. This was repeated for the different positions of the disk concealed inside the container in the centre, upper right, upper left, lower left and lower right positions, as shown in figure 7.6. After subtracting the full and empty enclosures with the disk in five different positions, the extracted disk was revealed, shown in figures 7.7 (ai) to (ei). The next step involved detecting the edge of the extracted disk and measuring the edge detected diameter for each of the five positions, with the results shown in figures 7.7 (aii) to (eii). The procedure for this was implemented in MATLAB as described in Section 5.2.

Figure 7.6 (ai) shows an image of the empty single enclosure and the figures 7.6 (bi to fi) show images of the enclosure with a Copper disk inside. The five positions show that the Copper disk is being detected. In this figure the disks are observable inside the enclosure before the empty enclosure phase values have been subtracted. This is not normally the case and in this example it is due to the enclosure being thin and specimen disk being close to the sensor coils, which is only separated by the bottom of the enclosure and a sheet of graph paper. With a uniform driving field and the single enclosure being close to the sensors, the image is clearer than with a previous single driver coil used for the same image, where the driving field was not uniform and the sensor coils were further away from the sample object. Figure 7.7 shows the Copper disk clearly extracted from the ferromagnetic enclosure by subtraction of the empty enclosure phase readings from those of the full enclosure. Edge detection was also applied to these extracted disk images. As can been seen from figure 7.7, the edge-detected diameter is slightly different for each of the five positions. This is due to the Copper disk’s location in relation to the sensor coils, such as on top of two coils or in between four coils, as described in Section 7.1. The edge detected diameter in figure 7.7 varies between (22 ± 4) mm and (26 ± 1) mm.

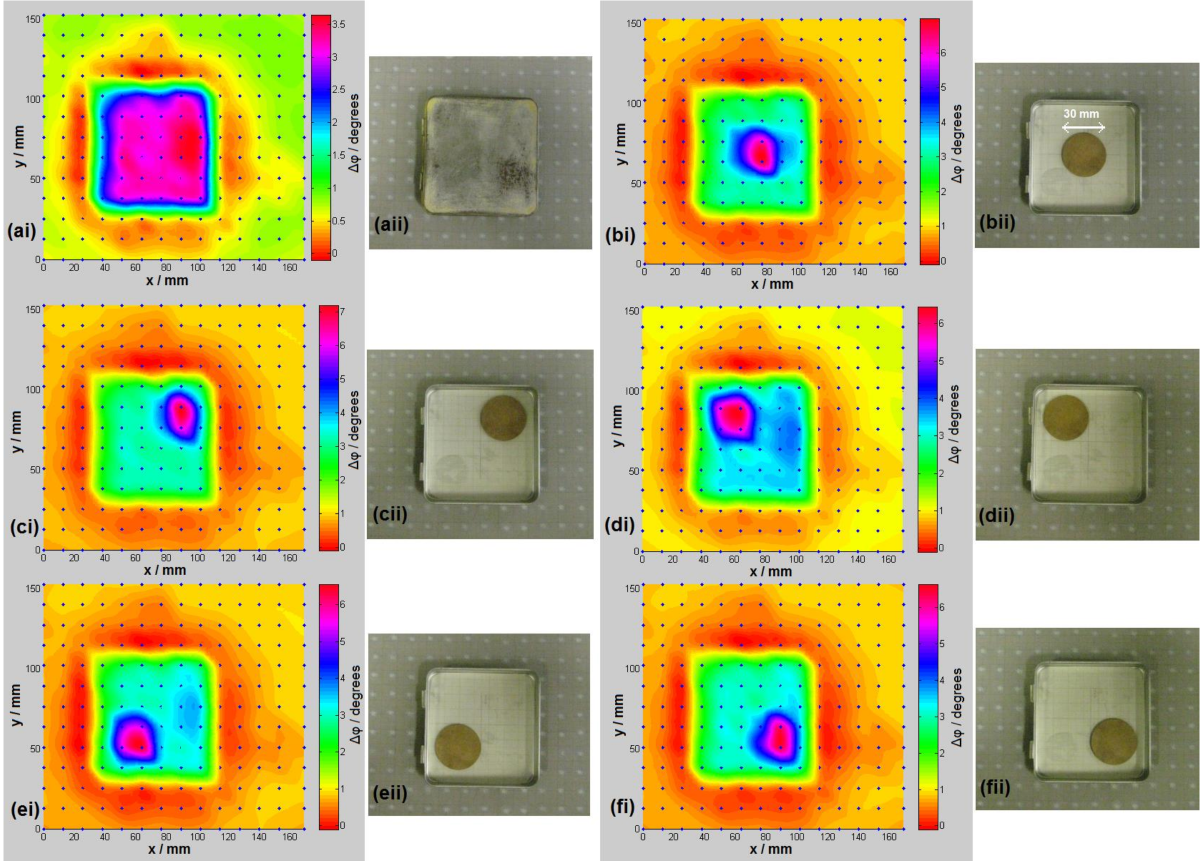

Figure 7.6. Raw images of Copper disk 30 mm diameter by 2mm thickness, concealed within a ferromagnetic container in 5 different positions (bi to fi) before extraction of the disk. Accompanying photographs are shown in the figures ending in (ii). Image (ai) is of the empty container as the background image. In these figures the disk is visible even before it is extracted via the method of subtraction-of-phases of full and empty enclosures.

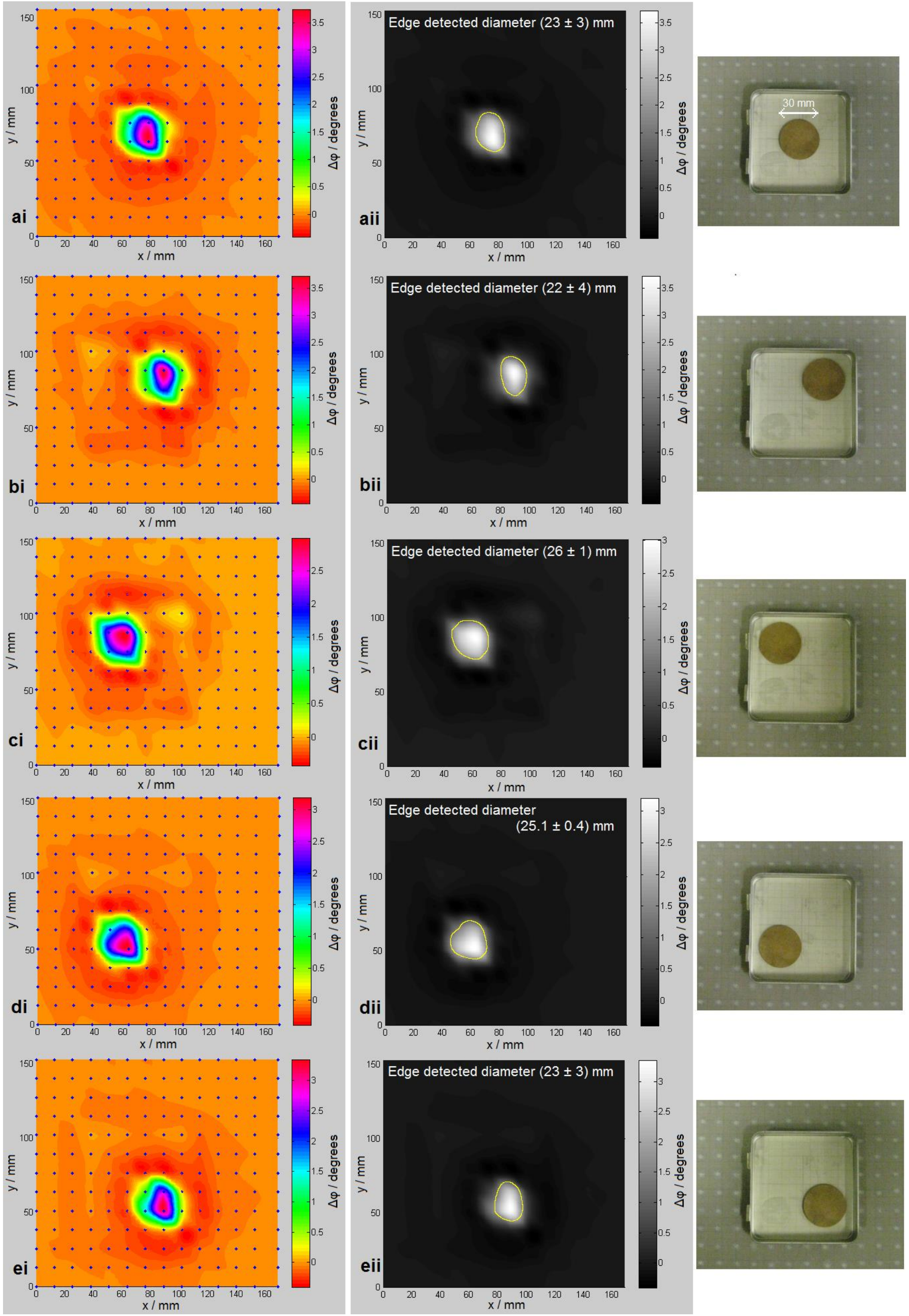

Figure 7.7. Extracted images of the Copper disk from within a ferromagnetic enclosure as in figure 7.6, after subtraction-of-phases of the full and empty enclosures, showing edge detected diameter in (ii).

Double Enclosure

Imaging an extracted Copper disk inside a double ferromagnetic enclosure is similar to the method for the single enclosure, using the same uniform driving field of (0.42 ± 0.02) mT and the frequency of the field set to 200 Hz. The disk size in this case was 40 mm diameter by 3 mm thickness. Two ferromagnetic containers were used. The larger container has dimensions 145 mm × 113 mm × 17 mm and material thickness (0.33 ± 0.01) mm. The smaller container has dimensions 88 mm × 89 mm × 9 mm with material thickness (0.24 ± 0.01) mm. The extracted disk was shown in three positions to clearly show that the disk was being detected inside the two enclosures. These positions were: centre, left and right, as shown in figure 7.8. The inner container was also moved to the centre, left and right, for the maximum displacement of the disk. Background images were taken of the two empty containers, enclosed within each other. The extracted image of the disk then resulted from the subtraction-of-phases of the full and empty enclosures.

Figure 7.8 (ai to di) shows the raw images of the empty double enclosure and the double enclosure with the disk inside, in the three positions. As can be seen from figure 7.8 (bi to di), it is not clear on visual examination of these images which position the disk is in, as the subtraction method has not been applied yet. Therefore by subtraction-of-phases of the full and empty double enclosures figure 7.8 (bii to dii) shows the revealed Copper disk in three different positions. The edge detected diameter of the enclosed disk varies between (31 ± 1) mm and (32.3 ± 0.7) mm, depending on the disk's positions relative to the sensor coils. The uncertainty in these values is due to the direct measurement of the Canny edge diameter on the image. It is not based on the processes of uncertainty relating to the disk's actual dimeter of 40 mm.

The important result described here is that a weak magnetic signature of the disk can be distinguished from the background of the enclosure and that such a signature can be extracted to clearly show the disk's size and position.

The ghostly outline of the containers in the magnetic images of figures 7.7 (ai to ei) and figure 7.8 (bii to dii), are possibly due to the slight fluctuation in phase measurements between the empty container backgrounds and the full container images. So that when their phases are subtracted, the container phases are not completely removed but leave a ghostly outline of their position. Another possibility is that the eddy currents induced in the Copper disk magnetically change the surrounding container and therefore affect its phase values. It could also be due to the container not being in exactly the same position after its contents were removed to image of the empty container.

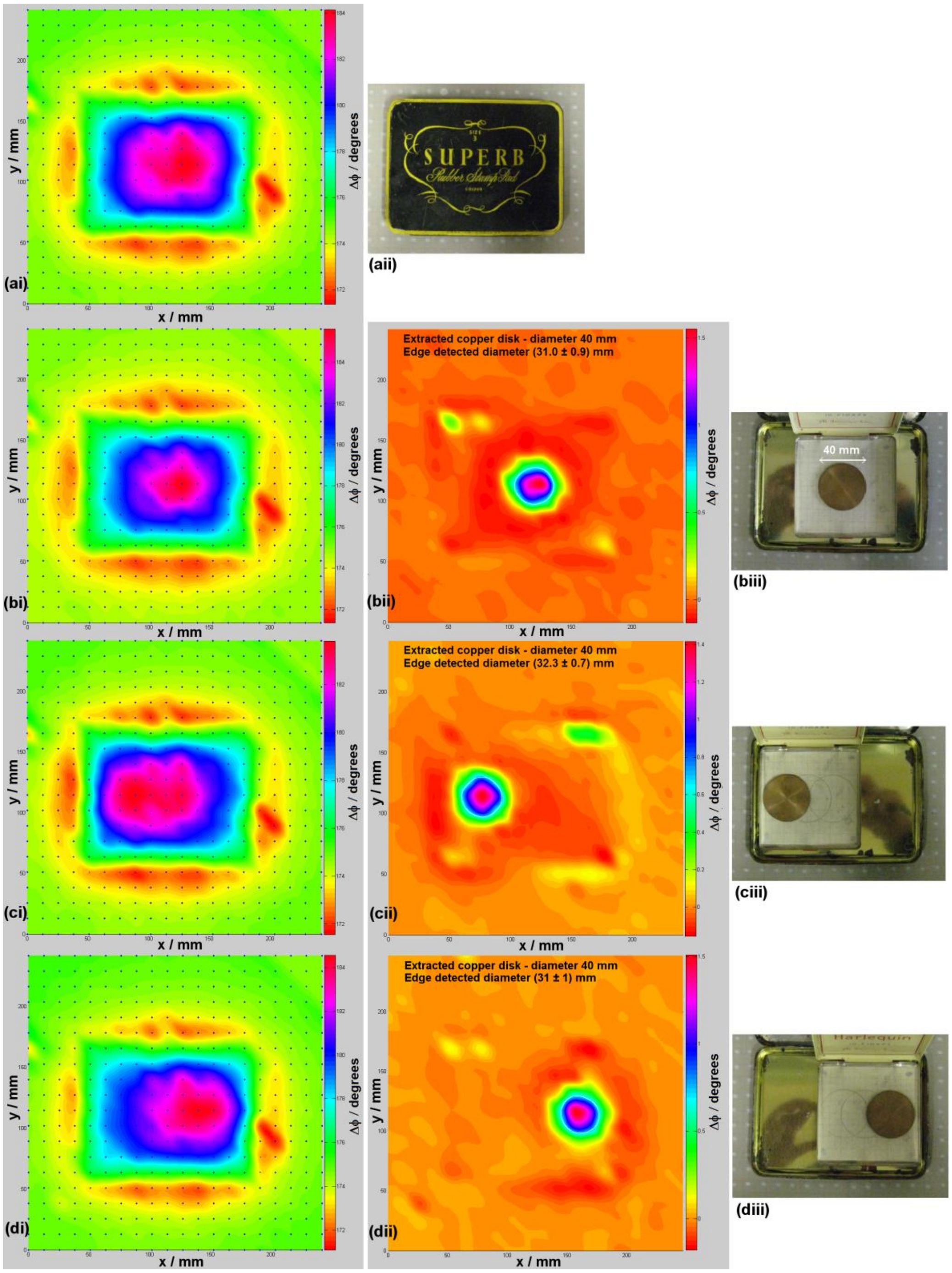

Figure 7.8. Illustration of magnetic imaging of a Copper disk through a double ferromagnetic enclosure. The copper disk is 40 mm diameter by 3 mm height. (ai) shows an image of the empty double enclosure with photograph in (aii). (bi) to (di) shows magnetic image of the closed double enclosure with concealed disk inside, in 3 positions of centre, left and right. (bii) to (dii) shows the extracted Copper disk in the 3 positions, after subtraction of the empty enclosures' phases was applied to the full enclosures. (biii) to (diii) displays photographs of ferromagnetic double enclosure with Copper disk in the 3 positions. Photographs were taken with enclosure lids open, but magnetic images were taken with the enclosure lids closed.

7.3 Technical issues with set-up and images

The sensor array has five sensor coils giving ‘anomalous’ values of voltage phase difference, displayed as large peaks in the MIT images that dwarf the image of the specimen under examination. The anomalies are most likely not in the sensor coils themselves, as on replacement of four of these sensors the peaks were still present. The fault is more likely to be in the connecting ribbon cable, the veroboard or the Agilent multiplexer. In addition the four corners of the array that are outside the Helmholtz coils’ uniform field, were giving high peaks in phase values which also dwarf the image of the sample object under inspection. Therefore adjustments have been made to correct the anomalous sensors and suppress the array corner peaks. The ‘anomalous’ sensors have been smoothed over, by taking the average phase of the four neighbouring sensors in the shape of a cross (‘+’). The phase peaks in the four corners of the array were suppressed by making the triangular area of sensors in the corners, that is four sensors in x and y, to be equal to the average of the hypotenuse of sensors (five diagonal sensors), starting five sensors in x and ending five sensors in y. The x and y sizes start from the corner. Therefore the four corners cannot be used as part of the magnetic image.

For the magnetic images of the Copper disks, both isolated and inside ferromagnetic enclosures except for the double enclosure, the placement of these objects was in a part of the array away from the anomalous sensor values. All images are also taken within the uniform driving field of the Helmholtz coils.

The uncertainties in figure 7.1, in the measurement of the edge detected diameter, were taken from four measurements of diameter on the magnetic image. A fuller analysis of uncertainties could be undertaken. These uncertainties would relate the electromagnetic processes that generate the voltage phase difference data, to the Canny edge detection algorithm applied to the magnetic image.

From the 2-D surface plots in figures 7.2 to 7.5 and from figure 7.1, the Canny edge detection gives approximately the correct value of diameter for 17.5 mm to 20 mm diameter Copper disks, centred on one sensor. However these images are outside the limit of resolution. At larger diameters of 50 to 150 mm the edge detected diameter is less than the ‘true’ diameter by (18 ± 3) mm in each case. A linear fit has been provided for these data points, but further work will be needed to understand why this is and whether it can be improved upon. For example can the Canny edge detection method within MATLAB be adjusted to obtain a more accurate edge? Or does the resolution of the sensor array need to be finer, in terms of smaller coils closer together?

Images of the Copper disks, including other images described throughout this study, appear to be diagonalized from the upper left to the lower right. Figure 7.9 (a-b) shows the five anomalous peaks with cubic interpolation, highlighting the diagonalization effect. The diagonal effect is due to the ‘cubic piecewise interpolation’ fitting function used to generate the images in MATLAB. Other interpolations were tested to compare the difference, where ‘natural neighbour’ (figure 7.9(e-f)) and ‘Biharmonic spline’ (figure 7.9 (c-d)) were two that gave a more rounded image.

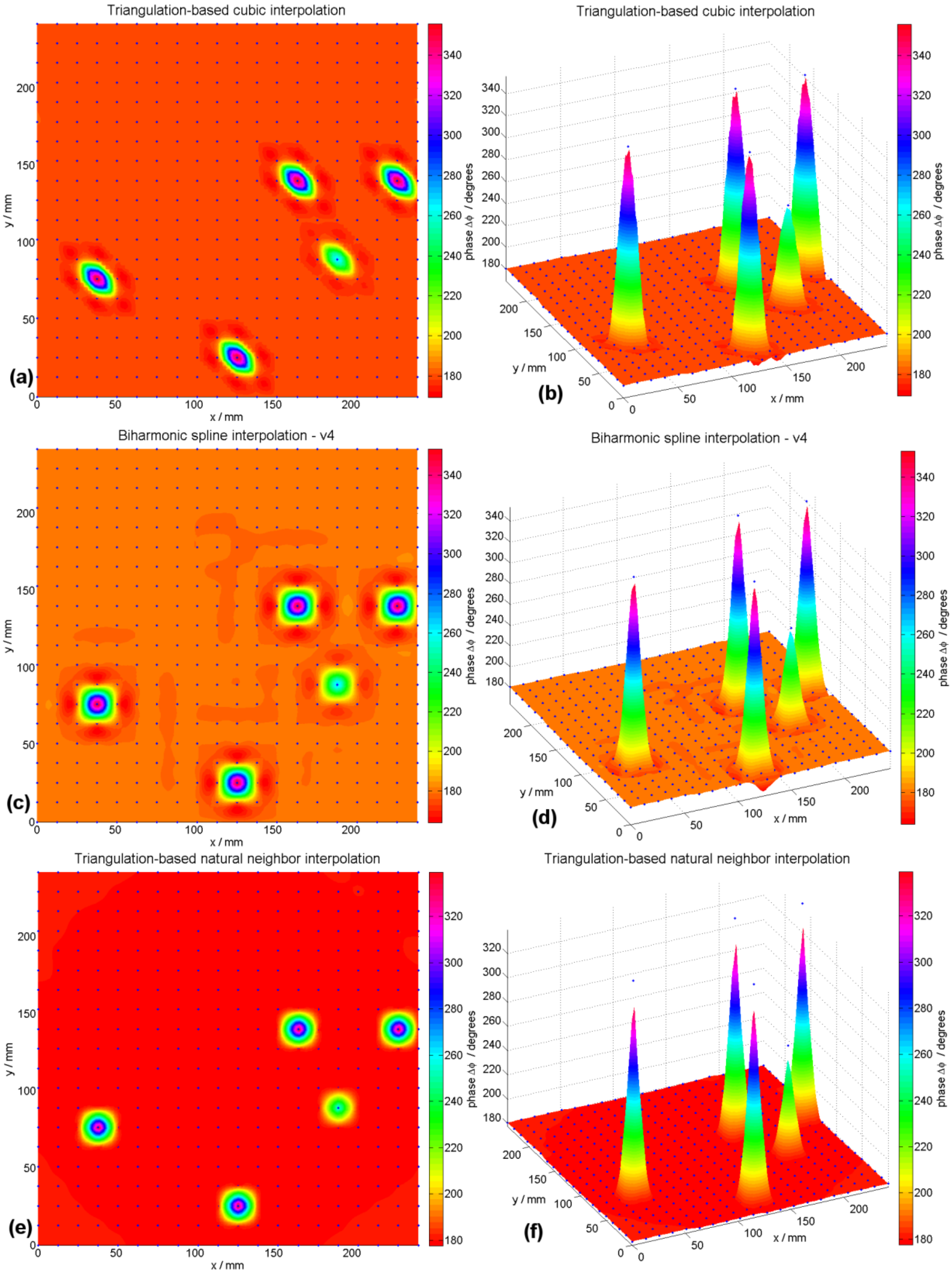

Figure 7.9. Three interpolations applied to the five anomalous peaks, showing aerial and 3D views. The interpolations are: (a) to (b) cubic, (c) to (d) Biharmonic and (e) to (f) natural neighbour.

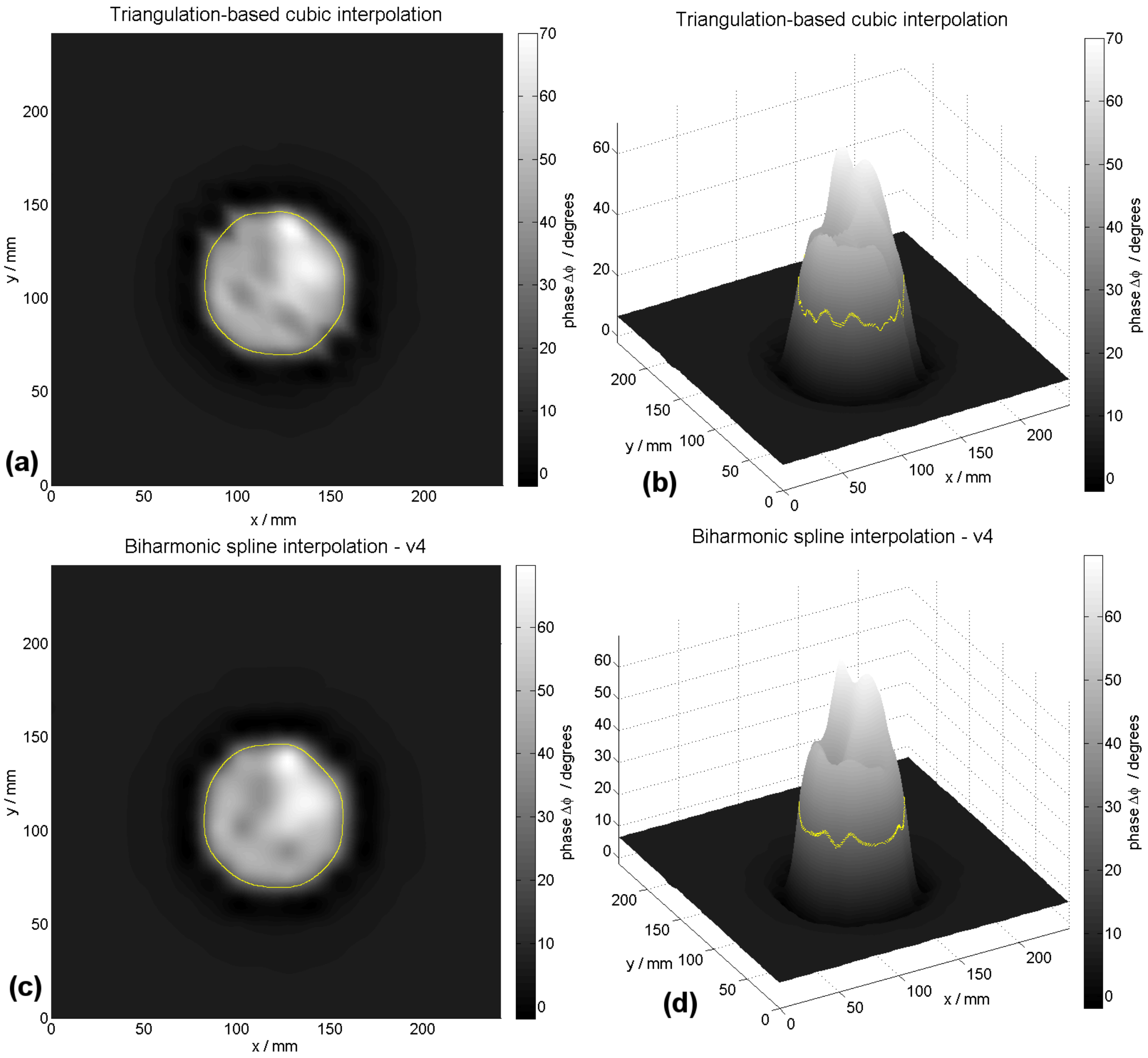

Figure 7.10. Images of 90 mm diameter Copper-disk by 2 mm thickness, showing aerial and 3D views. Plots (a) to (b) are cubic interpolation and (c) to (d) are Biharmonic.

The cubic interpolation gave a more curved image in the peaks of the surface plot that was considered more realistic than natural neighbour; where natural neighbour gave a spike in the peaks. The final choice was between Biharmonic and cubic interpolations, shown with the comparison in figure 7.10. However the cubic interpolation was chosen to generate the images, as it did not affect significantly the edge detected diameter compared to Biharmonic and for consistency all previous images had been made using the cubic interpolation.

When the background image with no sample present was subtracted from the image of the sample object, it was discovered that both images needed their corners suppressed and anomalous peaks smoothed over in order to give a valid image. A valid image could not be obtained by merely subtracting the raw background image from the raw sample object image, because the peaks in the corners and anomalous peaks fluctuated too much to allow this approach.

Some investigation was made of the magnetic images in regards to how much of the image was due to the metallic specimen and how much was due to the sensor coils themselves. In an image of a Copper disk 90 mm diameter by 2mm thickness, shown in figure 7.11, it was noted that peaks in the image data and other characteristics remained unchanged when the Copper disk was rotated 90° to a new position.

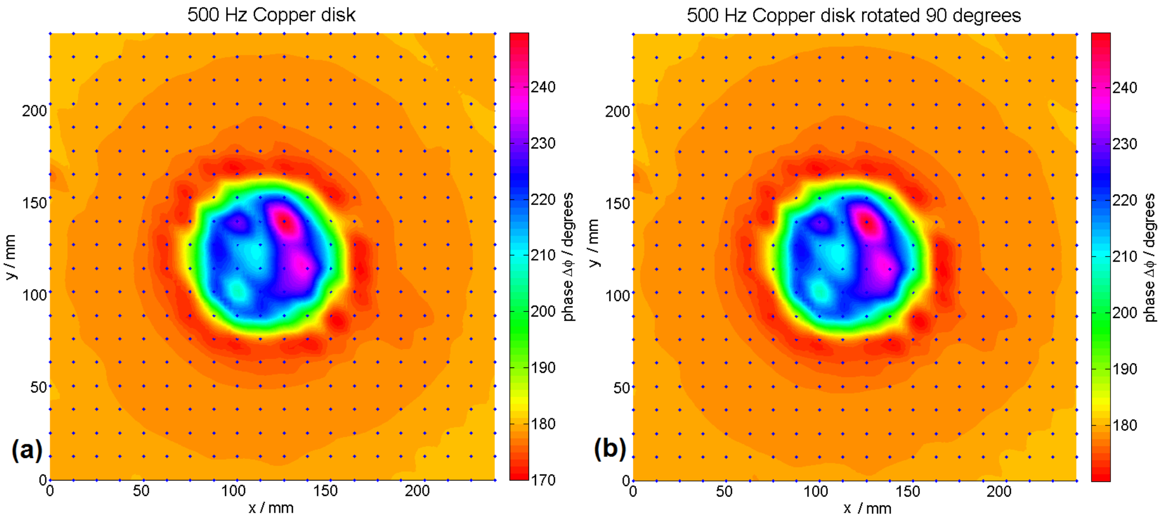

Figure 7.11. (a) Image of a Copper disk 90 mm diameter by 2 mm thick.
(b) The same disk rotated 90°.

This seems to indicate that peaks and troughs in the image are not due to the sample object alone, but are caused by a contribution from the sensor coils, the apparatus connected to the coils or possibly the Helmholtz coils' field. This is clearly seen in this case of a homogeneous object such as a Copper disk.

7.4 Conclusion

It has been demonstrated that by using an electromagnetic induction technique it is possible to penetrate ferromagnetic enclosures to image the metallic contents inside. It was shown that the concealed objects have magnetic signatures that can pass through the metal walls of the enclosure and be detected by sensor coils. By using an arrangement of array based sensor coils it has been possible to image inside the enclosures, revealing the position and shape of a concealed Copper disk. It was demonstrated firstly that a weak magnetic signature can be detected from within a double ferromagnetic enclosure, by subtraction of the empty enclosure phase values from that of the full enclosure; and secondly that the imaging system is sensitive to such a signature.

The next stage of the project involves research into the dual frequency method. This involves imaging inside ferromagnetic enclosures without having access to the empty enclosure and therefore towards a more practical MIT device.

8 Dual Frequency method

In this section the dual frequency method for imaging through ferromagnetic enclosures is reported [2].

A technique was introduced that could enable practical application of the MIT system. In the real world it is not practical to open a container and remove its contents, as we do with the proof-of-principle method shown in the results of Section 7.2. It is too time consuming to open enclosures in for example baggage scanning at airports. It is more efficient to simply image through an enclosure in a short time, using the method described as follows. This real world technique requires a high frequency image to approximate the empty enclosure and a low frequency image to penetrate deeper into it, detecting the concealed contents.

The main development here is that a principle has been demonstrated of imaging inside a metallic enclosure, without removing its contents using a new MIT method. The problem of the identification of an automatic process and relative algorithm, to extract an image of the concealed object from the measurements, is currently an object of research within our group. It is anticipated that it may be possible to determine the material type of the concealed object from its magnetic signature, with the appropriate reconstruction algorithm. This demonstration of the ability to image and with the possibility of identifying materials through multiple layers of ferromagnetic metallic enclosures; makes this technique a potential image scanning technology for the security industry.

8.1 Experiment to demonstrate dual frequency method

It is impractical in the real world to use the method of subtracting the empty enclosure from that of the full one, in order to image the sample inside, which only constitutes a proof-of-principle. To overcome this limitation a new method was introduced that involves approximating the empty enclosure by utilising a higher frequency image in place of it. At a sufficiently high frequency penetration of the enclosure is reduced due to the skin effect [45], thus allowing this image to be used in place of the empty enclosure.

The technique was demonstrated using a 30 mm diameter by 0.71 mm thick Copper disk, concealed in a single plated mild-steel enclosure, of dimensions 145 mm × 113 mm × 17 mm, with material thickness (0.33 ± 0.01) mm, as the one described in Section 7.2. Two images were taken of the enclosure containing the disk, one at low frequency, 200 Hz, and the other at high frequency, 2 kHz. After experimenting it was found that 200 Hz was low enough to image through the enclosure and obtain information about the metallic contents. It was also found that 2 kHz gave a sufficiently high frequency to obtain more information about the surface of the enclosure, thus providing an image that approximates the empty enclosure. These are only arbitrary values of frequency, as an investigation into testing a range of frequencies was not part of this work. After rescaling the low frequency image their phase values were subtracted from the high frequency one to reveal the disk inside. This dual frequency procedure was repeated for the disk in three positions, centre, lower-right and upper-left, to demonstrate that the disk was actually being detected. Also included is a 10 kHz image in figure 8.1 (aii) in place of the 2 kHz image, to show the effect of increasing the frequency. In figure 8.1 (ai) to 8.1 (ci) the 200 Hz image is shown with the disk in three positions and in figures 8.1 (aii) to 8.1 (cii) the high frequency images are shown. This is summarised in the following table 8.1.

Table 8.1: Parameters of images in preparation for the dual-frequency experiment.

Image	Notation	Frequency	Figure
High frequency	$f_{high\ freq}(x, y)$	10 kHz	5 (aii)
High frequency	$f_{high\ freq}(x, y)$	2 kHz	5 (bii), (cii)
Low frequency	$f_{low\ freq}(x, y)$	200 Hz	5 (ai), (bi), (ci)
Rescaled low-frequency	$f_{normalised}(x, y)$	200 Hz	Not shown
Dual frequency	$f_{high\ freq}(x, y) - f_{normalised}(x, y)$	10 kHz – 200 Hz, 2 kHz – 200 Hz	5 (aiii), (biii), (ciii)

The low frequency image, $f_{low\ freq}(x, y)$ was normalised to $f_{normalised}(x, y)$, to be the same order of phase values as the high frequency one, $f_{high\ freq}(x, y)$. In other words at an arbitrary location, (x_{ref}, y_{ref}), away from the concealed disk the positional phase value in the low frequency image was made to coincide with the corresponding value in the high frequency one, therefore bringing about a rescaling effect as shown in (8.1).

$$f_{normalised}(x,y) = f_{low\ freq}(x,y) \times \frac{f_{high\ freq}(x_{ref}, y_{ref})}{f_{low\ freq}(x_{ref}, y_{ref})} \tag{8.1}$$

With the high frequency image approximating the empty enclosure and the low frequency image rescaled to be of the same order, the method of subtraction-of-phase values was implemented as in the proof-of-principle method described Section 7.2. This dual frequency method is a completely new technique and takes this imaging system a step closer to a practical MIT modality, using planar sensor arrays and uniform driving fields.

8.2 Results

The resultant images revealing the extracted disk are shown in figures 8.1 (aiii) to (ciii). The Canny edge detection algorithm [42][73][74] was applied to the last figures 8.1 (aiii-ciii), showing the edge of the disk traced out in a white curved line, in order to identify it. Parts of the enclosure edge are also picked up by the Canny edge detector.

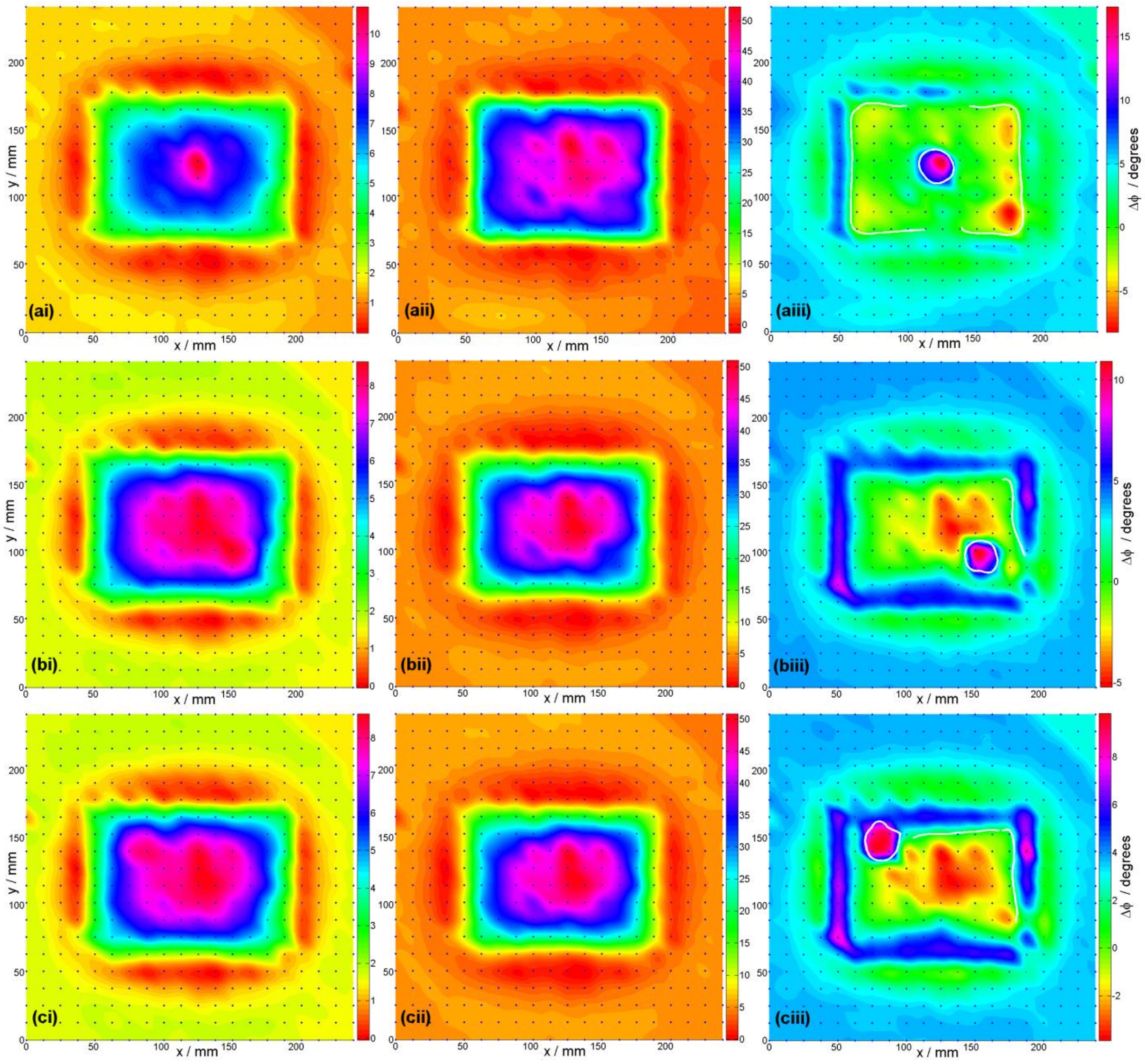

Figure 8.1. Magnetic images of a single ferromagnetic enclosure, for extracting a Copper disk using the dual frequency method. (ai) to (ci) show the low frequency images at 200 Hz of the enclosure, with the disk in 3 positions of, centre, lower right and upper left. (aii) to (cii) displays the corresponding high frequency images at 10 kHz in (aii) and 2 kHz in (bii) to (cii). (aiii) to (ciii) displays the resultant images of the extracted copper disk, of 30 mm diameter by 0.71 mm height, in the 3 positions. The last column showing the resultant extracted images, (aiii - ciii), also illustrates Canny edge detection, outlining the copper disk and parts of the enclosure edges in a white curved line.

The 10 kHz image used as the empty enclosure approximation in figure 8.1 (aii), appears to reduce the edge of the enclosure in the resultant image of figure 8.1 (aiii), more so than the 2 kHz images in figure 8.1 (biii-ciii). It is possible that the 10 kHz image approximates the empty enclosure better than the 2 kHz images. This is because at higher frequency of 10 kHz more of the outer parts of the enclosure were imaged due to the skin effect.

If the location of the disk is chosen for (x_{ref}, y_{ref}), this could cancel the disk's positional image when the high and low frequency images are subtracted; because the disk image normally gives the highest phase values in both images. Therefore a position for (x_{ref}, y_{ref}) away from the concealed disk is required. It was found that the position mid-way between the centre and edge of the enclosure along its central axis gave the best result. However, (x_{ref}, y_{ref}) can still be varied a certain amount within the enclosure and still give a valid result, i.e. it can detect the concealed disk; but not in the location of the disk or at the edge of the enclosure. This is due to the edges and disk being closer to unity in phase proportion in both images, but the phase space in between them has greater difference in proportion (see table 8.2); this effect lifts up the phase peak of the disk in the low frequency image when it is rescaled. When the images are subtracted the rescaled low frequency image highlights the detected disk and this is shown in the resultant image of the extracted disk. Therefore as the MIT system stands at the moment, if the location of the disk is not known, there would need to be trial-and-error in establishing (x_{ref}, y_{ref}). From an initial first image, the edge can be determined and then an edge chosen that is away from the disk. For example 2 or 3 edges could be tried and the mid-position chosen for (x_{ref}, y_{ref}), to see whether one of them revealed the concealed metallic object.

8.3 Investigation of dual frequency method

Some investigation was made of the dual frequency method to determine the robustness of the technique, i.e. how much the location of the reference point (x_{ref}, y_{ref}) assigned to the images could vary and still extract the concealed Copper disk (see Section 8.1 and 8.2). The reference point (x_{ref}, y_{ref}) is the position about which the rescaling of the low frequency image takes place, to make it the same order of phase values as the high frequency image, before they are subtracted from each other to reveal the concealed object. Figures 8.2 and 8.3 illustrate the results. Figure 8.2 (i) shows the low frequency image before normalisation, indicating the points A to I, where the following resultant images were rescaled at. Equation (8.1) in Section 8.1 shows the mathematical notation that describes this rescaling. The images A to I in figures 8.2 and 8.3 are the resultant images using the dual frequency method, with a high frequency of 2 kHz and low frequency of 200 Hz. This reveals the disk in the centre of the ferromagnetic enclosure that is the same enclosure described in Sections 8.1 and 8.2. The dual frequency technique was demonstrated to be robust in regards to the placement of (x_{ref}, y_{ref}). The images in figures 8.2 to 8.3 showed that the rescaling points could vary significantly within the enclosure image and still reveal the concealed disk. Figures 8.2 (A) and (B) do not effectively image the concealed disk, where the rescaling points A and B are near the edge of the enclosure. However images in figures 8.2 (C) to (E) and figures 8.3 (F) to (I) give a clearer image of the disk and parts of the enclosure walls. In figure 8.3 (I) the peak of the disk phase is nearly level with the background and in figure 8.3 (H) it is only 2° or 3° higher; compared with a more clearer extraction of the disk in figures 8.2 (D) to 8.3 (G), of 7° to 10° above the background. The rescaling factors for figure 8.2 (D) were used in figure 8.1 of the previous Sub-section.

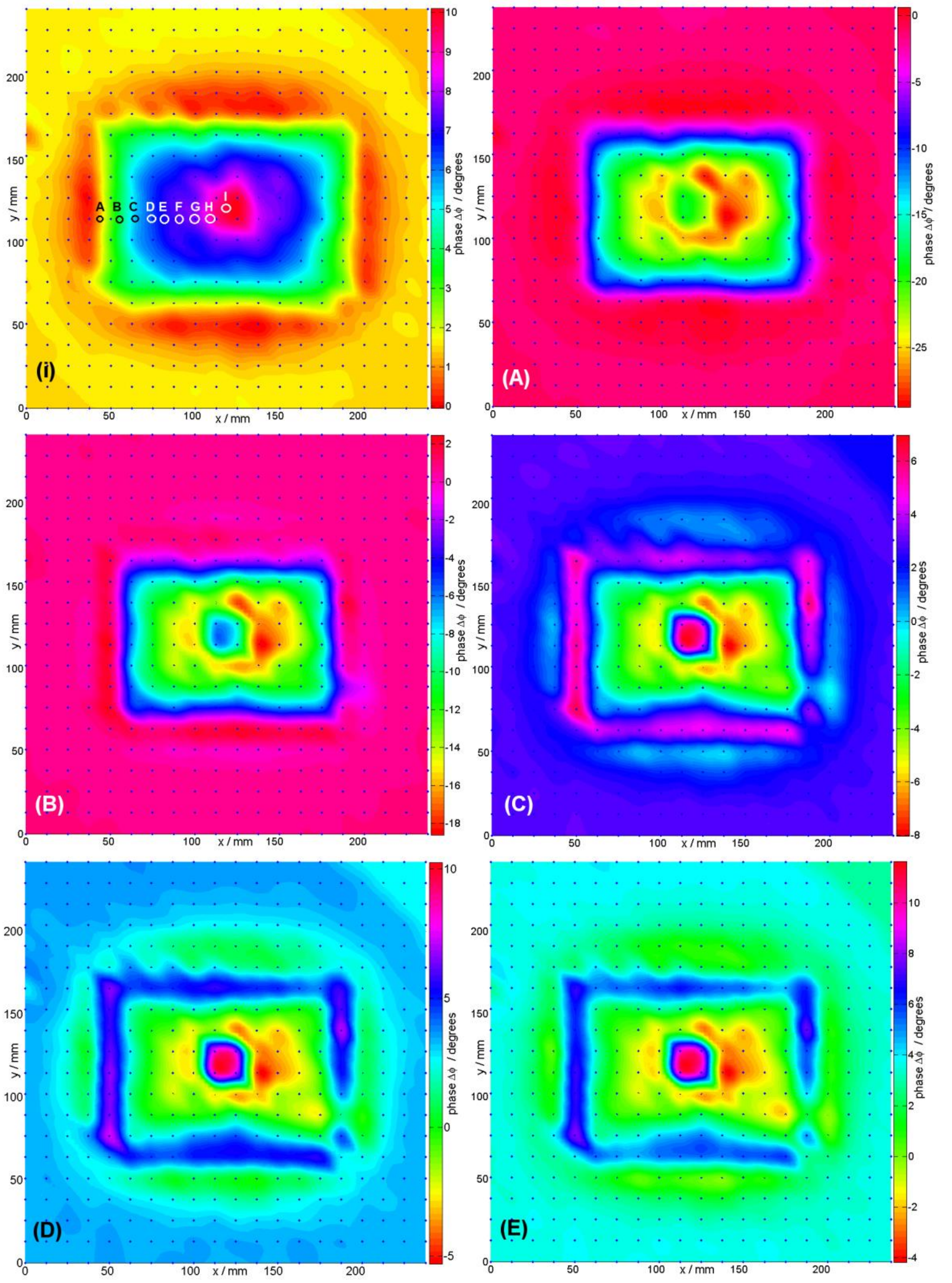

Figure 8.2. (i) Low frequency image showing rescaling points A to I. (A to E) dual frequency method applied to high frequency and normalised low frequency images, to reveal concealed Copper disk; using corresponding rescaling points A to E.

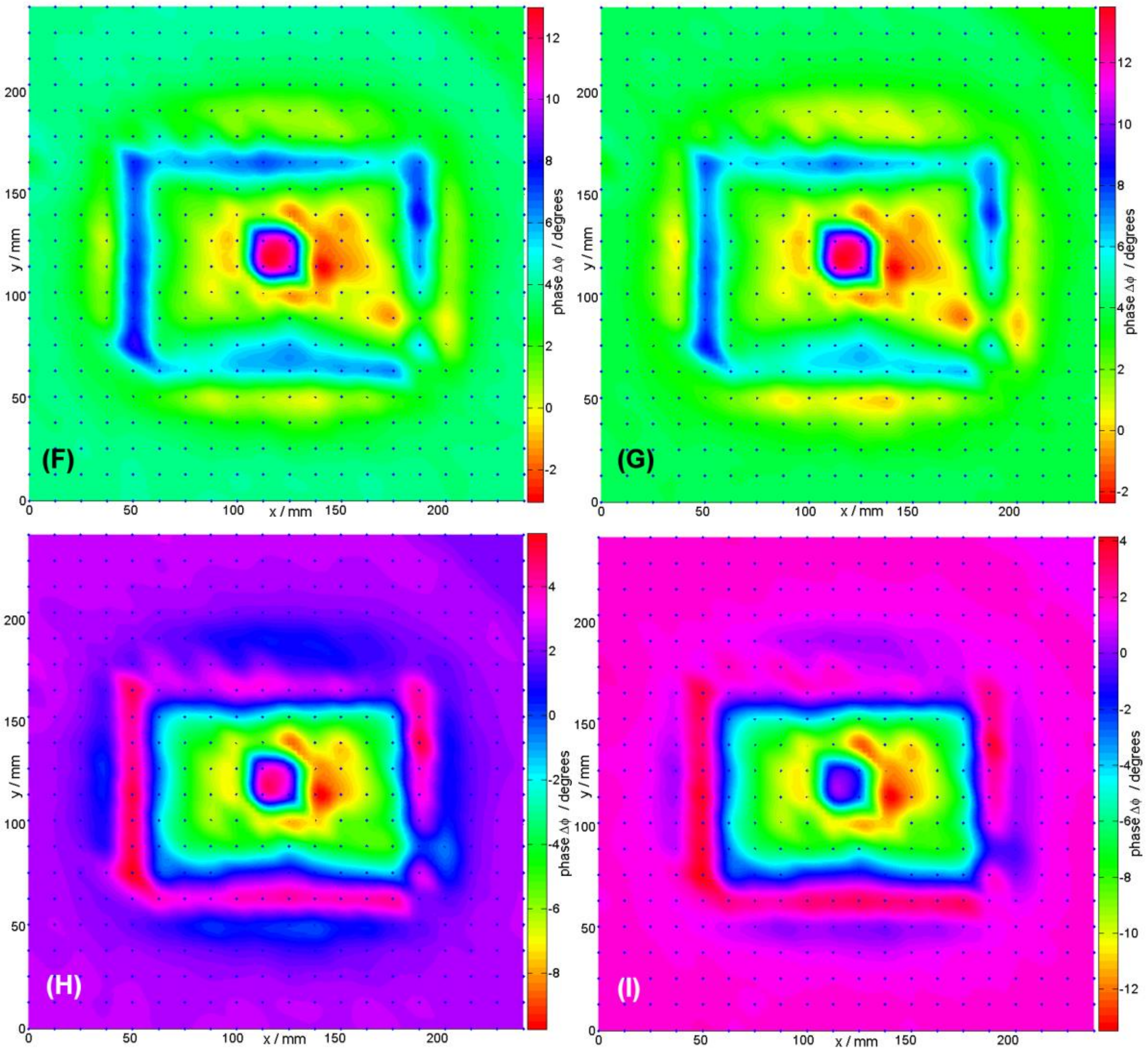

Figure 8.3. (F to I) dual frequency method applied to high frequency and normalised low frequency images, to reveal concealed Copper disk; using corresponding rescaling points F to I, shown in figure 8.2(i).

Table 8.2 below shows the rescaling factors for the images A to I. These factors were taken from the ratio (part of Equation (8.1)),

$$\frac{f_{high\ freq}(x_{ref}, y_{ref})}{f_{low\ freq}(x_{ref}, y_{ref})}$$

with values of 5.15 to 5.86 in C to G, giving the best extraction results, and satisfactory results in H to I of values 4.93 and 4.47.

Table 8.2: Rescaling values A to I – for investigation of varying reference points (x_{ref}, y_{ref}), in order to rescale the low frequency image, as part of the dual frequency method.

Rescaling points	(x_{ref}, y_{ref}) mm	$f_{high\,freq}(x_{ref}, y_{ref})$	$f_{low\,freq}(x_{ref}, y_{ref})$	$\frac{f_{high\,freq}(x_{ref}, y_{ref})}{f_{low\,freq}(x_{ref}, y_{ref})}$
A	(45,114.3)	3.50°	1.41°	2.48
B	(55,114.3)	13.77°	3.60°	3.83
C	(65,114.3)	27.79°	5.40°	5.15
D	(74,114.3)	34.20°	6.23°	5.49
E	(80,114.3)	37.69°	6.69°	5.63
F	(90,114.3)	42.19°	7.30°	5.78
G	(100,114.3)	44.56°	7.60°	5.86
H	(110,114.3)	42.95°	8.71°	4.93
I	(120, 120)	43.50°	9.74°	4.47

9 Penetrating power and skin effect

9.1 Introduction

The ability to image through metallic enclosures is an important goal of any scanning technology for security applications. Previous work [2] demonstrated the penetrating power of electromagnetic imaging through thin metallic enclosures (0.2 to 0.33 mm thickness), thus indicating the possibility of utilising it for security applications such as airport bag screening. In this section the limits of electromagnetic imaging through metallic enclosures are investigated, considering the performance of the imaging for different thicknesses of the enclosure [4]. The results show that this MIT system can detect the magnetic signature of a Copper disk, even when enclosed within a 20 mm thick Aluminium box [4]. The potential for imaging through enclosures of other materials such as Lead, Copper and Iron is also discussed.

9.2 Experimental set-up

The set-up is the same as the one described in Sections 4 to 8 and in previous work [2][3]. The metallic specimen for imaging rests on top of the sensor array, separated by a sheet of graph paper as shown in figure 9.1.

The 150 W AC amplifier increases an oscillator signal to 27 V rms across the driver coils. This gives drive currents of (2.05 ± 0.08) A rms and a magnetic flux density at the level of the sensors of (2.9 ± 0.6) mT rms at 10 Hz, with (21.4 ± 0.8) mA rms and (0.03 ± 0.01) mT rms at 2 kHz.

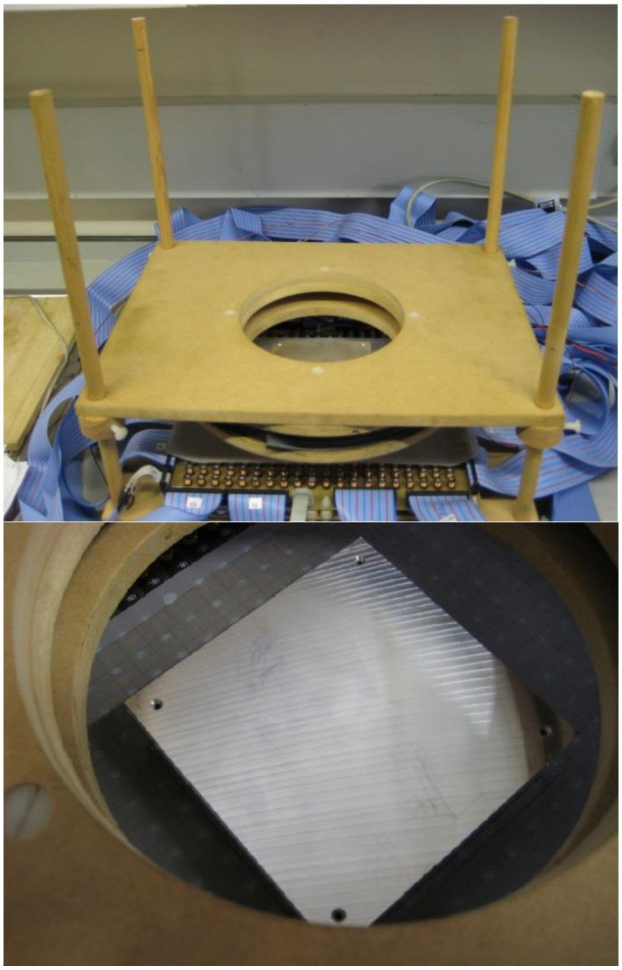

Figure 9.1. Helmholtz-coil assembly and sensor-coil array (top).
Aluminum box in position for imaging (bottom).

9.3 Imaging through Aluminium enclosures

In order to investigate the penetrating power of imaging through conductive enclosures, this experiment investigates imaging of a Copper disk through Aluminium enclosures of different thickness.

The method used here is the subtraction-of-phases of the full and empty enclosures, meaning that the phase values in first array are subtracted from corresponding values in the second one within MATLAB code. The boxes were completely closed with sides, top and bottom of the same thickness and a Copper disk concealed inside. All the boxes have a base of 10.5 cm by 10.5 cm and heights between 2.9 cm and 5 cm. Each was imaged at 6 different frequencies, 10 Hz to 5 kHz. The disk has 30 mm diameter and 2 mm thickness in all the boxes except in the 20 mm box, where the disk is 40 mm diameter by 3 mm thickness, as the 30 mm disk could not be detected for this size of enclosure.

Representative images are shown in figures 9.2 and 9.3. Images that could not distinguish the disk were not included. This would be due to the box walls being too thick in comparison to the skin depth at the applied frequency. For instance at 2 kHz the frequency produces a skin depth of 1.9 mm, prohibiting penetration at this frequency for the 10 and 20 mm thick Aluminium boxes. The results demonstrated that an image of the concealed disk could be extracted from five Aluminium box enclosures of 2 mm to 20 mm wall thickness. This was achieved at frequencies:

- 10 Hz to 5 kHz, for the 2 mm and 3 mm thick boxes (Figures 9.2 (ai) to 9.3 (aiii) and 9.2 (bi) to 9.3 (biii))
- 10 Hz to 2 kHz for the 5 mm box (Figures 9.2 (ci) to 9.3 (cii))
- 10 to 200 Hz for the 10 to 20 mm thick boxes (Figures 9.2 (di) to 9.2 (eiii))

Clearer disk images were obtained at the mid-range frequencies, 40 Hz to 1 kHz, for box thicknesses that were not too large, i.e. 2 mm to 5 mm compared with the 10 to 20 mm boxes.

At lower frequency and specifically 10 Hz, penetration of the driving field was sufficient to image the concealed disk for all thicknesses of the box enclosures, however the image was unstable and fluctuated, i.e. it could easily change when an additional image was taken. This could be due to smaller eddy currents induced in the specimen, giving a weaker potential difference across the sensors.

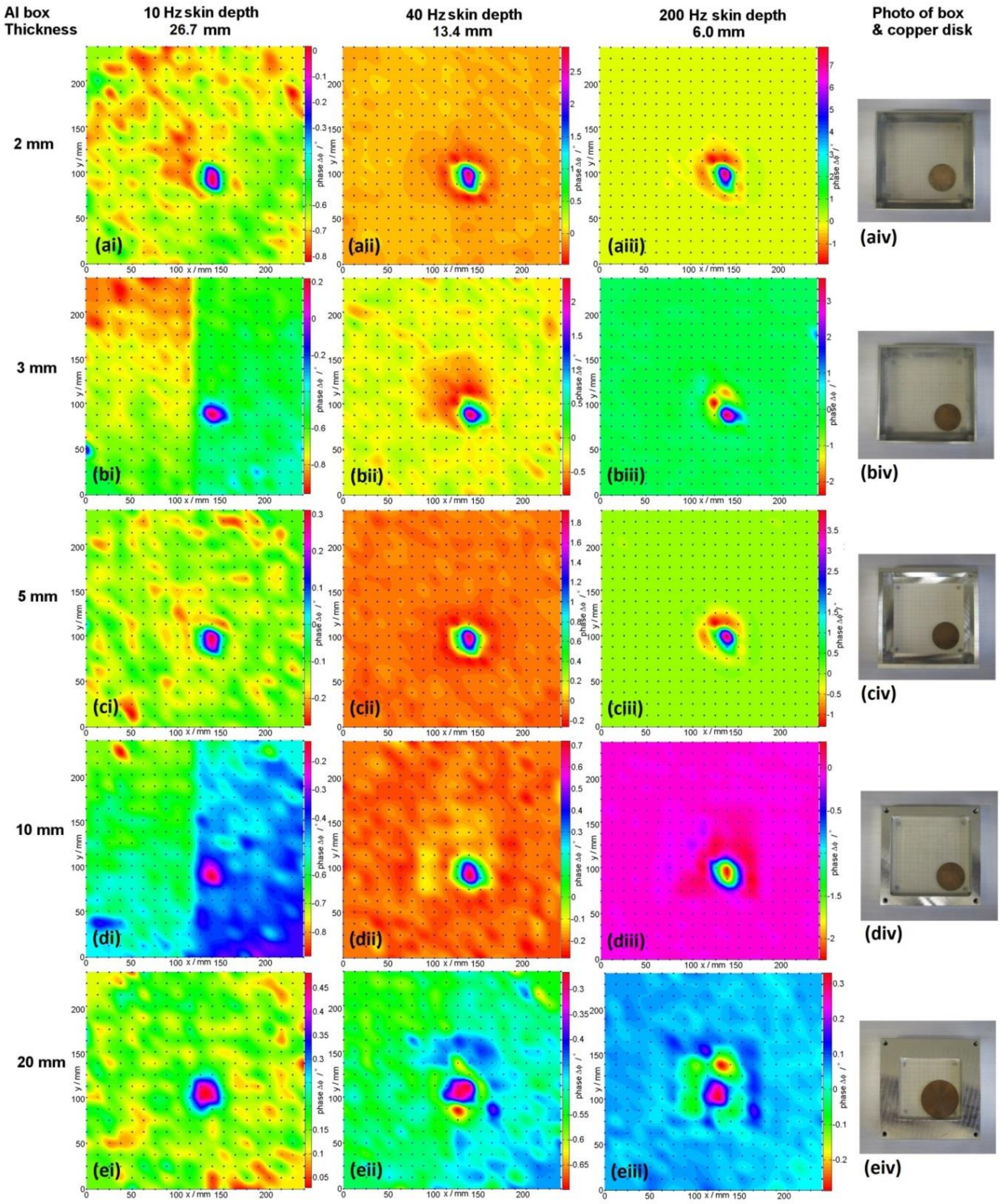

Figure 9.2. Magnetic image capture of a Copper disk concealed inside five separate Aluminium (Al) box enclosures of thicknesses, 2 mm to 20 mm. Images were captured at frequencies of 10 to 200 Hz, with *x* and *y* axes showing 2D position in mm and the *z* axis representing the phase values in degrees. Images are displayed as a table showing box thickness with respect to frequency and skin depth in (ai to eiii) and aerial photograph of the boxes with concealed disk in (aiv to eiv). Photographs show Aluminium boxes with the lid off, but images were taken with the lid on.

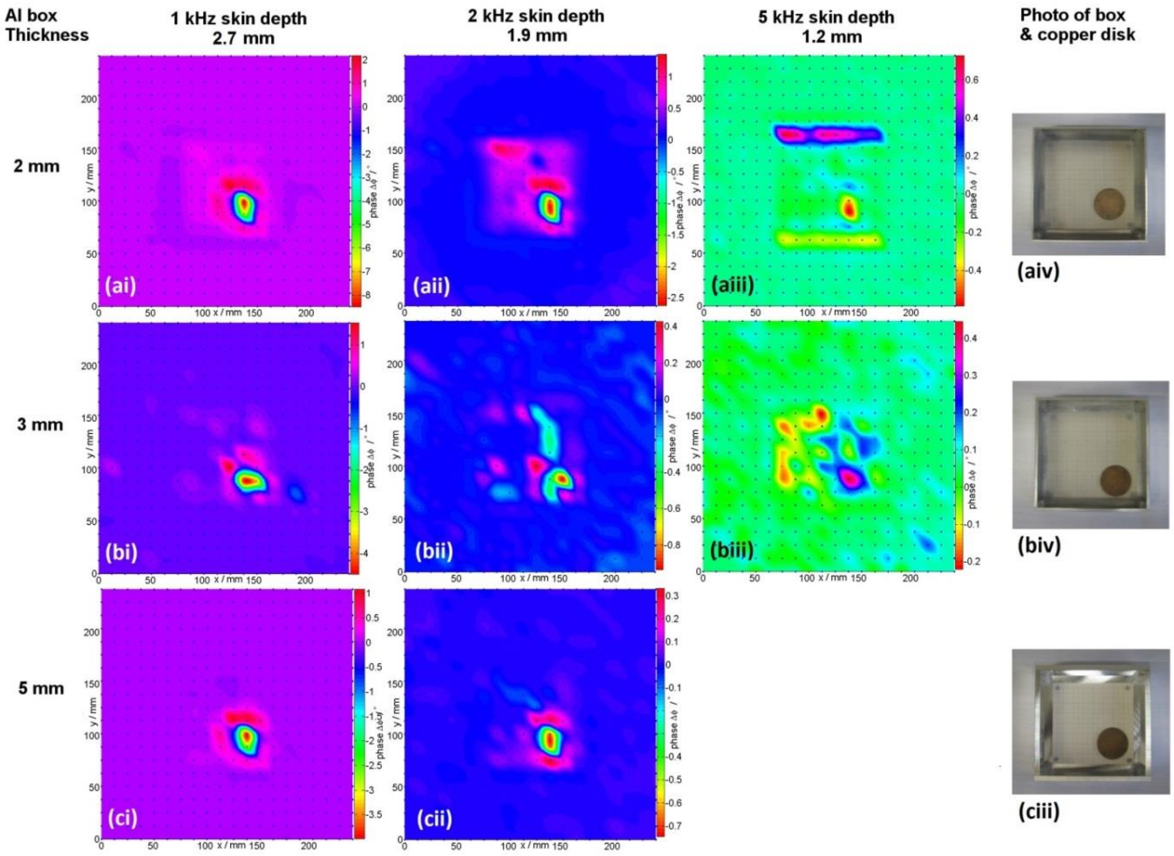

Figure 9.3. Magnetic image capture of a Copper disk concealed inside three separate Aluminium (Al) box enclosures of thicknesses, 2 mm to 5 mm. Images were captured at frequencies of 1 to 5 kHz, with *x* and *y* axes showing 2D position in mm and the *z* axis representing the phase values in degrees. Images are displayed as a table showing box thickness with respect to frequency and skin depth in (ai to cii) and aerial photograph of the boxes with concealed disk in (aiv to ciii). Photographs show Aluminium boxes with the lid off, but images were taken with the lid on.

It was also noticed that at 10 Hz the primary field is at its largest value of 2.9 mT (rms) due to the low impedance of the Helmholtz coils. A background image with no specimen present also shows instability at this frequency, i.e. the image could change easily if retaken. The background can be seen to fluctuate in figures 9.2 (ai to ei), in that part of the image that does not include the disk. At 10 Hz the strength of the source magnetic field is significantly reduced, inducing currents into the sensor coil of (23.5 ± 0.5) μA compared to (48 ± 1) μA at 5 kHz. Therefore at such a frequency there is not the power in the field to excite enough eddy currents into the sample object to generate a stabilized phase image. This is probably also due to the sensor coils not being sensitive enough to adequately detect the resultant field at 10 Hz, so that detection fluctuates visibly with successive images. This can also be seen in figure 9.6 (ai to aiv) of Section 9.5, where images are shown with decreasing applied primary fields.

The skin depth of the Aluminium enclosure and the enclosed Copper disk determines our ability to image through the enclosure. This is demonstrated by the images of figures 9.2 to 9.3. The disk images change shape slightly for the different thickness of the enclosure, but the overall shape remains consistent for different frequencies of the applied signals; except for the 10 and 20 mm thick boxes which gave varying shapes within the same overall location of the actual disk. The set-up is not biased towards imaging only circular disks because it has already been shown in Section 7.2, figure 7.6 (ai) that it can image a box shape.

The edges of the disk image can be observed in some of the images between 10 to 200 Hz, notably figures 9.2 (aii), (aiii), (cii) and (ciii). The image peaks at these frequencies in the disk centre and drops in phase below the background at the edges. For frequencies of 1 kHz to 5 kHz the phase values gave the opposite effect, dipping to lower values for the disk centre and rising above the background at the edges as shown in figure 9.3 (ai), (ci) and (cii). The absence of edge effects in some of the images could have been caused when removing the lid to place the disk inside, so that the full and empty enclosures were not identically repositioned. An additional cause may be the instability of the image.

The 5 kHz image of the 3 mm Aluminium box in figure 9.3 (biii) gave a peaked image as opposed to a dipped image in the central part of the disk, compared with its lower frequency images of 1 and 2 kHz in figures 9.3 (bi & bii). It was noted that the two 5 kHz images shown exhibited instability. This could be due to the very small magnetic field, less than (0.03 ± 0.01) mT, generated by the driver coils at this frequency, because the high impedance produces a much smaller current in the driver coils of 8.4 ± 0.3 mA rms. Additionally there is the factor due to the small skin depth of 1.2 mm at this frequency. The 5 kHz image for the 2 mm thick box shows strong image artefacts, i.e. anomalous image fragments that were not predicted to be in the image. These are revealed at the edge of the box, higher up in this image. This 2 mm box image was captured many times at 5 kHz, but due to its light weight it was vulnerable to being disturbed, i.e. not moved back into place properly, when removing and replacing back its lid. The images through 10 to 20 mm thick boxes at frequency ≥ 1 kHz were too fragmented and did not register the presence of the disk, as the skin depth, δ, varied between 2.69 to 1.2 mm in the considered range of frequencies. The skin depth was therefore too small compared with the box thickness thus denying penetration of the primary field.

The significant result presented in this section is that the MIT system has been able to penetrate an Aluminium enclosure of 20 mm wall thickness and that a magnetic signature of the disk can still be detected, even when the primary field has passed through 40 mm of Aluminium and a Copper disk of 40 mm diameter by 3 mm thickness. This was achieved at 10 to 200 Hz driving fields.

To quantify the penetrating power of the imaging system, reference is given to the number of skin depths that can be penetrated at a given frequency to capture an image of the object inside the enclosure. Tables 9.1 and 9.2 summarize the results for the depth of penetration at the different frequencies, as corresponding to the successful capture of an image. The penetration depth is given in terms of number n of skin depths, reported in units of the Aluminium (Al) skin depth δ [45] for each frequency. The penetration depth includes the contributions from the top and bottom sides of the Aluminium box, each of thickness, x_2, as well as from the Copper (Cu) disk enclosed of thickness x_1. The number of skin depths n penetrated at a given frequency is given by,

$$n = \frac{2x_2}{\delta} + \frac{x_1}{\delta_{Cu}} \tag{9.1}$$

where δ_{Cu} is the skin depth of Copper at the frequency of interest.

Table 9.1. Number of Skin Depths, n, Penetrated at Frequency 10 to 200 Hz.

Al box thickness	10 Hz n	40 Hz n	200 Hz n
2 mm	0.245	0.491	1.10
3 mm	0.320	0.640	1.43
5 mm	0.470	0.939	2.10
10 mm	0.844	1.69	3.77
20 mm	1.64	3.28	7.33

Table 9.2. Number of Skin Depths, n, Penetrated at Frequency 1 to 5 kHz.
(The disk could not be detected in the 5 mm thick box at 5 kHz, nor the 10 and 20 mm boxes at 1 to 5 kHz).

Al box thickness	1 kHz n	2 kHz n	5 kHz n
2 mm	2.45	3.47	5.48
3 mm	3.20	4.53	7.16
5 mm	4.70	6.64	-

A more practical technique that does not require opening the enclosure and removing its contents is the dual frequency method described in Section 8. This method relies on a low frequency signal to produce an image that penetrates the enclosure and a high frequency signal to approximate an image of the empty enclosure. While this technique works for conductive enclosures of 0.24 mm and 0.33 mm thickness, it does not appear to be valid for Aluminium boxes of > 1.6 mm thickness. This is because the high frequency image generates peaks of phase that are inconsistent with the low frequency image and therefore the extraction of the concealed disk no longer works. The disk image becomes overshadowed by the much larger anomalous peaked phases. The identification of the exact mechanisms behind such behaviour will constitute the object of a separate investigation.

9.4 Potential for Imaging through Other Materials

The previous parts of Section 9 dealt specifically with Aluminium enclosures and Copper disks. This Section now looks at three other metallic boxes and extrapolates the potential for imaging through such shields.

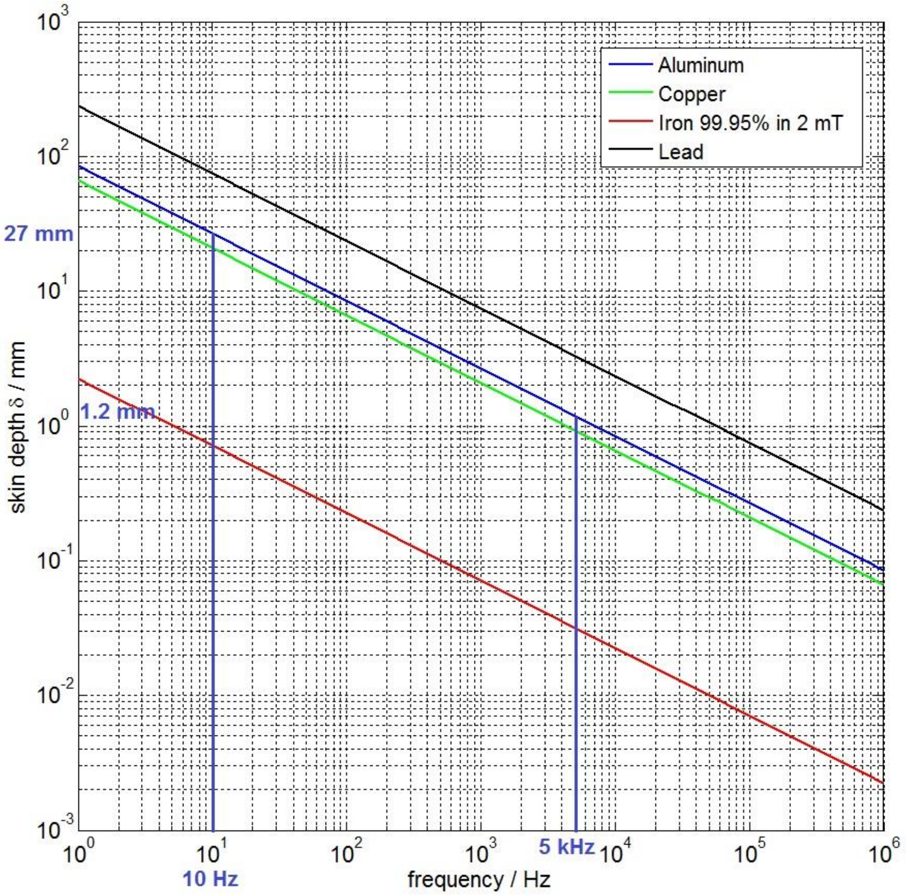

Figure 9.4. Log-log plot of skin depth versus frequency for 4 common metals: Aluminium, Copper, Iron (99.95% purity in 2 mT field) and Lead. The purity of Iron is highlighted because two different types of Iron will be compared later in this section. The purity of the other metals is not known so the standard values are given. The frequency range of the experiment is indicated in blue on the x axis along with the corresponding skin depth (δ) values in blue on the y axis [81].

Figure 9.4 displays a log-log plot of skin depth vs. frequency for 4 common metals, Aluminium, Copper, Iron (99.95% pure in 2 mT field) and Lead [81]. Indicated in the plot in blue is the range of frequencies used in the present experiment, 10 Hz to 5 kHz.

As from the plot of figure 9.4, Copper is less penetrable than Aluminium whereas greater penetrability is associated with Lead. Iron (99.95%) shows a much poorer penetration due to its larger relative permeability of $\mu_r \sim 5 \times 10^3$. A slightly less pure Iron (99.91% pure in 2 mT field) has μ_r equal to 200 and is therefore more penetrable [81].

The results presented here, as indicated in tables 9.1 and 9.2 and figures 9.2 and 9.3, have shown that 7.33 skin depths in terms of thickness of metal, were penetrated for imaging through the 20 mm Aluminium box at 200 Hz. Beyond this value there is no visible detection of the Copper disk. This result for the penetration depth of imaging and relative optimum frequency will be used to discuss the potential for imaging through other materials.

Using figure 9.4 it is possible to extrapolate the thickness of Fe, Cu and Pb enclosures through which imaging should be possible with our current set up. For a given material M of skin depth δ_M at the imaging frequency, seven skin depths (n = 7) correspond to a thickness of the enclosure equal to x_2 in (9.2),

$$x_2 = \left(n - \frac{x_1}{\delta_{Cu}}\right)\frac{\delta_M}{2} = \left(7 - \frac{x_1}{\delta_{Cu}}\right)\frac{\delta_M}{2} \qquad (9.2)$$

where x_1 is the thickness of the Copper disk and δ_{Cu} the skin depth of Copper at the imaging frequency. As discussed above 200 Hz is adopted as the reference frequency to determine the maximum thickness of the different materials through which the set up should be able to image. Proceeding as detailed above it was identified that there is potential for imaging through an enclosure of thickness 54.8 mm for Lead, 0.52 mm for Iron (99.95% pure in 2 mT field) and 15.4 mm for Copper.

9.5 Investigation of dual frequency method & imaging for Aluminium enclosures

The dual frequency method was applied to some of the thick Aluminium enclosures above (3 mm, 5 mm thickness), in order to extract the Copper disk but without success. The dual frequency technique breaks down because the high frequency image approximating the empty enclosure, in figures 9.5 (aiv - civ), produces anomalous image artefacts that can be seen in the images as peaks of phase. These artefacts are not seen in the low frequency image. They are inconsistent with the low frequency image because the disk signal is much smaller than the artefacts. Therefore the dual frequency method fails to reveal the concealed object under these circumstances, in terms of visual examination of the result. This issue will be discussed as follows.

The disk is revealed in figures 9.5 (aii - dii) when the subtraction of the empty enclosure is applied, but not for the dual frequency method in figures 9.5 (ai - ci). These artefacts appear to be a result of more thickness of material being penetrated by the driving field. This could be due to eddy currents forming on multiple layers, causing larger phases in some locations of the Aluminium due to the higher frequency, where more inhomogeneity in the material is encountered with more bulk of Aluminium. This hypothesis is supported out by figure 9.5 (di) of a 1.6 mm thick Aluminium enclosure, where the dual frequency method proved successful. The dual frequency method was tested for a range of frequencies with the 3 mm thick Aluminium enclosure, but without success. As can be seen in figures 9.5 (ai - ci) the resultant image is smeared and broad and does not give the disk's location. In figure 9.5 (ci) there is a hint of the disk's position at x = 100 mm and y = 100 mm, but this is made unclear by another artefact directly above it at x = 115 mm and y = 120 mm.

This result prompted a need to investigate the imaging system more closely to obtain a better understanding of how the images were being formed.

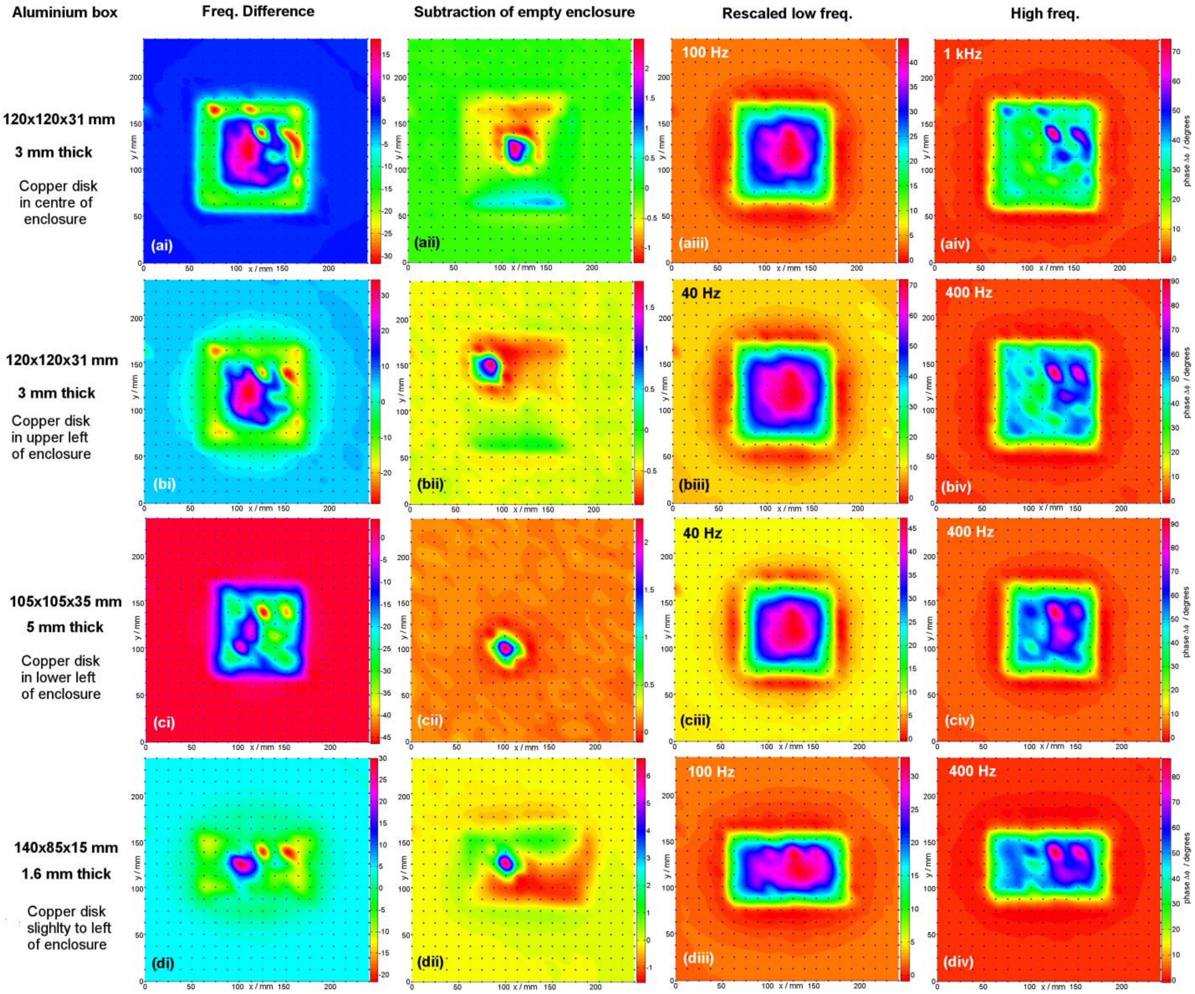

Figure 9.5. Images showing dual frequency method applied to thick Aluminium enclosures. (ai) to (di) showing the resultant image. (ai) to (ci) did not reveal the disk in the 3 mm and 5 mm thick Aluminium enclosures. In (di) the 1.6 mm thick enclosure does reveal the disk. (aii) to (dii) show the subtraction-of-empty enclosure method and reveals the disk in its different positions. (aiii) to (diii) shows the rescaled low frequency images for each enclosure. (aiv) to (div) is the high frequency image use to approximate the empty enclosure.

Firstly as a test the driving field was changed to see if lower magnitude fields could clarify and remove the artefacts, noting the normal size of driving voltage used was (27 ± 1) V, near to the largest value allowed for the AC amplifier. In figure 9.6 (ai - aiv) driving voltages of 8.31 V, 1.04 V, 0.42 V and 0.04 V gave the resultant images shown at 400 Hz driving frequency.

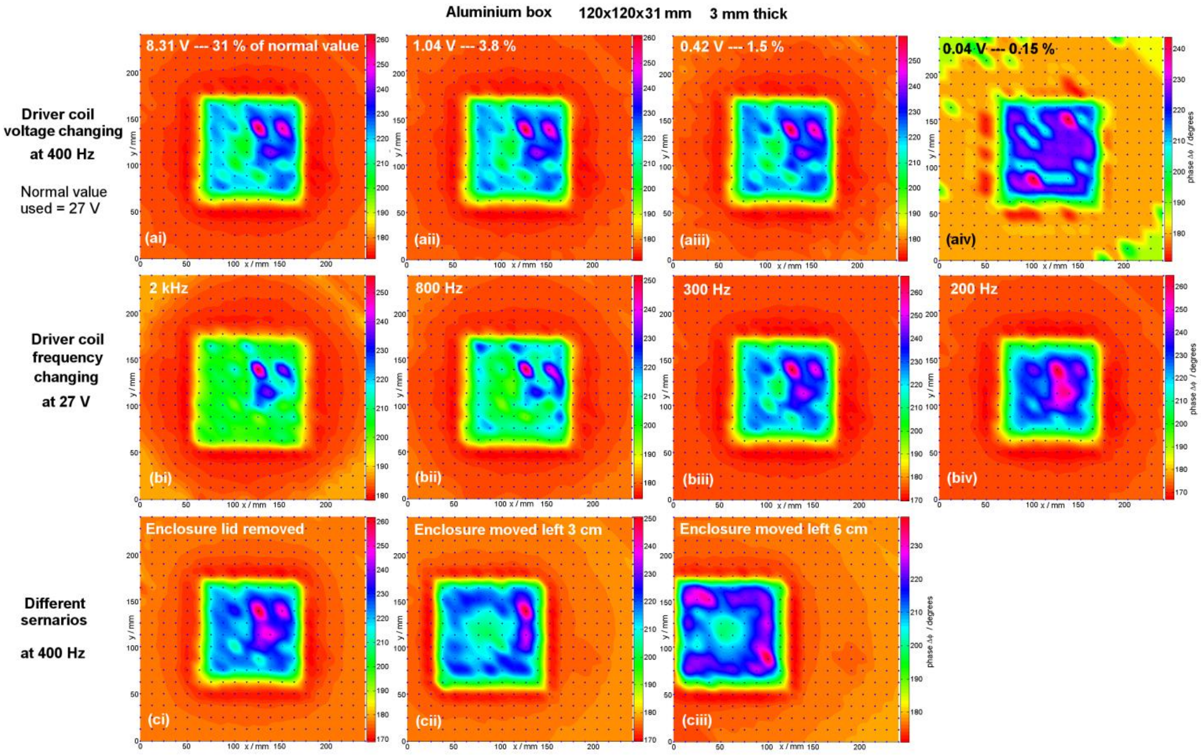

Figure 9.6. Images of an Aluminium enclosure (120 × 120 × 3) mm, showing changes in driving voltage and frequency; the lid removed and the enclosure moved into different positions. In (ai) to (aiv) images were taken of the Aluminium enclosure at reduced driving voltages, 8.31 V, 1.04 V, 0.42 V and 0.04 V rms (normally 27 V was used) and at 400 Hz. In these images the Copper disk, 30 mm Ø by 2 mm thickness, is in the lower left of the enclosure. (bi) to (biv) show the same enclosure with the disk in the centre at driving frequencies 2 kHz to 200 Hz, all with applied voltage 27 V rms across the driver. (ci) is an image with the enclosure lid off and the disk in the lower left at 400 Hz and 27 V. (cii) to (ciii) are the enclosure moved 3 cm and 6 cm to the left with the disk positioned in the centre at 400 Hz and 27 V.

As can be seen from figures 9.6 (ai - aiv), even if the driving field is reduced to 1.5 % of its normal operating value, the image remains almost unchanged. At 0.15 % the image fragments and becomes distorted, although the phases are only reduced a small amount. So it appears that reducing the field makes little difference and if it reduced by a large amount the image fragments, as not enough eddy currents can be generated. A more important factor was the changes due to frequency as this was causing the peaked phases. It can be seen from figures 9.6 (bi - biv) that at high frequencies, such as 2 kHz, the image captures more of the outer part of the enclosure due to the skin effect. However also included are artefacts, picked up by sensors in upper right of the image, where there is no specimen disk to account for it. One hypothesis for this is discussed above in this Section. The problem starts when the high frequency image is utilised to approximate the empty enclosure. At lower frequencies such as 200 Hz in figure 9.6 (biv), more depth of the enclosure is imaged due to the skin effect, and previously isolated artefacts merge with other parts of the enclosure. Figure 9.6 (ci) captures the same enclosure with the lid removed at 400 Hz and 27 V, but the image remains relatively unchanged with the three artefacts in the upper right corner and centre right clouding the disk signal, in comparison with the low frequency image (figure 9.5biii). Finally the enclosure was moved into different positions on the sensor array platform to test the effect of different sensor coils. The enclosure was moved 3 cm and 6 cm to the left from its original centre position (figures 9.6 cii to ciii). The artefacts continued to appear around the periphery of the enclosure and were more dominant in the ‘6 cm to the left’ image.

Other explanations for the artefacts may be due to:

- The Helmholtz coils’ field not being completely uniform
- Inductive coupling with sensor coils, where each sensor is not completely identical due to manufacture
- The way it has been soldered and the soldered track causing a resonance issue of an LRC circuit
- It could be that there is some influence of the sensor coil’s ferrite core on the magnetic field and on the electromagnetic coupling process that gives

variation at higher frequencies, causing inconsistency between the low and high frequency images

- Additionally it could be due to the behaviour of the field on the Aluminium at different frequencies

9.6 Conclusion

Investigation was undertaken of the limits of magnetic imaging through metallic enclosures, analysing the performance of imaging for different thickness of the enclosure. The results show that the system can image a Copper disk, even when enclosed within a 20 mm thick Aluminium box. On the basis of the reported results discussion was given of the potential for imaging through different conductive materials.

The results presented here demonstrate the penetrating power of this imaging system and are of relevance to security applications such as cargo screening.

Apart from the success of detecting the disk’s magnetic signature through a 20 mm thick Aluminium enclosure, investigation was undertaken of the dual frequency method suitable for real world applications. Peaked phase artefacts in the high frequency images render this technique invalid for the present in thick Aluminium enclosures, until a method can be found to solve this issue.

Setting up the apparatus and software to implement image reconstruction via an inverse problem may resolve the artefact problem. I.e. modelling the set up and taking the inverse of the model and inputting the coil voltages to obtain conductivity images. This may be able to account for the source of the artefacts and therefore eliminate them. Additionally sensor coils that are air cored instead of ferrite cored could be tried, because the ferrite cores contribute to the voltage detected due to their magnetic properties. Re-soldering sensor coils that appear to cause artefacts could also be undertaken or even commissioning coils that are wound near-to-identical.

10 Determining suitability of system for 3D imaging

10.1 Introduction

Utilising the same setup and method of imaging described in Sections 6 to 9, the imaging system was tested to determine its suitability for imaging in 3D. The planar geometry of the sensor coil array makes the system scalable to a full 3D imaging system, by simply adding two more driver and sensor assemblies orthogonally to the existing one. This would require, for example back projection techniques (described in Section 12), by combining cross sectional images to reconstruct them into a 3D image, or modelling via the inverse problem by a similar 3D reconstruction from 2D slice images. However this requires the ability to image objects at a finite distance from the array plane. An experiment was conducted to explore the imaging capability for various heights of sample lift-off above the array, as illustrated in the photograph of figure 10.1. This proved that the system is scalable to a full 3D imaging system.

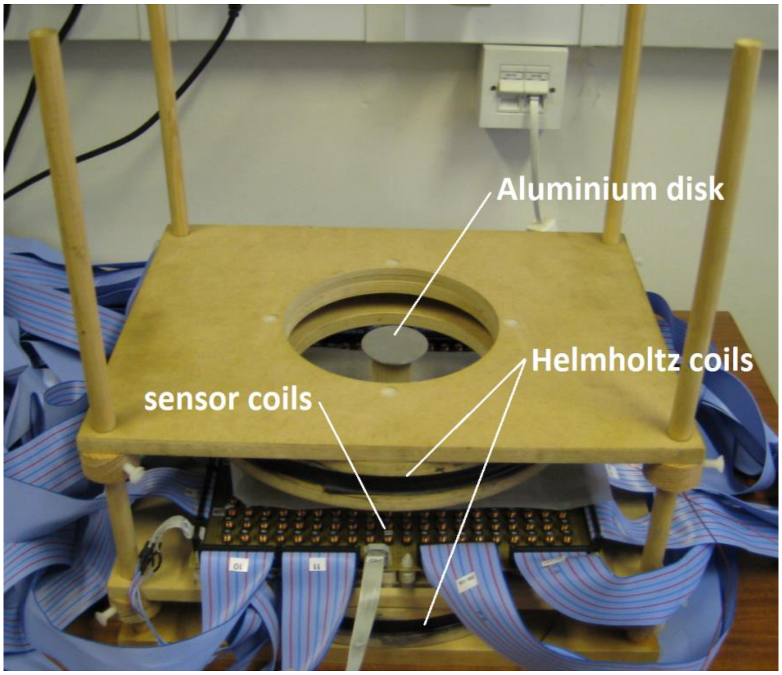

Figure 10.1. Photograph of the Helmholtz coil assembly and the 20 × 20 sensor coil array used to image metallic objects. In the centre of the photo an Aluminium disk is positioned for imaging at a lift-off height above the sensor coils.

10.2 Imaging power at finite lift-off

The planar geometry of the array makes it easily scalable to a full 3D imaging system. This can be realized by adding two more 2D imaging systems orthogonally to the existing one and then combining the images in the three different directions. However this requires the capability to image objects at a finite lift-off from the array plane. This is precisely investigated here.

The ability of imaging objects at finite lift-off, where the object was lifted above the sensing coils is qualitatively illustrated in figure 10.2 which also shows the distortion introduced by increasing lift-off.

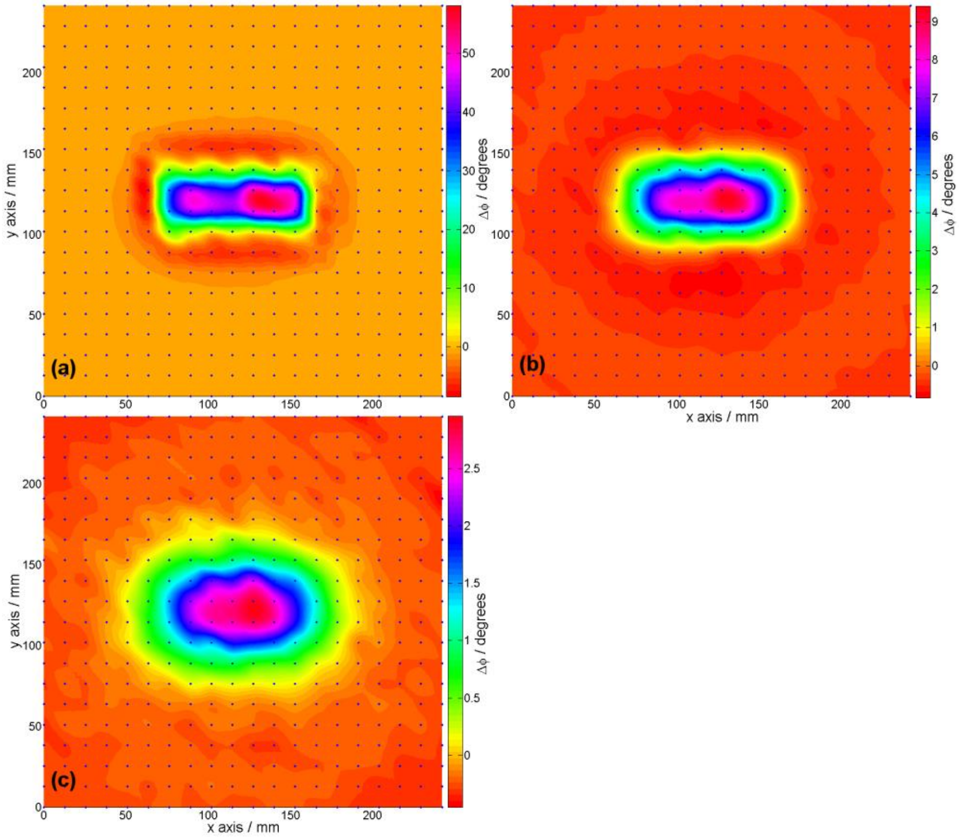

Figure 10.2. Images of a Copper rectangular cuboid: 99 mm × 45 mm × 2mm, raised up (a) 0 mm, (b) 20 mm and (c) 40 mm above planar sensor coil array.

At a more quantitative level an experiment was conducted to determine the power of the system to image objects raised above the sensor coil array, with a 500 Hz driving frequency. Five disks of Copper and five disks of Aluminium with diameters between 20 mm to 150 mm and all with thickness 2 mm were imaged. For each disk MIT images were taken with the instrument for different lift-off heights. The diameter of the imaged disks was studied as a function of the lift-off distance. The diameter was determined from the images by applying a Canny edge-detection algorithm [42][74][73] to each disk image and measuring the diameter traced out by the edge detection. The results of the measurements are presented in figure 10.3.

A batch file program was written in MATLAB to automatically generate images with Canny edge detection and measure the diameter from every pixel point along the edge. Therefore the average diameter was automatically determined around the edge of the disk, including the uncertainty in this measurement. The edge detection traced out around the disk was not a pure circle but an estimated one. The images in figures 7.2 to 7.5 shows similar edge detection to the ones described here. The batch file is shown in Appendix 14.1.2. For disks raised to a high level above the sensor array, for example the Copper disk of 50 mm diameter raised above 5 cm, it was not possible to use the batch file technique, as low phase values produced noticeable fragmentation in the image. Therefore the diameter in these images had to be measured manually using the cursor on the MATLAB plot.

First of all it was noticed that Copper and Aluminium disks of the same size gave a similar result for the edge detected diameter at lift-off heights. This is not surprising as they have both large and comparable conductivities. The results are now analysed in detail shown in figure 10.3.

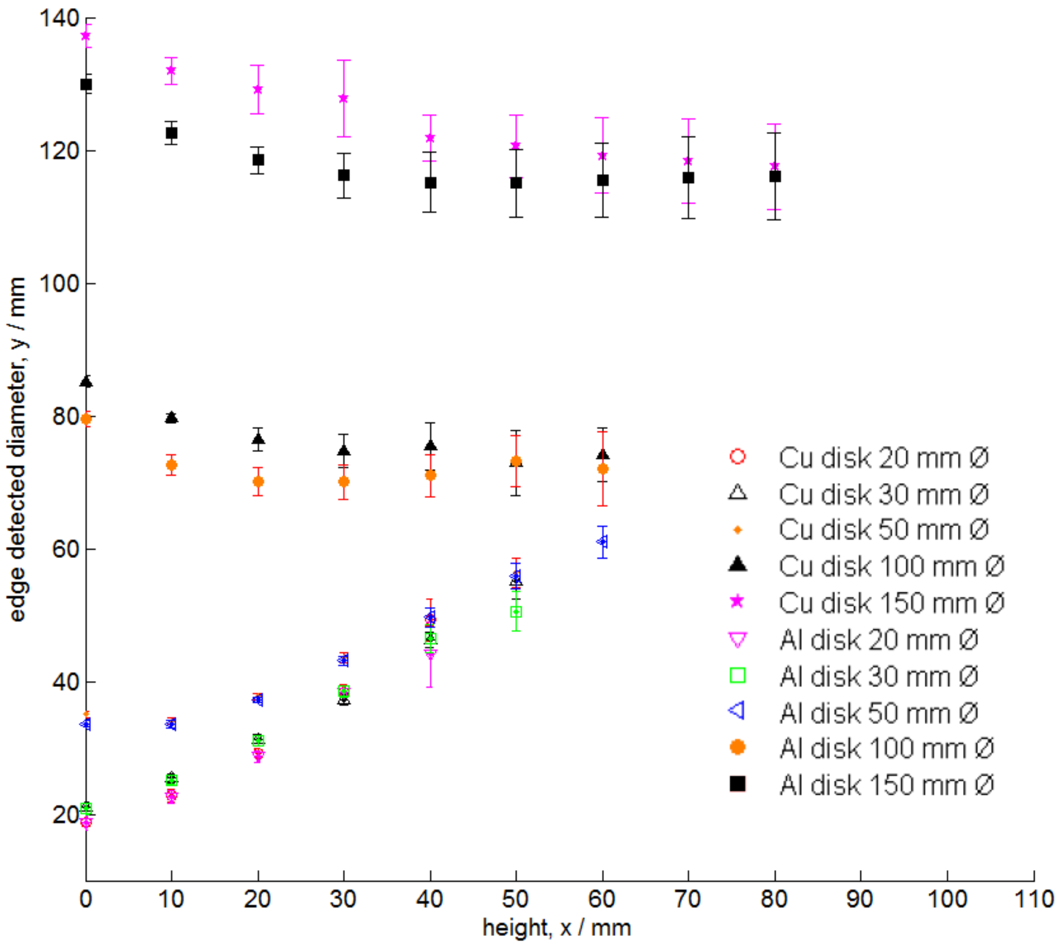

Figure 10.3. Calibration curves for Copper (Cu) and Aluminium (Al) disks of varying diameters (Ø), 20 to 150 mm, and all 2 mm thickness. The plot shows edge detected diameter against lift-off height above sensor coil array. The measurements were made with a driving magnetic field of 500 Hz, to excite eddy currents in the disk, with the resultant field picked by the sensor coils. Uncertainties in the edge detected diameters were obtained from the measurements of diameter on the images.

In the plane of the array at a height of 0 mm lift-off, i.e. level with the top of the sensor coils, the system has a horizontal resolving power of (30 ± 5) mm. This is the minimum size disk resolvable in the array plane for both Copper and Aluminium. For disk diameter larger than 50 mm the edge detected diameter is proportional to the actual diameter. Specifically it is smaller than the diameter by (18 ± 3) mm, indicating a linear relationship with a slope close to unity in the plane of the array at 0 mm lift-off-height. For vertical resolution, described in the rest of this Section, figure 10.3 also shows the changes in edge detected diameter with disk lift-off. This was up to a height of 40 mm for the 20 mm diameter disks and up to 80 mm height for the 150 mm diameter disks. The curves end after these heights when edge detection becomes too fragmented to measure a diameter from the image. The imaging system can thus detect disks up to 80 mm lift-off height for 150 mm diameter disks and up to 40 mm for the 20 mm diameter disks. The images are poorer quality at greater heights as the disk image is more fragmented. As can be seen in figure 10.3, different size disks give a different response in the size of the images generated with increasing disk lift-off. For the small Copper and Aluminium disks with diameter equal to or smaller than 50 mm, there is a progressive increase in disk image diameter with disk lift-off. This behaviour can be attributed to the system operating near or below the limit for vertical resolution of ~ 50 mm diameter. The instrument is not suitable for imaging disks of this dimension. For the larger disks with diameter equal to or larger than 100 mm diameter, the disk image reduces in size whilst being raised up to 10-20 mm disk lift-off and then levels off with low gradients. This shows that the system is capable of imaging objects at a lift-off distance of up to 80 mm, provided that the object size is larger than the resolution limit.

Some investigation was also made on how the performance of the instrument depends on the driving frequency. Figure 10.6 shows the results of comparing disk lift-off for 50 mm and 100 mm diameter Copper disks, at 4 different driving frequencies. For all the frequencies considered of the 50 mm diameter disk the image shows an increasing dependence on the actual diameter. This is in agreement with the previous statement that the system is operating near the resolution limit and thus these images do not provide reliable data. A change in the driving frequency does not significantly change this. The 100 mm disk was included in figure 10.6 with uncertainties in the measurements of the edge detected diameter shown for each frequency. Figure 10.6 plots edge detected diameter against lift-off height, for both Aluminium and Copper disks of 50 mm and 100 mm diameter, at four different frequencies 200 Hz, 500 Hz, 2 kHz and 10 kHz.

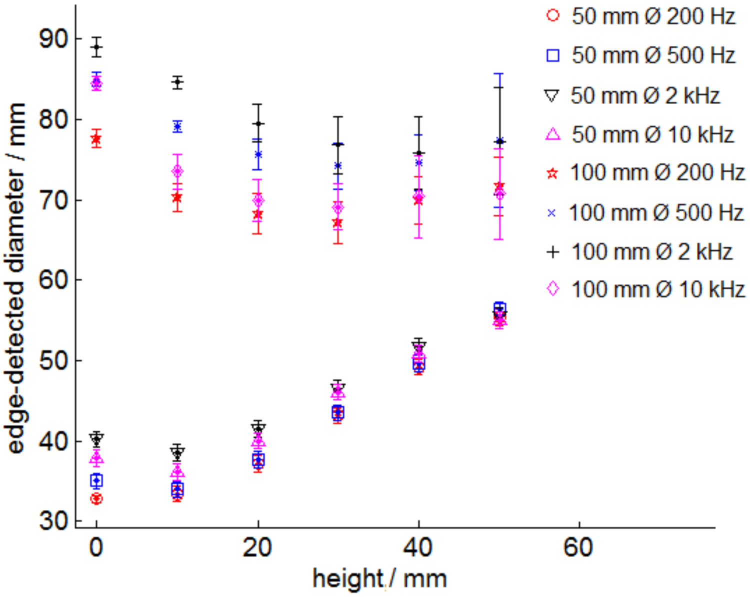

Figure 10.4. Calibration curve for two Copper (Cu) disks of diameters, 50 mm and 100 mm by 2 mm thickness. The plot shows edge detected diameter against lift-off height above the sensor coil array. The measurements were made with a driving field of 200 Hz, 500 Hz, 2 kHz and 10 kHz.

10.3 Conclusion

In this section, the suitability of the imaging system to image in 3D was determined. The automated MIT system used was based on the same modality described in Sections 4 to 9, that is a 20 × 20 planar sensor coil array and Helmholtz coils for the driving field.

The planar geometry makes the system suitable to be scaled up to a full 3D imaging system. The 3D system will comprise three imaging assemblies as the one described in this Section, oriented along three perpendicular axes. The 3D image could then be generated by combining the images produced by the three individual assemblies. This approach requires the ability to image objects at finite lift-off from the array plane. The results given in this Section, for imaging of objects at different lift-off heights, indicates a 3D imaging system to be viable.

It is interesting to compare these results with the planar MIT system by Ma et al. [82]. That set up can detect an Aluminium rod up to a depth of 30-40 mm beneath the planar array, using a 50 kHz driving frequency. The imaging system described in this Section can detect up to 80 mm depth (lift-off height) for 150 mm diameter disks and up to 40 mm depth for the 20 mm diameter disks; although these images are poorer quality. The driving frequency used was 500 Hz.

11 Summary and Conclusions

11.1 Summary

This work has undertaken the development of a new MIT system, starting from basic principles of eddy current detection to a real world technique that can image inside a metallic enclosure without removing its contents. This is to aid further research towards MIT imaging for security applications, such as airport bag scanning. MIT has the advantage over current x-ray scanners, in that it is non-invasive and so does not require radiological safety precautions for its use. It is also relatively low cost in comparison. However due to its soft-field nature MIT has a disadvantage of low resolution preventing its widespread commercialisation [83]. Some MIT applications do not require high resolution, such as pipeline inspection, but for security MIT this would need to be improved upon.

In summary this work has included the following.

Chapter 3 lays the groundwork for this study, introducing eddy current imaging from the basic principles by utilising a driver coil of 1.8 mm thick Copper wire and a ferrite cored inductor as the sensor. A Perspex rig platform was designed and constructed and the specimen to be imaged was moved manually into each position, with phase measurements taken to obtain a phase image in 2D positional space. The resolution of the system, in terms of imaging steel ball bearings, was determined at ~ 20 mm and imaging through a ferromagnetic shield was demonstrated for a mild steel bar.

In chapter 4 the concept was developed of using a planar array of the same sensors. Helmholtz coils provided a uniform driving field that was fully automated by LabVIEW, to generate the images in 1 to 3 minutes, compared with several days for the manual set up of chapter 3. Here also is a description of the instrumentation, an explanation of the principle of the lock-in amplifier and some description of the multiplexer.

In chapter 5 the Canny edge-detection algorithm is explained in detail and how it is incorporated into MATLAB code that generates the image with the detected edge. Canny edge detection was integral part of determining the resolution of the system.

In chapter 6 imaging of magnetic and non-magnetic conductive materials was examined, including the phenomena of edge effects in the MIT images. It was found that an Aluminium disk of 150 mm diameter by 2 mm thickness gives higher phase values than Copper in the main body of the disk. The opposing secondary field of Copper is larger than Aluminium giving a smaller resultant field detected. The edge effect voltage of the Copper was also larger than Aluminium, with Iron giving the smallest edge effect voltage. Iron shows a smaller secondary field and smaller phase in the main body of the disk than in the Aluminium and Copper disks. Part of this may be due to magnetization of the Iron disk, producing a positive real component of $\Delta\mathbf{B}$ in opposition to the eddy current field.

Chapter 7 describes an experiment to determine the resolution and penetrating power of the imaging system. It was shown in this chapter that the weak magnetic signature of a metallic object can still be detected and imaged even when concealed inside a double ferromagnetic enclosure of thickness 0.33 and 0.24 mm. The resolving power was found to be ~30 mm. For disks ≥ 50 mm diameter the edge detected diameter was found to be proportional to the true diameter by a linear relationship close to unity, becoming smaller than the true diameter by (18 ± 3) mm in the plane of the array. Some technical issues were discussed here and solutions given, such as some sensor coils giving anomalous phase values. Additionally the corners of the array corresponding corners of the image needed to be suppressed, in order to give a valid image, as these sensors were outside the uniform field of the Helmholtz coils. Different image plotting interpolations were also examined to determine the most appropriate one, in this case the cubic piecewise interpolation was chosen. A demonstration was given of imaging a Copper disk (90 mm diameter) at 90 degrees rotation, with no change in the peaks and troughs of the image, indicating that they were not due to inhomogeneity the sample disk.

In chapter 8 the real world dual-frequency technique is described with accompanying experiment to show that the specimen Copper disk was actually being detected in three different positions. The flexibility of this technique was investigated and it was found that rescaling of the low frequency image could have its reference point (x_{ref}, y_{ref}) varying within 38% of the enclosure's length, along its central axis and still give a valid image of the concealed specimen, i.e. the disk image could be visually identified after its extraction from the enclosure, providing (x_{ref}, y_{ref}) was not at the edge of the enclosure or at the position of the specimen disk.

In chapter 9 the penetrating power and skin effect was examined in more detail, by performing an experiment with five Aluminium enclosures varying between 2 mm and 20 mm wall thickness, with a concealed specimen disk inside. It was shown that the weak magnetic signature of a metallic disk can still be imaged even when concealed within an Aluminium enclosure of 20 mm wall thickness. The disk was extracted from the background of the enclosure by the proof-of-principle method. The dual frequency method was found to be inappropriate for these thick enclosures, due to peaks in phase in the high frequency images that was inconsistent with the rescaled low frequency image, therefore dwarfing the signal of the concealed specimen. Here the high frequency image was used to approximate the empty enclosure. Some investigation into this 'dual frequency issue' was carried out and remedies suggested, such as involving the forward and inverse problems applied to the imaging system. The objective here would be to see if computer modelling of the set up and inputting measured voltages, to obtain conductivity images, could anticipate these phase peak 'anomalies'. Additionally changing the sensor array from ferrite cored inductors to air cored ones could be tried, as well as re-soldering some of the sensor coils.

In chapter 10 an experiment was undertaken to determine the compatibility of this imaging system to be adapted to 3D imaging. This was achieved by taking a series of images of Copper and Aluminium disks, of 2 mm thickness and varying diameters between 20 and 150 mm, raised up above the sensor array and using Canny edge detection to measure the diameter via automation. It was shown that a 20 mm diameter disk could be imaged when raised 40 mm lift-off height and a 150 mm diameter disk could be imaged when raised 80 mm. Therefore this validated the system for imaging in 3D, because the specimen disks could be imaged in plane of the array at 0 cm lift-off and raised above it, up to 8 cm. For raised disks in this experiment the vertical resolving limit was estimated at ~50 mm disk diameter. 3D imaging would involve adding together 2D slices, obtained by either filtered back projection or solution to an inverse problem.

11.2 Limitations of current research

The main limitations to the current imaging system are as follows. It is unable to resolve small scale objects of dimensions less than 30 mm, although these objects are detected their images remain similar in size. The images are proportional conductivity maps of the specimen, but are not measurable as actual conductivity, which would be more valuable information of the material's characteristic. Edge effects distort images due to the electric field condensing at the boundary of the metallic sample with air, shown as phase dipping in the image below the background values at the sample's edge. Artefacts in high frequency images prevent the practical dual frequency technique from being applied to Aluminium enclosures of thickness greater than 1.6 mm. If specimen objects such as a Copper disk of 90 mm diameter is raised up and titled the resulting image is distorted and difficult to interpret, giving higher phase nearer the sensors and much smaller phase for the part that is further away.

In order to image objects in 3D it may be necessary to employ a reconstructing algorithm such as soft field back projection [84], to obtain voltage slice images and then further reconstruct them into 3D. Another approach may be to implement the inverse problem applied to this set up [14] [80] [82]. The inverse problem models the entire set up in a computer simulation, and then estimates the objects dimensions and conductivity via an iterative process, having first input the sensor coil voltages into the computer model. These techniques are beyond the scope of this study.

In this PhD study, the ground work has been laid for detection of concealed metallic objects inside metallic enclosures for security applications.

12 Future work

12.1 Filtered back projection and the inverse problem

It may be possible to set up this imaging modality to make cross sectional voltage images of metallic specimens, such as a metal box, utilising the hard field tomography method in filtered back projection, providing the Helmholtz coils' field as a uniform field can imitate hard field rays normally associated with x-ray tomography. The work of Al-Zeibak and Saunders [5] has indicated this to be the case. Hard field back projection is much simpler to replicate than the soft field case. MIT is normally considered soft field, due to the curved flux lines generated by cylindrical driver coils. If the Helmholtz coil system cannot imitate hard fields, then work would need to be carried out to develop a soft-field filtered back projection alternative. However this would require a greater theoretical input to the project currently not available. It may be more worthwhile developing an 'inverse problem' solution to the set up in order to image conductivity in 3D. However inverse problems are computationally more demanding than standard filtered back projection.

12.1.1 Filtered back projection in Hard field MIT

Computer tomography (CT) produces cross sectional images that enable imaging inside an object to analyse its structure. Back projection and filtered back projection are two types of CT algorithms that reconstruct images from experimental data. Back projection is a mathematical technique used mostly in straight ray (or hard field) computed tomography to create images from a set of multiple projection profiles.

An example of back projection in x-ray tomography is also known as CAT scanning. Figure 12.1A shows some radioactive sources to be imaged. A finite number of projections are made at 45° angles, shown by the sides of an octagon. In figure 12.1B the projections are projected back through the image, producing an approximation of the original. The projections interact constructively in the region of the emittive sources. The limitation of back projection can be seen by the artefacts in the resultant image. A high pass filter can be used to eliminate this blurring. One way this is done is to pass the back projected image through a ramp filter. This is called filtered back projection [85].

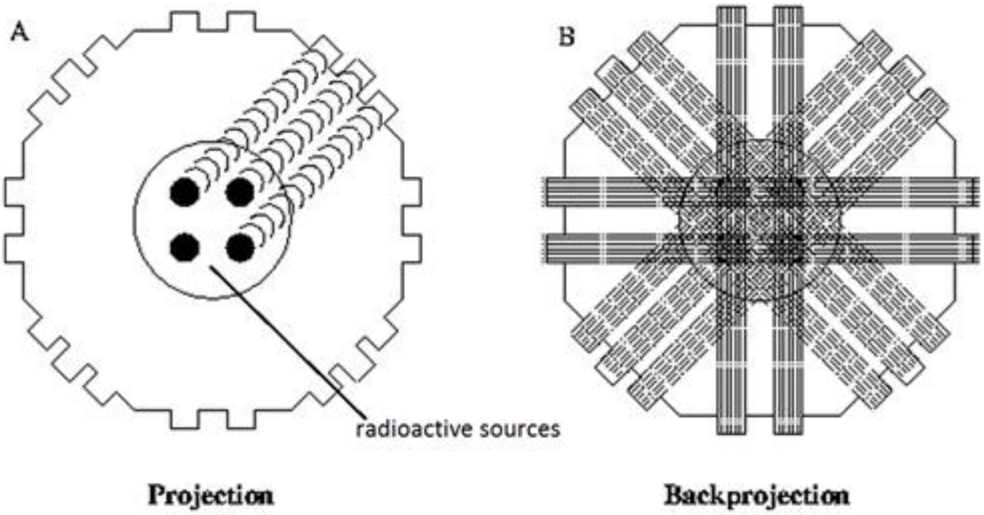

Figure 12.1. Illustration of Back-projection in x-ray tomography. Radioactive source-object is detected from four angles within 180° rotation [86]. An image is formed from µ, which is the x-ray linear attenuation coefficient [85].

In a future project cross sectional voltage images could be reconstructed of a metallic object using filtered back projection. MIT is normally considered a soft field or diffractive tomography, which is conceptually difficult to model. However using Helmholtz coils as the source field could provide straight lines of magnetic flux. The imaging system could therefore be treated as a simplified hard field or non-diffracting straight ray tomography.

A 3D Helmholtz coil assembly consists of 3 orthogonal coil pairs, providing uniform field in each plane of (x, y, z), as shown in figure 12.2a. Future work will use all three coil pairs with an inversion algorithm simulating the complete set up, to obtain conductivity images from inputted voltage measurements of the sensors. A first step towards the inversion technique will be to implement the simpler filtered back-projection method.

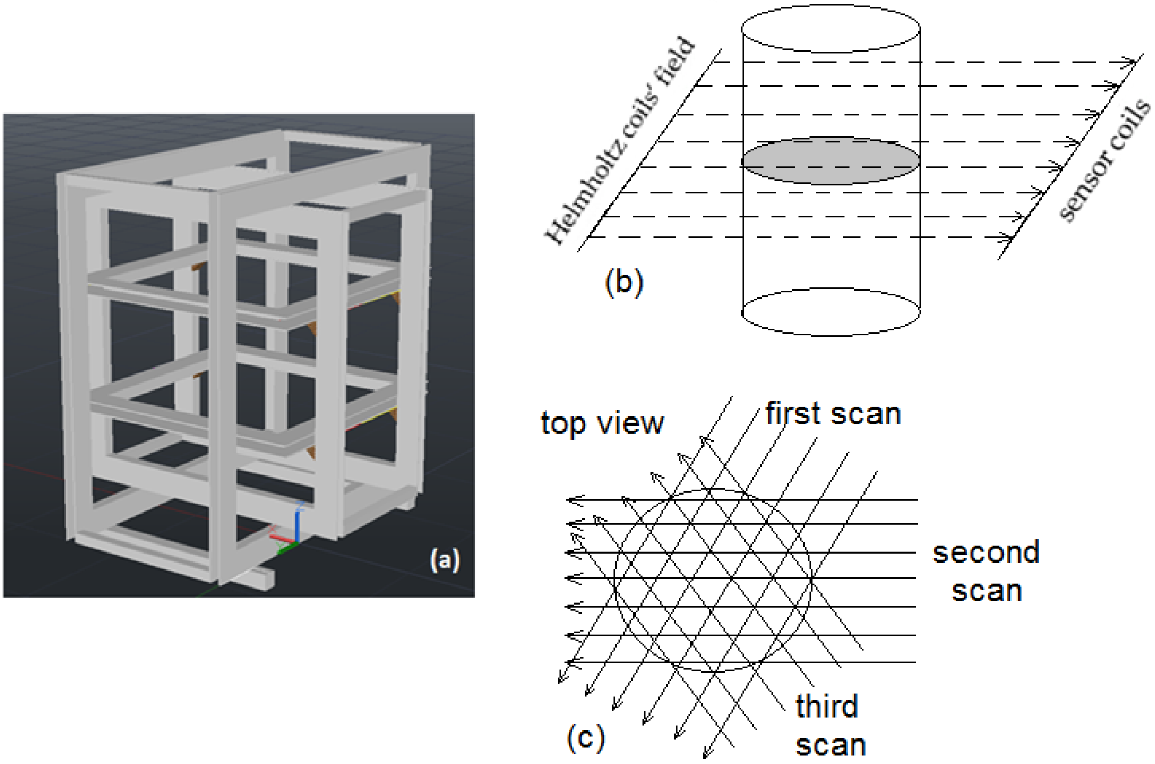

Figure 12.2. (a) Three axes square Helmholtz-coils, providing straight lines of flux in 3 orthogonal directions. (b) Diagram showing the straight line magnetic-flux from Helmholtz coils detected by a line of sensor coils. (c) Aerial view of straight line flux from 3 angles about 360°.

Three sensor coil arrays of air cored coils are placed orthogonally at the edges of each Helmholtz coil pair. Voltage measurements are taken in each plane of the source field (figure 12.2b) for 'n' rotations about 360° around the object. Figure 12.2c shows a simplification of three projections from the top view. The Helmholtz coils or the sample object are rotated for each angle. Back projection code for this operation would need to incorporate 360° rotations, as code adapted from x-ray back projection only needs 180°. This is because the rays from the x-ray method penetrate completely through the sample, whereas in MIT they do not, as they are due to eddy currents either near or far from the sensor coils.

Al-Zeibak and Saunders [5] demonstrated filtered back projection in MIT, using a straight line flux between a driver and sensor coil (figure 12.3), to imitate hard field tomography.

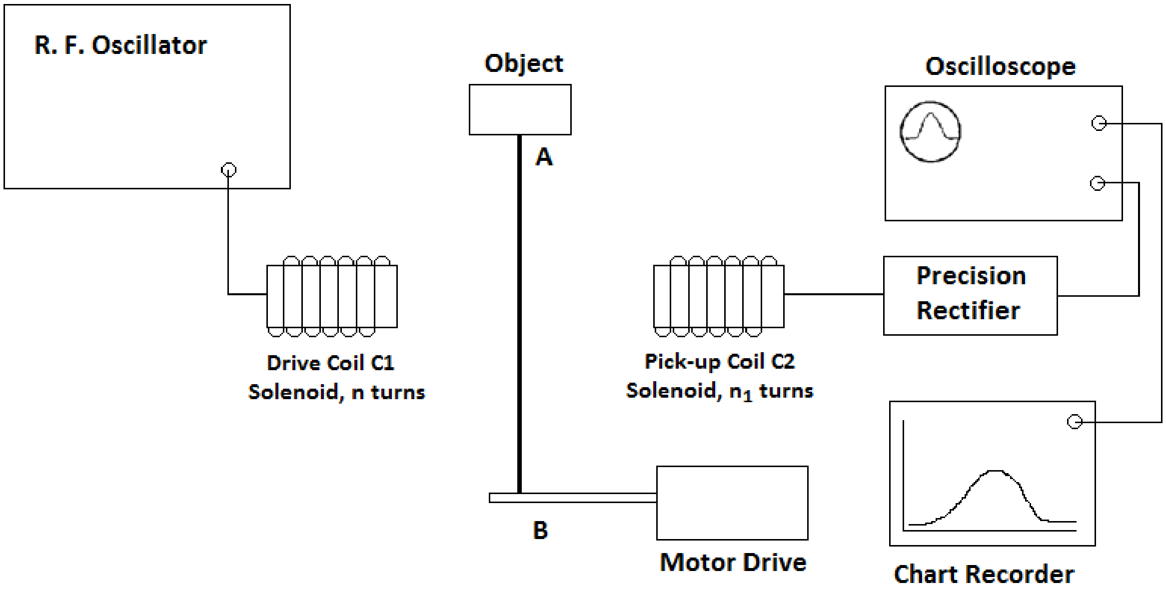

Figure 12.3. Schematic of MIT experiment to make cross sectional voltage images via filtered back projection [5].

The sample object was moved between A and B for each angle of rotation, with voltage readings taken for each position. Two images of boxes filled by saline solution are shown in figure 12.4.

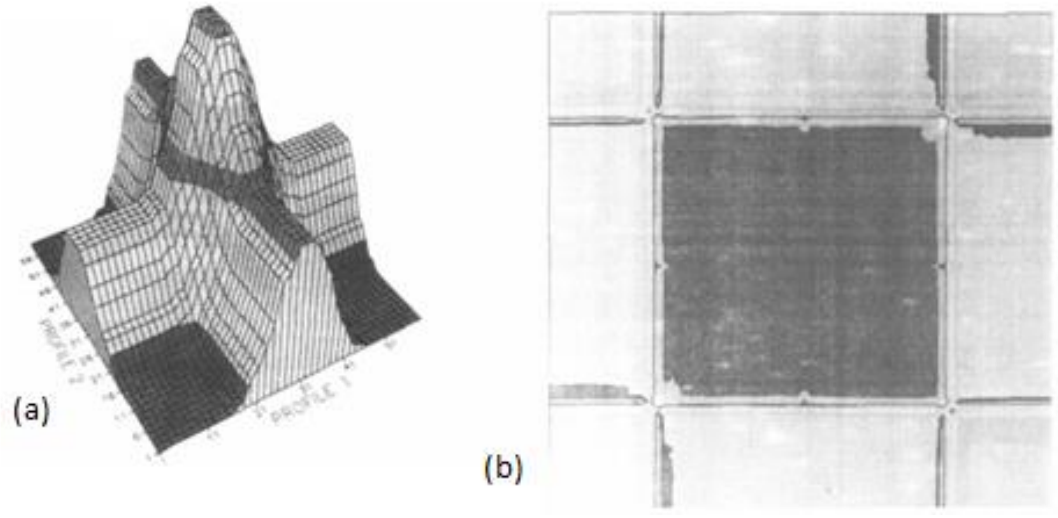

Figure 12.4. Two images of plastic boxes containing saline solution. (a) Angled view of rectangular box using back projection from 2 projections. (b) Top view of square box from 12 projections [5].

The filtered back-projection algorithm in MIT will use Fourier theory to find the voltage potentials at various points in the cross section of an object. A fundamental result connecting Fourier transforms to the cross sectional images of the object is the Fourier Slice Theorem. Parallel beam projection data is assumed due to the Helmholtz coils' uniform source field.

12.1.2 Design and assembly of three-axes Helmholtz coils

The three axes Helmholtz coils were designed using AutoCAD and Autodesk Inventor Professional design software, shown figure 12.5. The perspex formers will support 300 turns of enamelled 0.8 mm diameter Copper wire in each coil.

Figure 12.5. Photograph of three-axes Helmholtz coils made with perspex.

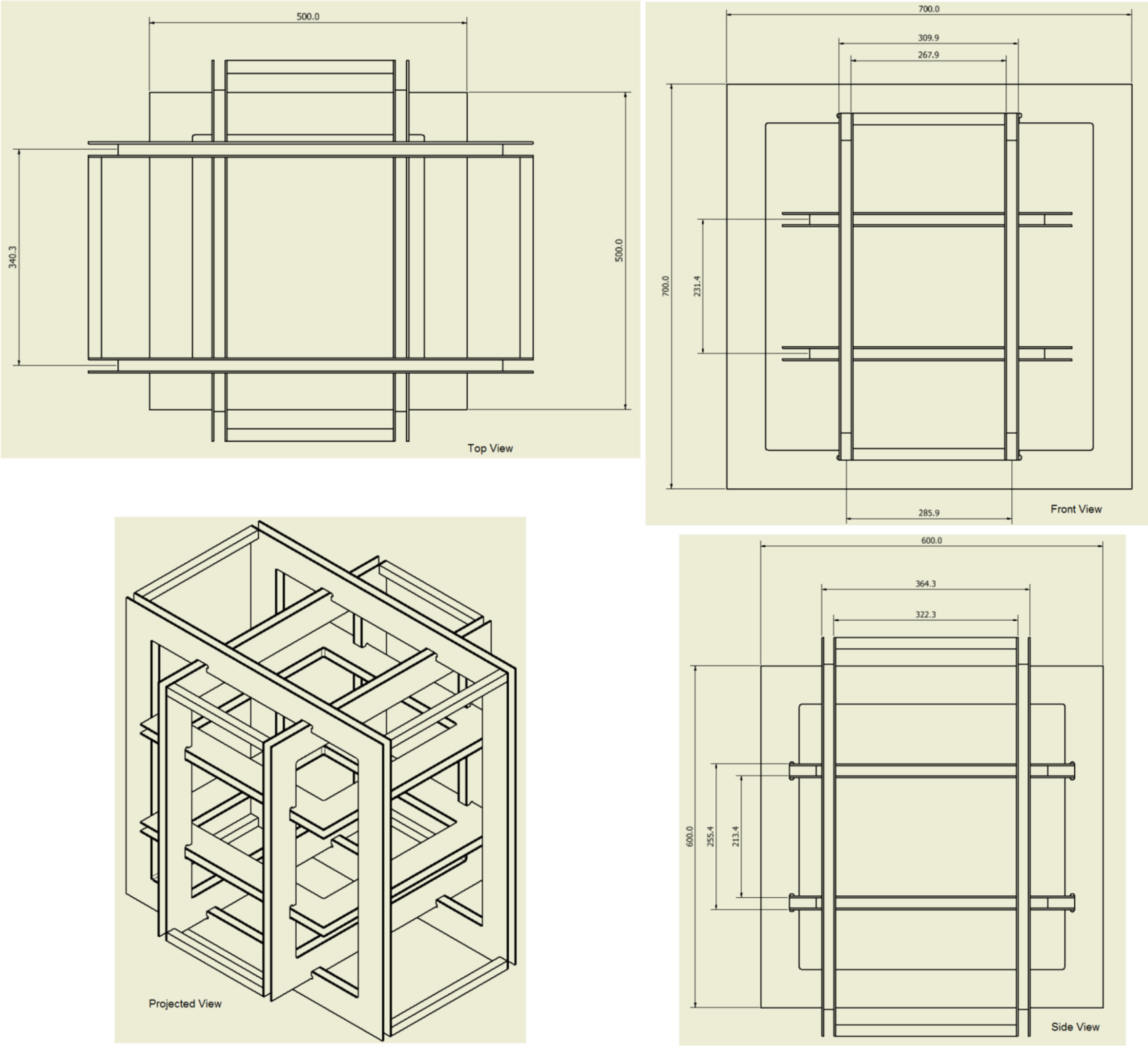

Figure 12.6 Drawing plans of three-axes Helmholtz coils, with dimensions shown in millimetres.

The formers were designed by the author and assembled by Engineering & Design Plastics Ltd. in the UK and by James Percival of the MAPS Workshop at University College London. The former wings are 3 mm thickness. Design drawings showing the dimensions of the formers are shown in figure 12.6. An array of air-cored sensor coils of inter-coil spacing 12.7 mm will be included in the next stage of this project. The array was assembled by Grand Chain Ltd. and is photographed in figure 12.7.

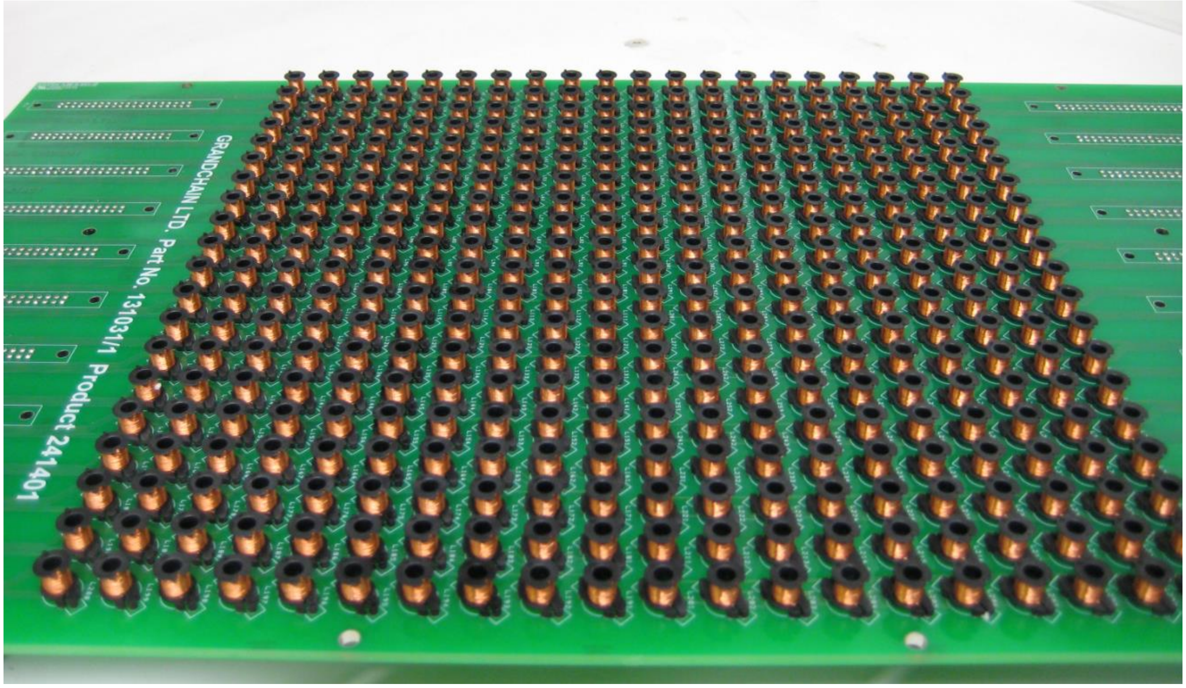

Figure 12.7. New air-cored sensor coil array with inter-coil spacing of 12.7 mm between centre points. The coils have 200 turns of 0.1 mm diameter enamelled copper wire; with series inductance between 1.9 mH and 126 μH and parallel inductance of 64.4 mH to 152 μH, for 100 Hz to 20 kHz respectively. The coils have DC resistance of 7.49 Ω.

13 References

[1] B. Darrer, P. Bartlett, J. Watson, and F. Renzoni, “Magnetic induction tomography : resolution and penetrating power through metal shields,” in *7th World Congress on Industrial Process Tomography, WCIPT7, 2-5 September 2013, Krakow, Poland*, 2013, no. September, pp. 51–60.

[2] B. J. Darrer, J. C. Watson, P. Bartlett, and F. Renzoni, “Magnetic Imaging: a New Tool for UK National Nuclear Security,” *Sci. Rep.*, vol. 5, no. 7944, pp. 1–6, 2015.

[3] B. J. Darrer, J. C. Watson, P. Bartlett, and F. Renzoni, “Toward an Automated Setup for Magnetic Induction Tomography,” in *IEEE Transactions on Magnetics*, 2015, vol. 51, no. 1.

[4] B. J. Darrer, J. C. Watson, P. A. Bartlett, and F. Renzoni, “Electromagnetic imaging through thick metallic enclosures,” *AIP Adv.*, vol. 5, no. 087143, pp. 1–8, 2015.

[5] S. Al-Zeibak and N. Saunders, “A feasibility study of in vivo electromagnetic imaging,” *Phys. Med. Biol.*, vol. 38, no. 1, pp. 151–160, 1993.

[6] A. J. Peyton, Z. Z. Yu, G. Lyon, S. Al-Zeibak, J. Ferreira, J. Velez, F. Linhares, a R. Borges, H. L. Xiong, N. H. Saunders, and M. S. Beck, “An overview of electromagnetic inductance tomography: description of three different systems,” *Meas. Sci. Technol.*, vol. 7, no. 3, pp. 261–271, Mar. 1996.

[7] A. Korjenevsky and V. Cherepenin, “Progress in realization of magnetic induction tomography,” *Ann. N. Y. Acad. Sci.*, vol. 873, pp. 346–352, 1999.

[8] H. Griffiths, W. Stewart, and W. Gough, “Magnetic induction tomography: a measuring system for biological tissues,” *Ann. N. Y. Acad. Sci.*, vol. 873, pp. 335–345, 1999.

[9] H. Griffiths, “Magnetic induction tomography,” *Meas. Sci. Technol.*, vol. 12, no. 8, pp. 1126–1131, 2001.

[10] H. Griffiths, W. Gough, S. Watson, and R. J. Williams, “Residual capacitive coupling and the measurement of permittivity in magnetic induction tomography,” *Physiol. Meas.*, vol. 28, no. 7, pp. S301–S311, Jul. 2007.

[11] M. Soleimani, “Simultaneous reconstruction of permeability and conductivity in magnetic induction tomography,” *J. Electromagn. Waves Appl.*, vol. 23, pp. 785–798, 2009.

[12] M. Zolgharni, H. Griffiths, and P. D. Ledger, “Frequency-difference MIT imaging of cerebral haemorrhage with a hemispherical coil array: numerical modelling,” *Physiol. Meas.*, vol. 31, no. 8, pp. S111–25, Aug. 2010.

[13] H.-Y. Wei and M. Soleimani, “A Magnetic Induction Tomography System for Prospective Industrial Processing Applications,” *Chinese J. Chem. Eng.*, vol. 20, no. 2, pp. 406–410, Apr. 2012.

[14] H.-Y. Wei, L. Ma, and M. Soleimani, “Volumetric magnetic induction tomography,” *Meas. Sci. Technol.*, vol. 23, pp. 1–9, May 2012.

[15] A. J. Peyton, M. S. Beck, A. R. Borges, J. E. de Oliveira, G. M. . Lyon, Z. Z. . Yu, M. W. . Brown, and J. . Ferrerra, “Development of electromagnetic tomography (EMT) for industrial applications. Part 1: Sensor design and instrumentation,” in *Proceedings of the 1st world congress on industrial process tomography*, 1999, p.

308.

[16] M. Soleimani, W. R. B. Lionheart, A. J. Peyton, and X. Ma, “Image Reconstruction in 3D Magnetic Induction Tomography Using a FEM Forward Model,” in *3rd World Congress on Industrial Process Tomography, Banff, Canada*, 2003, pp. 252–255.

[17] E. Somersalo, “Introduction to Inverse Problems I.” Copenhagen, 2014.

[18] W. R. B. Lionheart, “EIT reconstruction algorithms: pitfalls, challenges and recent developments.,” *Physiol. Meas.*, vol. 25, no. 1, pp. 125–126, 2004.

[19] G. J. Saulnier, R. S. Blue, J. C. Newell, D. Isaacson, and P. M. Edic, “Electrical impedance tomography,” *Signal Process. Mag. IEEE*, vol. 18, no. 6, p. 31, 2001.

[20] M. Zolgharni, “Magnetic Induction Tomography for Imaging Cerebral Stroke,” Swansea University, 2010.

[21] T. K. Bera and J. Nagaraju, “A LabVIEW Based Electrical Impedance Tomography (EIT) System for Radiation Free Medical Imaging,” in *National Instruments Graphical System Design Achievement Awards 2011 (NI GSDAA 2011), National Instruments Inc.*, 2011, pp. 1–6.

[22] W. Daily, A. Ramirez, A. Binley, and D. LeBrecque, “Electrical resistance tomography,” *Lead. Edge*, vol. 23, no. 5, pp. 438–442, 2004.

[23] F. Dickin and M. Wang, “Electrical resistance tomography for process applications,” *Meas. Sci. Technol.*, vol. 7, no. 3, pp. 247–251, 1999.

[24] E. Al Hosani, M. Zhang, and M. Soleimani, “A limited region electrical capacitance tomography for detection of deposits in pipelines,” *IEEE Sens. J.*, vol. 15, no. 11, p. 6091, 2015.

[25] H. Yan, L. J. Liu, and D. Z. Qiang, “An Iterative Electrical Capacitance Tomography Image Reconstruction Algorithm,” *2009 Second Int. Symp. Comput. Intell. Des.*, vol. 1, no. 2, pp. 9–12, 2009.

[26] Q. Marashdeh, L.-S. Fan, B. Du, and W. Warsito, “Electrical Capacitance Tomography − A Perspective,” *Ind. Eng. Chem. Res.*, vol. 47, no. 10, pp. 3708–3719, 2008.

[27] M. M. Rezos, J. J. Schultz, R. a. Murdock, and S. a. Smith, “Controlled research utilizing a basic all-metal detector in the search for buried firearms and miscellaneous weapons,” *Forensic Sci. Int.*, vol. 195, no. 1–3, pp. 121–127, 2010.

[28] ETI Project 549, “Induction Balance Metal Detector,” *Electronics Today International*, pp. 1–6, 1977.

[29] F. Ross, “Metal Detector Buyer’s Guide,” *Cabela’s Official Website*. [Online]. Available: http://www.cabelas.com/product/Metal-Detector-Buyers-Guide/531663.uts.

[30] C. Bruschini, “A Multidisciplinary Analysis of Frequency Domain Metal Detectors for Humanitarian Demining The Current Situation in Humanitarian Demining,” Free University of Brussels, 2002.

[31] D. E. Hughes, “Induction-balance and Experimental Researches therewith,” *Proceedings of the Royal Society of London*, vol. 29. pp. 56–65, 1879.

[32] T. Campbell, A. Fenwick, S. K. Sandberg, R. De Janeiro, C. Campbell, K. E. Umbach, and E. a Nichols, “Electromagnetic Sounding for Hydrocarbons,” *Oilf. Rev.*, vol. 21, no. Spring, pp. 4–19, 2009.

[33] R. Guilizzoni, J. C. Watson, P. Bartlett, and F. Renzoni, “Imaging by electromagnetic induction with resonant circuits,” in *Proc. of SPIE*, 2015, vol. 9481, no. 94810Q, pp. 1 – 12.

[34] L. Marmugi, S. Hussain, C. Deans, and F. Renzoni, “Magnetic induction imaging with optical atomic magnetometers: towards applications to screening and surveillance,” *Proc. SPIE*, vol. 9652, no. October, pp. 1–11, 2015.

[35] I. M. Savukov, S. J. Seltzer, and M. V. Romalis, “Detection of NMR signals with a radio-frequency atomic magnetometer,” *J. Magn. Reson.*, vol. 185, no. 2, pp. 214–220, 2007.

[36] R. C. McMaster, *Nondestructive testing handbook*. New York: The Ronald Press Comapny, 1959.

[37] P. J. Shull, *Nondestructive evaluation: theory, techniques, and applications*. New York: Marcel Dekker, 2002.

[38] G. R. Quinn, “Handbook of nondestructive evaluation,” C. J. Hellier, Ed. New York: McGraw-Hill, 2003.

[39] P. B. Nagy, *Ultrasonic and Electromagnetic NDE for Structure and Material Characterization: Engineering and Biomedical Applications*. Boca Raton: CRC Press Talyor & Francis group, 2012.

[40] L. F. S. G. Rosado, “Non-Destructive Testing Based on Eddy Currents,” Technical University of Lisbon, 2009.

[41] H. Scharfetter, R. Casañas, and J. Rosell, “Biological tissue characterization by magnetic induction spectroscopy (MIS): requirements and limitations.,” *IEEE Trans. Biomed. Eng.*, vol. 50, no. 7, pp. 870–880, 2003.

[42] J. Canny, “A Computational Approach to Edge Detection,” *IEEE Trans. Pattern Anal. Mach. Intell.*, vol. PAMI-8, no. 6, pp. 679–698, Nov. 1986.

[43] W. R. Smythe, *Static and Dynamic Electricity*, 3rd ed. United States of America: Taylor & Francis, 1989.

[44] W. J. Duffin, *Electricity and Magnetism*, 3rd ed. London: McGraw-Hill, 1980.

[45] H. A. Wheeler, “Formulas for the Skin Effect,” *Proc. IRE*, vol. 30, no. 9, p. 415, 1942.

[46] P. Lorrain and D. Corson, *Electromagnetic fields and waves*. San Francisco: W. H. Freeman and Company, 1970.

[47] R. C. Phillips and E. B. Turner, “Construction and Calibration Techniques of High Frequency Magnetic Probes,” *Rev. Sci. Instrum.*, vol. 36, no. 12, p. 1822, 1965.

[48] E. L. Bronaugh, “Helmholtz coils for calibration of probes and sensors: limits of magnetic field accuracy and uniformity,” *Proc. Int. Symp. Electromagn. Compat.*, p. 73, 1995.

[49] J. McFerran, “An electromagnetic method for cancer detection,” The Ohio State University, 2010.

[50] R. H. Good, *Classical Electromagnetism*. Orlando: Saunders College Publishing, 1999.

[51] H. Schafetter, “correspondence with author.” 2015.

[52] M. Zhang, L. Ma, and M. Soleimani, “Magnetic induction tomography guided

electrical capacitance tomography imaging with grounded conductors," *Measurement*, vol. 53, pp. 171–181, 2014.

[53] S. Chikazumi, *Physics of Magnetism*. United States of America: John Wiley & Sons, Inc., 1964.

[54] M. Polichetti, M. G. Adesso, D. Zola, A. Vecchione, M. Gombos, R. Ciancio, R. Fittipaldi, M. R. Cimberle, and S. Pace, "Magnetic history dependence of the AC susceptibility of GdSr 2RuCu2Qz," *Phys. Status Solidi Curr. Top. Solid State Phys.*, vol. 3, no. 9, p. 3064, 2006.

[55] Multicomp, "MCSCH895-681KU," 2011. [Online]. Available: http://uk.farnell.com/multicomp/mcsch895-681ku/inductor-680-h-10-radial-leaded/dp/1864389.

[56] D. Jiles, *Introdution to magnetism and magnetic materials*, 2nd ed. Boca Raton: Taylor & Francis/CRC, 1998.

[57] M. K. Kazimierczuk, G. Sancineto, G. Grandi, U. Reggiani, and A. Massarini, "High frequency small sigal model of ferrite core inductors," *IEEE Transactions on Magnetics*, vol. 35, no. 5. pp. 4185–4191, 1999.

[58] J. Rivas, C. Pereira, and E. Martín, "Simple Approximation for Magnetization Curves and Hysteresis Loops," *IEEE Trans. Magn.*, vol. 17, no. 4, pp. 1498–1502, 1981.

[59] Y. Saotome, Hideo; Sakaki, "Iron loss analysis of Mn-Zn ferrite cores," *IEEE Trans. Magn.*, vol. 33, no. 1, p. 728, 1997.

[60] Y. Chung, J. Galayda, and A. P. Source, "Effect of Eddy Current in the Laminations on the Magnet Field," no. 200. 1992.

[61] A. Korjenevsky, V. Cherepenin, and S. Sapetsky, "Magnetic induction tomography: experimental realization.," *Physiol. Meas.*, vol. 21, no. 1, pp. 89–94, 2000.

[62] J. Gyselinck, L. Vandevelde, J. Melkebeek, P. Dular, F. Henrotte, and W. Legros, "Calculation of eddy currents and associated losses in electrical steel laminations," *IEEE Trans. Magn.*, vol. 35, no. 3, p. 1192, 1999.

[63] S. R. Trout, "Use of Helmholtz coils for magnetic measurements.," *IEEE Trans. Magn.*, vol. 24, no. 4, p. 2109, 1988.

[64] Signal Recovery, "Model 7230 DSP Lock-in Amplifier, Instruction Manual." Ametek advanced measurement technology, Inc., 2011.

[65] M. L. Meade, *Lock-in amplifiers: principles and applications*. London: Peter Peregrins Ltd., 1983.

[66] O. Haderka, V. Michálek, V. Urbásek, and M. Jezek, "Fast time-domain balanced homodyne detection of light.," *Appl. Opt.*, vol. 48, no. 15, p. 2884, 2009.

[67] K. L. Kaiser, *Electromagnetic compatibility handbook*. Florida: CRC Press, 2005.

[68] P. K. Dixon and L. Wu, "Broadband digital lock-in amplifier techniques," *Rev. Sci. Instrum.*, vol. 60, no. 10, pp. 3329–3330, 1989.

[69] J. H. Scofield, "Frequency-domain description of a lock-in amplifier," *Am. J. Phys.*, vol. 62, no. 2, pp. 130–131, 1994.

[70] "griddata - Interpolate scattered data," *The MathWorks, Inc.*, 2016. [Online]. Available: http://www.mathworks.com/help/matlab/ref/griddata.html. [Accessed: 12-Apr-2016].

[71] J. R. Parker, *Algorithms for image processing and computer vision*. United States of America: John Wiley & Sons, Inc., 1997.

[72] R. C. Gonzalez and R. E. Woods, *Digital image processing*, 3rd ed. Upper Saddle River: Pearson Prentice Hall, 2008.

[73] R. Deriche, “Using Canny’s criteria to derive a recursively implemented optimal edge detector,” *Int. J. Comput. Vis.*, vol. 1, no. 2, p. 179, 1987.

[74] J. Canny, “Finding edges and lines in images,” Massachusetts Institute of Technology, 1983.

[75] 09gr820, “Canny Edge Detection.” pp. 1–7, 2009.

[76] E. E. Cureton, “Unbiased Estimation of the Standard Deviation,” *Am. Stat.*, vol. 22, no. 1, p. 22, 1968.

[77] S. J. Chapman, D. P. Hewett, and L. N. Trefethen, “Mathematics of the faraday cage,” *SIAM Rev.*, vol. 57, no. 3, p. 398, 2015.

[78] H. D. Young and R. A. Freedman, *University Physics*, 10th ed. San Francisco: Addison Wesly Longman, Inc., 2000.

[79] X. Ma, A. J. Peyton, M. Soleimani, and W. R. B. Lionheart, “Imaging internal structure with electromagnetic induction tomography,” in *Conference Record - IEEE Instrumentation and Measurement Technology Conference*, 2006, no. April, p. 300.

[80] L. Ma, “Magnetic Induction Tomography for Non-destructive Evaluation and Process Tomography,” University of Bath, 2014.

[81] “CRC handbook of chemistry and physics: A ready-reference book of chemical and physical data.” CRC Press, p. E–85 – E–125, 1981.

[82] L. Ma, H.-Y. Wei, and M. Soleimani, “Planar magnetic induction tomography for 3D near subsurface imaging,” *Prog. Electromagn. Res.*, vol. 138, pp. 65–82, 2013.

[83] L. Ma, A. Hunt, and M. Soleimani, “Experimental evaluation of conductive flow imaging using magnetic induction tomography,” *Int. J. Multiph. Flow*, vol. 72, pp. 198–209, 2015.

[84] A. C. Kak and M. Slaney, “Tomographic Imaging with Diffracting Sources,” in *Principles of Computerized Tomographic Imaging*, Society of Industrial and Applied Mathematics, 2001, pp. 203–273.

[85] R. A. Brooks and G. Di Chiro, “Principles of computer assisted tomography (CAT) in radiographic and radioisotopic imaging.,” *Phys. Med. Biol.*, vol. 21, no. 5, pp. 689–732, 1976.

[86] B. Amini, M. Björklund, R. Dror, and A. Nygren, “Tomographic Reconstruction of SPECT Data,” 1997. [Online]. Available: http://www.owlnet.rice.edu/~elec539/Projects97/cult/report.html.

14 Appendices

14.1 MATLAB code

14.1.1 Overlaying Copper disk edge onto MIT Image

```
% 2D MIT surface plots of p.d. phase-difference against x-y coordinates.
% For overlaying edge of copper disk onto 2D MIT surface plot.
% Written by Brendan Darrer
% Date 5th October 2013.
% oscillator = 2.6 V at f = 500 Hz, lock-in amplifier: sensitivity = 50 mV, time constant =
500 ms.

% Load .txt file arrays of, 2D positional data, background image phase and sample
% object phase (e.g. Copper(Cu) Disks).
B = load('C:\work\PhD_in_MIT\LabVIEW\labviewData\positionsData2_20x20_3.txt'); % position
data: 2 x 400 array
C = load('C:\work\PhD_in_MIT\LabVIEW\labviewData\helm2Coils124.txt') % background: 40 x 40
array
D = load('C:\work\PhD_in_MIT\LabVIEW\labviewData\helm2Coils119.txt'); % Cu disk: 40 x 40
array

% Correcting phase offset, before sensor error correction.
for i=1:10   % columns
    for j=1:40 % rows
        if (D(j,i) < 0) % correct offset, if e.g. phase = -179 when it should be 181.
            D(j,i) = 360 + D(j,i);
        end
        if (C(j,i) < 0) % correct offset, if e.g. phase = -179 when it should be 181.
            C(j,i) = 360 + C(j,i);
        end
    end
end

% Correcting error sensors in SAMPLE OBJECT image, by taking average of 4
% adjacent sensor coils, in the cross shape. Array size(D)=[40,10].
D(14,4) = ( D(13,4) + D(14,3) + D(15,4) + D(14,5) ) /4;
%D(15,6) = ( D(14,6) + D(15,5) + D(16,6) + D(15,7) ) /4;
% D(15,6) => Soldering of inductor/sensor corrected error, by Rafid Jwad.
D(38,1) = ( D(37,1) + D(18,10) + D(39,1) + D(38,2) ) /4;
D(33,6) = ( D(32,6) + D(33,5) + D(34,6) + D(33,7) ) /4;
D(29,4) = ( D(28,4) + D(29,3) + D(30,4) + D(29,5) ) /4;
D(29,9) = ( D(28,9) + D(29,8) + D(30,9) + D(29,10) ) /4;

% Correcting 4 corners outside Helmholtz coil field, by taking average of 5
% sensors (or phases) of the diagonal/ hypotenuse starting 5 sensors in x
% and ending 5 sensors in the y axis. Applying this value to the remaining
% sensors in the triangular area of the corner. Repeat this for each
% corner.
D(1,1) = ( D(1,5) + D(2,4) + D(3,3) + D(4,2) + D(5,1) ) / 5;  % top LH corner 1
D(1,2) = ( D(1,5) + D(2,4) + D(3,3) + D(4,2) + D(5,1) ) / 5;  % top LH corner 2
D(1,3) = ( D(1,5) + D(2,4) + D(3,3) + D(4,2) + D(5,1) ) / 5;  % top LH corner 3
D(1,4) = ( D(1,5) + D(2,4) + D(3,3) + D(4,2) + D(5,1) ) / 5;  % top LH corner 4
D(2,1) = ( D(1,5) + D(2,4) + D(3,3) + D(4,2) + D(5,1) ) / 5;  % top LH corner 5
D(2,2) = ( D(1,5) + D(2,4) + D(3,3) + D(4,2) + D(5,1) ) / 5;  % top LH corner 6
D(2,3) = ( D(1,5) + D(2,4) + D(3,3) + D(4,2) + D(5,1) ) / 5;  % top LH corner 7
D(3,1) = ( D(1,5) + D(2,4) + D(3,3) + D(4,2) + D(5,1) ) / 5;  % top LH corner 8
D(3,2) = ( D(1,5) + D(2,4) + D(3,3) + D(4,2) + D(5,1) ) / 5;  % top LH corner 9
D(4,1) = ( D(1,5) + D(2,4) + D(3,3) + D(4,2) + D(5,1) ) / 5;  % top LH corner 10

D(21,10) = ( D(21,6) + D(22,7) + D(23,8) + D(24,2) + D(25,1) ) / 5;  % top RH corner 1
D(21,9) = ( D(21,6) + D(22,7) + D(23,8) + D(24,2) + D(25,1) ) / 5;  % top RH corner 2
```

```
D(21,8) = ( D(21,6) + D(22,7) + D(23,8) + D(24,2) + D(25,1) ) / 5;  % top RH corner 3
D(21,7) = ( D(21,6) + D(22,7) + D(23,8) + D(24,2) + D(25,1) ) / 5;  % top RH corner 4
D(22,10) = ( D(21,6) + D(22,7) + D(23,8) + D(24,2) + D(25,1) ) / 5;  % top RH corner 5
D(22,9) = ( D(21,6) + D(22,7) + D(23,8) + D(24,2) + D(25,1) ) / 5;  % top RH corner 6
D(22,8) = ( D(21,6) + D(22,7) + D(23,8) + D(24,2) + D(25,1) ) / 5;  % top RH corner 7
D(23,10) = ( D(21,6) + D(22,7) + D(23,8) + D(24,2) + D(25,1) ) / 5;  % top RH corner 8
D(23,9) = ( D(21,6) + D(22,7) + D(23,8) + D(24,2) + D(25,1) ) / 5;  % top RH corner 9
D(24,10) = ( D(21,6) + D(22,7) + D(23,8) + D(24,2) + D(25,1) ) / 5;  % top RH corner 10

D(20,1) = ( D(16,1) + D(17,2) + D(18,3) + D(19,4) + D(20,5) ) / 5; % bottom LH corner 1
D(20,2) = ( D(16,1) + D(17,2) + D(18,3) + D(19,4) + D(20,5) ) / 5; % bottom LH corner 2
D(20,3) = ( D(16,1) + D(17,2) + D(18,3) + D(19,4) + D(20,5) ) / 5; % bottom LH corner 3
D(20,4) = ( D(16,1) + D(17,2) + D(18,3) + D(19,4) + D(20,5) ) / 5; % bottom LH corner 4
D(19,1) = ( D(16,1) + D(17,2) + D(18,3) + D(19,4) + D(20,5) ) / 5; % bottom LH corner 5
D(19,2) = ( D(16,1) + D(17,2) + D(18,3) + D(19,4) + D(20,5) ) / 5; % bottom LH corner 6
D(19,3) = ( D(16,1) + D(17,2) + D(18,3) + D(19,4) + D(20,5) ) / 5; % bottom LH corner 7
D(18,1) = ( D(16,1) + D(17,2) + D(18,3) + D(19,4) + D(20,5) ) / 5; % bottom LH corner 8
D(18,2) = ( D(16,1) + D(17,2) + D(18,3) + D(19,4) + D(20,5) ) / 5; % bottom LH corner 9
D(17,1) = ( D(16,1) + D(17,2) + D(18,3) + D(19,4) + D(20,5) ) / 5; % bottom LH corner 10

D(40,10) = ( D(36,10) + D(37,9) + D(38,8) + D(39,7) + D(40,6) ) / 5;  % bottom RH corner 1
D(40,9) = ( D(36,10) + D(37,9) + D(38,8) + D(39,7) + D(40,6) ) / 5;  % bottom RH corner 2
D(40,8) = ( D(36,10) + D(37,9) + D(38,8) + D(39,7) + D(40,6) ) / 5;  % bottom RH corner 3
D(40,7) = ( D(36,10) + D(37,9) + D(38,8) + D(39,7) + D(40,6) ) / 5;  % bottom RH corner 4
D(39,10) = ( D(36,10) + D(37,9) + D(38,8) + D(39,7) + D(40,6) ) / 5;  % bottom RH corner 5
D(39,9) = ( D(36,10) + D(37,9) + D(38,8) + D(39,7) + D(40,6) ) / 5;  % bottom RH corner 6
D(39,8) = ( D(36,10) + D(37,9) + D(38,8) + D(39,7) + D(40,6) ) / 5;  % bottom RH corner 7
D(38,10) = ( D(36,10) + D(37,9) + D(38,8) + D(39,7) + D(40,6) ) / 5;  % bottom RH corner 8
D(38,9) = ( D(36,10) + D(37,9) + D(38,8) + D(39,7) + D(40,6) ) / 5;  % bottom RH corner 9
D(37,10) = ( D(36,10) + D(37,9) + D(38,8) + D(39,7) + D(40,6) ) / 5;  % bottom RH corner 10
%------------------------------------------------------------------------------------------
% Correcting error sensors of BACKGROUND, by taking average of 4 adjacent sensor coils,
% array size(D)=[40,10].
C(14,4) = ( C(13,4) + C(14,3) + C(15,4) + C(14,5) ) /4;
%C(15,6) = ( C(14,6) + C(15,5) + C(16,6) + C(15,7) ) /4;
% C(15,6) => Soldering of inductor/sensor corrected by Rafid Jwad.
C(38,1) = ( C(37,1) + C(18,10) + C(39,1) + C(38,2) ) /4;
C(33,6) = ( C(32,6) + C(33,5) + C(34,6) + C(33,7) ) /4;
C(29,4) = ( C(28,4) + C(29,3) + C(30,4) + C(29,5) ) /4;
C(29,9) = ( C(28,9) + C(29,8) + C(30,9) + C(29,10) ) /4;

%Correcting 4 corners outside Helmholtz coil field, as described above.
C(1,1) = ( C(1,5) + C(2,4) + C(3,3) + C(4,2) + C(5,1) ) / 5;  % top LH corner 1
C(1,2) = ( C(1,5) + C(2,4) + C(3,3) + C(4,2) + C(5,1) ) / 5;  % top LH corner 2
C(1,3) = ( C(1,5) + C(2,4) + C(3,3) + C(4,2) + C(5,1) ) / 5;  % top LH corner 3
C(1,4) = ( C(1,5) + C(2,4) + C(3,3) + C(4,2) + C(5,1) ) / 5;  % top LH corner 4
C(2,1) = ( C(1,5) + C(2,4) + C(3,3) + C(4,2) + C(5,1) ) / 5;  % top LH corner 5
C(2,2) = ( C(1,5) + C(2,4) + C(3,3) + C(4,2) + C(5,1) ) / 5;  % top LH corner 6
C(2,3) = ( C(1,5) + C(2,4) + C(3,3) + C(4,2) + C(5,1) ) / 5;  % top LH corner 7
C(3,1) = ( C(1,5) + C(2,4) + C(3,3) + C(4,2) + C(5,1) ) / 5;  % top LH corner 8
C(3,2) = ( C(1,5) + C(2,4) + C(3,3) + C(4,2) + C(5,1) ) / 5;  % top LH corner 9
C(4,1) = ( C(1,5) + C(2,4) + C(3,3) + C(4,2) + C(5,1) ) / 5;  % top LH corner 10

C(21,10) = ( C(21,6) + C(22,7) + C(23,8) + C(24,2) + C(25,1) ) / 5;  % top RH corner 1
C(21,9) = ( C(21,6) + C(22,7) + C(23,8) + C(24,2) + C(25,1) ) / 5;  % top RH corner 2
C(21,8) = ( C(21,6) + C(22,7) + C(23,8) + C(24,2) + C(25,1) ) / 5;  % top RH corner 3
C(21,7) = ( C(21,6) + C(22,7) + C(23,8) + C(24,2) + C(25,1) ) / 5;  % top RH corner 4
C(22,10) = ( C(21,6) + C(22,7) + C(23,8) + C(24,2) + C(25,1) ) / 5;  % top RH corner 5
C(22,9) = ( C(21,6) + C(22,7) + C(23,8) + C(24,2) + C(25,1) ) / 5;  % top RH corner 6
C(22,8) = ( C(21,6) + C(22,7) + C(23,8) + C(24,2) + C(25,1) ) / 5;  % top RH corner 7
C(23,10) = ( C(21,6) + C(22,7) + C(23,8) + C(24,2) + C(25,1) ) / 5;  % top RH corner 8
C(23,9) = ( C(21,6) + C(22,7) + C(23,8) + C(24,2) + C(25,1) ) / 5;  % top RH corner 9
C(24,10) = ( C(21,6) + C(22,7) + C(23,8) + C(24,2) + C(25,1) ) / 5;  % top RH corner 10

C(20,1) = ( C(16,1) + C(17,2) + C(18,3) + C(19,4) + C(20,5) ) / 5; % bottom LH corner 1
C(20,2) = ( C(16,1) + C(17,2) + C(18,3) + C(19,4) + C(20,5) ) / 5; % bottom LH corner 2
C(20,3) = ( C(16,1) + C(17,2) + C(18,3) + C(19,4) + C(20,5) ) / 5; % bottom LH corner 3
C(20,4) = ( C(16,1) + C(17,2) + C(18,3) + C(19,4) + C(20,5) ) / 5; % bottom LH corner 4
C(19,1) = ( C(16,1) + C(17,2) + C(18,3) + C(19,4) + C(20,5) ) / 5; % bottom LH corner 5
C(19,2) = ( C(16,1) + C(17,2) + C(18,3) + C(19,4) + C(20,5) ) / 5; % bottom LH corner 6
C(19,3) = ( C(16,1) + C(17,2) + C(18,3) + C(19,4) + C(20,5) ) / 5; % bottom LH corner 7
```

```
C(18,1) = ( C(16,1) + C(17,2) + C(18,3) + C(19,4) + C(20,5) ) / 5; % bottom LH corner 8
C(18,2) = ( C(16,1) + C(17,2) + C(18,3) + C(19,4) + C(20,5) ) / 5; % bottom LH corner 9
C(17,1) = ( C(16,1) + C(17,2) + C(18,3) + C(19,4) + C(20,5) ) / 5; % bottom LH corner 10

C(40,10) = ( C(36,10) + C(37,9) + C(38,8) + C(39,7) + C(40,6) ) / 5;  % bottom RH corner 1
C(40,9) = ( C(36,10) + C(37,9) + C(38,8) + C(39,7) + C(40,6) ) / 5;  % bottom RH corner 2
C(40,8) = ( C(36,10) + C(37,9) + C(38,8) + C(39,7) + C(40,6) ) / 5;  % bottom RH corner 3
C(40,7) = ( C(36,10) + C(37,9) + C(38,8) + C(39,7) + C(40,6) ) / 5;  % bottom RH corner 4
C(39,10) = ( C(36,10) + C(37,9) + C(38,8) + C(39,7) + C(40,6) ) / 5;  % bottom RH corner 5
C(39,9) = ( C(36,10) + C(37,9) + C(38,8) + C(39,7) + C(40,6) ) / 5;  % bottom RH corner 6
C(39,8) = ( C(36,10) + C(37,9) + C(38,8) + C(39,7) + C(40,6) ) / 5;  % bottom RH corner 7
C(38,10) = ( C(36,10) + C(37,9) + C(38,8) + C(39,7) + C(40,6) ) / 5;  % bottom RH corner 8
C(38,9) = ( C(36,10) + C(37,9) + C(38,8) + C(39,7) + C(40,6) ) / 5;  % bottom RH corner 9
C(37,10) = ( C(36,10) + C(37,9) + C(38,8) + C(39,7) + C(40,6) ) / 5;  % bottom RH corner 10
%------------------------------------------------------------------------------------------
% Transposing array D twice.
pD = D'
D2 = pD(:)' % make 2D array 'D' = image of sample object, into single row = D2

% Transposing array C twice.
pBackgrd = C'
C2 = pBackgrd(:)' % make 2D array 'C' = image of background, into single row = C2

% Subtracting background phases from sample object phases
for i=1:400   % 400 columns of one row
    D3(i) = D2(i) - C2(i); % subtract background from D2 (= sample object)
end

% Find the lowest value in D3, so as to zero data in - single row array, D4
% 400 columns long.
[D4,I]=min(D3(:));
[ID,JD] = ind2sub(size(D3),I)
display(D4)
display(ID);display(JD)

for i=1:400   % columns for one row
        D3(i) = D3(i) - D4; % subtract minimum value D4 to zero the data
end

% Transpose D3 to make it a single column array
D = D3'

% Concatenate position data array, B (2 columns 400 rows) and phase data,
% D (1 column 400 rows) to make position and phase array, B2 (3 columns 400
% rows).
B2 = [B D]
%==========================================================================
% Creating Piecewise cubic interpolation function, fo(x,y), to fit MIT image showing
% contours; fo(x,y) is to be used latter on to overlay edge onto MIT plot.

% Assign array 'B2' to x, y position and z as phase.
x=B2(:,1); y=B2(:,2); z=B2(:,3);
% Make figure the size stated below.
FigHandle = figure('Position', [100, 100, 1049, 910]);

% Create 100 linearly spaced vectors between minimum x and y. i.e. fitting
% function to 100 divisions in x and y.
% From: http://www.mathworks.co.uk/help/matlab/ref/linspace.html
xlin=linspace(min(x),max(x),100);  % was 50
ylin=linspace(min(y),max(y),100); % was 50

% Fitting Piecewise cubic interpolation function, fo(x,y,z), to the data.
% From: http://www.mathworks.co.uk/help/curvefit/fit.html
fo = fit( [x, y], z, 'cubicinterp', 'normalize', 'on' );

% 'meshgrid' replicates the grid vectors xlin and ylin to produce a full grid.
% This grid is represented by the output coordinate arrays X and Y.
% From: http://www.mathworks.co.uk/help/matlab/ref/meshgrid.html
[X,Y]=meshgrid(xlin,ylin);

% Plot fitted cubic piecewise interpolation function with contours.
```

```
plot( fo, 'Style', 'Contour' );

colormap( copper )
colorbar
%===========================================================================
% Creating 2D surface plot => MIT image, and save as a grayscale .jpg image,
% convert to a true garyscale image in next section.

% Make figure the size stated below.
Fig2Handle = figure('Position', [100, 100, 1049, 910]);

% Z = griddata(x,y,z,X,Y,'cubic') fits a surface of the form z = f(x,y) to the scattered
% data in the vectors (x,y,z). The griddata function interpolates the surface at the
% query points specified by (X,Y) and returns the interpolated values, Z. The
% surface always passes through the data points defined by x and y.
% Z = griddata(..., 'cubic') uses a specified interpolation 'cubic' to compute Z.
% From: http://www.mathworks.co.uk/help/matlab/ref/griddata.html
Z=griddata(x,y,z,X,Y,'cubic');

% surf(X,Y,Z) creates a three-dimensional shaded surface, uses Z for the color data
% and surface height. X and Y are vectors or matrices defining the x and y components
% of a surface. If X and Y are vectors, length(X) = n and length(Y) = m,
% where [m,n] = size(Z). In this case, the vertices of the surface faces are
% (X(j), Y(i), Z(i,j)) triples. To create X and Y matrices for arbitrary domains,
% use the meshgrid function, already run in the above code.
% From: http://www.mathworks.co.uk/help/matlab/ref/surf.html
surf(X,Y,Z)

% 'axis tight' sets the axis limits to the range of the data.
% From: http://www.mathworks.co.uk/help/matlab/ref/axis.html
axis tight;

% 'hold on' retains the current graph and adds another graph to it.
% MATLAB adjusts the axes limits, tick marks, and tick labels as necessary
% to display the full range of the added graph.
% From: http://www.mathworks.co.uk/help/matlab/ref/hold.html
hold on

% View plot 2D surface from on top, looking down.
view(0,90);

% Removing grid lines from plot and smoothing colour boundaries.
% From: http://www.mathworks.co.uk/help/matlab/ref/shading.html
shading flat
shading interp

% The plot3 function displays a three-dimensional plot of a set of data points.
% From: http://www.mathworks.co.uk/help/matlab/ref/plot3.html
plot3(x,y,z,'.','Marker','none')

% Remove axes labels and make figure fill the whole window.
% From: http://stackoverflow.com/questions/7561999/how-to-set-the-plot-in-matlab-to-a-
specific-size
set(gca, 'XTickLabel',[], 'YTickLabel',[], ...
    'Units','normalized', 'Position',[0 0 1 1])

% Set plot figure to 1000 by 1000 pixels.
set(Fig2Handle, 'Position', [0 0 1000 1000])

% Set color map to grayscle.
colormap (gray)

%***********CHANGE FILE NAME HERE...
% Save above plot image as .jpg file.
saveas(gcf,'C:\work\PhD_in_MIT\LabVIEW\labviewData\CuDiskGrayscale.jpg')

%***********CHANGE FILE NAME HERE...
% Open .jpg file image saved above.
open('C:\work\PhD_in_MIT\LabVIEW\labviewData\CuDiskGrayscale.jpg')

%===========================================================================
```

```
% Appying 'Canny' edge detection to grayscale image saved and opened above.

% Make figure the size stated below.
Fig3Handle = figure('Position', [100, 100, 1049, 910]);

% Applying edge detection to 'sample object image' and then overlaying
% 'detected edge' result in green over the original image. Using imoverlay
% function downloaded from:
% https://www.mathworks.co.uk/matlabcentral/fileexchange/10502-image-
overlay/content/imoverlay.m

% A = imread(filename, fmt) reads a grayscale or color image from the file
% specified by the string filename. If the file is not in the current folder,
% or in a folder on the MATLAB® path, specify the full pathname.
% From: http://www.mathworks.co.uk/help/matlab/ref/imread.html
I1 = imread('CuDiskGrayscale.jpg');

% Convert grayscale image 'CuDiskGrayscale.jpg' to 'true' grayscale.
I2 = rgb2gray(I1);

% Resize 'CuDiskGrayscale.jpg' as I2, to 1000 by 1000 pixels.
I = imresize(I2, [1000 1000]);

% Find edge of object in image, I, using matlab's canny edge detection
% algorithm, with thresholding = 0.61 (= thresh) as high threshold
% => 0.4*thresh is therefore used for the low threshold.
% Using sigma = sqrt(1000) - as the standard deviation of the Gaussian filter
% From: http://www.mathworks.co.uk/help/images/ref/edge.html
bw = edge(I, 'canny', 0.61, sqrt(1000));

% OUT = IMOVERLAY(IN, MASK, COLOR) takes an input image, IN, and a binary
% image, MASK, and produces an output image whose pixels in the MASK
% locations have the specified COLOR, in this case green = [0 1 0].
% Therefore, overlay edge detection result in green over the original image.
% From: https://www.mathworks.co.uk/matlabcentral/fileexchange/10502-image-
overlay/content/imoverlay.m
rgb = imoverlay(I, bw, [0 1 0]);

% Display resultant image.
imshow(rgb)

% find(bw) -> y, x coordinates of bw, size(find(bw)) gives e.g. sy = 966 &
% sx = 1. So it is the number of x and y's i.e. twice the number of (x,y) values in
% bw.
[sy, sx] = size(find(bw));

% Setting row in cannyXYZ(row,column) to zero.
c = 0;

% Setting cannyXYZ array to zero values. cannyXYZ is the array produced to plot
% the 'canny edge' of the 'sample object' onto the 2D MIT surface plot in the next
% section. cannyXYZ is made from scanning each pixel (1000 x 1000) from the
% overlayed Canny edge in image, rgb, obtained above.
cannyXYZ=zeros(sy,3);

% Nested for loop to check every pixel in 1000 by 1000 pixel image of rgb.
for i=1:1000 % pixel rows of image
    for j=1:1000 % pixel columns of image

        % Finding green edge in rgb(i,j,color),
        % see: http://stackoverflow.com/questions/15406816/finding-1st-red-255-0-0-pixel-
possition-using-matlab
        if squeeze( rgb(i,j,:) ) == [0;255;0]
            c = c + 1;

            % Scaling pixels to match MIT plot of 0 to 242 mm in x and y.
            % Filling array x values scaled as 242 mm = 1000 pixels.
            cannyXYZ(c,1) = j*242/1000;

            % Filling array y values scaled as 242 mm = 1000 pixels.
            cannyXYZ(c,2) = 242 - i*242/1000;
```

```
            % Filling array phase values = fo(x,y) => cubic piecewise
            % interpolation function of MIT image defined and implemented
            % earlier in the code.
            cannyXYZ(c,3) = fo(cannyXYZ(c,1),cannyXYZ(c,2));
        end
    end
end
%***********CHANGE FILE NAME HERE...
% Write array cannyXYZ to a text file.
dlmwrite('C:\work\PhD_in_MIT\LabVIEW\labviewData\cannyXYZ8c.txt', cannyXYZ, 'delimiter',
'\t', ...
         'precision', 6)
%***********CHANGE FILE NAME HERE...
% load cannyXYZ text file saved above above.
E = load('C:\work\PhD_in_MIT\LabVIEW\labviewData\cannyXYZ8c.txt'); % canny edge as x,y,z
points

% Assign array 'E'(= cannyXYZ) to xC, yC position and zC as phase.
xC=E(:,1); yC=E(:,2); zC=E(:,3);

%===========================================================================
% Plotting edge of sample object onto MIT surface plot.

% Make figure the size stated below.
Fig4Handle = figure('Position', [100, 100, 1049, 910]);

% Fitting surface of the form z = f(x,y) to the scattered data in the
% vectors (x,y,z) from the array 'B2' of the MIT surface image, run earlier
% in the code. The griddata function interpolates the surface at the
% query points specified by (X,Y) and returns the interpolated values, Z;
% using a specified interpolation 'cubic piecewise function' to compute Z.
% From: http://www.mathworks.co.uk/help/matlab/ref/griddata.html
Z=griddata(x,y,z,X,Y,'cubic');

% surf(X,Y,Z) creates a three-dimensional shaded surface, uses Z for the color data
% and surface height. X and Y are vectors or matrices defining the x and y components
% of a surface. To create X and Y matrices for arbitrary domains, the
% 'meshgrid' function is used, already run earlier in the code.
% From: http://www.mathworks.co.uk/help/matlab/ref/surf.html
surf(X,Y,Z)

% 'axis tight' sets the axis limits to the range of the data.
axis tight;

% 'hold on' retains the current graph and adds another graph to it.
% MATLAB adjusts the axes limits, tick marks, and tick labels as necessary
% to display the full range of the added graph.
hold on

view(0,90);

% Remove gridlines.
shading flat
shading interp

% Plotting MIT 2D surface plot of sample object
% The plot3 function displays a three-dimensional plot of a set of data points.
% surf(X,Y,Z) needed has already been called earlier on.
% From: http://www.mathworks.co.uk/help/matlab/ref/plot3.html
plot3(x,y,z,'.','Marker','none');
hold on

% Plotting 'Canny edge' of sample object, as markers of '.' in yellow on
% top of MIT surface plot
plot3(xC,yC,zC,'.','MarkerSize',1,'MarkerEdgeColor',[1 1 0]);

% 'hold off' resets hold state to the default behaviour, in which MATLAB
% clears the existing graph and resets axes properties to their defaults
% before drawing new plots.
hold off
```

```
% Set plot figure to 1000 by 1000 pixels.
set(Fig4Handle, 'Position', [0 0 1000 1000])

% colormap = grayscale.
colormap (gray)

% Labelling x, y and z (=phase) axes.
xlabel('x / mm')
ylabel('y / mm')
zlabel('phase \Delta\phi  / degrees')
%===========================================================================
```

14.1.2 Batch file code to measure diameter of disk image

Below is a MATLAB batch file code to automatically measure the diameter and its uncertainty of the Canny detected edge, for each of 32 disk images generated from a 50 mm diameter Copper disk. The disk was imaged from 0 to 7 cm above the sensors at 200 Hz, 500 Hz, 2 kHz and 10 kHz.

```
% Written by Brendan Darrer
% 3rd June 2014
% Department of Physics and Astronomy, University College London
%
% file name: paper3_LiftOffCanny_altogetherHz_Cu_mit4b2.m
% Matlab code to generate 2D MIT surface plots of p.d. phase-difference against x-y
coordinates.
% For comparing lift off height of copper disks
%
% oscillator = 2.6V at f = 200 Hz, 500Hz, 2 kHz, 10 kHz; lock-in amplifier: sensitivity =
% 50mV, time constant (TC) = 50ms, LabVIEW coil time (CoilT) = 500ms
% see directory:
% C:\Users\MIT1\Documents\Brendan_Darrer\UCL_AMOPP\LabVIEW\labviewData2\Cu_Al_disk_raised_up

for imageN = 1:32  % Number of images (sample & background); for loop ends at end of program

fileN = [455, 456, 457, 458, 459, 460, 461, 462, 561, 562, 563, 564, 565, 566, 567, 568,
570, 571, 572, 573, ...
    574, 575, 576, 577, 579, 580, 581, 582, 583, 584, 585, 586] % data file number of sample
image

imageDiam = [5, 5, 5, 5, 5, 5, 5, 5, 5, 5, 5, 5, 5, 5, 5, 5, 5, 5, 5, 5, ...
    5, 5, 5, 5, 5, 5, 5, 5, 5, 5, 5, 5] % disk diameter in cm

raisedUp = [0, 1, 2, 3, 4, 5, 6, 7, 0, 1, 2, 3, 4, 5, 6, 7, 0, 1, 2, 3, 4, ...
    5, 6, 7, 0, 1, 2, 3, 4, 5, 6, 7] % lift-off height in cm

material = ['Cu' 'Cu' 'Cu' 'Cu' 'Cu' 'Cu' 'Cu' 'Cu' 'Cu' 'Cu' 'Cu' 'Cu' 'Cu' 'Cu' 'Cu' 'Cu'
'Cu' 'Cu' 'Cu' 'Cu' ...
    'Cu' 'Cu' 'Cu' 'Cu' 'Cu' 'Cu' 'Cu' 'Cu' 'Cu' 'Cu' 'Cu' 'Cu']; % Copper (Cu) disk

frequency = [500, 500, 500, 500, 500, 500, 500, 500, 200, 200, 200, 200, 200, 200, 200, 200,
2000, 2000, 2000, 2000, 2000, 2000, 2000, 2000, ...
    10000, 10000, 10000, 10000, 10000, 10000, 10000, 10000] % in Hz

background = [428, 428, 428, 428, 428, 428, 428, 428, 560, 560, 560, 560, 560, 560, 560,
560, 569, 569, 569, 569, 569, 569, 569, 569, 578, 578, 578, 578, 578, 578, 578, 578] % data
file number of background image
```

```
number = num2str(fileN(imageN))

name1 =
strcat('C:\Users\MIT1\Documents\Brendan_Darrer\UCL_AMOPP\LabVIEW\labviewData2\helm2Coils',
number, '.txt')

m = 32; % number of images to process.
s = zeros(m,1);  % s = sample standard deviation.
mean_diameter_disk = zeros(m,1); % for m images

% Load .txt file arrays of, 2D positional data, background image phase and sample
A = load(name1) % raised “--”cm lift-off - Al disk: 5cm by 2mm diameter (“--” Hz): 20 x 20
array

B =
load('C:\Users\MIT1\Documents\Brendan_Darrer\UCL_AMOPP\LabVIEW\labviewData2\positionsData2_2
0x20_3.txt') % position data: 2 x 400 array

bckgrdNumber = num2str(background(imageN))
nameBckgrd =
strcat('C:\Users\MIT1\Documents\Brendan_Darrer\UCL_AMOPP\LabVIEW\labviewData2\helm2Coils',
bckgrdNumber, '.txt')

C = load(nameBckgrd) % 4 backgrounds (at freq 500 Hz, 200 Hz, 2 kHz, 10 kHz): 20 x 20 array

% correcting phase offset before sensor error correction!
% A( 1:40, 1:10 ) => A( j, i )
for i=1:10   % columns
    for j=1:40 % rows
        if (A(j,i) < 0) % correct offset, if e.g. phase = -179 when it should be 181.
            A(j,i) = 360 + A(j,i);
        end

        if (C(j,i) < 0) % correct offset, if e.g. phase = -179 when it should be 181.
            C(j,i) = 360 + C(j,i);
        end
    end
end

% Correcting error sensors in SAMPLE OBJECT image, by taking average of 4
% adjacent sensor coils, in the corss shape. Array size(D)=[40,10].
A(14,4) = ( A(13,4) + A(14,3) + A(15,4) + A(14,5) ) /4;
% D(15,6) => Soldering of inductor/sensor corrected error, by Rafid Jwad.
A(38,1) = ( A(37,1) + A(18,10) + A(39,1) + A(38,2) ) /4;
A(33,6) = ( A(32,6) + A(33,5) + A(34,6) + A(33,7) ) /4;
A(29,4) = ( A(28,4) + A(29,3) + A(30,4) + A(29,5) ) /4;
A(29,9) = ( A(28,9) + A(29,8) + A(30,9) + A(29,10) ) /4;

% Correcting 4 corners outside helmholtz coil field, by taking average of 5
% sensors (or phases) of the diagnonal/hypothenuse starting 5 sensors in x
% and ending 5 sensors in the y axis. Applying this value to the remaining
% sensors in the triangular area of the corner. Repeat this for each
% corner.
A(1,1) = ( A(1,5) + A(2,4) + A(3,3) + A(4,2) + A(5,1) ) / 5;  % top LH corner 1
A(1,2) = ( A(1,5) + A(2,4) + A(3,3) + A(4,2) + A(5,1) ) / 5;  % top LH corner 2
A(1,3) = ( A(1,5) + A(2,4) + A(3,3) + A(4,2) + A(5,1) ) / 5;  % top LH corner 3
A(1,4) = ( A(1,5) + A(2,4) + A(3,3) + A(4,2) + A(5,1) ) / 5;  % top LH corner 4
A(2,1) = ( A(1,5) + A(2,4) + A(3,3) + A(4,2) + A(5,1) ) / 5;  % top LH corner 5
A(2,2) = ( A(1,5) + A(2,4) + A(3,3) + A(4,2) + A(5,1) ) / 5;  % top LH corner 6
A(2,3) = ( A(1,5) + A(2,4) + A(3,3) + A(4,2) + A(5,1) ) / 5;  % top LH corner 7
A(3,1) = ( A(1,5) + A(2,4) + A(3,3) + A(4,2) + A(5,1) ) / 5;  % top LH corner 8
A(3,2) = ( A(1,5) + A(2,4) + A(3,3) + A(4,2) + A(5,1) ) / 5;  % top LH corner 9
A(4,1) = ( A(1,5) + A(2,4) + A(3,3) + A(4,2) + A(5,1) ) / 5;  % top LH corner 10

A(21,10) = ( A(21,6) + A(22,7) + A(23,8) + A(24,2) + A(25,1) ) / 5;  % top RH corner 1
A(21,9) = ( A(21,6) + A(22,7) + A(23,8) + A(24,2) + A(25,1) ) / 5;  % top RH corner 2
A(21,8) = ( A(21,6) + A(22,7) + A(23,8) + A(24,2) + A(25,1) ) / 5;  % top RH corner 3
A(21,7) = ( A(21,6) + A(22,7) + A(23,8) + A(24,2) + A(25,1) ) / 5;  % top RH corner 4
A(22,10) = ( A(21,6) + A(22,7) + A(23,8) + A(24,2) + A(25,1) ) / 5;  % top RH corner 5
A(22,9) = ( A(21,6) + A(22,7) + A(23,8) + A(24,2) + A(25,1) ) / 5;  % top RH corner 6
```

```
A(22,8) = ( A(21,6) + A(22,7) + A(23,8) + A(24,2) + A(25,1) ) / 5;  % top RH corner 7
A(23,10) = ( A(21,6) + A(22,7) + A(23,8) + A(24,2) + A(25,1) ) / 5;  % top RH corner 8
A(23,9) = ( A(21,6) + A(22,7) + A(23,8) + A(24,2) + A(25,1) ) / 5;  % top RH corner 9
A(24,10) = ( A(21,6) + A(22,7) + A(23,8) + A(24,2) + A(25,1) ) / 5;  % top RH corner 10

A(20,1) = ( A(16,1) + A(17,2) + A(18,3) + A(19,4) + A(20,5) ) / 5; % bottom LH corner 1
A(20,2) = ( A(16,1) + A(17,2) + A(18,3) + A(19,4) + A(20,5) ) / 5; % bottom LH corner 2
A(20,3) = ( A(16,1) + A(17,2) + A(18,3) + A(19,4) + A(20,5) ) / 5; % bottom LH corner 3
A(20,4) = ( A(16,1) + A(17,2) + A(18,3) + A(19,4) + A(20,5) ) / 5; % bottom LH corner 4
A(19,1) = ( A(16,1) + A(17,2) + A(18,3) + A(19,4) + A(20,5) ) / 5; % bottom LH corner 5
A(19,2) = ( A(16,1) + A(17,2) + A(18,3) + A(19,4) + A(20,5) ) / 5; % bottom LH corner 6
A(19,3) = ( A(16,1) + A(17,2) + A(18,3) + A(19,4) + A(20,5) ) / 5; % bottom LH corner 7
A(18,1) = ( A(16,1) + A(17,2) + A(18,3) + A(19,4) + A(20,5) ) / 5; % bottom LH corner 8
A(18,2) = ( A(16,1) + A(17,2) + A(18,3) + A(19,4) + A(20,5) ) / 5; % bottom LH corner 9
A(17,1) = ( A(16,1) + A(17,2) + A(18,3) + A(19,4) + A(20,5) ) / 5; % bottom LH corner 10

A(40,10) = ( A(36,10) + A(37,9) + A(38,8) + A(39,7) + A(40,6) ) / 5;  % bottom RH corner 1
A(40,9) = ( A(36,10) + A(37,9) + A(38,8) + A(39,7) + A(40,6) ) / 5;  % bottom RH corner 2
A(40,8) = ( A(36,10) + A(37,9) + A(38,8) + A(39,7) + A(40,6) ) / 5;  % bottom RH corner 3
A(40,7) = ( A(36,10) + A(37,9) + A(38,8) + A(39,7) + A(40,6) ) / 5;  % bottom RH corner 4
A(39,10) = ( A(36,10) + A(37,9) + A(38,8) + A(39,7) + A(40,6) ) / 5;  % bottom RH corner 5
A(39,9) = ( A(36,10) + A(37,9) + A(38,8) + A(39,7) + A(40,6) ) / 5;  % bottom RH corner 6
A(39,8) = ( A(36,10) + A(37,9) + A(38,8) + A(39,7) + A(40,6) ) / 5;  % bottom RH corner 7
A(38,10) = ( A(36,10) + A(37,9) + A(38,8) + A(39,7) + A(40,6) ) / 5;  % bottom RH corner 8
A(38,9) = ( A(36,10) + A(37,9) + A(38,8) + A(39,7) + A(40,6) ) / 5;  % bottom RH corner 9
A(37,10) = ( A(36,10) + A(37,9) + A(38,8) + A(39,7) + A(40,6) ) / 5;  % bottom RH corner 10
%------------------------------------------------------------------------------------------

% Correcting error sensors of BACKGROUND, by taking average of 4 adjacent sensor coils,
% array size(D)=[40,10].
C(14,4) = ( C(13,4) + C(14,3) + C(15,4) + C(14,5) ) /4;
% C(15,6) => Soldering of inductor/sensor corrected by Rafid Jwad.
C(38,1) = ( C(37,1) + C(18,10) + C(39,1) + C(38,2) ) /4;
C(33,6) = ( C(32,6) + C(33,5) + C(34,6) + C(33,7) ) /4;
C(29,4) = ( C(28,4) + C(29,3) + C(30,4) + C(29,5) ) /4;
C(29,9) = ( C(28,9) + C(29,8) + C(30,9) + C(29,10) ) /4;

%Correcting 4 corners outside Helmholtz coil field, as described above.
C(1,1) = ( C(1,5) + C(2,4) + C(3,3) + C(4,2) + C(5,1) ) / 5;  % top LH corner 1
C(1,2) = ( C(1,5) + C(2,4) + C(3,3) + C(4,2) + C(5,1) ) / 5;  % top LH corner 2
C(1,3) = ( C(1,5) + C(2,4) + C(3,3) + C(4,2) + C(5,1) ) / 5;  % top LH corner 3
C(1,4) = ( C(1,5) + C(2,4) + C(3,3) + C(4,2) + C(5,1) ) / 5;  % top LH corner 4
C(2,1) = ( C(1,5) + C(2,4) + C(3,3) + C(4,2) + C(5,1) ) / 5;  % top LH corner 5
C(2,2) = ( C(1,5) + C(2,4) + C(3,3) + C(4,2) + C(5,1) ) / 5;  % top LH corner 6
C(2,3) = ( C(1,5) + C(2,4) + C(3,3) + C(4,2) + C(5,1) ) / 5;  % top LH corner 7
C(3,1) = ( C(1,5) + C(2,4) + C(3,3) + C(4,2) + C(5,1) ) / 5;  % top LH corner 8
C(3,2) = ( C(1,5) + C(2,4) + C(3,3) + C(4,2) + C(5,1) ) / 5;  % top LH corner 9
C(4,1) = ( C(1,5) + C(2,4) + C(3,3) + C(4,2) + C(5,1) ) / 5;  % top LH corner 10

C(21,10) = ( C(21,6) + C(22,7) + C(23,8) + C(24,2) + C(25,1) ) / 5;  % top RH corner 1
C(21,9) = ( C(21,6) + C(22,7) + C(23,8) + C(24,2) + C(25,1) ) / 5;  % top RH corner 2
C(21,8) = ( C(21,6) + C(22,7) + C(23,8) + C(24,2) + C(25,1) ) / 5;  % top RH corner 3
C(21,7) = ( C(21,6) + C(22,7) + C(23,8) + C(24,2) + C(25,1) ) / 5;  % top RH corner 4
C(22,10) = ( C(21,6) + C(22,7) + C(23,8) + C(24,2) + C(25,1) ) / 5;  % top RH corner 5
C(22,9) = ( C(21,6) + C(22,7) + C(23,8) + C(24,2) + C(25,1) ) / 5;  % top RH corner 6
C(22,8) = ( C(21,6) + C(22,7) + C(23,8) + C(24,2) + C(25,1) ) / 5;  % top RH corner 7
C(23,10) = ( C(21,6) + C(22,7) + C(23,8) + C(24,2) + C(25,1) ) / 5;  % top RH corner 8
C(23,9) = ( C(21,6) + C(22,7) + C(23,8) + C(24,2) + C(25,1) ) / 5;  % top RH corner 9
C(24,10) = ( C(21,6) + C(22,7) + C(23,8) + C(24,2) + C(25,1) ) / 5;  % top RH corner 10

C(20,1) = ( C(16,1) + C(17,2) + C(18,3) + C(19,4) + C(20,5) ) / 5; % bottom LH corner 1
C(20,2) = ( C(16,1) + C(17,2) + C(18,3) + C(19,4) + C(20,5) ) / 5; % bottom LH corner 2
C(20,3) = ( C(16,1) + C(17,2) + C(18,3) + C(19,4) + C(20,5) ) / 5; % bottom LH corner 3
C(20,4) = ( C(16,1) + C(17,2) + C(18,3) + C(19,4) + C(20,5) ) / 5; % bottom LH corner 4
C(19,1) = ( C(16,1) + C(17,2) + C(18,3) + C(19,4) + C(20,5) ) / 5; % bottom LH corner 5
C(19,2) = ( C(16,1) + C(17,2) + C(18,3) + C(19,4) + C(20,5) ) / 5; % bottom LH corner 6
C(19,3) = ( C(16,1) + C(17,2) + C(18,3) + C(19,4) + C(20,5) ) / 5; % bottom LH corner 7
C(18,1) = ( C(16,1) + C(17,2) + C(18,3) + C(19,4) + C(20,5) ) / 5; % bottom LH corner 8
C(18,2) = ( C(16,1) + C(17,2) + C(18,3) + C(19,4) + C(20,5) ) / 5; % bottom LH corner 9
C(17,1) = ( C(16,1) + C(17,2) + C(18,3) + C(19,4) + C(20,5) ) / 5; % bottom LH corner 10
```

```
C(40,10) = ( C(36,10) + C(37,9) + C(38,8) + C(39,7) + C(40,6) ) / 5;  % bottom RH corner 1
C(40,9) = ( C(36,10) + C(37,9) + C(38,8) + C(39,7) + C(40,6) ) / 5;  % bottom RH corner 2
C(40,8) = ( C(36,10) + C(37,9) + C(38,8) + C(39,7) + C(40,6) ) / 5;  % bottom RH corner 3
C(40,7) = ( C(36,10) + C(37,9) + C(38,8) + C(39,7) + C(40,6) ) / 5;  % bottom RH corner 4
C(39,10) = ( C(36,10) + C(37,9) + C(38,8) + C(39,7) + C(40,6) ) / 5;  % bottom RH corner 5
C(39,9) = ( C(36,10) + C(37,9) + C(38,8) + C(39,7) + C(40,6) ) / 5;  % bottom RH corner 6
C(39,8) = ( C(36,10) + C(37,9) + C(38,8) + C(39,7) + C(40,6) ) / 5;  % bottom RH corner 7
C(38,10) = ( C(36,10) + C(37,9) + C(38,8) + C(39,7) + C(40,6) ) / 5;  % bottom RH corner 8
C(38,9) = ( C(36,10) + C(37,9) + C(38,8) + C(39,7) + C(40,6) ) / 5;  % bottom RH corner 9
C(37,10) = ( C(36,10) + C(37,9) + C(38,8) + C(39,7) + C(40,6) ) / 5;  % bottom RH corner 10
%------------------------------------------------------------------------------------------

p = A';
A2 = p(:)'   % make 2D array A into single row

pBackgrd1 = C';
C2 = pBackgrd1(:)' % 2D array background into single row

%_____________________________________________________________________
%subtract background from sample image
for i=1:400   % columns for one row

    A4(i) = A2(i) - C2(i); % subtract background C2 from A2

end
%_____________________________________________________________________

% check for lowest value to zero data in single row array A4 of 400 columns
% long
[A5,location] = min(A4(:));
[R_min,C_min] = ind2sub(size(A4),location)
display(A5)

for i=1:400   % columns for one row -> subtract min. value

        A4(i) = A4(i) - A5; % subtract minimum value for A4

end

result = A4'

B2 = [B result]

%==========================================================================
% Creating Piecewise cubic interpolation function, fo(x,y), to fit MIT image showing
% contours; fo(x,y) is to be used latter on to overlay edge onto MIT plot.

% Assign array 'B2' to x, y positions and z as phase.
x=B2(:,1); y=B2(:,2); z=B2(:,3);
% Make figure the size stated below.
FigHandle = figure('Position', [100, 100, 1049, 910]);

% Create 100 linearly spaced vectors between minimum x and y. i.e. fitting
% function to 100 divisions in x and y.
% From: http://www.mathworks.co.uk/help/matlab/ref/linspace.html
xlin=linspace(min(x),max(x),100);  % was 50
ylin=linspace(min(y),max(y),100); % was 50

% Fitting Piecewise cubic interpolation function, fo(x,y,z), to the data.
% From: http://www.mathworks.co.uk/help/curvefit/fit.html
fo = fit( [x, y], z, 'cubicinterp', 'normalize', 'on' );

% 'meshgrid' replicates the grid vectors xlin and ylin to produce a full grid.
% This grid is represented by the output coordinate arrays X and Y.
% From: http://www.mathworks.co.uk/help/matlab/ref/meshgrid.html
[X,Y]=meshgrid(xlin,ylin);

% Plot fitted cubic piecewise interpolation function with contours.
plot( fo, 'Style', 'Contour' );

set(gcf,'visible','off') % To make the current figure not visible.
```

```
colormap( copper )
colorbar

title('Al disk 5cm by 2mm')
xlabel('x / mm')
ylabel('y / mm')
c=colorbar
ylabel(c,'phase \Delta\phi  / degrees')

%===========================================================================
% Creating 2D surface plot => MIT image, and save as a grayscale .jpg image,
% convert to a true grayscale image in next section.

% no axes grayscale for canny edge
% Make figure the size stated below.
Fig2Handle = figure('Position', [100, 100, 1049, 910]);

% Z = griddata(x,y,z,X,Y,'cubic') fits a surface of the form z = f(x,y) to the scattered
% data in the vectors (x,y,z). The griddata function interpolates the surface at the
% query points specified by (X,Y) and returns the interpolated values, Z. The
% surface always passes through the data points defined by x and y.
% Z = griddata(..., 'cubic') uses a specified interpolation 'cubic' to compute Z.
% From: http://www.mathworks.co.uk/help/matlab/ref/griddata.html
Z=griddata(x,y,z,X,Y,'cubic');

% surf(X,Y,Z) creates a three-dimensional shaded surface, uses Z for the color data
% and surface height. X and Y are vectors or matrices defining the x and y components
% of a surface. If X and Y are vectors, length(X) = n and length(Y) = m,
% where [m,n] = size(Z). In this case, the vertices of the surface faces are
% (X(j), Y(i), Z(i,j)) triples. To create X and Y matrices for arbitrary domains,
% use the meshgrid function.
% From: http://www.mathworks.co.uk/help/matlab/ref/surf.html
surf(X,Y,Z)

% 'axis tight' sets the axis limits to the range of the data.
% From: http://www.mathworks.co.uk/help/matlab/ref/axis.html
axis tight;

% 'hold on' retains the current graph and adds another graph to it.
% MATLAB adjusts the axes limits, tick marks, and tick labels as necessary
% to display the full range of the added graph.
% From: http://www.mathworks.co.uk/help/matlab/ref/hold.html
hold on

% View plot 2D suface from on top, looking down.
view(0,90);

% Removing grid lines from plot.
% 'shading fla't each mesh line segment and face has a constant color determined
% by the color value at the endpoint of the segment or the corner of the face
% that has the smallest index or indices.
% 'shading interp' varies the color in each line segment and face by interpolating
% the colormap index or true color value across the line or face.
% From: http://www.mathworks.co.uk/help/matlab/ref/shading.html
shading flat
shading interp

% The plot3 function displays a three-dimensional plot of a set of data points.
% From: http://www.mathworks.co.uk/help/matlab/ref/plot3.html
plot3(xfd,yfd,zfd,'.','Marker','none'); %************ image stopped with ;

set(gcf,'visible','off') % To make the current figure not visible.

% Remove axes labels and make figure fill the whole window.
% From: http://stackoverflow.com/questions/7561999/how-to-set-the-plot-in-matlab-to-a-
specific-size
set(gca, 'XTickLabel',[], 'YTickLabel',[], ...
    'Units','normalized', 'Position',[0 0 1 1])

% Set plot figure to 1000 by 1000 pixels.
```

```
set(Fig2Handle, 'Position', [0 0 1000 1000])

% Set color map to grayscle.
colormap (gray)

name3 =
strcat('C:\Users\MIT1\Documents\Brendan_Darrer\UCL_AMOPP\LabVIEW\labviewData2\CuDiskGrayscal
e', number, '.jpg')


%***********CHANGE FILE NAME HERE...
% Save above plot image as .jpg file. e.g. :
%saveas(gcf,'C:\Users\MIT1\Documents\Brendan_Darrer\UCL_AMOPP\LabVIEW\labviewData2\CuDiskGra
yscale455.jpg')
saveas(gcf,name3)

%***********CHANGE FILE NAME HERE...
% Open .jpg file image saved above.
open(name3)

%=========================================================================
% Appying 'Canny' edge detection to grayscale image saved and opened above.

% Make figure the size stated below.
Fig3Handle = figure('Position', [100, 100, 1049, 910]);

% Applying egde detection to 'sample object image' and then overlaying
% 'detected edge' result in green over the original image. Using imoverlay
% function downloaded from:
% https://www.mathworks.co.uk/matlabcentral/fileexchange/10502-image-
overlay/content/imoverlay.m

% A = imread(filename, fmt) reads a grayscale or color image from the file
% specified by the string filename. If the file is not in the current folder,
% or in a folder on the MATLAB® path, specify the full pathname.
% From: http://www.mathworks.co.uk/help/matlab/ref/imread.html
%I1 = imread('CuDiskGrayscale.jpg');
I1 = imread(name3);

% Convert grayscale image 'CuDiskGrayscale.jpg' to 'true' grayscale.
I2 = rgb2gray(I1);

% Resize 'CuDiskGrayscale.jpg' as I2, to 1000 by 1000 pixels.
I = imresize(I2, [1000 1000]);

% Find edge of object in image, I, using matlab's canny edge detection
% algorithm, with thresholding = 0.61 (= thresh) as high threshold
% => 0.4*thresh is therefore used for the low threshold.
% Using sigma = sqrt(1000) - as the standard deviation of the Gaussian filter
% From: http://www.mathworks.co.uk/help/images/ref/edge.html
%bw = edge(I, 'canny', 0.61, sqrt(1000));

bwname = [sqrt(1000), sqrt(1500)]
bwc = 1;
if (imageN > 36)  % ***************** IS THIS CORRECT NUMBER - CECK EACH TIME RUN
*******************
    %bwname2 = num2str(bwname(1))
    bwc = 2;
end

bw = edge(I, 'canny', 0.61, bwname(bwc));

%bw = edge(I, 'canny', 0.61, sqrt(1000));

% OUT = IMOVERLAY(IN, MASK, COLOR) takes an input image, IN, and a binary
% image, MASK, and produces an output image whose pixels in the MASK
% locations have the specified COLOR, in this case green = [0 1 0].
% Therefore, overlay edge detection result in green over the original image.
% From: https://www.mathworks.co.uk/matlabcentral/fileexchange/10502-image-
overlay/content/imoverlay.m
rgb = imoverlay(I, bw, [0 1 0]);
```

```
% Display resultant image.
imshow(rgb)  %************ image stopped = NOT

% find(bw) -> y, x coordinates of bw, size(find(bw)) gives e.g. sy = 966 &
% sx = 1. So it is the number of x and y's i.e. twice the number of (x,y) values in
% bw.
[sy, sx] = size(find(bw));

% Setting row in cannyXYZ(row,column) to zero.
c = 0;

% Setting cannyXYZ array to zero values. cannyXYZ is the array produced to plot
% the 'canny edge' of the 'sample object' onto the 2D MIT surface plot in the next
% section. cannyXYZ is made from scanning each pixel (1000 x 1000) from the
% overlayed Canny edge in image, rgb, obtained above.
cannyXYZ=zeros(sy,3);

% Nested for loop to check every pixel in 1000 by 1000 pixel image of rgb.
for i=1:1000 % pixel rows of image
    for j=1:1000 % pixel columns of image

        % Finding green edge in rgb(i,j,color),
        % see: http://stackoverflow.com/questions/15406816/finding-1st-red-255-0-0-pixel-
possition-using-matlab
        if squeeze( rgb(i,j,:) ) == [0;255;0]
            c = c + 1;

            % Scaling pixels to match MIT plot of 0 to 242 mm in x and y.
            % Filling array x values scaled as 242 mm = 1000 pixels.
            cannyXYZ(c,1) = j*242/1000;

            % Filling array y values scaled as 242 mm = 1000 pixels.
            cannyXYZ(c,2) = 242 - i*242/1000;

            % Filling array phase values = fo(x,y) => cubic piecewise
            % interpolation function of MIT image defined and implemented
            % earlier in the code.
            cannyXYZ(c,3) = fo(cannyXYZ(c,1),cannyXYZ(c,2));
        end
    end
end

name4 =
strcat('C:\Users\MIT1\Documents\Brendan_Darrer\UCL_AMOPP\LabVIEW\labviewData2\cannyXYZ',
number, '.txt')

%***********CHANGE FILE NAME HERE...
% Write array cannyXYZ to a text file.
dlmwrite(name4, cannyXYZ, 'delimiter', '\t', ...
         'precision', 6)

% load cannyXYZ text file saved above.
E = load(name4); % canny edge as x,y,z points

% Assign array 'E'(= cannyXYZ) to xC, yC position and zC as phase.
xC=E(:,1); yC=E(:,2); zC=E(:,3);
%==========================================================================
% Calculating mean diameter of each image & it’s sample standard deviation.
c=0;
egde_hypthenuse_large = zeros(sy,1);

for i=1:sy % pixel staring points

            c = c + 1;

            egde_hypthenuse = zeros(sy,1);

            for k=1:sy % each point on circle
```

```
                egde_hypthenuse(k,1) = sqrt(( cannyXYZ(k,2) - cannyXYZ(c,2) )^2 + (
cannyXYZ(k,1) - cannyXYZ(c,1) )^2);

                if (egde_hypthenuse(k,1) > egde_hypthenuse_large(c,1))
                        egde_hypthenuse_large(c,1) = egde_hypthenuse(k,1);
                end

            end
end

sum_of_diameters = 0;

for i=1:sy

    sum_of_diameters = sum_of_diameters + egde_hypthenuse_large(i,1);

end
mean_diameter_disk(imageN,1) = sum_of_diameters/sy

sum_of_squares = 0;

for i=1:sy

    sum_of_squares = sum_of_squares + ( egde_hypthenuse_large(i,1) -
mean_diameter_disk(imageN,1) )^2;

end

s(imageN,1) = sqrt( (1/(sy-1)) * ( sum_of_squares ) ) % s = sample standard deviation.

number2b = num2str(imageDiam(imageN))
number3b = num2str(raisedUp(imageN))
mtype1b = material((imageN*2)-1)
mtype2b = material(imageN*2)
freq1 = num2str(frequency(imageN))

name2 =
strcat('C:\Users\MIT1\Documents\Brendan_Darrer\UCL_AMOPP\LabVIEW\labviewData2\LiftOffCannyDi
ameter2\LiftOffCannyDiameter2 - ', freq1,'Hz - ', mtype1b, mtype2b,' Disk - ', number2b ,'cm
by 2mm - raised up ~', number3b,'cm - data',number,'.txt')

q1 = mean_diameter_disk(imageN,1)
q2 = s(imageN,1)

save(name2,'q1','q2','-ascii')
%==========================================================================
% Plotting edge of sample object onto MIT surface plot.

% Make figure the size stated below.
Fig4Handle = figure('Position', [100, 100, 1049, 910]);

% Fitting surface of the form z = f(x,y) to the scattered data in the
% vectors (x,y,z) from the array 'B2' of the MIT surface image, run earlier
% in the code. The griddata function interpolates the surface at the
% query points specified by (X,Y) and returns the interpolated values, Z;
% using a specified interpolation 'cubic piecewise function' to compute Z.
% From: http://www.mathworks.co.uk/help/matlab/ref/griddata.html
Zfd=griddata(xfd,yfd,zfd,Xfd,Yfd,'cubic');

% surf(X,Y,Z) creates a three-dimensional shaded surface, uses Z for the color data
% and surface height. X and Y are vectors or matrices defining the x and y components
% of a surface. To create X and Y matrices for arbitrary domains, the
% 'meshgrid' function is used, already run earlier in the code.
% From: http://www.mathworks.co.uk/help/matlab/ref/surf.html
surf(Xfd,Yfd,Zfd)

% 'axis tight' sets the axis limits to the range of the data.
axis tight;

% 'hold on' retains the current graph and adds another graph to it.
% MATLAB adjusts the axes limits, tick marks, and tick labels as necessary
```

```
% to display the full range of the added graph.
hold on

view(0,90);

% Remove gridlines.
shading flat
shading interp

% Plotting MIT 2D surface plot of sample object
% The plot3 function displays a three-dimensional plot of a set of data points.
% surf(X,Y,Z) needed has already been called earlier on.
% From: http://www.mathworks.co.uk/help/matlab/ref/plot3.html
%plot3(xfd,yfd,zfd,'.','Marker','none');
plot3(xfd,yfd,zfd,'.','MarkerSize',10)

set(gcf,'visible','off') % To make the current figure not visible.

hold on

% Plotting 'Canny edge' of sample object, as markers of '.' in white on
% top of MIT surface plot
plot3(xC,yC,zC,'.','MarkerSize',5,'MarkerEdgeColor',[1 1 1]);

set(gcf,'visible','off') % To make the current figure not visible.

% 'hold off' resets hold state to the default behavior, in which MATLAB
% clears the existing graph and resets axes properties to their defaults
% before drawing new plots.
hold off

% Set plot figure to 1000 by 1000 pixels.
set(Fig4Handle, 'Position', [0 0 1000 1000])

colormap hsv
colorbar

number2 = num2str(imageDiam(imageN))
number3 = num2str(raisedUp(imageN))
mtype1 = material((imageN*2)-1)
mtype2 = material(imageN*2)
freq2 = num2str(frequency(imageN))

name5 = strcat(freq2,'Hz Phase - Canny edge - :', mtype1, mtype2,' disk :', number2,'cm by
2mm - raised up :', number3','cm')

name6 =
strcat('C:\Users\MIT1\Documents\Brendan_Darrer\UCL_AMOPP\LabVIEW\labviewData2\Cu_4freqs_disk
_raised_up_canny3\', freq2,'Hz - PHASE - ', mtype1, mtype2,' Disk - ', number2 ,'cm by 2mm -
canny edge - raised up ~', number3,'cm - data',number,'.png')

title(sprintf(name5))
%for example: title('500 Hz Phase - Canny edge - Al disk 5cm by 2mm - raised up ~0cm')
xlabel('x / mm')
ylabel('y / mm')
c = colorbar
ylabel(c,'\Delta\phi  / degrees')

saveas(gcf,name6)

end
%==========================================================================
```